Impact of Climate Change on Geostructures with Reference to Transport Infrastructure

Christopher Brice Walker

Submitted in accordance with the requirements for the degree of
Doctor of Philosophy

The University of Leeds
School of Civil Engineering

October, 2024

The candidate confirms that the work submitted is his own, except where work which has formed part of jointly-authored publications has been included. The contribution of the candidate and the other authors to this work has been explicitly indicated below. The candidate confirms that appropriate credit has been given within the thesis where reference has been made to the work of others. *Further details of the jointly-authored publications and the contributions of the candidate and the other authors to the work should be included below this statement.*

This copy has been supplied on the understanding that it is copyright material and that no quotation from the thesis may be published without proper acknowledgement.

The right of Christopher Brice Walker to be identified as Author of this work has been asserted by him in accordance with the Copyright, Designs and Patents Act 1988.

© 2024 The University of Leeds Christopher Brice Walker

Acknowledgements

I would like to express my sincere gratitude to my supervisor Dr Ana Heitor for her excellent supervision, valuable discussions, proofreading, untiring support, friendship, belief in me and approachability throughout this research. The guidance and advice she provided helped me grow as a researcher and individual. I cannot thank her enough for inspiring the confidence in me to complete this project, while always providing opportunities that go beyond my PhD. I would also like to thank my secondary supervisor Professor Barry Clarke whose helpful advice, comments and suggestions helped guide me through the initial conception of the project.

I also wish to thank Andrew Birch for his support with fabrication of equipment, trouble shooting and laboratory testing at the University of Leeds. As well as give thanks to Dr Genoveva Burca and Dr Robert Atwood for their support during testing at the Diamond Light Source Synchrotron. I would also like to thank Dr Candice Keane and Asher Lawrence-Cole for the opportunity of spending 3 months on a research Internship at the Department of Transport focussing on the resilience of the UK transport network to geological hazards.

During the period of my candidature I have also been very fortunate to receive support from the British Geotechnical Association (BGA) including the BGA fund award and Georesilience 2023 conference registration waiver. As well as the Yorkshire Geological Society Fearnsides award which allowed me to present my research at prestigious international conferences, for which I'm deeply grateful.

Special thanks is also given to Engineering and Physical Sciences Research Council – Doctoral Training partnership (DTP) scheme for funding this project. Finally, to my parents, brothers and family for supporting me throughout my PhD.

Abstract

Transport infrastructure is linear and therefore comprised of geostructures consisting of several soils of differing characteristics i.e. particle size, mineralogy and thus plasticity. Furthermore, many geostructures in the United Kingdom (UK) were constructed prior to the implementation of regulation and therefore not built to modern standards. For asset management, this is particularly important when considering predicted changes in climate patterns owing to climate change, which are expected to yield larger seasonal soil-atmosphere moisture fluctuations. This will likely result in increased drying-wetting amplitude of compacted soils following their initial compaction.

This doctoral thesis investigates the impact of drying-wetting due to climate change on the geomechnical behaviour of different compacted UK soils. This is important to determine transport infrastructure asset management strategies for future climate scenarios to ensure resilience of the rail and road networks.

To achieve this a novel drying-wetting methodology underpinned by soil water retention behaviour was developed which allows for comparison between drying-wetting of soils with different water retention characteristics. Drying-wetting boundaries were also controlled using gravimetric water content levels in order to mimic realistic field conditions typically observed at substructure level. Drying-wetting was conducted for 10 cycles on three soil mixtures representative of those incorporated into the UK transport network. This includes a low plasticity clayey sandy silt, representative of Devensian glacial tills, a high plasticity clayey silt (commercial kaolin) used to benchmark against experimental findings in the literature and a very high plasticity silty clay, similar to the London clay.

This study incorporates the use of ultrasonic pulse transmission testing validated against conventional bender element, the measurement of saturated drained stress-strain behaviour and micro X-ray computed tomography (CT) to characterise changes in microstructure at select water contents.

During drying-wetting the very high plasticity silty clay experienced the greatest reduction in small strain stiffness due to significant macroscopic cracking, while the low plasticity clayey sandy silt experienced small deviation from the compacted conditions. The results were also analysed by normalising changes in small strain stiffness and showed that an increased drying amplitude, i.e. from the transition zone to residual conditions, resulted in a reduction small strain stiffness. However, an increased wetting amplitude, from the compacted state to full saturation, resulted in a smaller comparative reduction in small strain stiffness. These findings were not

surprising and were generally in line with the microstructural changes observed for the soils following drying-wetting processes.

The results from the saturated drained stress-strain behaviour showed that irrespective of the drying and wetting boundaries adopted all soils exhibited an increase in strain softening, initial tangent modulus (E_i), peak deviator stress (q_{peak}) and dilatancy ratio (d_g). This was attributed to the increase in effective stress during drying-wetting captured by the current suction ratio (CSR)..

From a practical standpoint, when results were plotted against modified plasticity index (I_p') an inverse correlation was obtained following drying-wetting for small strain stiffness and changes in volume. In practice these findings indicate the potential for plasticity to be used as an indicator for the performance of soils, incorporated into both historic and modern infrastructure, to the impacts of climate change. Furthermore, the results highlight that soils with high Volume Change Potential (VCP) in southern England are vulnerable to post compacted changes in behaviour (e.g. cracking) when compared to Devensian glacial tills located in northern England. Indeed, UKCP18 future climate scenarios show that southern England will likely also experience increased deviations from mean rainfall and summer temperatures compared to the northern England which may exacerbate this contrast in soil behaviour.

List of Publications

The following papers are used within and related to this PhD thesis:

Refereed scholarly journal papers

Walker, C., Heitor, A. and Clarke, B. 2022. Influence of Weather-Driven Processes on the Performance of UK Transport Infrastructure with Reference to Historic Geostructures. Applied Sciences. 12(15), p7461. (included in Chapter 2)

Walker, C., Heitor, A. and Clarke, B.G. 2023. Impact of drying-wetting cycles on the small strain behaviour of compacted clay. Transportation Geotechnics. 42, p101063. (included in Chapter 4 and Chapter 6)

Refereed scholarly journal papers in preparation

Walker, C., Heitor, A. 2024. Small strain properties of compacted soil subjected to drying and wetting cycle using pulse transmission tests. Bulletin of Engineering Geology and the Environment (under review). (included in Chapter 3)

Walker, C., Heitor, A. and Clarke, B. 2024. Impact of drying-wetting cycles on the small strain behaviour of compacted soil in the UK. Géotechnique (in preparation). (included in Chapter 4 and Chapter 6)

Walker, C., Heitor, A. and Clarke, B. 2024. Saturated shear strength of compacted clay soils after drying-wetting cycles. Journal of Geotechnical and Geoenvironmental Engineering (in preparation). (included in Chapter 5)

Refereed conference papers

Walker, C., Heitor, A. and Clarke, B. 2023. Shear Wave Velocity Response of Compacted Kaolin during Drying-Wetting Cycles. In: E3S Web of Conferences: EDP Sciences, p.06011. (partially included in Chapter 2 and 3)

Walker C and Heitor A. 2024. Assessment of Shear Wave Velocity Variation in Compacted Soil Using Pulse Transmission Techniques. XVIII European Conference on Soil Mechanics and Geotechnical Engineering (in press). (partially included in Chapter 3)

Walker C, Heitor A, Clarke B. 2024. Small Strain Behaviour of Compacted Soils in Transport Infrastructure Formations Subjected to Drying and Wetting. International Conference on Transportation Geotechnics (in press). (partially included in Chapter 6)

Esteem factors

- 2024 British Geotechnical Association fund award (£1000) to support the costs associated with presenting a paper on the 5th International Conference in Transportation Geotechnics (Sydney, Australia)

- 2023 Yorkshire Geological Society Fearnsides award (£500) to support the costs associated with presenting a paper on the XVIII European Conference on Soil Mechanics and Geotechnical Engineering in Lisbon, Portugal.

- 2023 School of Civil Engineering Postgraduate Award Prize for outstanding progress in academic performance (£300)

- 2023 Department for Transport internship (£6000 scholarship)
- 2023 Yorkshire Geotechnical Group U32 presentations - 3rd place on Young professional presentations
- 2023 Georesilience 2023 conference - Registration waiver (value of £100)
- 2022 Water@Leeds SPRING Award (£500 to support the purchase of laboratory equipment)

Table of Contents

Acknowledgements ..... **II**
Abstract ..... **III**
List of Publications ..... **V**
Table of Contents ..... **VII**
List of Figures ..... **XI**
List of Tables ..... **XX**
List of Symbols ..... **XXI**
Chapter 1 Introduction **1**
1.1 Background 1
1.2 Research motivation 2
1.3 Aims and objectives 2
1.4 Thesis structure 3
Chapter 2 Literature Review **5**
2.1 Introduction 5
2.2 Transport Infrastructure Construction History in the UK 7
2.2.1 Pre-Regulation 7
2.2.1.1 Railway - 19th and early 20th Century 7
2.2.1.2 Highway - 19th and early 20th Century 10
2.2.2 Post-Regulation 10
2.2.2.1 Railway – Mid 20th and 21st Century 11
2.2.2.2 Highway – Mid 20th and 21st Century 12
2.2.3 Current Regulations 13
2.3 Geostructures vulnerabilities 14
2.4 Failure mechanisms 17
2.5 Impact of climate change on transport infrastructure assets 19
2.6 Soil-atmosphere interaction research methods 22
2.7 Impacts of hydraulic history on compacted soils 25
2.7.1 Soil water retention behaviour and hysteresis 26
2.7.2 Small strain behaviour 28
2.7.2.1 Application of small strain stiffness for the assessment of compacted soils 28
2.7.2.2 Impact of hydraulic history on small strain stiffness 31
2.7.2.3 Empirical modelling of unsaturated small strain shear modulus 39

2.7.3 Impact of hydraulic history on stress-strain behaviour 44
2.7.4 Microstructure 49
2.8 Summary and contribution 55
Chapter 3 Laboratory Testing Programme 57
3.1 General 57
3.2 Materials 59
3.3 Compaction 62
3.4 Drying and wetting 65
3.5 Determination of water retention behaviour 68
3.5.1 Suction 68
3.5.1.1 Filter paper method 69
3.5.2 Drying-wetting extents 72
3.6 Determination of volume 75
3.7 Determination of small strain stiffness 75
3.7.1 Bender element system 76
3.7.1.1 Bender element tests 77
3.7.2 Ultrasonic pulse system 77
3.7.2.1 Ultrasonic pulse test system 81
3.7.3 Benchmarking ultrasonic pulse transmission 82
3.7.3.1 Waveforms 83
3.7.3.2 Testing frequency 84
3.7.3.3 Signal to noise ratio and wave amplitude 88
3.7.3.4 Bender element and ultrasonic system comparison 89
3.7.3.5 Ultrasonic testing repeatability 93
3.7.3.6 Drying-wetting hysteresis 94
3.7.4 Determination of saturated stress-strain behaviour 97
3.7.5 Micro X-ray CT scan 100
3.8 Summary 104
Chapter 4 Small Strain Behaviour 105
4.1 General 105
4.2 Unsaturated small strain behaviour: clayey silt (high plasticity) 106
4.2.1 Shear modulus variation with water content 108
4.2.2 Void ratio variation with drying-wetting 111
4.2.3 The effects of hydraulic pathway on small strain shear modulus 113

4.3 Unsaturated small strain behaviour: clayey sandy silt (Low plasticity) ... 118
4.3.1 Drying-wetting behaviour ... 119
4.4 Unsaturated small strain behaviour: silty clay (very high plasticity) 125
4.4.1 Drying-wetting behaviour ... 127
4.5 Small stain stiffness comparison ... 132
4.5.1 Initial drying-wetting cycle behaviour ... 132
4.5.3 Drying-wetting microstructure ... 139
4.6 Summary ... 148
Chapter 5 Saturated Drained Triaxial Testing ... 150
5.1 General ... 150
5.2 Triaxial shearing in drained conditions ... 150
5.2.1 Stress-strain relationship ... 156
5.2.2 Shear-induced volume changes ... 159
5.3 Summary ... 163
Chapter 6 Engineering Application ... 164
6.1 General ... 164
6.2 Effect of plasticity small strain stiffness during drying-wetting ... 164
6.2.1 Small strain stiffness drying-wetting behaviour in the G_{max}-e space ... 172
6.3 Summary ... 176
Chapter 7 Conclusions and Recommendations ... 177
7.1 General summary ... 177
7.1.1 Key Findings ... 178
7.2 Ultrasonic pulse transmission testing ... 178
7.3 Drying-wetting small strain shear modulus behaviour ... 179
7.4 Microstructure following drying-wetting ... 180
7.5 Saturated stress strain behaviour following drying-wetting ... 181
7.6 Engineering applications ... 181
7.7 Recommended future work ... 183
List of references ... 185
Appendix A Literature Review Addendum ... 200
A.1 General ... 200
A.2 Climate change ... 200
A.3 Plasticity ... 204
A.4 Desiccation cracking ... 204

Appendix B Methodology Addendum 211
B.1 General 211
B.2 Ultrasonic Attenuation 215
B.3 Silty clay drying-wetting waveform 220

List of Figures

Figure 2-1 Painting by John Cooke Bourne (1837) showing a temporary wooden viaduct spanning a large failure alongside ongoing end-tipping works, during the construction of the Wolverton embankment. Public domain image (2004). 8

Figure 2-2 Image showing end-tipping construction method, used during early construction of the British railway, at Blackbird Road, Leicester circa 1897 (Photo reproduced with permission of Record Office for Leicestershire, Leicester and Rutland). 8

Figure 2-3 Pore water pressure profiles for London Underground Ltd clay embankments (likely consisting of uncompacted London Clay fill) constructed in the late 19th century, measured by Ridley et al. (2004) in spring 2001 and organised by foundation material including: (a) stiff London Clay and (b) river terrace deposits and chalk (modified after Briggs et al. (2013)). 17

Figure 2-4 Embankment cross section showing the development of progressive failure mechanism, where (a) is the early development of a rupture surface at the toe of the slope, followed by (b) just before failure (modified after Network Rail (2021)). 19

Figure 2-5 Cross section of a railway embankment showing the impacts relating to changing climatic patterns associated with climate change, and seasonal variation of water content and temperature with depth along the centre line, modified after Heitor et al. (2021). ... 21

Figure 2-6 Aerial photograph of the Stonehaven train derailment on the 12th of August (Photo reproduced with permission of Rail Accident Investigation Branch, 2021). 22

Figure 2-7 Unsaturated soil variables effect on transport infrastructure slope stability (modified after Gitirana (2005)). 23

Figure 2-8 Ground profile showing annual changes in moisture of geomatrials (modified after Heitor (2013)). 25

Figure 2-9 Deterioration curves showing the change in performance of an embankment over time, where: curve (a) represents a high plasticity highway embankment; (b) historic railway embankment with relict failure; (c) failure triggered by an excessively wet winter; (d) increase in seasonal extremes owing to climate change and (e) maintenance to improve performance (modified after Briggs et al. (2019)). 26

Figure 2-10 Hysteretic SWRC and associated commonly used definitions (modified after Pham et al. (2005)). 27

Figure 2-11 Typical shear strain levels for different geotechnical applications, in situ and laboratory techniques (Sawangsuriya, 2012). 28

Figure 2-12 Gloucestershire Warwickshire heritage railway embankment shear wave velocities for 5 m depth and corresponding meteorological conditions including temperature and rainfall time series recorded during 2013/2014 (Gunn et al., 2016)..... 30

Figure 2-13 Small strain shear modulus evolution for drying and wetting cycle of Esperance sand, Georgia kaolinite and Denver claystone (Dong and Lu, 2016) 32

Figure 2-14 Relationship between $\boldsymbol{Gmax/f(e)}$ and degree of saturation for three drying-wetting cycles (Ngoc et al., 2019). 32

Figure 2-15 Effect of gas saturation on both the shear and compressional wave velocity, where β is the porosity(Nakagawa et al., 1997). 33

Figure 2-16 Small strain stiffness during drying-wetting for a (a) compacted silty sand and a (b) compacted silt with and without lime treatment (Heitor et al., 2015; Tang et al., 2011). 35

Figure 2-17 Elements of large strain soil behaviour (Leroueil, 2001). 44

Figure 2-18 The variation in shear strength of different soil types at increasing matric suctions (Vanapalli, 2009). 45

Figure 2-19 Stress-strain curves for sand kaolin mixture on drying and wetting pathways (Goh et al., 2014). 45

Figure 2-20 Volume change behaviour of a silty clay subject to 6 drying-wetting cycles (Liu et al., 2020). 46

Figure 2-21 Stress-strain behaviour of compacted Po silt after Proctor compaction and post compacted embankment fill (Rojas et al., 2009). 47

Figure 2-22 Relationship between deviator stress at failure and drying/wetting cycles (drying limit 15% water content and wetting to 22% water content) for a compacted sandy clay derived from the Durham Lower Boulder Clay, tested at different confining pressure levels (modified after Stirling et al. (2020)). 48

Figure 2-23 Environmental Scanning Electron Microscopy showing the development of micro cracking for three drying-wetting cycles: (a)-(c) x15 magnification and (d)-(f) x100 magnification (Stirling et al., 2020). 48

Figure 2-24 Drying-wetting pathways after the application of an increase in suction (Stirling et al., 2020). 49

Figure 2-25 Conceptual model of the fabric of compacted clay (Wang and Wei, 2015)..... 50

Figure 2-26 Pore size groups for Proctor compaction (white dashed boxes) and static compaction methods (grey solid boxes) (Li et al., 2023)..... 51

Figure 2-27 Variation of the aggregate volume for the (a) Bioley silt and (b) kaolinitic–illitic clay during drying-wetting cycle (Koliji et al., 2010; Farulla et al., 2010). 51

Figure 2-28 Evolution of silty soil microstructure drying (Koliji et al., 2006). 52

Figure 2-29 Conceptual model for swelling of aggregates into the inter-aggregate pore space during wetting (Sivakumar et al., 2006). 53

Figure 2-30 Change in void ratio for loosely and densely compacted mixtures of bentonite and silt during one wetting and drying cycle (Nowamooz and Masrouri, 2010). 54

Figure 2-31 Environmental Scanning Electron Microscopy (ESEM) micrographs of a compacted low plasticity clayey silt, dried to a water content of 0.38% and wetted to the compacted water content (20%), where: (a) shows clay peds (aggregates), clay particles C, silt particles S, and macropores; (b) clays ped (aggregate) and macropores; (c) mesopores and; (d) ped (aggregate) breakage after undergoing drying and wetting cycles (reproduced from Azizi et al. (2019), © Canadian Science Publishing or its licensors)..... 55

Figure 3-1 Summary of laboratory testing programme for compacted specimens. 59

Figure 3-2 Particle size distribution of clayey sandy silt, clayey silt and silty clay used in this study. 61

Figure 3-3 Casagrande chart showing the plasticity of three compacted soils in this study (solid) and different soils present in the UK (hollow). 62

Figure 3-4 XRD analysis of clayey sandy silt, clayey silt and silty clay. 62

Figure 3-5 Comparison between standard Proctor compaction and static compaction (1400 kPa) for a) dry unit weight and b) void ratio. 64

Figure 3-6 Schematic diagram showing the configuration used during wetting specimens..... 65

Figure 3-7 Illustration of subsampling method to determine distribution of water content following drying-wetting. 66

Figure 3-8 Compacted clayey silt specimen water content distribution after 1hr, 12hr and 24hr equilibration time for a) full saturation, b) drying to 15% water content (w_T), c) drying to 1% water content (w_R). 66

Figure 3-9 Compacted clayey sandy silt specimen water content distribution after 1hr, 12hr and 24hr equilibration time for a) full saturation, b) drying to 5% water content (w_T), c) drying to 1% water content (w_R)..... 67

Figure 3-10 Compacted silty clay specimen water content distribution after 24hr and 7 days equilibration time for a) full saturation, b) drying to17% water content (w_T), c) drying to 1.5% water content (w_R). 67

Figure 3-11 Methods for both total (Ψ_t) and matric suction (Ψ_m) measurements in soils (Li et al., 2009)..... 68

Figure 3-12 Filter paper configuration during measurement of both contact and non-contact suctions. 70

Figure 3-13 Filter paper precision weight scales and accessories (left) and filter paper configuration (right). 70

Figure 3-14 Whatman No. 42 filter paper calibration curves for Leong and Rahardjo (2002) and ASTM D5298-10..... 71

Figure 3-15 The van Genuchten (1980) SWRC, drying-wetting boundaries and the 1st drying-wetting suction measurements for the clayey sandy silt (figures a and b), clayey silt (figures c and d) and the silty clay (figure e and f). 74

Figure 3-16 Illustration showing measurements made to determine volume of specimens. 75

Figure 3-17 Schematic diagram showing a comparison between wave propagation in soils using bender elements and ultrasonic shear wave transducers and ultrasonic compression wave transducers (modified after Mulmi et al., 2008)..... 80

Figure 3-18 Measurement of ultrasonic shear wave and compression wave transducer delay using a) shear wave face-to-face tests, b) shear wave calibration rod (known compression wave 25.4 µs travel time)..... 82

Figure 3-19 Target water contents during drying and wetting for statically compacted kaolin clay and clayey sandy silt..... 83

Figure 3-20 Variation of shear wave arrival in time domain traces (compacted clayey silt) for bender elements testing method (first deflection and first bump for frequencies ranging from 1-20 kHz)..... 85

Figure 3-21 Frequency spectra of ultrasonic system during face-to-face tests with acoustic couplant for shear wave transducers at both f_{in} 24 kHz and f_{in} 200 kHz..... 86

Figure 3-22 Variation of shear wave arrival in time domain traces (compacted clayey silt) for ultrasonic testing method (first deflection for frequencies ranging from 24-200 kHz)..... 88

Figure 3-23 Typical received wave forms in the time domain generated using ultrasonic shear wave transducers and bender elements on compacted clayey silt highlighting their characteristics used for visual picking..... 90

Figure 3-24 Ultrasonic time domain shear wave drying and wetting wave forms for a) clayey silt and b) clayey sandy silt (arrows indicate wave arrival)..... 91

Figure 3-25 Bender elements time domain shear wave drying and wetting wave forms for a) clayey silt and b) clayey sandy silt (arrows indicate wave arrival)..... 92

Figure 3-26 Ultrasonic and bender element wave velocity data during drying and wetting for: a) clayey silt shear wave and b) clayey sandy silt shear wave. 92

Figure 3-27 Shear wave velocity comparison between ultrasonic and bender element pulse transmission techniques for clayey silt and clayey sandy silt. 93

Figure 3-28 Ultrasonic shear wave traces measured on identical clayey silt specimens compacted at OMC. 94

Figure 3-29 Typical ultrasonic shear wave trace evolution in time domain during drying and wetting cycle, arrows indicate interpretation of shear wave arrival time. 95

Figure 3-30 Shear wave velocity data for single drying-wetting path (CT) measured at constant water content, presented using variables a) gravimetric water content, b) matric suction and c) suction data and main drying SWRC 96

Figure 3-31 Illustration of VJ Tech triaxial setup. 98

Figure 3-32 Change in pore water pressure during drained shearing for specimens statically compacted at OMC. 100

Figure 3-33 Schematic illustration of specimen configuration during testing (left) and specimen arrangement on sample table 1 (right). .. 101

Figure 3-34 Configuration of the imaging detector at I12 beamline (Drakopoulos et al., 2015). 102

Figure 4-1 Clayey silt drying-wetting pathway and discrete G_{max} measurement points (solid symbol) for a) FT conditions, b) FR conditions, c) CT conditions and d) CR conditions. 108

Figure 4-2 Small strain shear modulus of compacted clayey silt specimens subjected to D/W 1, 3, 6, and 10 for a) FT – full saturation to transition zone, b) FR – full saturation to residual conditions, c) CT – compacted OMC to transition zone and d) CR – compacted OMC to residual conditions (note the horizontal arrows indicate the extent of drying-wetting cycles). 109

Figure 4-3 Small strain shear modulus of compacted clayey silt specimens subjected to D/W 1, 3, 6, and 10 for a) FT – full saturation to transition zone, b) FR – full saturation to residual conditions, c) CT – compacted OMC to transition zone and d) CR – compacted OMC to residual conditions. 111

Figure 4-4 Volume change of compacted clayey silt specimens subjected to D/W 1, 3, 6, and 10 for a) FT – full saturation to transition zone, b) FR – full saturation to residual conditions, c) CT – compacted OMC to transition zone, d) CR – compacted OMC to residual conditions (note the horizontal arrows indicate the extent of drying-wetting cycles). 112

Figure 4-5 Normalized small strain shear modulus of compacted clayey silt specimens at constant water content levels during drying-wetting cycles, for amplitudes: a) FT – full saturation to transition zone, b) FR – full saturation to residual conditions, CT – compacted OMC to transition zone and d) CR – compacted OMC to residual conditions. 115

Figure 4-6 Volumetric strain at drying and wetting boundaries during the application of 10 cycles for a) FT – full saturation to transition zone, b) FR – full saturation to residual conditions, c) CT - compacted OMC to transition zone and d) CR – compacted OMC to residual conditions (compressive strains considered negative). 116

Figure 4-7 Clayey sandy silt drying-wetting pathway and discrete G_{max} measurement points (solid symbol) for a) FT, b) FR, c) CT and d) CR conditions. 119

Figure 4-8 Small strain shear modulus of compacted clayey sandy silt specimens subjected to D/W 1, 3, 6, and 10 for a) FT, b) FR, c) CT and d) CR conditions (note the horizontal arrows indicate the extent of drying-wetting cycles). 121

Figure 4-9 Volume change of compacted clayey sandy silt specimens subjected to D/W 1, 3, 6, and 10 for a) FT, b) FR, c) CT and d) CR (note the horizontal arrows indicate the extent of drying-wetting cycles). 121

Figure 4-10 Small strain shear modulus of compacted clayey sandy silt specimens subjected to D/W 1, 3, 6, and 10 for a) FT, b) FR, c) CT and d) CR conditions 122

Figure 4-11 Normalized small strain shear modulus for compacted clayey sandy silt specimens at selected water content levels during drying-wetting 123

Figure 4-12 Volumetric strain at drying and wetting boundaries for the clayey sandy silt during the application of 10 cycles for a) FT, b) FR, c) CT and d) CR conditions (compressive strains considered negative). 124

Figure 4-13 Silty clay drying-wetting pathway and discrete G_{max} measurement points (solid symbol) for a) FT, b) FR, c) CT and d) CR conditions. 126

Figure 4-14 Images showing the final failed specimens of silty clay for: a) FT – 6^{th} D/W cycle on wetting path at w_{OMC}=22%, b) FR – 3^{rd} D/W cycle on wetting path at w_{OMC}=22%, c) CT – 3^{rd} D/W cycle on wetting path at w=19% and d) CR – 2^{nd} D/W cycle on wetting path at w_{OMC}=22% 126

Figure 4-15 Small strain shear modulus of compacted silty clay specimens subjected to D/W 1, 3, 6, and 10 for a) FT, b) FR, c) CT and d) CR (note the horizontal arrows indicate the extent of drying-wetting cycles) 128

Figure 4-16 Volume change of compacted silty clay specimens subjected to D/W 1, 3, 6, and 10 for a) FT, b) FR, c) CT and d) CR (note the horizontal arrows indicate the extent of drying-wetting cycles). 129

Figure 4-17 Small strain shear modulus of compacted silty clay specimens subjected to D/W 1, 3, 6, and 10 for a) FT, b) FR, c) CT and d) CR conditions 129

Figure 4-18 Normalized small strain shear modulus for compacted silty clay specimens at selected water content levels during drying-wetting..... 130

Figure 4-19 Volumetric strain at drying and wetting boundaries during the application of 10 cycles for a) FT, b) FR, c) CT and d) CR (compressive strains considered negative). 131

Figure 4-20 Comparison of clayey sandy silt, clayey silt and silty clay for initial drying-wetting cycle showing: a) small strain shear modulus, b) void ratio, c) normalised small strain shear modulus and d) normalised void ratio. 133

Figure 4-21 Small strain shear modulus comparison of clayey sandy silt, clayey silt and silty clay during the application of 10 drying-wetting cycles for: a) FT, b) FR, c) CT and d) CR conditions. 134

Figure 4-22 Void ratio comparison for the clayey sandy silt, clayey silt and silty clay during the application of 10 drying-wetting cycles for: a) FT, b) FR, c) CT and d) CR conditions. 135

Figure 4-23 Volumetric strain comparison for the clayey sandy silt, clayey silt and silty clay during the application of 10 cycles for: a) FT, b) FR, c) CT and d) CR conditions (compressive strains considered negative). 135

Figure 4-24 Change in normalised small strain stiffness for the clayey sandy silt (10 D/W cycles), clayey silt (10 D/W cycles)and silty clay (2-6 D/W cycles) after application of all drying-wetting cycles at the compacted water content (W_{OMC}). 136

Figure 4-25 Normalised small strain shear modulus at compacted water content for clayey sandy silt (W_{OMC}=13.5%), clayey silt (W_{OMC}=28%), and silty clay (W_{OMC}=22%) comparing: a) CT/FT, b) CR/FR, c) FT/FR and d) CR/CT pathways. 137

Figure 4-26 Difference in normalised small strain shear modulus between wetting boundaries (FT/CT and FR/CR) and drying boundaries (FT/FR and CT/CR) after application of all drying-wetting cycles at the compacted water content (W_{OMC}). 138

Figure 4-27 Micro X-ray CT micrographs (com_w_{OMC}) of the compacted clayey sandy silt, clayey silt and silty clay with..... 142

Figure 4-28 Micro X-ray CT micrographs of clayey sandy silt, clayey silt and silty clay at residual conditions (initial_w_R), ... 143

Figure 4-29 Micro X-ray CT micrographs of clayey sandy silt, clayey silt and silty clay after FT (FT_10D/W_w_{OMC}_d) 144

Figure 4-30 Micro X-ray CT micrographs of clayey sandy silt, clayey silt and silty clay after FR (FR_10D/W_w_{OMC}_d) 145

Figure 4-31 Micro X-ray CT micrographs of clayey sandy silt, clayey silt and silty clay after CT (CT_10D/W_w_{OMC}_d) 146

Figure 4-32 Micro X-ray CT micrographs of clayey sandy silt, clayey silt and silty clay after CR (CR_10D/W_w_{OMC}_d)..... 147

Figure 5-1 Clayey silt stress-strain relationship (a-d) and corresponding volumetric strains (e-f) for compacted, 3rd, 6th and 10th drying-wetting cycle at 50 kPa confining stress. 154

Figure 5-2 Clayey sandy silt stress-strain relationship (a-d) and corresponding volumetric strain (e-h) for compacted, 3rd, 6th and 10th drying-wetting cycle at 50 kPa confining stress. 155

Figure 5-3 Silty clay stress-strain relationship (a) and corresponding volumetric strains (b) for drying-wetting cycle at 50 kPa confining stress. 156

Figure 5-4 Clayey sandy silt and clayey silt initial tangent modulus and peak deviator stress during drying wetting for different drying-wetting amplitudes. 157

Figure 5-5 Clayey silt stress path in *e-p'* space. 159

Figure 5-6 Clayey sandy silt stress path in *e-p'* space. 160

Figure 5-7 Silty clay stress path in *e-p'* space. 160

Figure 5-8 Influence of drying-wetting cycles on the stress-dilatancy response of clayey silt for different drying-wetting amplitudes. 161

Figure 5-9 Influence of drying-wetting cycles on the stress-dilatancy response of clayey sandy silt for different drying-wetting amplitudes. 162

Figure 5-10 Influence of drying-wetting cycles on the stress-dilatancy response of silty clay for different drying-wetting amplitudes. 162

Figure 6-1 Normalised change in void ratio (from initial compacted state) against modified plasticity index. 166

Figure 6-2 Shear wave velocity amplitude at w_{OMC} against clay activity (A) for the compacted state (black) and for FT/FR/CT/CR conditions (grey) following 10 D/W cycles for the clayey silt and clayey sandy silt and between 2-6 D/W cycles for the silty clay 167

Figure 6-3 The relationship between normalised small strain shear modulus at w_{OMC} and weighted plasticity index after all drying drying-wetting cycles for the clayey sandy silt (10 D/W cycles), kaolin clay (10 D/W cycles) and silty clay(2-6 D/W cycles). 169

Figure 6-4 UK shrink-swell potential map, based on VCP (left) (Jones and Hobbs, 2004) and annual average rainfall between 1991-2020 (right) (Met Office, 2020). 169

Figure 6-5 UKCP18 RCP 4.5 probabilistic projections for changes in rainfall (top) and temperature (bottom) in 2070 for 1981-2000 baseline (Met Office, 2024). 170

Figure 6-6 Relationship between void ratio and small strain shear modulus at constant water content for compacted clayey silt subject to 10 drying and wetting cycles for all boundary conditions (FT/FR/CT/CR). 174

Figure 6-7 Relationship between void ratio and small strain shear modulus at constant water content for compacted clayey sandy silt subject to 10 drying and wetting cycles for all boundary conditions (FT/FR/CT/CR)..... 174

Figure 6-8 Relationship between void ratio and small strain shear modulus at constant water content for compacted silty clay subject drying and wetting cycles for all boundary conditions (FT 6D/W cycles, FR 3 D/W cycles, CT 3 D/W cycles and CR 2 D/W cycles)... 175

Figure 6-9 Comparison between the relationship between normalised void ratio and normalised small strain shear modulus for the compacted clayey sandy silt (green), clayey silt (blue) and silty clay (grey) during drying-wetting..... 175

Figure A-1 UK weather data (black lines) and UKCP18 forecasts (median value blue and red lines, while the 5th, 10th, 25th, 50th, 75th, 90th, and 95th percentiles are shaded) represented in terms of: (a) mean temperature; (b) percentage summer precipitation change and (c) percentage winter precipitation change, for both RCP 2.6 in blue and 8.5 in red (contains public sector information licensed under the Open Government Licence v3.0, http://www.nationalarchives.gov.uk/doc/open-government-licence/version/3/, © Crown copyright, Met Office, (2019)). 203

Figure A-2 Example of desiccation cracks observed in Baile Hill (York) heritage asset..... 207

Figure B-1 Transmission coefficient of shear wave soil ultrasonic transducer interface during drying and wetting for compacted: a) clayey silt and b) clayey sandy silt. 217

Figure B-2 Variation in $\ln(A_r)$ against aluminium and clayey silt specimen lengths for ultrasonic shear wave transducers. 218

Figure B-3 Attenuation coefficient of shear waves in clayey silt and clayey sandy silt using the ultrasonic system during a drying and wetting cycle..... 219

Figure B-4 Silty clay waveforms collected during drying-wetting at select water content levels for FT conditions..... 220

List of Tables

Table 2-1 Comparison between both the pre-regulation and post-regulation construction techniques for embankments used during the founding of the UK railway and highway (motorway) network. 14

Table 2-2 Failure mechanism for both embankments and cutting formed in soils in the UK (adapted from Network Rail (2021)). 18

Table 2-3 Summary of literature investigating impact of drying-wetting cycles on small strain stiffness. 36

Table 2-4 Macromechanical empirical relationships for G_{max} for compacted soils, modified after Heitor et al. (2013). 41

Table 3-1 Summary of the index properties of the kaolin and target compaction conditions. 61

Table 3-2 Summary of Van Genuchten (1980) fitting parameters used to derive the main drying water retention curves for kaolin clay clayey sandy silt and silty clay. 72

Table 3-3 Drying and wetting boundaries water content. 73

Table 3-4. Summary of literature testing conditions used in ultrasonic and acoustic pulse transmission techniques. 79

Table 3-5 Summary of literature using Micro X-ray CT testing in compacted soils. 103

Table 4-1 Summary of initial compacted conditions for clayey silt specimens. 107

Table 4-2 Summary of initial compacted conditions for clayey sandy silt specimens. 118

Table 4-3 Summary of initial compacted conditions for silty clay specimens. 125

Table 4-4 Conditions of micro X-ray CT imaging 139

Table 5-1 Summary of clayey silt peak state for drained triaxial tests 152

Table 5-2 Summary of clayey sandy silt peak state for drained triaxial tests 152

Table 5-3 Summary of silty clay peak state for drained triaxial tests 153

Table 6-1 Classification of soil shrink–swell VCP (BRE, 1993). 164

Table A-1 RCPs and their resulting global mean surface temperature change from pre-industrial baseline by 2100 (adapted from Met Office (2018) and van Vuuren et al. (2011)). 201

Table B-1 Proportion of components used to create soil mixtures. 211

Table B-2 Summary of the properties of select engineering clays within the UK 212

List of Symbols

Letters

A	parameter associated with soil structure
D/W	drying wetting cycle
d_g	dilatancy ratio
e	void ratio
E_i	initial tangent modulus
E_s	secant modulus
e_w	water ratio
f	frequency
f_{in}	input frequency
f_{out}	output frequency
g	gravity acceleration
G_{max}	small strain shear modulus
I_p	plasticity index
L_b	bender element length
L_{pp}	ultrasonic transducer platen-to-platen distance
L_{tt}	bender element tip-to-tip distance
m_{final}	final mass
$m_{initial}$	initial mass
OCR	over consolidation ratio
p’	mean normal effective stress
p'_{peak}	peak mean effective stress
p_a	atmospheric pressure
p_r	reference pressure
q_f	peak deviator stress
q_{peak}	peak deviator stress
S_a	effective saturation of trapped air
S_{app}	apparent saturation
S_e	effective saturation
S_r	degree of saturation
t	wave arrival time
u_a	pore air pressure
u_w	pore water pressure
V_p	compressional wave velocity
V_s	shear wave velocity

V_s	shear wave velocity
V_s	volume of solids
V_w	volume of water
w	water content
wc_{fp}	filter paper water content
w_{final}	final water content
$w_{initial}$	initial water content
W_L	liquid limit
w_{OMC}	boundary optimum moisture content
W_P	plastic limit
w_R	boundary water content level at residual conditions
w_T	boundary water content level within the transition zone
$f(e)$	void ratio function

Greek Letters

γ_d	dry unit weight
ε_1	axial strain at failure
ε_f	strain at peak deviator stress
ε_{vs}	volumetric strain
θ	volumetric soil water content
λ	wavelength
σ	stress invariant/stress tensor
σ'	mean effective stress
σ_1'	effective major principle stress
σ_3'	effective confining pressure/effective minor principal stress
σ'_{eq}	equivalent effective stress
χ	effective stress parameter
Ψ	suction, also represented by (u_a-u_w)
$\Psi_{current}$	current suction
Ψ_m	matric suction
Ψ_{max}	maximum suction
Ψ_t	total suction

Abbreviations

AEV	Air Entry Value
CID	Consolidate Isotropic Drained shearing

CR	Drying-wetting from compacted OMC (w_{OMC}) residual conditions (w_R)
CSL	Critical State Line
CSR	Current Suction Ratio
CT	Drying-wetting from compacted OMC (w_{OMC}) and transition zone (w_T)
ESS	Equivalent Effective Stress
FR	Drying-wetting from full saturation (S_r=1) to residual conditions (w_R)
FT	Drying-wetting from full saturation (S_r=1) to the transition zone (w_T)
MDUW	Maximum Dry Unit Weight
MIP	Mercury Intrusion Porosimetry
OMC	Optimum Moisture Content
REV	Representative Element Volume
SWRC	Soil Water Retention Curve
VCP	Volume Change Potential

Chapter 1
Introduction

1.1 Background

Compacted soils included in earth structures, such as transport infrastructure embankments, are exposed to a range of persistent cyclical oscillations in hydraulic loads resulting from soil-atmosphere interactions. The extent of these interactions results from the incidence of precipitation, relative humidity and surface temperature associated with prevailing weather conditions. In addition, they are also influenced by soil properties/features such as permeability, plasticity, particle size, desiccation cracking and presence of vegetation. These geomaterials are placed and compacted using plant (e.g. vibrating or sheep foot rollers) to meet specified compaction criteria (e.g. dry unit weight and water content) and typically remain in an unsaturated condition during most of their service life, which governs their stress-strain behaviour. However, during operation, the small strain (0.001% or less) properties of these geomaterials governs the response of an earth structure subjected to dynamic loading resulting from passing traffic, while the stress-strain behaviour controls its overall stability.

In light of predicted future changes in climate, it's likely that these soils will experience conditions which alter the amplitude of seasonal hydraulic cycles. For instance, the increase in climatic extremes owing to climate change may generate increased degrees of drying and therefore more prevalent desiccation of soils. The corresponding increased suction stresses during these hotter summer periods may result in an increased amplitude of seasonal water content changes, and thus a greater volume change observed in seasonal shrink-swell cycles. This drying-wetting process can also result in weather driven deterioration relating to change in the soil microstructure i.e. the formation of micro-cracks. However, as yet the impact of drying-wetting with regards to the water retention behaviour of soils is not fully understood. Furthermore, the impact of soil composition on drying-wetting behaviour, pertinent to the geology and construction history of the UK, is also unclear. However, this is critical for asset management of geostructures to the impacts of climate change.

In this thesis, the behaviour of three compacted soils, representative of those in the UK, are examined during the application of four different amplitudes of drying-wetting. The behaviour of the soils is compared using saturated stress-strain behaviour and unsaturated small strain stiffness testing for 10 drying-wetting cycles and linked to changes in microstructure.

1.2 Research motivation

The principal motivation behind the study presented herein is related to impacts of climate change on the geostructures that support transport networks in the UK. The impacts of climate change explored in this study primarily relate to changes in water content of soils relating to the incidence of precipitation. Furthermore, many of these geostructures were constructed prior to the introduction of modern standards, which in turn exacerbates their vulnerability to climatic extremes (e.g. severe droughts and intense rainfall periods). In order to manage these assets considering future climate scenarios, a complete understanding of the geomechanical behaviour of compacted soils due to variation in moisture is required. This is critical to mitigate potential social and economic losses and ensure that infrastructure is resilient to climate change.

1.3 Aims and objectives

The goal of the study is to quantify and examine the impact of drying-wetting processes on the geomechanical behaviour of compacted soils present in the UK. In particular, the project intends to explore how drying-wetting amplitude and different hydraulic boundaries influence the behaviour of these compacted soils at different strain levels (e.g. small strain using non-destructive techniques and large strain using triaxial testing).

In addition, the project aims to provide a greater insight into how soils behave in both unsaturated and saturated conditions, considering their water retention behaviour which will be critical to develop asset management strategies to cope with a changing climate. Furthermore, a comparison of the performance of different soils present in the UK allows for an assessment of the spatial impacts of climate change, relating to underlying geology and construction history.

To achieve this, the study primarily focuses on standardisation of experimental techniques to evaluate the change in behaviour of compacted soils upon drying and wetting.

The specific objectives are as follows:

I. Development of drying-wetting techniques for determination of post compacted performance, including:
    a. a rationale for drying-wetting amplitudes for comparison between soils with different water retention behaviour,
    b. drying-wetting methodology allowing for testing at select water content levels and,
    c. validation of ultrasonic pulse transmission testing for drying-wetting of soils in unsaturated conditions.

II. Quantification of the impact of drying-wetting amplitude, hydraulic boundaries and cycles at different strain levels (e.g. small strain and large strain).

III. The determination and evaluation of the role of soil composition, primarily in terms of plasticity, on the performance of compacted soils following drying-wetting.

IV. Evaluation of the associated change in microstructure for differing drying-wetting amplitudes, number of cycles and soil compositions.

1.4 Thesis structure

The dissertation in divided in to 7 chapters. Chapter 1 introduces the background and motivation for the thesis and outlines its structure and organisation.

Chapter 2 initially reviews historic geostructures in the UK in terms of construction, vulnerabilities and the impacts of climate change. This is the followed by a state of the art review of the research methods and findings pertaining to the impact of drying-wetting cycles on the behaviour of compacted soils including soil microstructure. In particular, the behaviour at small strain using non-destructive techniques and at large strain using triaxial testing.

Chapter 3 outlines the testing programme, apparatus and methodology used in the thesis. This includes a description of basis for selection of properties for three soils created to represent soils in the UK and methodology for their compaction. The determination of water retention characteristics of the soils is also presented and the rationale behind selection of drying-wetting amplitudes is explained. A novel method for standardising drying-wetting testing using water content as a control variable is then introduced and explained. This is followed by a benchmarking exercise validating the use of a ultrasonic pulse transmission technique against bender elements for determination of small strain stiffness in soils during drying-wetting, discussing selection of appropriate testing variables. The apparatus and methodology used to conduct isotopically consolidated saturated drained triaxial (CID) testing is also discussed. Finally, specimen preparation and testing conditions adopted for the microstructure testing conducted at the I12 beamline at the Diamond Light Source synchrotron used for micro X-ray computed tomography (CT) is presented.

Chapter 4 describes the experimental results of small strain stiffness testing during drying-wetting at selected constant water content levels measured using the ultrasonic pulse transmission technique. This includes small strain shear modulus (G_{max}) and corresponding volume measurements represented by void ratio (e) for four drying-wetting amplitudes which include two wetting boundaries (full saturation and compacted water content) and two drying boundaries (transition zone and residual conditions). The

results are presented for the each of the soils and then compared and analysed by normalising results against the initial compacted conditions. The micro X-ray CT micrographs obtained for specimens tested at selected water content levels are then presented and discussed to compliment observed small strain stiffness behaviour.

Chapter 5 then presents the results of isotopically consolidated saturated drained (CID) testing for each of the soils with different hydraulic histories (e.g. drying-wetting amplitude and number of cycles). The change in stress-strain behaviour for 3, 6 and 10 drying-wetting cycles is discussed and presented using initial secant modulus (E_i) and peak deviatoric stress (q_{peak}). The volume change behaviour is also discussed primarily using the dilation ratio (d_g).

Chapter 6 provides an overview and analysis of all the results presented in the previous chapters in the context of their practical applications in the development of asset management strategies for geostructures in the UK. To achieve this the behaviour of the different soils during drying-wetting cycles is correlated to their plasticity. For this analysis, the modified plasticity index (I_p') was selected and the associated volume change potential (VCP) for the selected drying-wetting amplitudes is discussed. Furthermore, the amplitude of small strain shear modulus is also correlated to clay activity (A) of the different soils. The existence of a generalised relationship between G_{max} and I_p' for all soils tested was evaluated using normalised shear modulus. These results are then compared to the volume change potential of soils present in the UK, prevailing weather conditions and predicted climate change. Finally, the generalised relationship between G_{max}-e at selected water content levels for all soils is presented.

Chapter 7 presents a final summary of the main findings from the thesis and offers some recommendations for future work.

Chapter 2
Literature Review

2.1 Introduction

The performance of geostructures in the UK's transport network is significantly impacted by their construction age. A considerable portion of railway geostructures were constructed in the late 19th and early 20th century (Skempton, 1996). These structures were empirically designed resulting in variable geometry and material compositions, often associated with inadequate compaction conditions producing large, short term deformations and excessive settlement (Loveridge et al., 2010; O'Brien et al., 2004; Mcginnity and Russell, 1995). Early Victorian era construction was later followed by the rapid growth of highway geostructures between the 1960s and 1990s. Their design contrasts with previous efforts due to the utilisation of modern techniques such as limit equilibrium methods and principles of saturated soil mechanics (Briggs et al., 2017). Demand for transportation thereafter continued, with railway passenger numbers in 2019 twice that of the inter-war period (Noakes et al., 2020). This makes historic geostructures, which would be considered poorly constructed by contemporary standards, integral to the UK transport network. However, both their poor construction and deterioration linked to the formation of internal pore water pressures driven by atmospheric changes has been shown to impact their performance. For this reason they are comparatively more vulnerable to climate change when compared with the modern geostructures built using modern construction techniques.

Furthermore, it is likely the UK will experience more extreme weather conditions with reference to past climatic trends, due to climate change (Lowe et al., 2019). A comparison between rainfall and geostructure failures conducted by Network Rail showed a strong correlation between both variables for data between 2003 and 2020 (Network Rail, 2021). It is therefore probable that these predicted climatic changes will result in performance shortcomings of historic structures owing to unprecedented changes in hydraulic stresses (e.g. hotter summers and wetter winters). Consequently, there may be loss of productivity, increased costs, and disruption to the UK transport network. As of late 2020, these issues have been further brought to national attention by the fatal railway derailment at Stonehaven where an interim report by Network Rail acknowledged that the effects of climate change are progressing faster than initially anticipated (RAIB, 2021; Network Rail, 2021; BBC News, 2020).

Geotechnical assets in transport infrastructure, often referred as 'geostructures', are primarily split into embankments and cuttings, but also can form smaller scale works for widening, diversions, site filling or levelling (Nowak and Gilbert, 2015). Embankments

are fundamentally used to maintain formation level and provide a stable platform for placement of road-pavement or railway which experiences dynamic loading due to passing traffic. Small strain properties are therefore integral for evaluating their performance. The non-linearity of shear modulus with increasing strain makes accurate determination of small strain properties essential for accurate determination of ground movements, for example due to changes in rolling sto

ck from passenger to freight (Clayton, 2011; Dong et al., 2018). For railway it is also important to minimise differential settlement which has a small tolerable limit – usually up to five millimetres between running rails (Nowak, 2012). Cuttings somewhat differ as they often require stabilisation of side slopes to ensure debris does not impede the traffic corridor.

Network Rail alone oversees a portfolio of 190,000 earthwork geostructures (assets) of approximately 19,000 km in length, which requires continuous asset management. As of 2012 a specific earthwork risk-based management system was implemented to identify at risk earthworks to target interventions. The system is constantly being reviewed to increase resilience of the network to extreme weather (Network Rail, 2018). This encapsulates several broad vulnerabilities and allows for a general differentiation between geotechnical risks posed by different assets. However, recent research has also shown that the response of unsaturated compacted soils at both small and large strains is influenced by the soil water retention behaviour and the microstructure. This links to both the compacted soils' initial placement and the pore structure evolution following the development of a hydraulic history (Azizi et al., 2018; Azizi et al., 2019; Cheng et al., 2020; Stirling et al., 2020; Dong and Lu, 2016).

This chapter therefore aims to analyse both the historical legacy of geostructure construction in the UK, while also reviewing the current state of research pertaining to the impacts of climate change on compacted subgrade soils. It begins by providing insight into the link between historic construction practices employed during the evolution of the transport network and the present and future vulnerability of its geotechnical components to the impacts of climate change. This is then followed by a detailed review of the latest research with regard to the impacts of hydraulic history on the behaviour of compacted soils at both small and large strains. Thereafter, a review of the impact of hydraulic history on the microstructure of compacted soil is also included, which is often overlooked in practice but strongly influences compacted soil behaviour. Finally, the findings are summarised and the contribution of the current study are defined.

2.2 Transport Infrastructure Construction History in the UK

The UK has an extensive legacy of earthwork construction. This is important to consider when investigating current geostructures, as historical earthworks form a large portion of the transport network – particularly in the rail sector. It is evident that the construction history of highways and railways is extremely distinct with the majority of the railway network built prior to the implementation of regulation. As a consequence consideration of adequate compaction, suitable fill materials, slope angles and foundation were not made to modern standards.

2.2.1 Pre-Regulation

Examples of regulated construction date back to Roman Britain, but don't directly affect the current transport infrastructure network. In this paper, pre-regulation is defined as construction techniques used from the 19th century to the early 20th century – whereafter regulation was introduced. The majority of the rail network was built during this period, followed by the highway network in the mid 20th century.

2.2.1.1 Railway - 19th and early 20th Century

During 1830s/1840s nine mainline railways were empirically designed and constructed in the UK, totalling 660 miles, and included 54 million m^3 of earthwork material (Skempton, 1996). Their construction characterises the methods used during the 19th century. Compaction techniques were used in the construction of roads which were normally built at grade. In the case of the rail network, compaction was only conducted at abutments to avoid differential settlement between the rigid abutment structure and the approach embankments. End tipping was used as a cost and time saving measure to construct the embankments. Often comprising a singular lift, in which horse drawn earth wagons tipped the fill material from the advancing head (Figure 2-1 and Figure 2-2) (Nowak, 2012). This resulted in a number of failures during construction (Figure 2-1) (Skempton, 1996). Embankment settlements were large but its effects were mitigated by speed restriction and packing of ballast or locomotive ash beneath sleepers until movement subsided (O'Brien et al., 2004).

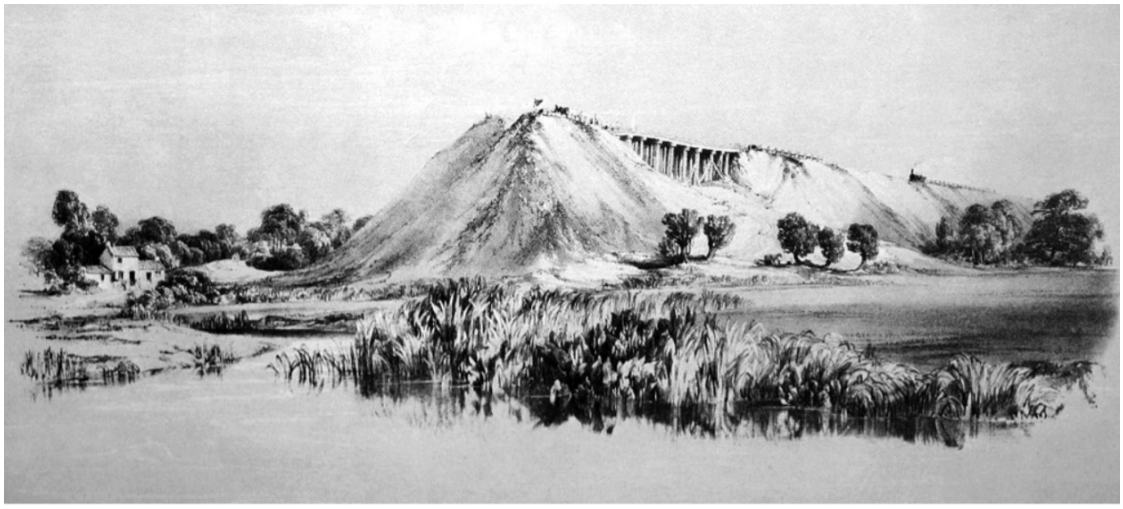


Figure 2-1 Painting by John Cooke Bourne (1837) showing a temporary wooden viaduct spanning a large failure alongside ongoing end-tipping works, during the construction of the Wolverton embankment. Public domain image (2004).

The fill material was typically taken from adjacent cuttings and thus a balance of cut and fill was ensured. This was a time saving measure which allowed large volumes to be transported over short distances for embankment construction, rather than sourcing more suitable material from borrow pits (Skempton, 1996). No foundations were prepared. In many cases embankment construction was undertaken without the removal of topsoil and other soft superficial deposits (Briggs et al., 2017).



Figure 2-2 Image showing end-tipping construction method, used during early construction of the British railway, at Blackbird Road, Leicester circa 1897 (Photo reproduced with permission of Record Office for Leicestershire, Leicester and Rutland).

At this time side slopes were covered in vegetation, and lineside fires stemming from embers emitted from passing trains, somewhat controlled its growth. Over time vegetation became mature and increased in density, therefore measures were put in place to control the likelihood of lineside fires with regular maintenance. This was important as it would have altered the dynamic balance between the beneficial and detrimental effects of vegetation on embankment stability and serviceability (Gellatley et al., 1995). For example, a significant reduction in the density of vegetation may have a positive effect on stability for restructures constructed with highly plastic, due to a decrease in seasonal soil moisture changes and therefore a reduction in differential movement along embankment crests (O'Brien et al., 2004). However, this management approach also reduces surface shielding (which would result in an increase in both surface erosion and water ingress by infiltration), root reinforcement and negatively impact ecological and environmental conditions (Gellatley et al., 1995).

Thereafter, in the early 20th century Proctor (1933) introduced modern compaction methods for dam construction. They were based on achieving soil compaction to its maximum dry density at its optimum moisture content, which could be validated using a standard compaction test. By 1936 mechanised plant (e.g. bulldozers and scrappers) were used in the UK to form a compacted embankment fill for Chingford dam (Nowak and Gilbert, 2015). In addition, Atterberg (1911) introduced consistency limits, further developed by Terzaghi (1926) and Casagrande (1932) for use in soil selection. The Transport Research Laboratory was also established in 1933 and in 1948 BS 1377 was published which included guidance on the use of Proctor compaction testing (Nowak and Gilbert, 2015).

The relationship between the beneficial and detrimental effects of vegetation continued in the early 20th century. Lineside fires still posed some risks, therefore, regular maintenance of vegetation by ‘lineside gangs’ continued. This included techniques such as grass scything and tree coppicing. Gellatley et al. (1995) also noted that earthwork slopes on the London Underground were subject to regular burning resulting in increased grass cover as fires eliminated any young vegetation preferentially.

During this period, earthwork construction on the UK railway network still remained largely empirical. For instance, an intrusive investigation of London Underground (completed circa 1930) by Mcginnity and Russell (1995) showed that embankment construction continued with minimal compaction effort. Embankments were often built directly on virgin ground; i.e. topsoil was not removed, there was no ground improvement and foundations were not routinely considered. This resulted in failures during construction and large settlements post construction (Mcginnity and Russell, 1995).

2.2.1.2 Highway - 19th and early 20th Century

Construction of turnpike roads (non-government toll roads) provided the first opportunity for standard empirical road construction methods, one of the most notable being John Loudon McAdam (1756–1836) (Nowak and Gilbert, 2015).

McAdam's system, incorporated drainage, ignored use of stone foundations and included a 30 cm layer of aggregate stone broken up and compressed by passing traffic (Kodikara et al., 2018). This technique was adopted worldwide due to its speed and low cost, however, the advent of the automobile meant a gravel surface and lack of firm foundations was not suitable for large vehicles (Nowak and Gilbert, 2015). During this early period of road construction, earthworks were less commonplace due to the ability for roads to be constructed at steeper gradients owing to the small traffic loads and slower speeds (compared to the present day). Prior to the mid-20th century, roads followed the contours of the land known as 'sidelong ground' and therefore earthworks were avoided where possible (Briggs et al., 2017). Some roads, constructed for horse and cart traffic, contained substantial earthworks in rural hilly areas. However, it wasn't until the construction of the first major highway (motorways) where lengths of continuous embankments were constructed (Perry et al., 2003).

With the advent of automobiles in the early 20th century, the structure of roads changed to accommodate a faster method of transport, but the fundamentals remained much the same as the previous century. The most significant development stemming from road infrastructure construction was the introduction of the California Bearing Ratio (CBR) by Porter (1939), which could be used to assess the thickness of subbase for a given subgrade strength and traffic load. The test was developed in the 1930s by the California Division of Highways to quantify subgrade strength by comparing its bearing capacity with a well-graded crushed stone, with a CBR value of 100%. Due to its economic, simple procedure the test has continued to be adopted for earthwork and pavement construction (Alawia and Rajab, 2013).

2.2.2 Post-Regulation

In the latter half of the 20th and 21st century several pivotal regulations, based on evolving scientific understanding of soils, were standardised for all earthworks including roads and railway, as follows (Nowak and Gilbert, 2015):

- 1951 - Specification for Road and Bridge Works introduced 'end-product' criteria
- 1959 - BS 6031 set out the code of practice for earthworks
- 1969 and 1976 - Specification for Highway Works (SWH) introduced 'method compaction'

- 1975 - BS 1377 was updated with new testing procedures
- 1986 - SHW included various updates to end-product criteria, method compaction and fill suitability selection
- 2004 - Eurocode 7 (EC7) European standards introduced into UK practice
- 2009 - BS 6031 Code of Practice for Earthworks fully updated to reflect modern methods and EC7
- 2021 – Underlying principles of the current SHW remain unchanged after the various updates in the 1970s and 1980s

2.2.2.1 Railway – Mid 20th and 21st Century

With the rise of the automobile, major railway construction slowed in comparison to construction of highways. However, due to the transition from steam power towards combustion engines and electricity for propulsion, vegetation growth became an increasing issue. For example, with the electrification of the London Underground and introduction of diesel engines, there was a decrease in the risk of lineside fires caused by the embers deriving from coal driven locomotives. This therefore resulted in reduced maintenance efforts. By the late 1960s most traditional vegetation controls were terminated and replaced with simpler herbicide treatment to control vegetation on and around the tracks themselves (Sargent, 1984). This led to vegetation growth on earthworks banks which over time was allowed to mature and diversify, leading to several issues including (Gellatley et al., 1995):

- disturbance of substructure and tracks,
- fallen branches,
- fallen trees,
- loss of traction owing to leaf fall,
- settlement or heave of overconsolidated clay soils (plastic clay fills),
- penetration or blocking of drains and ditches.

This resulted in inefficiency and disruption to running services and thus the subsequent publication of vegetation specifications in the Landscape Management Handbook *(Highways England, 2004)* for highways and Network Rail standards. Despite this, the conflict between management/removal of vegetation and potential instability (or beneficial/detrimental impacts), particularly in plastic clay fills, still poses issues. For instance, London Underground now recommends vegetation removal in the upper part of an embankment slope. This is designed to maintain stability but minimise disruption due to plasticity of the London Clay soils (Glendinning et al., 2009). The interest in these beneficial aspects was landmarked by the CIRIA publication ‘Use of Vegetation in Civil

Engineering' which introduced the concept of enhancing soil properties with vegetation (Greenwood et al., 2004).

2.2.2.2 Highway – Mid 20th and 21st Century

The Preston By-Pass was the first motorway built in the UK to highway standards and was completed by 1958 (Yeadon, 2010). Due to the increased speed of traffic, a low gradient was required (approximately 1 in 25) which required the implementation of extensive earthworks (Briggs et al., 2017). The earthworks were constructed to the Specification for Road and Bridge Works which formalised compaction to an 'end-product' criterion by setting a required percentage of dry density to be achieved during testing (Yeadon, 2010). Early highways were constructed with 8 ton deadweight rollers, including vibratory rollers by 1976 (SHW edition 5), which later became more commonplace (Nowak and Gilbert, 2015).

The construction of the Preston By-Pass took place in glacial tills and alluvial sands and silts. Due to the new specification, material was still sourced from cuttings but now exceptions were made for material deemed 'unsuitable' such as peat. This therefore produced more homogeneous fill material compared to past construction techniques (Yeadon, 2010).

Modern earthwork construction on highways continued at a rapid rate between the 1960s and 1990s, with various improvements made to specifications (Briggs et al., 2017). This led to a design-based approach, which vastly improved on pre-regulation empirical construction. This largely underpins modern earthwork design with BS 6031 Code of Practice for Earthworks, which introduced the identification of problems such as soft cohesive soils or peat during ground investigation and remediation practices. In addition, in the early 1960s excess capacity in the chemical industry led to manufacture of geotextiles for use in construction. At this time their main function was for separation and infiltration between natural ground and fill (Sarsby, 2013) but further development meant that they could be used as reinforcement in engineered soils.

In contrast to the railway network, motorways have implemented vegetation standards since the 1950s. Consideration for grass establishment was made by introducing a grass dominated topsoil layer with partial management to remove trees. In comparison, railways contains a more mixed mature line side vegetation owing to natural seeding (Glendinning et al., 2009). This means that the relationship between the beneficial and detrimental effects of vegetation, and thus impacts of climate change, are vastly different on the railway network in comparison to highways in the UK.

2.2.3 Current Regulations

Due to the recent increased recognition of climate change, it now being considered in the construction and management of the UK transport network. Both Network Rail and Highways England have developed strategies to increase resilience of their networks, which are showcased in the 'Highways England Climate Change Adaptation Strategy' and 'Network Rail Climate Change Adaptation Report', respectively (Highways England, 2009; Network Rail, 2015). Moreover, more emphasis is being put on the consideration of lineside and roadside ecosystems and its incorporation into design standards (Varley, 2018). For example, Network Rail has reduced its use of herbicide glyphosate by 25% since 2008 (Network Rail, 2020). It's probable that these changes to vegetation management are again likely to have an effect on the diversity and density of lineside vegetation in the future.

Furthermore, it is evident that the construction history of highways and railways is extremely distinct (Table 2-1). This is particularly important to consider for the railway network, due to the presence of older structures, often built before the implementation regulation. These structures therefore may produce areas of localised increased vulnerability to the impacts of climate change. This is also being considered and is a prominent part of Network Rails earthwork management review and earthworks technical strategy (Network Rail, 2021; Network Rail, 2018).

Table 2-1 Comparison between both the pre-regulation and post-regulation construction techniques for embankments used during the founding of the UK railway and highway (motorway) network.

Construction/ maintenance	Railway Only	Railway and Highway
	Pre-regulation - 19th and early 20th Century	*Post-regulation - Mid 20th and 21st Century*
Fill Material	Embankment fill sourced from adjacent cuttings with no quality control	Due to the new specifications, material was still sourced from cuttings but now exceptions were made for material deemed 'unsuitable'
Compaction	End tipping with no compaction except at bridge abutments	Earthworks were constructed to an 'end-product' criterion by setting a required percentage density or method compaction
Slope Angle	Angle of repose, due to end tipping, trimmed to 2:1	Based on stability analysis and empirical observation of different geologies
Foundations	No consideration	Topsoil stripped and various ground improvement techniques used to provide adequate foundation conditions
Vegetation Management	Line side gangs/line side fires due to steam locomotion	Mid-late 20th century no management of vegetation was made on railway geostructures
Interventions	Ash packed under the tracks if settlement occurred	Asset management procedures including various monitoring techniques

2.3 Geostructures vulnerabilities

The performance of geostructures on the transport network is related to the interactions between the atmosphere and its constituent soils. For the UK rail network, it also directly links back to the construction history of the geostructure. For instance, end tipped soils in historic embankments have been shown to form a unique microfabric which consists of stiff clods which are between 50 and 300 mm in size, surrounded by a softer matrix consisting of remoulded clay. Furthermore, London Clay embankments have been found to comprise of a clay core with relatively high water content compared to the side slopes which contain much lower water contents (O'Brien et al., 2004). Indeed following placement of fill, the growth of vegetation, cyclic soil-atmosphere interaction and cycling loading has resulted in micro-scale and macro-scale deterioration such as alteration of soil fabric due to weathering processes and irrecoverable deformations and accumulation of strains i.e. formation of micro-cracking and resultant changes in

permeability and unsaturated shear strength (Briggs et al., 2023). Loveridge et al. (2010) reported the presence of variable permeability for clay fill due to embankment age and therefore construction techniques. This variation is important to consider as the degree of permeability impacts the pore water pressure/atmospheric response of a structure. In addition, the heterogeneity of the fill material (again linked to its construction history) is also an important factor for the resilience of compacted soil. This was demonstrated by O'Brien (2013) using numerical modelling, where the inclusion of soft alluvial clay lenses within London Clay embankment fill material and small changes in maximum winter pore water pressures, significantly decreased the number of shrink-swell cycles required until slope failure.

Despite this, Loveridge et al. (2010) suggests that due to the likelihood of increased future evapotranspiration in certain future scenarios (i.e. where Very High Water Demand, VHWD, trees are situated), infiltration may be reduced and an increase in surface run-off may be predominant. Although counterintuitive, this demonstrates the complexities of contrasting stabilising and destabilising forces produced by the interaction between the atmosphere, clay fill and vegetation. An understanding of this is important, as generally in design it's assumed that saturated soil under hydrostatic conditions is the 'worst case' scenario. However, when evaluating the relative risk of comparable embankments this assumption is overly simplistic as a myriad of factors are involved, often dealing with unsaturated soil mechanics. This also includes factors which add further complexity and are both transient and highly variable – i.e. the soil microstructure and its behaviour dependency on seasonal variation in climate. Loveridge et al. (2010) suggests a list of several further important factors including:

- plasticity,
- susceptibility to erosion and degradation,
- vegetation type and distribution,
- permeability and permeability contrasts,
- underdrainage and 'hidden defects' (relict failures, or pockets of different permeability).

Loveridge et al. (2010) further suggested that permeability and vegetation may be of most significance due to their role in formation of pore water pressures, but are not considered in routine site investigations, risk assessments or analysis. O'Brien (2013) drew similar conclusions, adding that permeability and vegetation directly relate to the development and evolution of seasonal pore water pressures, which ultimately control stability. This was most intuitively shown by Briggs et al. (2013) using VADOSE modelling of a railway embankment with Newbury weather data for 2005/2006, where

the Soil Moisture Deficit varied between 0mm and 150 mm. The results of sensitivity analyses showed that upon tree removal in the upper two-thirds of the slope, much larger positive pore water pressures were observed during the winter in the near surface (upper 2 m). However, negative pore pressures (i.e., suction) were maintained at depth. It was also determined that clay fill permeability within a critical range between 5×10^{-8} m/s and 5×10^{-7} m/s had a significant influence on the development of positive pore water pressures.

Similarly, Loveridge et al. (2010) also suggests that the permeability of railway embankments are closer (than highways embankments) to 'a band of critical permeability'. The critical permeability corresponds to UK average rainfall rates and was identified as being 1×10^{-7} m/s (i.e. soil permeability which allows water to ingress in slopes during periods of rainfall). This is likely the result of reduced compactive effort being employed on historic railway embankments, but also the presence of tree roots (evapotranspiration) and desiccation cracking (Loveridge et al., 2010). As a result, it's probable that water is able to percolate more deeply into historic embankments as opposed to running off the surface. In addition, as the embankments have often remained under unsaturated conditions, this in turn influences the infiltration rates as unsaturated permeability can be directly linked to the soil water retention behaviour. Furthermore, as these processes take place seasonally, slight changes in negative pore pressures can induce hydraulic hysteresis and this in turn has a significant effect on unsaturated permeability.

In-situ testing has demonstrated the implication of these factors on embankment pore water pressures, the most notable of which is the Achilles Bionics test embankment (Hughes et al., 2009). A full-scale model embankment was constructed in glacial till considering different densities and capping fill materials. The observations made over time in this field embankment demonstrated that change in compaction level, and therefore permeability, had a significant impact on the variability of both negative and positive pore water pressures (Hughes et al., 2009). In addition, field monitoring of negative pore water pressure, undertaken by Toll et al. (2011) at Boissy-le Châtel, France, further demonstrated the hysteretic nature of pore water pressures. Monitoring took place at depths of 0.25 m and 0.45 m between May and June 2004. It was shown that the change in negative pore water pressure was greater at 0.45 m than 0.25 m after four separate rainfall events. Toll et al. (2011) attributed this to hysteresis, as the upper 0.25 m was closer to the bounding wetting curve compared to 0.45 m depth, resulting in a greater loss of negative pore pressure at 0.45 m. Deeper in-situ pore water pressure measurements made by Ridley et al. (2004) of London Underground historic embankments between March and August 2001, demonstrated the complex effect of

contrasting permeabilities. It was shown that under drainage resulting from high permeability foundation material produced conditions which reduced positive pore water pressures at depth. The results of Ridley et al. (2004) data collection, and interpretation made by Briggs et al. (2013) are shown in Figure 2-3. The contrasting pore water pressure profiles for an initially uncompacted stiff clay overlying stiff London Clay, Chalk and coarse grained soils is evident, with embankments overlying stiff London Clay trending much closer to hydrostatic pore water pressures within the same period of time. This research thus highlights that compaction conditions, hysteresis of the near surface and foundation drainage conditions (which are highly influenced by construction history) can alter the pore pressure profile of a geostructure and therefore affect its vulnerability to the effects of climate.

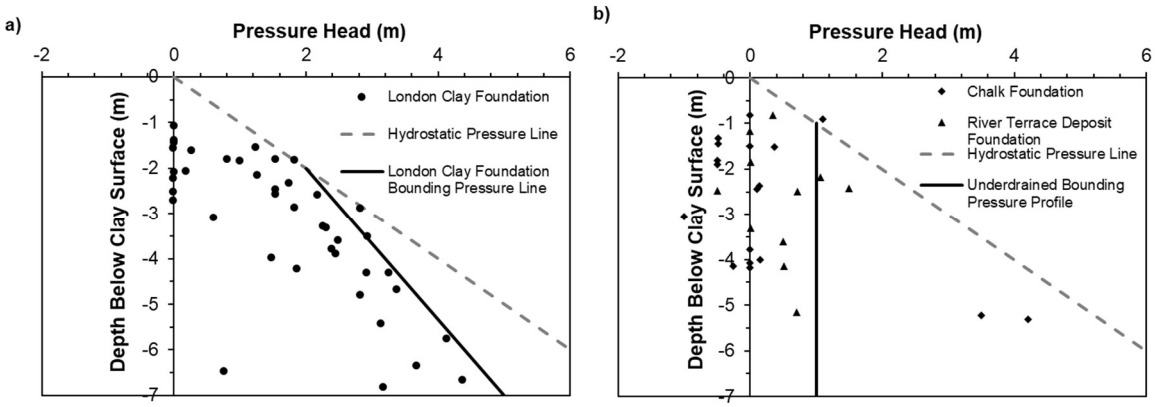


Figure 2-3 Pore water pressure profiles for London Underground Ltd clay embankments (likely consisting of uncompacted London Clay fill) constructed in the late 19th century, measured by Ridley et al. (2004) in spring 2001 and organised by foundation material including: (a) stiff London Clay and (b) river terrace deposits and chalk (modified after Briggs et al. (2013)).

2.4 Failure mechanisms

The combination of climate, resultant pore pressures and relict vulnerabilities owing to construction methods, such as end tipping (prominent on the railway network) have led to infrastructure failures, most recently the Stonehaven train derailment in August 2020. In response to this, Network Rail appointed a Task Force led by Professor Lord Robert Mair to compile a report with the aim of reviewing asset management in light of climate change. The Network Rail (2021) review details the most recent industry experience and observations. Table 2-2 summarises the most significant findings of the report relating to failure mechanisms. It presents the relationship between both failure mechanisms and vulnerability to climate, identifying four main failure types including deep-seated failure, shallow translational failure, washouts and debris flows.

Table 2-2 Failure mechanism for both embankments and cutting formed in soils in the UK (adapted from Network Rail (2021)).

Failure Mechanisms	Causes of Climate Vulnerability
Deep-seated Rotational Failure	• Presence of relict failure surfaces due to poor historic construction practices • Over steepened cut slopes in plastic clays (26 degrees rather than stable 14 degrees) and embankment slopes • Reactivation of low strength residual shear surfaces due to increase in pore water pressure (inadequacy of historic drainage) • Increase in destabilising forces including loading of the head of a slope, train loading on embankments or unloading of the toe of the slope due to erosion and shallow failures • Formation of progressive failure due to ratcheting of the slope surface resulting from shrink-swell of the weathered surface
Shallow Translational Failure	• Formation of a weathered zone owing to seasonal shrink-swell and formation of micro-cracking and desiccation • Increase in permeability of the surficial weathered layer allowing penetration of water in the near surface, reducing negative pore pressures, resulting in downslope flow and formation of perched water tables • Intense summer rainfall and presence of desiccation cracks possibly allowing for hydraulic forces to act between cracks and thus initiate a shallow slump • Presence of vegetation which increases seasonal shrink-swell cycles, aiding in the deterioration of the weathered front • Internal erosion and undercutting resulting from the increased permeability and outflow of water from the slope surface
Washout	• Erosion resulting from over-ground flow during intense rainfall, usually resulting from the presence of insufficient drainage
Debris Flow	• Movement of vegetation and soil resulting from intense rainfall and surface flows initiated from washouts or earth flows from a shallow failure

The report demonstrates that both deep seated and shallow translational failure types are directly related to the interaction of climate and geostructures over extended periods. Indeed, researchers including Kovacevic et al. (2001), Nyambayo et al. (2004) and Take and Bolton (2011) have shown that seasonal cycles of pore water pressures (in the near surface) in clay embankments produces a progressive deep-seated failure mechanism. This is most notable for embankments in the Midlands and southern England in stiff overconsolidated sedimented clays, where soil plasticity is higher in comparison to Devensian glacial tills found more commonly in northern parts of the UK. Numerical and centrifuge modelling has demonstrated that a ‘ratcheting’ effect of seasonal pore water pressures takes place, where outwards deformation during winter is only partially recovered by shrinkage during the summer. This type of failure has been shown to

develop at the toe of a slope and propagate to the centre under repeated hydraulic stress cycling. This results in a non-uniform distribution of strength where the toe of the slope is at residual strength and the crest at peak strength (Figure 2-4). Importantly, it was found the permeability of the clay fill material controls the number of cycles until failure.

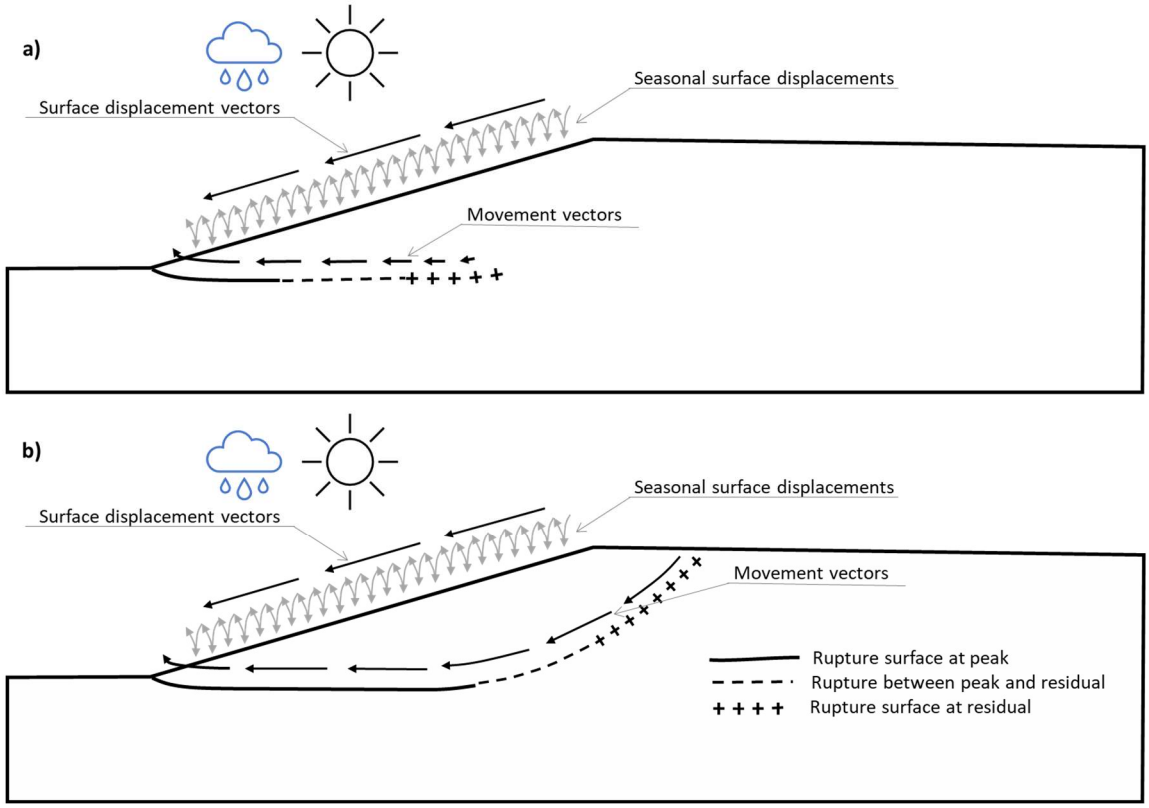


Figure 2-4 Embankment cross section showing the development of progressive failure mechanism, where (a) is the early development of a rupture surface at the toe of the slope, followed by (b) just before failure (modified after Network Rail (2021)).

Deep-seated failure mechanisms have also been attributed to historic construction practices. This generally results from over steepened cut slopes and embankment gradients and the presence of relict failure surfaces, particularly in cuttings. This produces highly localised vulnerabilities, which exacerbate geotechnical risk especially with respect to climatic changes.

2.5 Impact of climate change on transport infrastructure assets

UKCP18 predicts (for a high emissions scenario RCP 8.5) by the year 2070 the UK climate will experience more climatic extremes. It predicts increased seasonal temperatures for both winter (warming range of 0.7°C – 4.2°C) and summer (warming range of 0.9°C – 5.4°C). An increased frequency of hot spells from once every four years to four times every year. Average winter precipitation is projected to increase by 35% and summer rainfall is expected to decrease by 47%. Finally, a 25% increase in the likelihood of extreme hourly intense rainfall is also projected (Lowe et al., 2019). As a

consequence, the intensity and frequency of periods of drought and the intensity of rainfall will provide significant deviation from weather patterns experienced by compacted soils in previous centuries. More details regarding climate change modelling in the UK can be found in Walker et al. (2022) and are included in Appendix A for completeness.

These climatic changes are expected to yield several transient and spatially complex effects on the geotechnical assets of the transport infrastructure network. Several important aspects associated with the transport infrastructure performance in a changing climate have been outlined by Tang et al. (2018) and Heitor et al. (2021), and are illustrated in Figure 2-5:

- the impact of climate change on the European subcontinent will vary with location; the northwest being affected most greatly by increased winter precipitation, soil water content and therefore rainfall induced slope instability, while the Mediterranean region is expected to experience larger temperature rises compared to the European average and reduced annual precipitation,
- increased surface runoff may result in external erosion owing to the loss of vegetation during drought periods (this requires consideration for future drainage design),
- desiccation will increase infiltration resulting in increased pore pressure response and internal erosion (further discussed in Appendix A.4),
- the impact of shrink swell in plastic soils will increase due to the cyclic nature of wetter winters and drier summers,
- the frequency of these shrink swell cycles may also increase due to summer storms (which will intensify progressive failure mechanisms),
- saturation, resulting from increased average rainfall and extreme events, in combination with the above factors will increase the pore water response in winter months.

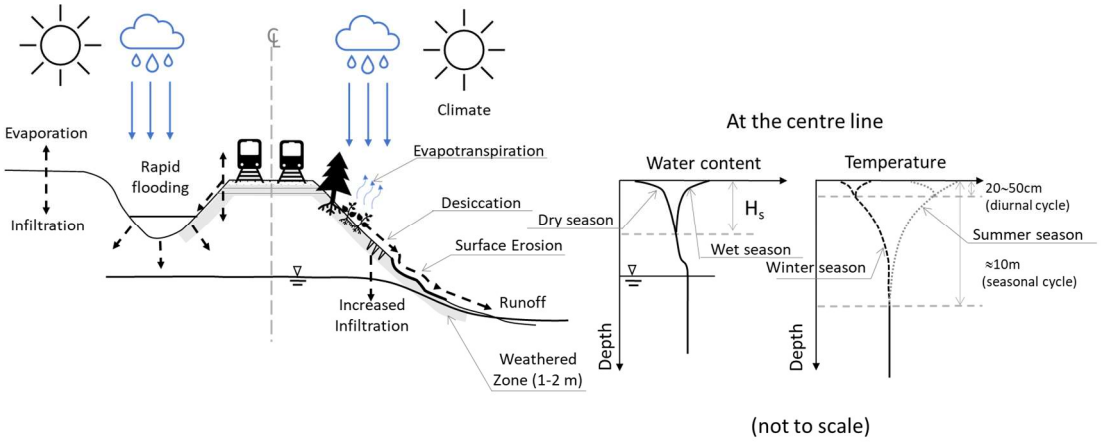


Figure 2-5 Cross section of a railway embankment showing the impacts relating to changing climatic patterns associated with climate change, and seasonal variation of water content and temperature with depth along the centre line, modified after Heitor et al. (2021).

Some of these factors have been previously investigated by Clarke and Smethurst (2010) using numerical modelling based on UKCP09 predictions, focusing on the UK and its predicted future climate. It was shown that future climate change will likely have a significant effect on the soil moisture of geostructures incorporating clay materials. In particular this would be more prevalent for the southeast of England as the soil moisture deficit range would increase. This was mainly attributed to an increased loss of moisture during the summer months, resulting in a larger winter to summer moisture cycles (Figure 2-5). It was therefore surmised that a London Clay slope, for example, would undergo increased desiccation and a resultant loss of vegetation as it reaches the wilting point (the minimum amount of soil moisture required for a plant to no longer wilt). It would also experience increased shrink-swell and erosion due to surface runoff resulting from the lack of vegetative protection.

Empirical evidence of the impact of climate on geostructures is also beginning to emerge, e.g. train derailment between Aberdeen and Glasgow, near Stonehaven (Figure 2-6). This rail incident further emphasised the need to proactively manage the impacts of climate change on historical transport infrastructure assets. The incident report postulated that the cause of the derailment was associated with a washout from the adjacent cutting which was a result of heavy locally intense rainfall and thunderstorms (RAIB, 2021).

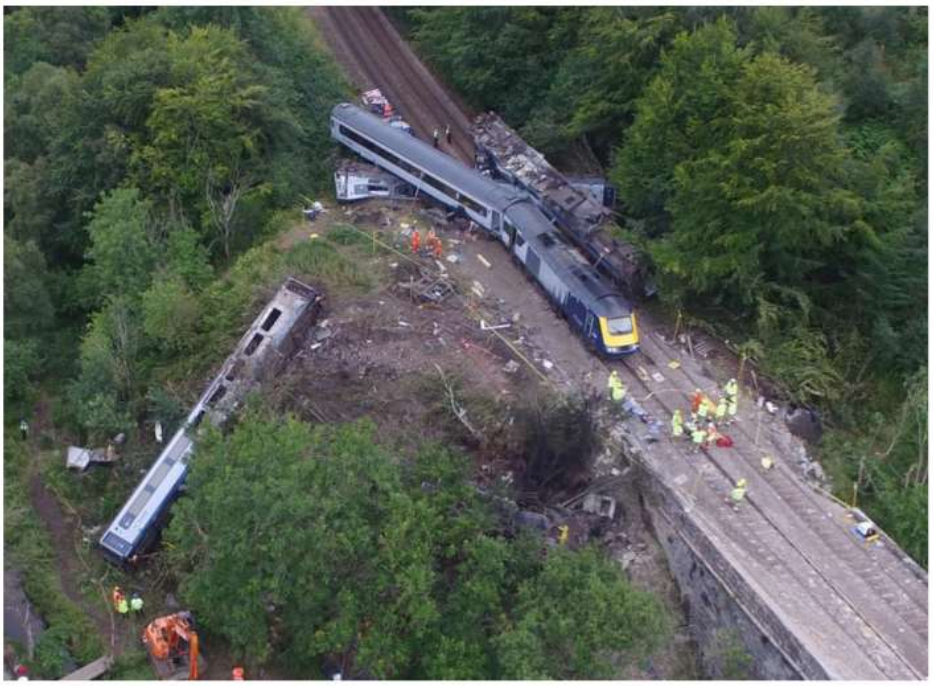


Figure 2-6 Aerial photograph of the Stonehaven train derailment on the 12th of August (Photo reproduced with permission of Rail Accident Investigation Branch, 2021).

2.6 Soil-atmosphere interaction research methods

The UK's historical geotechnical infrastructure experiences several changes between saturated and unsaturated states annually, which impact behaviour of the soil. The issue can be conceptualised using a framework of unsaturated variables set out by Gitirana (2005), which are useful to consider when designing an investigation into the interaction of geostructures and weather related geohazards. The flow diagram in Figure 2-7 outlines their relationship to the Factor of Safety (FOS). The square boxes represent 'fixed' values while the circular boxes are 'uncertain' variables. This approach demonstrates the considerable quantity of complex interactions between unsaturated soil variables required for assessing slope stability.

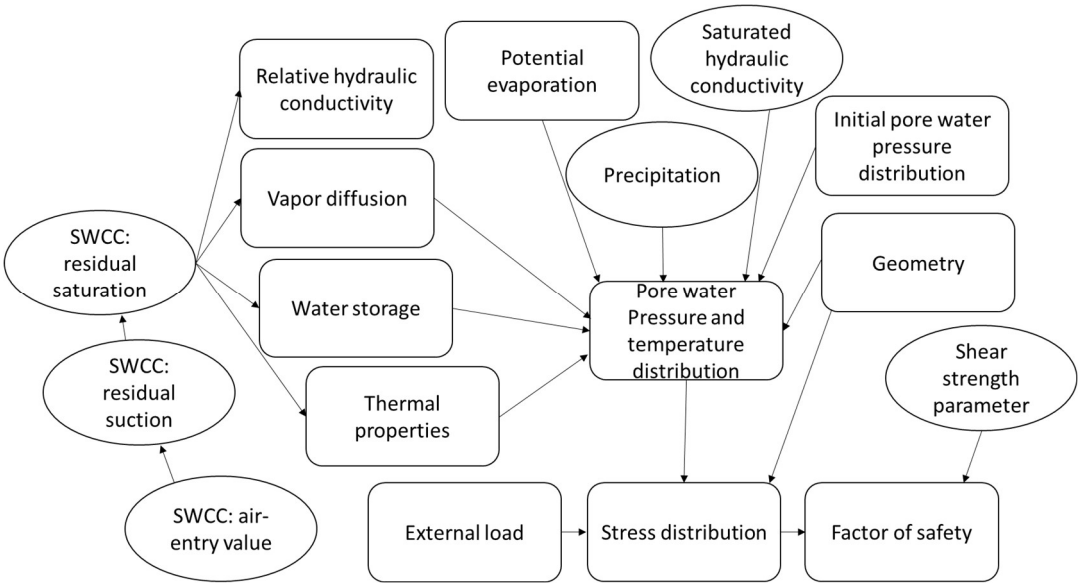


Figure 2-7 Unsaturated soil variables effect on transport infrastructure slope stability (modified after Gitirana (2005)).

It is notoriously difficult to test these complex soil-atmosphere interactions in the laboratory in a truly representative manner. Furthermore, the interaction of these factors with the soil fabric provides further complexity which is difficult to capture and measure. Therefore, it is generally considered that full scale embankment testing to be a more representative approach. This was shown by Glendinning et al. (2014) where laboratory permeability tests were a magnitude lower than the in-situ equivalent. This was a result of the absence of macroscale features (e.g., desiccation cracks and plant roots) in laboratory samples, sampling time and differences in testing depth.

The Bionics test embankment in northeast England was constructed to circumvent this problem and allow for field monitoring of soil behaviour on a full-scale embankment (Hughes et al., 2009; Toll et al., 2012). The testing regime included permeability testing, pore water pressure monitoring and Electrical Resistivity Tomography (ERT) (Glendinning et al., 2015; Toll et al., 2012; Mendes, 2011). The results were able to demonstrate the heterogeneity of pore water response within the embankment owing to prevailing wind direction, vegetation type, capping type (surface permeability) and compaction conditions (Glendinning et al., 2014). This approach allowed for the investigation of both micro and macro structures that element testing alone could not capture. However, the number of monitoring points in terms of depth and spatial distribution, as well as the occurrence of uncontrollable variables such as pooling water on the slope surface, provide some limitations (Glendinning et al., 2014). Moreover, in the wider context of transport network, the spatial variability of historical geostructures (including their construction materials and techniques) produces an additional layer of complexity which is difficult to evaluate. These limitations make it challenging to come to absolute conclusions owing to variability at all scales, especially for a prolonged time

period and variable climatic conditions.

The limitations of full-scale testing are partially mitigated using physical modelling techniques. A prime example was reported by Take and Bolton (2011) with regards to seasonal climatic cycling of hydraulic stresses on a centrifuge model and limit-equilibrium back analysis. This approach allowed the problem to be scaled down in its entirety, including temporally, to account for numerous seasonal variations. Their testing reported the 'ratcheting' effect of seasonal volumetric changes, measured using vector displacements, propagating from the toe of the embankment. This has a significant advantage as negative pore water pressures could easily be measured using a small number of high capacity tensiometers placed in the slope face. Furthermore, a scaled calendar year of seepage flow was completed in only 2.43 hours. However, this approach was also limited as many of the micro and macro structures were disregarded, as such pore water response is somewhat simplified.

In addition to full-scale and physical modelling, numerical analysis has been employed by several researchers to undertake sensitivity analysis using boundary flux parameters. A novel application of numerical modelling was presented by Stirling et al. (2017) where desiccation crack formation was modelled in FLAC 2D using laboratory data from the Durham Boulder Clay. This allowed for a sensitivity analysis of crack formation during drying to be completed. It was shown that sensitive materials with high plasticity which have larger Air Entry Values (AEVs) were more likely to exhibit pervasive fine cracking patterns, while glacial tills were more likely to exhibit permanent deeper cracks. This approach allowed for the reduction in laboratory testing as changes in soil properties could simply be inferred from baseline tests. However, this smaller scale, concentrated approach to modelling means that the impact of this on slope stability must be inferred rather than quantified.

Testing of soil-atmosphere interaction at a laboratory scale is typically used to measure and observe several fundamental geotechnical properties. These tests are explicitly concentrated on a singular mechanism under controlled conditions, so the dependant variable may be quantified against its independent counterparts, often for modelling and design purposes. For instance, Mendes and Toll (2016) and Azizi et al. (2019) investigated the effects of variation in hydraulic stresses on unsaturated compacted soils. Azizi et al. (2019) undertook measurement of permeability, volumetric changes, pore structure and unsaturated shear strength (consolidated drained) after six hydraulic wetting and drying cycles on samples of compacted clayey silt. In comparison, Mendes and Toll (2016) investigated the effect of compaction water content (an additional variable) under similar conditions, also observing its impacts during unsaturated triaxial shearing (consolidated drained). In both studies, the ability for laboratory testing to allow

for controlled analysis of unsaturated soil variables with various hydraulic histories was demonstrated, which is not possible at a field scale. However, somewhat similarly to field testing, the increased testing time and complexity required for capturing the behaviour of unsaturated soils, pertinent to realistic soil-atmosphere interaction, remains a challenge.

2.7 Impacts of hydraulic history on compacted soils

During a geostructures service life, subgrade compacted soils and fills are exposed to environmental conditions which results in persistent moisture and suction changes, caused by infiltration (wetting) and evaporation (drying) (Figure 2-8). The most pronounced water content changes occur within the unsaturated drying-wetting zone from 0 to 2 m depth (Glendinning et al., 2014). Notably, the effects of extreme climatic events associated with climate change may alter the rate/amplitude of this seasonal variation experienced by soils previously. Past studies have shown that the resultant predicted increase in climatic extremes generate higher suction stresses during hotter summer periods, leading to increased amplitude of water content during drying and wetting, and thus a greater volume change observed in the seasonal shrink-swell cycles (Clarke and Smethurst, 2010; Glendinning et al., 2015). As a consequence, unsaturated conditions and the hydraulic history that the soil experiences, significantly influence the post-compacted response of geomaterials over time. Despite this the impact of extreme seasonal variation (drying and wetting) owing to climate change on compacted geomaterials is not well understood.

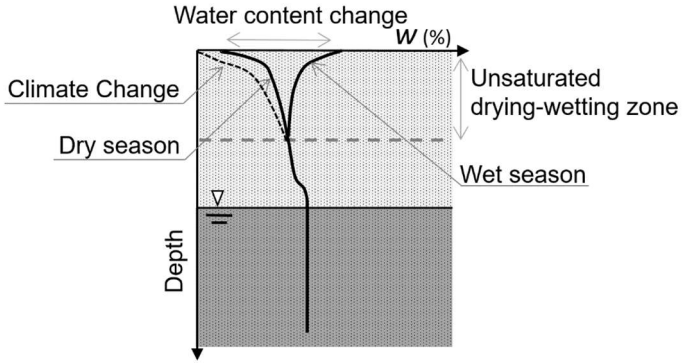


Figure 2-8 Ground profile showing annual changes in moisture of geomatrials (modified after Heitor (2013))

Empirical observations from practice validate the occurrence of reduced geostructure performance due to seasonal variation in moisture, extreme climatic conditions, soil plasticity and historic construction techniques. This has been classified using a performance curve shown in Figure 2-9. It shows a comparison between the performance of embankments under different climatic conditions and construction

histories. It also shows the performance of current transport infrastructure geostructures in the UK, based on construction methods i.e. pre and post regulation techniques. Although no direct measurement has been made recording this change in performance within this time scale, due to obvious constraints, it provides a theoretical framework from which to evaluate geostructures incorporated in the UK transport network.

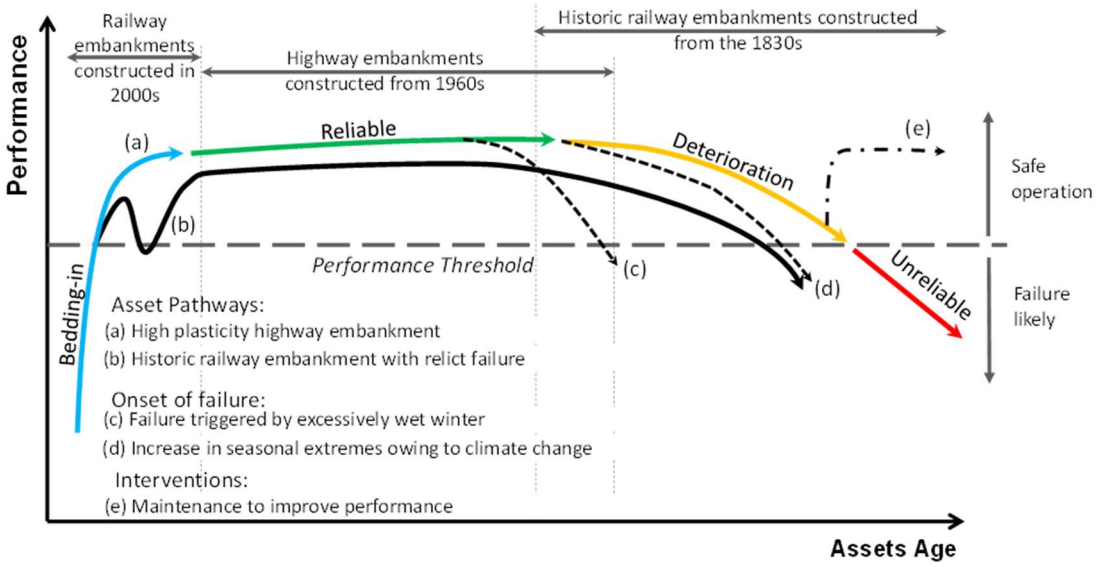


Figure 2-9 Deterioration curves showing the change in performance of an embankment over time, where: curve (a) represents a high plasticity highway embankment; (b) historic railway embankment with relict failure; (c) failure triggered by an excessively wet winter; (d) increase in seasonal extremes owing to climate change and (e) maintenance to improve performance (modified after Briggs et al. (2019)).

2.7.1 Soil water retention behaviour and hysteresis

Unsaturated changes in moisture due to seasonal variation produces unique hysteretic hydraulic pathways which are dependent on the soil characteristics and desorption or absorption of water. For a given soil, this behaviour is defined using the Soil Water Retention Curve (SWRC) which represents the relationship between the amount of water retained in the soil typically expressed in terms of volume (e.g. volumetric soil water content, θ or degree of saturation, S_r) or weight (gravimetric water content, w) and matric suction (Ψ). Matric suction is formed due to the differential between soil water pressure and air pressure, which results in a tensile force at the air-water interface, producing an additional normal stress between soil particles. Note that henceforth the term suction will be used to define negative pore water pressures in reference to capillary potential rather than osmotic potential unless stated otherwise.

Figure 2-10 shows an illustration of a typical hysteretic SWRC. It includes an initial drying

curve, main wetting curve and main drying curve. The main wetting and drying curves form the 'main' hysteresis loop. From the main drying curve different domains can be identified relating to differences in the proportion of gas and liquid phases. This includes both the bulk water zone and meniscus dominated zone, delineated by the AEV. These regimes are determined using the tangent line of the inflection point, where the concavity of SWRC changes. The abscissa of the intersection of this line with a horizontal line extended from fully saturated conditions defines the AEV. The residual water content is then determined from the intersection of the tangent of the inflection point and the straight portion of the tail end of the SWRC (Sivakugan, 2021). In accordance with Kelvin's equation the SWRC in these regimes are largely dependent on the pore size distribution.

Between main drying and wetting curves an infinite number of scanning curves can develop when transitioning from main wetting to main drying and vice versa. This hysteretic response results from non-uniformity of interconnected pores (ink bottle effect), changes in pore structure during wetting and drying cycles, differences in the liquid contact angle, air entrapment and capillary condensation (Likos and Lu, 2004). The hysteretic behaviour of unsaturated soils in geostructures has a significant effect on their behaviour and has been shown to be affected by plasticity (further discussion included in Appendix A.3 for completeness). For instance, the variation in permeability between both unsaturated and saturated states, but also for drying/wetting pathways, may be significant (O'Brien, 2013).

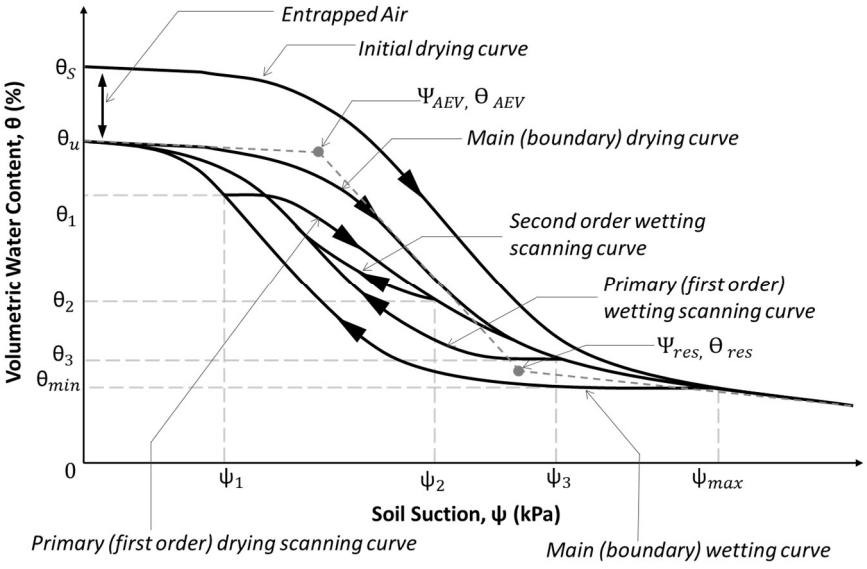


Figure 2-10 Hysteretic SWRC and associated commonly used definitions (modified after Pham et al. (2005)).

2.7.2 Small strain behaviour

2.7.2.1 Application of small strain stiffness for the assessment of compacted soils

During the operation of transport infrastructure, the small strain (0.001% or less) properties of geomaterials incorporated into the substructure govern the response to dynamic loading resulting from passing traffic (Figure 2-11). Small strain shear modulus (G_{max}) is therefore an intrinsic property used for pavement design (Clayton, 2011; Dong et al., 2018).

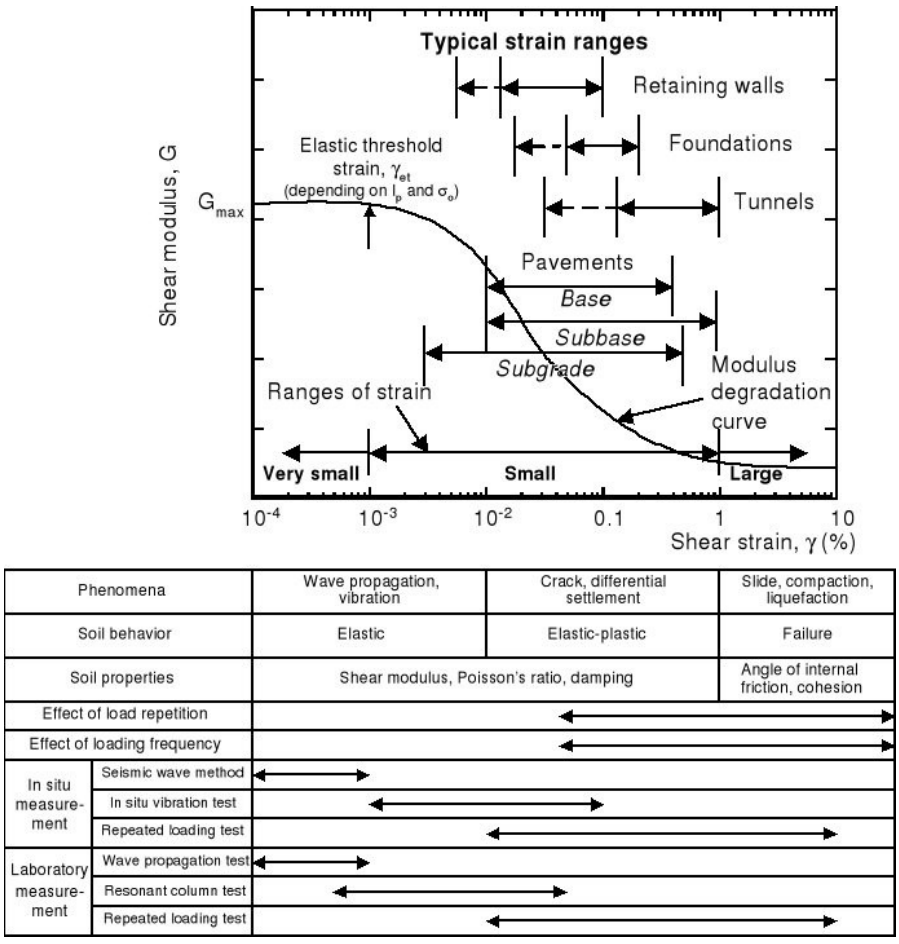


Figure 2-11 Typical shear strain levels for different geotechnical applications, in situ and laboratory techniques (Sawangsuriya, 2012).

In practice, both field and laboratory wave propagation techniques are used to evaluate small strains, for example; seismic cross hole (borehole), seismic down hole/up hole (borehole), seismic cone penetration testing (SCPT), seismic refraction/reflection, spectral (continuous/multichannel) analysis surface wave surveys (e.g. spectral analysis of surface waves or SASW, continuous surface wave or CSW and multichannel analysis of surface wave or MASW), bender element, ultrasonic pulse or resonant column techniques. These methods can be used to measure the propagation of body waves,

e.g. compressional (P-wave) and shear waves (S-wave), which travel both longitudinal and transverse to the direction of transmission, respectively (Krautkrämer et al., 1990). As the waves travel at a given frequency and amplitude over a known distance the shear wave velocity (V_s) and compressional wave velocity (V_p) can be determined for evaluation of stiffness behaviour of geomaterials in both saturated or unsaturated conditions.

Due to their non-invasive (advantageous when access is difficult i.e. railway embankment) and cost effective nature, small strain techniques have been used to monitor a number historic geostructures for identification of subsurface stiffness and assess performance and deterioration during service.

For instance, Gunn et al. (2016) undertook both CSW and MASW surveys along sections of Great Central Railway (GCR) embankment near East Leake, Knottingley and Goole canal embankment and Gloucester and Warwickshire heritage railway embankment. The stiffness profiles obtained not only allow for identification of different engineered materials but also facilitate the identification of areas of heterogeneity arising from both differences in construction techniques and levels of deterioration. Furthermore, Shrestha et al. (2019) showed that SASW was an effective method to monitor changes in stiffness of a section of a dyke in Pathumthani (Thailand). The most striking finding was that a reduction in shear wave velocity was recorded during a drying period corresponding to an increase in suction. This was the opposite trend obtained in element tests conducted at the same suction level in the laboratory, owing to formation of shrinkage cracks on the dyke. Continuous MASW monitoring of the Gloucester and Warwickshire heritage railway embankment by Bergamo et al. (2016) throughout 2014 showed the significant impact of seasonal variation in moisture on the shear wave velocity profile of a geostructure. Indeed, Figure 2-12 shows much lower shear wave velocities (<110m/s) were recorded in the upper 3 m due to heavy rainfall during January 2014 compared to proceeding months which experienced less precipitation. However, Gunn et al. (2016) notes that further investigation into the effect of saturation (due to seasonal variation in moisture) and index properties of fine grained soils on shear wave velocity is required to allow for a more effective understanding of surface wave surveys for routine monitoring and management i.e. to detect subsurface deterioration for preventative interventions .

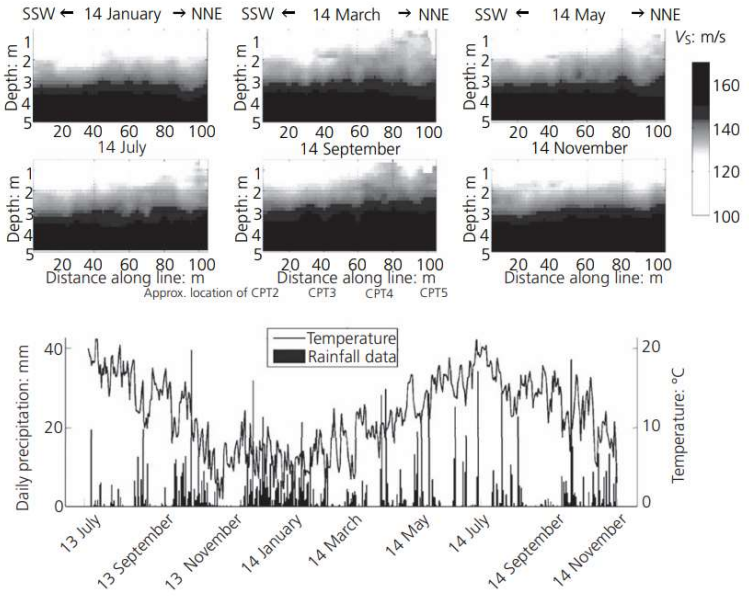


Figure 2-12 Gloucestershire Warwickshire heritage railway embankment shear wave velocities for 5 m depth and corresponding meteorological conditions including temperature and rainfall time series recorded during 2013/2014 (Gunn et al., 2016)

The use of wave propagation to evaluate compaction in terms of dry unit weight (γ_d) has also been explored by several researchers. Yesiller et al. (2000) measured ultrasonic through-transmission compressional velocity for standard and modified Proctor compacted clay soils. The results showed that the peak velocity approximately corresponded to the optimum moisture content (OMC) identified using dry density and void ratio. However use of ultrasonic surface-transmission method, for field application, introduced greater error compared to through-transmission while also introducing uncertainties for the determination of the wave path length.

These findings are intuitive as the compacted stiffness of soils and thus propagation of waves relates to changes in the void ratio, pore structure and suction during compaction. In fact, by measuring small strain shear modulus for different compaction states in different soils, Heitor et al. (2016) and Sawangsuriya et al. (2008) identified distinct behaviour across the compaction plane related to changes in soil microstructure. In addition, the results showed that maximum shear modulus was attained on the dry side of optimum moisture content due to the contribution of matric suction to stiffness.

Kim et al. (2001) employed both laboratory and field determination of small strain stiffness using Resonant column (RC) tests and SASW respectively, for establishing the relationships between shear wave velocity and dry density in granular materials. While the findings indicated that there is a direct proportional correlation between shear wave velocity and dry density, the role of suction was not considered. While this is an acceptable limitation for granular soils, where suctions are smaller, for clay soils that can

sustain greater suctions in as-compacted conditions, it introduces substantial inaccuracies as demonstrated by Heitor et al. (2016) and Sawangsuriya et al. (2008).

More recently, Moon et al. (2018) developed a semi-empirical method for determining the bulk unit weight (γ_t) of soils using shear wave velocity based on Hardin (1978) void ratio function and the phase relationship equation. The results show that for saturated soils the semi-empirical equation is within ±1 standard deviation (1.63 kN/m^3). However, similarly to Kim et al. (2001), due to the simplicity of the model, the role of suction cannot be captured.

2.7.2.2 Impact of hydraulic history on small strain stiffness

The propagation and attenuation of waves has been found to be significantly different in saturated, unsaturated and fully dry conditions owing to the change in proportion of the solid, liquid and gas phases, packing and resultant inter-particle forces and interaction with the soil skeleton.

In an unsaturated medium that represents compaction conditions, an increase in the magnitude of suction typically results in an increase in stiffness of the soil skeleton and thus small strain shear modulus G_{max}. Furthermore, several studies covering a wide range of different soils have shown that there is a correlation between the ranges in the SWRC and G_{max} while the soil undergoes a desaturation process, including Azizi et al. (2019); Ngoc et al. (2019); Heitor et al. (2015); Khosravi and McCartney (2012); Ng et al. (2009), among others. For instance, Mancuso et al. (2002) reported that in low suction range there was a linear increase between shear modulus and suction (bulk water zone prior to AEV) whereas a nonlinear relationship was observed once the AEV was exceeded (meniscus dominated zone). The propagation of shear waves has also been found to depend on saturation levels, void ratio, matric suction and net stress during isotropic loading conditions (Cho and Santamarina, 2001; Whalley et al., 2012; Santamarina, 2003). Numerous studies have also reported that small strain stiffness exhibits similar hysteretic behaviour during drying and wetting to the SWRC (Ng and Xu, 2012; Dong and Lu, 2016; Khosravi and McCartney, 2012). Most studies have employed axis translation technique to control drying and wetting while G_{max} was monitored at selected matric suction levels. There is a good agreement between all studies carried out for a wide range of soil types that shows that the shear modulus is found to be greater on the wetting path compared to the drying path when plotted in the G_{max} – suction plane.

Nonetheless, when drying-wetting results are shown in the G_{max}- volumetric water content plane (e.g. Figure 2-13) the opposite trend is observed, with higher G_{max} on the drying path. Dong and Lu (2016) also showed that for some materials (e.g. high plasticity Denver claystone) the G_{max} behavior in drying-wetting cycles may be more linear.

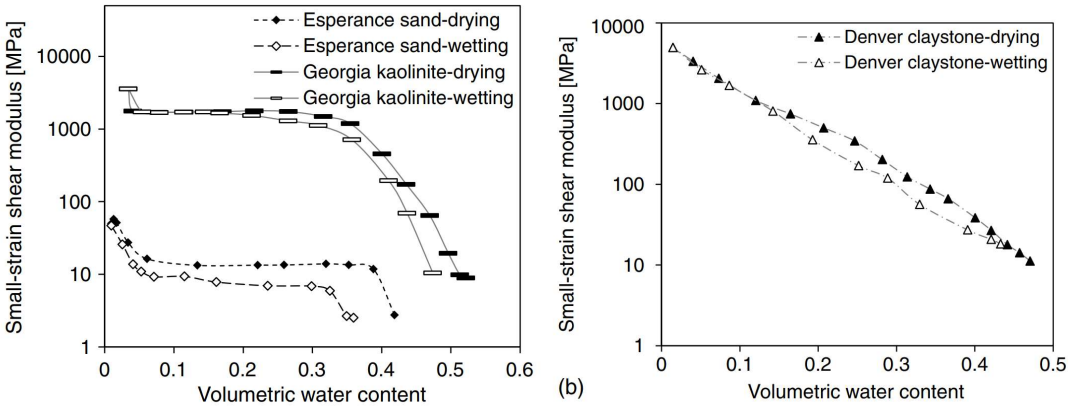


Figure 2-13 Small strain shear modulus evolution for drying and wetting cycle of Esperance sand, Georgia kaolinite and Denver claystone (Dong and Lu, 2016)

At lower water contents at residual conditions other physiochemical forces have been found to contribute to matric potential in addition to suction. This was investigated by Ngoc et al. (2019) on a compacted sand and kaolin mixture for three drying-wetting cycles. When shear modulus was normalised using Hardin (1978) void ratio function at constant net stress and levels of matric suction, higher $G_{max}/f(e)$ was observed at both higher matric suction levels but also at lower saturations (Figure 2-14). This is somewhat expected as at a constant net stress the changes in the interparticle forces induced by matric suction (e.g. capillary stresses) are proportional to stiffness (except for the dry state). However, Ngoc et al. (2019) suggests the interparticle forces formed through the contact area between pore water and particle surfaces is also proportional to the amount of water and thus the degree of saturation. Consequently the results indicate that other inter-particle forces, in addition to matric suction, contribute to changes in stiffness during drying-wetting cycles.

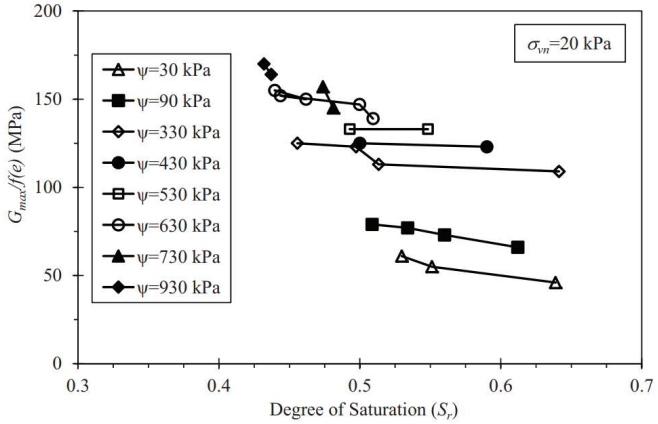


Figure 2-14 Relationship between $G_{max}/f(e)$ and degree of saturation for three drying-wetting cycles (Ngoc et al., 2019).

Ngoc et al. (2019) proposed that these inter-particles forces could be the result from both van der Waals attraction and electric double-layer repulsion. This is because as the

degree of saturation is reduced during a drying path an increase in the intermolecular attractive forces between atoms of adjacent particles (van der Waals attractions) is formed. During a wetting path the cations in the electric double layers are hydrated, reducing the van der Waals attractions and increasing the electric double-layer repulsions. As both forces are proportional to particle diameter and saturation, fine grained soils may therefore experience greater physicochemical inter-particle forces during drying-wetting.

Propagation of compression waves during changes in moisture significantly differ to shear waves. Compressional waves apply volumetric strains and therefore their velocity is affected by the bulk modulus of the soil and thus variation in the degree of saturation. In some cases the velocity of the wave due to the soil skeleton may be masked by changes in the degree of saturation. For instance, Kitsunezaki (1986) showed that the compressional wave velocity decreases by 25% of the fully saturated compression wave velocity when the degree of saturation changes from 100% to 99.9% (0.1% gas saturation) (Figure 2-15). Consequently shear waves velocity and shear modulus, which are not directly influenced by the presence of water, are more suitable for determining changes in the microstructural arrangement of particles forming the soil skeleton.

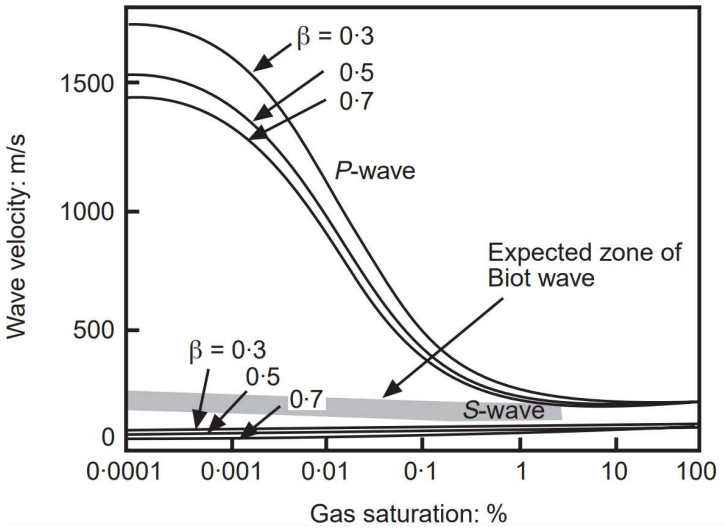


Figure 2-15 Effect of gas saturation on both the shear and compressional wave velocity, where β is the porosity(Nakagawa et al., 1997).

In the field, changes in the pore water regime occur continuously due to seasonal soil-atmosphere interactions. Using element testing this variation in moisture content is simulated by the application of several drying-wetting cycles, allowing for controlled observation of the impact of hydraulic history on small strain shear modulus. A summary of past studies which employ this approach are presented in Table 2-3. The table shows that in general many studies investigate only one soil type for a defined range of drying-wetting. Comparison may be made between different studies, however, they often have

significantly different preparation conditions and methodologies, such as compaction criteria, confining stresses, techniques for applying drying-wetting cycles and number of drying-wetting cycles. Indeed, Dong and Lu (2016) used a 'drying cake' method to alter specimen moisture content by air drying in unconfined conditions to explore the entire range of the SWRC. Consequently, measurements of shear modulus where made at differing volumetric water contents. This contrasts with studies by Ng and Xu (2012) who conducted drying-wetting using a triaxial apparatus to confine specimens (100 kPa) and altered matric suction at constant levels using the axis translation technique, limiting drying to a matric suction of 300 kPa.

Furthermore the results of studies presented in Table 2-3 indicate that after the application of hydraulic history both a decrease or increase in small strain stiffness may occur. For instance, after the application of two drying-wetting cycles (water content range of 17-25%) to a compacted silt (I_p 10%, W_L 24%), Ying et al. (2021) observed significant cracking and loss of small strain shear modulus. Furthermore, Tang et al. (2011) also found that for a similar compacted silt (I_p 24%, W_L 45%) the application of two drying wetting cycles (water content range of 14-21%) induced visible cracking which resulted in total specimen failure (Figure 2-16b). However, both Ngoc (2020) and Heitor et al. (2015) report increases in small strain shear modulus for a compacted mixture of kaolin and sand, and a compacted silty sand respectively. Heitor et al. (2015) showed that the compacted silty sand (I_p 10%, W_L 25.5) increased by 17m/s on the second drying wetting cycle, while hysteresis between drying and wetting pathway reduced (Figure 2-16a). This observation was attributed to irrecoverable changes in microstructure due to alteration of pore size distribution.

Its therefore clear that impact of hydraulic history on compacted soils is complex and depends on several variables including: matric suction (drying-wetting) amplitude, soil particle size distribution, confining stress, plasticity, mineralogy, microstructure, and consequently the as-compacted conditions (i.e water content and compaction energy). However, there is little quantitative evidence investigating the causes of the differences in observed behavior.

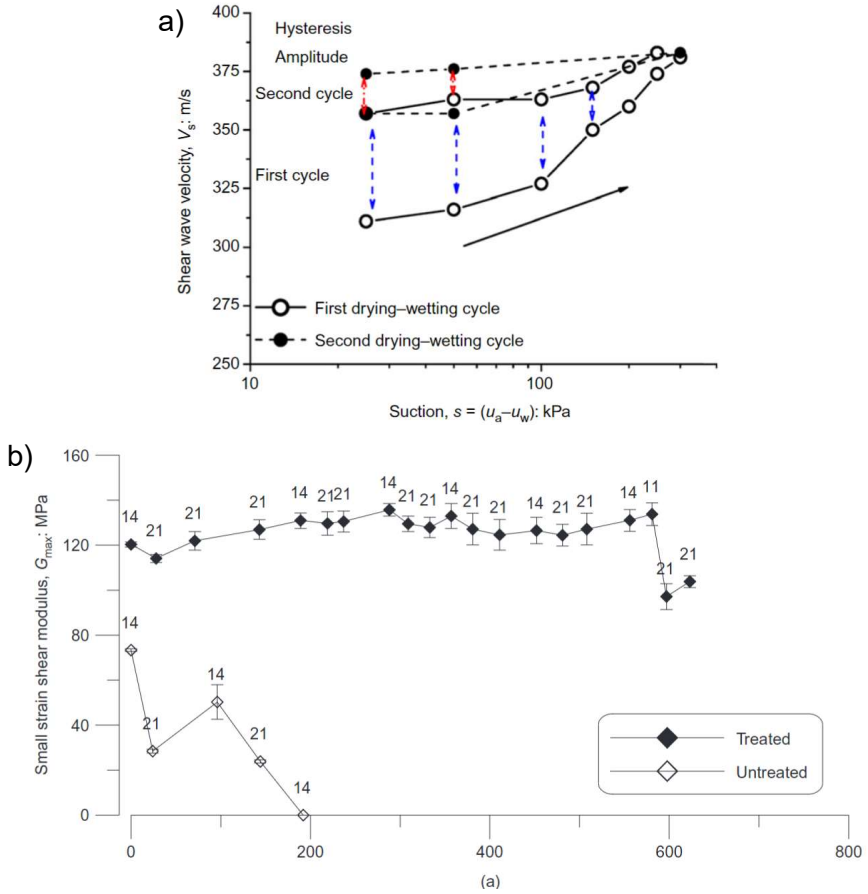


Figure 2-16 Small strain stiffness during drying-wetting for a (a) compacted silty sand and a (b) compacted silt with and without lime treatment (Heitor et al., 2015; Tang et al., 2011).

Table 2-3 Summary of literature investigating impact of drying-wetting cycles on small strain stiffness.

Authors	Material	Equipment/drying-wetting method	Specimen dimensions (diameter × length; mm)	Confining stress (kPa)	Suction range (kPa) / water content (%)	Number of D/W cycles
Ma et al. (2023)	Compacted clayey silt	One-dimensional oedometer cell axis translation and bender elements	26×90	-	0-1000 kPa	2
Walker et al. (2023)	Compacted kaolin clay	Ultrasonic apparatus, air drying and wetting by addition of water	38×76	Unconfined	Saturated-15% Saturated-1.5% 28-15% 28-1.5%	10
Ying et al. (2021)	Compacted lime treated silt	Bender elements and air drying and wetting by the addition of water	-	Unconfined	17-25%	7
Khosravi et al. (2020)	Compacted Bonny silt and Ardabil silt	Modified triaxial cell with bender elements and axis translation	60×120	40, 200 and 600	Drying: 0-50 kPa Scanning curve: 50-20-80 kPa Scanning curve: 80-40-110 kPa Wetting: 110-0 kPa	2 scanning curves and 1 full drying-wetting cycle
Ngoc et al. (2019)	Compacted clayey sand (75% fine sand and 25% kaolin clay)	Modified Rowe cell with bender elements and axis translation	31×100	-	30 – 930 kPa	3
Khosravi et al. (2018)	Poorly graded sands	Modified triaxial cell with bender elements and axis translation	60×120	24, 70 and 100	15 kPa	1

Table 2-3 continued

Authors	Material	Equipment/drying-wetting method	Specimen dimensions (diameter × length; mm)	Confining stress (kPa)	Suction range (kPa) / water content (%)	Number of D/W cycles
Dong and Lu (2016)	Esperance sand, Hopi silt, Bonny silt, BALT silt, Missouri clay, Denver claystone, Georgia kaolinite	Bender elements and an environmental chamber for air-drying and wetting using mist	20×76.2	Unconfined	Saturated-0%	1
Ng et al. (2009)	Compacted decomposed tuff	Triaxial apparatus using axis translation, Hall-effect transducer and vertical and horizontal bender elements	76×152	110 and 300	0-250 kPa	1
Heitor et al. (2015)	Compacted silty sand	Triaxial apparatus using axis translation and bender elements	50×100	50	25-150 kPa 25-300 kPa	2
Ng and Xu (2012)	Compacted decomposed tuff	Triaxial apparatus using axis translation, Hall-effect transducer and vertical and horizontal bender elements	76×152	100	95-150 kPa 95-300 kPa	1
Kumar and Madhusudhan (2012)	Poorly graded sand	Bender elements and water added by volume to desired saturation	50×100	100 and 300	Saturated - dry	drying
Khosravi and McCartney (2012);	Compacted Bonny silt	Fixed-free resonant column with suction-saturation control	36×72	100, 150 and 200	0-70 kPa	1
Tang et al. (2011)	Lime treated and untreated compacted silt	Bender elements, air drying and wetting by the addition of water	50×50	Unconfined	14-21% and 18-21%	5
Sawangsuriya et al. (2009)	Compacted clayey sand, silt, lean clay and fat clay	Triaxial cell with horizontally inclined bender elements and axis translation	25×73	35	0-10,000 kPa	drying

Table 2-3 continued

Authors	Material	Equipment/drying-wetting method	Specimen dimensions (diameter × length; mm)	Confining stress (kPa)	Suction range (kPa) / water content (%)	Number of D/W cycles
Ng et al. (2009)	Compacted decomposed tuff	Triaxial apparatus using axis translation, Hall-effect transducer and vertical and horizontal bender elements	76×152	110 and 300	0-250 kPa	1
George et al. (2009)	Compacted Bonny silt and heterogeneous sand, silt and clay mixture	Acoustic transducers and axis translation	100×125	-	0-100 kPa	1
Biglari et al. (2012)	Compacted kaolin	Fixed-free resonant column – torsional shear (RCTS) and axis translation	36×72	50-450 kPa	0, 50, 150, and 300 kPa	1
Vassallo et al. (2007)	Compacted Po silt	Fixed-free resonant column, triaxial cell and axis translation	-	25-700	50, 100, 200 and 400 kPa	2
Mendoza and Colmenares (2006)	Compacted kaolin	Bender elements, air drying and wetting by the addition of water	38×76	Unconfined	Compacted- <10%	drying
Inci et al. (2003)	Compacted low plasticity clays and mix of clay and bentonite	Ultrasonic testing and air drying	110×110	Unconfined	Compacted- 0%	drying
Kim et al. (2003)	Compacted well graded sand	Modified fixed-free Stokoe-type resonant column (RC) and axis translation	-	41	5-200 kPa	drying
Mancuso et al. (2002)	Compacted decomposed granite	Resonant column – torsional shear (RCTS) cell and axis translation	-	100-400	0-400 kPa	drying

2.7.2.3 Empirical modelling of unsaturated small strain shear modulus

Micromechanical analysis has shown that small strain shear modulus in dry and saturated conditions is stress dependant and can be fitted with a power equation (Hardin and Richart, 1963). In this state the void ratio (e), over consolidation ratio (OCR) and mean effective stress (σ') (confining stress) are primarily used to estimate small strain shear modulus. Table 2-4 shows that in unsaturated conditions the relationship was extended by including the Bishop (1959) effective stress variables, net normal stress (σ-u_a) and matric suction (u_a-u_w). While also requiring fitting parameters which are used to account for the microstructure and stress state of the soil i.e. particle characteristics, anisotropy, and bonding/cementation (Bui et al., 2010). Sawangsuriya et al. (2009) applied this approach by incorporating independent stress variable concept and a form of Bishops effective stress parameter (x) proposed by Vanapalli and Fredlund (2000) (Θ^k) which includes empirical parameter k to describe the dependency of small strain stiffness on the SWRC. The model was calibrated against five unsaturated compacted soils for drying paths during an increase in suction and showed satisfactory results. Its noted, however, that this model is limited between 0 kPa and 15,000 kPa and does not account for hysteresis during drying-wetting cycles.

However, several studies have now shown at a constant matric suction, small strain shear modulus is greater on the wetting path compared to the drying path (Khosravi and McCartney, 2011; Ng et al., 2009). This was captured by Khosravi and McCartney (2012) for a single drying-wetting cycles for low plasticity soils by incorporating a double-hardening mechanism introduced by Wheeler et al. (2003). When matric suction, net stress and void ratio are constant the difference in saturation between wetting and drying pathways results in changes in the inter-particle contact forces transmitted through the soil skeleton. The elastoplastic hardening surface thus accounts for both plastic deformation of the soil skeleton under a change in effective stress and saturation. The effective saturation (S_e), was also incorporated and defined using van Genuchten (1980) SWRC parameters, limiting the models use to the main drying-wetting pathways. More recently Khosravi et al. (2020) extended the model to capture scanning loops by adopting an empirical approach to evaluating effective saturation, proposed by Parker and Lenhard (1987). This approach incorporates apparent saturation (S_{app}) and effective saturation of trapped air (S_a) to account for air entrapment during wetting. Results showed good agreement with the data for different silty soils presented in past studies. However, the model application is limited to low plasticity soil as a consequence of the separation between hardening due to plastic changes in volume and matric suction. The model also employs macroscopic elastoplastic parameters developed for large strain modelling to the small strain range which may not fully capture wave propagation

behaviour.

It's also notable that although these models account for matric suction and saturation they do not account for other physiochemical forces such as van der Wall attraction. For instance, at constant matric suction Ngoc et al. (2019) found the latter had greater contribution to normalised small strain shear modulus ($G_{max}/f(e)$) upon changes in saturation during unloading. Consequently, as both these forces are both proportional and inversely proportional to saturation respectively, Ngoc et al. (2019) evaluated them separately. To achieve this parameters m and k were also introduced for variations in saturation and parameters b and c were used to evaluate their magnitude (Table 2-4). The results were validated for a complex stress path while applying changes in both matric suction and net stress. The results were in good agreement with observed data and showed the ability to capture the greater influence of matric suction, and thus saturation, on small strain shear modulus compared to an equal isotropic stress change.

The practical use of these models in the field also presents limitations due to the difficulty measuring the required variables such as saturation, matric suction or void ratio. Recently, Zhang et al. (2021) proposed the addition of a water content function to Hardin and Richart (1963) equation to allow simple determination of small strain shear modulus without the requirement additional unsaturated stress variables. However, it's believed that there is no unique relationship between matric suction, water content and small strain shear modulus. This suggests its unsuitable to be used as to predict small strain shear modulus. Zhang et al. (2021) however undertook resonant column testing of a compacted silt, for a range of confining stresses (50 kPa to 400 kPa), after drying between 5% and 20% water content. Surprisingly, results showed a nonlinear relationship between normalised small strain shear modulus ($G_{max}/f(e)$) and water content. Similarly, the A parameter also showed a nonlinear relationship with water content while the n parameter presented a linear relationship. While the proposed model did not consider the micromechanical complexity during changes in water content (e.g. saturation and soil fabric), a remarkable good fit was obtained likely due to the narrow range of water contents adopted. It's therefore unlikely that the model will be accurate in drier conditions. However, the results do suggest that at low matric suctions (lower than AEV) the water content may be suitable for determination of small strain shear modulus.

Table 2-4 Macromechanical empirical relationships for G_{max} for compacted soils, modified after Heitor et al. (2013).

References	General Form of the Relationship	Soil Type	Testing Method
Hardin and Richart (1963)	$G_{max} = AF(e)\sigma'^{n}$	Saturated soils	N/A
Wu et al. (1984)	$G_{\max} = [1 + H(S_r)]G_{\max}^{dry}$	Fine grained sands	Resonant column
Alonso (1998); Vinale et al. (1999)	$G_{\max} = G_{\max}^{(i=1} * f(s)$	Metrano silty sand	Torsional tests
Mancuso et al. (2002)	$\frac{G_{max}}{p_a} = A\left[\frac{(\sigma - u_a)+s}{p_a}\right]^{n} OCR^{m}$ (before AEV)	Metrano silty sand	Resonant column Torsional tests
Leroueil and Hight (2003)	$G_{max} = (G_{max})_s\{(1-r)e^{-\beta(s-s^*)} + r\}$ $G_{\max} = G_{\max}^{ST=1} + f(s)$	Metrano silty sand	
Ng and Menzies (2007)	$G_{max} = Af(e)\left[\frac{\sigma - u_a}{p_r}\right]^{n}\left[1 + \frac{s}{p_r}\right]^{2b}$	Clayey silt	Bender Elements
Ng and Yung (2008)	$G_{\max} = C_{ij}^2 f(e)\left(\frac{\sigma_i - u_a}{p_r} \times \frac{\sigma_j - u_a}{p_r}\right)^{n}\left(1 + \frac{u_a - u_w}{p_r}\right)^{2b}$	Clayey silt	Bender Elements
Sawangsuriya et al. (2008)	$G_{\max} = \left(w\frac{E}{E_{\text{std}}}\frac{w_{\text{opt}}}{w_{\text{opt,std}}}\right)\{\alpha\log(s) - \beta\}and$	Subgrade soils	Bender Elements
Sawangsuriya et al. (2009)	$G_{\max} = Af(e)(\sigma_m - u_a)^{n} + C\Theta^{k}(u_a - u_w)$ $G_{\max} = Af(e)[(\sigma_m - u_a) + \Theta^{k}(u_a - u_w)]^{n}$	Subgrade soils	Bender Elements

Table 2-4 continued

References	General Form of the Relationship	Soil Type	Testing Method
Khosravi and McCartney (2011)	$G_{\max} = A(OCR)^k p_a^{1-n}[p_n + S_r(u_a - u_w)]^n$ $OCR = \frac{p_0'}{p_n + S_r(u_a - u_w)}$	Bonny silt	Bender Elements
Khosravi and McCartney (2012)	$G_{\max} = AP_a\left[\frac{p_{c0}'}{p_n}\exp\left(\frac{\Delta e^p}{\lambda - k}\right)\right]^K\left[\frac{p_n}{p'}\exp\left(b[S_{e0} - S_e]\right)\right]^{K'}\left(\frac{p'}{P_a}\right)^n$ $S_e = \left[\frac{1}{1 + (\alpha_{vG}\psi)^{n_{\Downarrow G}}}\right]^{1-1/n_{\iota G}}$	Bonny silt	Resonant column
Heitor (2013)	$G_{\max} = G_{\max,S}Af(e)\left[\frac{(p - u_a) + S_r^k(u_a - u_w)}{p_r}\right]^n$	Silty sand	Bender Element
Xu and Zhou (2016)	$G_0 = C_0(1 + e)^{-3}\left[\left(\frac{p^*}{p_r}\right)^{0.5} + C_s\xi^{0.5}\right]$.	Clayey silt Sand	N/A
Ngoc et al., (2020)	$G_{\max} = p_r f(e)\left[a\left(\frac{\sigma_n}{p_r}\right)^n + b\left(\frac{\psi S_r}{p_r}\right)^m + c(1 - S_r)^k\right]$	Kaolin clay mixture	Bender Element
Khosravi et al., (2020) (see next page)	$G_{\max} = AP_a\left[\frac{p_{c0}'}{p_n}\exp\left(\frac{\Delta e^p}{\lambda - k}\right)\right]^K\left[\frac{p_n}{p'}\exp\left(b[S_{e0} - S_e]\right)\right]^{K'}\left(\frac{p'}{P_a}\right)^n$ $S_e = S_{app} - S_a$	Bonny Silt Ardabil Silt	Bender Element

Table 2-4 continued

References	General Form of the Relationship	Soil Type	Testing Method
Khosravi et al., (2020) continued	$S_{app} = \frac{\left[S_{vG}^{j} - S_{vG}^{j}(\psi_{i-1})\right](S_i - S_{i-1})}{S_{vG}^{j}(\psi_i) - S_{vG}^{j}(\psi_{i-1})} + S_{i-1}$ $S_a = \Delta S_{\psi=0}\left(\frac{S_{app} - S_{rev}}{1 - S_{rev}}\right)$ $\Delta S_{\psi=0} = \frac{1 - S_{rev}}{1 - R(1 - S_{rev})}$ $R = \frac{1}{\Delta S_{\max,\psi=0}} - 1$	Bonny Silt Ardabil Silt	Bender Element
Zhang et al. (2021)	$G_0 = A^* \cdot W(w_c) \cdot F(e) \cdot \left(\frac{P'}{P_a}\right)^n$ $A = A^* \cdot {w_c}^{-m}$	Silt	Resonant column

2.7.3 Impact of hydraulic history on stress-strain behaviour

Large strain behaviour is typically defined for strains greater than 0.1% (Atkinson and Sallfors (1991)). Figure 2-17 shows the different strain domains for triaxial conditions. Zone 1 represents small strain stiffness and only constitutes immediate loading. At larger strains within elastic region both the secant or a tangent of stress-strain relationship define Young's modulus stiffness (E_s/E_t) (Zone 2). Upon increased loading and the development of visco-plastic strains (Zone 3), failure occurs at a peak deviator stress (q_{peak}) at a given strain (ε_f) and followed by post peak strength (residual strength) and critical state conditions (CSL). Behaviour is dependent on both positive pore water pressures and matric suction, the microstructure (arrangement of soil particles and their bonding), mesostructure (fissures and cracks) and macrostructure (major heterogeneities such as bedding planes and joints) of the soil (Leroueil, 2001).

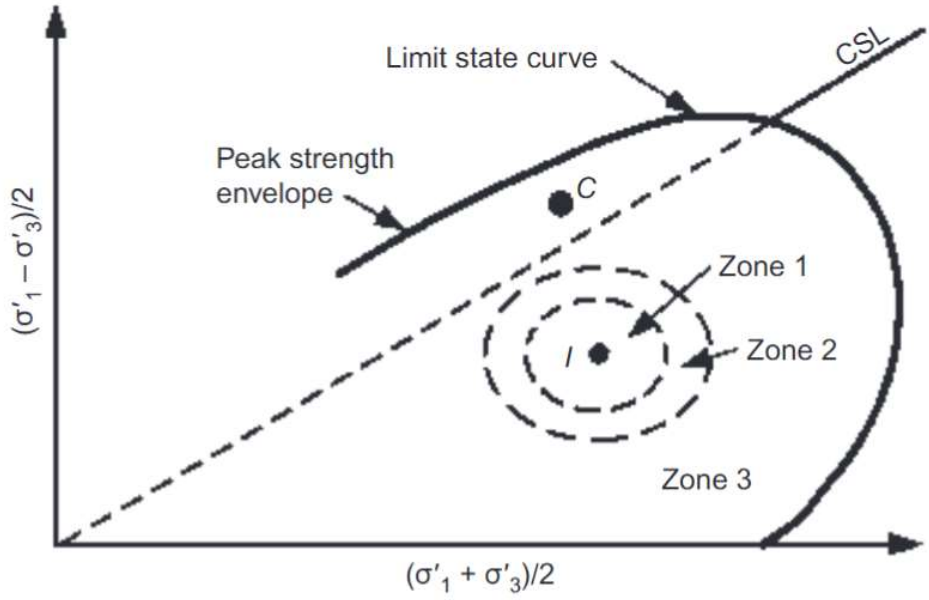


Figure 2-17 Elements of large strain soil behaviour (Leroueil, 2001).

It has also been well established that in unsaturated conditions, for a given net normal stress (σ-u_a), upon an increase in negative pore water pressures (u_a-u_w) an increase shear strength is also observed (e.g. Vanapalli et al. (1996)). This relationship has been shown to be non-linear upon exceeding the AEV, due to the relationship described by the SWRC and thus a characteristics of the soil (i.e. particle size but also compaction water content etc) (Figure 2-18).

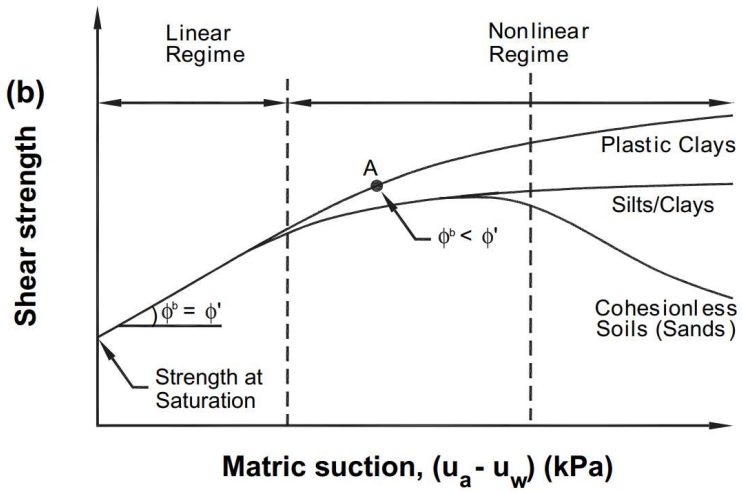


Figure 2-18 The variation in shear strength of different soil types at increasing matric suctions (Vanapalli, 2009).

More recently, hysteresis between the drying and wetting paths has also been shown to impact the stress-strain behaviour of unsaturated compacted soils. Goh et al. (2014) demonstrated this on statically compacted kaolin and sand using unsaturated triaxial at constant matric suction levels of 100 kPa and 300 kPa. When shearing on the first drying path specimens showed a higher peak shear strength, higher axial strains at failure, more ductility and contraction during shearing. On the other hand, when shearing on the first wetting path specimens were stiffer and more brittle, had lower axial strains at failure and showed dilation (Figure 2-19). While strain softening behaviour was more prevalent at higher confining stresses. Consequently, at larger strains the configuration of water within the pores, microstructure and changes in the degree of saturation at constant matric suctions during drying and wetting also influence shear strength. This response remained present within subsequent wetting and drying tests as the magnitude of suction was kept constant.

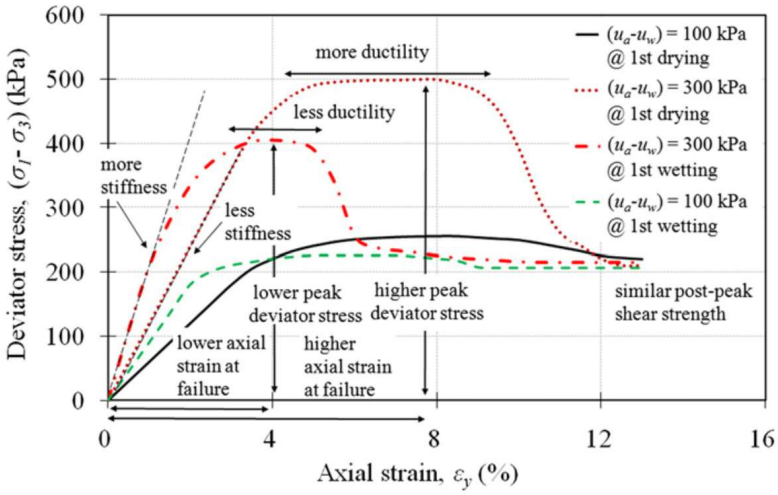


Figure 2-19 Stress-strain curves for sand kaolin mixture on drying and wetting pathways (Goh et al., 2014).

Several studies have also investigated the impact of further drying-wetting cycles on large strain behaviour. For instance, Liu et al. (2020) applied six drying-wetting cycles (saturated to 5% water content) to a silty clay (I_p 11%, W_L 23%). In saturated conditions during consolidated drained (CID) shearing, the hydraulic history resulted in a slight increase in maximum deviator stress at 50 kPa confining stress and change from strain hardening to strain softening behaviour. Little to no differences in stress-strain behaviour were observed at higher confining stresses (100 kPa and 200 kPa) and constant suction levels (50 kPa, 100 kPa and 200 kPa). However, for both 50 kPa and 100 kPa confining stresses, shear induced volume change was shown to reduce with drying-wetting cycles due to an increase in dilatancy (Figure 2-20).

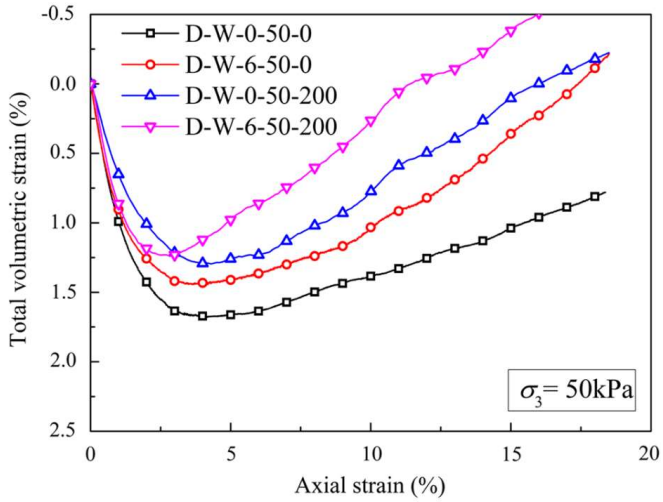


Figure 2-20 Volume change behaviour of a silty clay subject to 6 drying-wetting cycles (Liu et al., 2020).

This behaviour was also observed to a greater degree by Rojas et al. (2009) for a compacted Po silt (I_p 20%, W_L 48%). The consolidated drained (CID) stress-strain behaviour was compared between Proctor compacted specimens and post compacted specimens sampled from embankment fill seven years after placement. The results presented in Figure 2-21 show at constant 100 kPa suction the maximum deviator stress increased while also transforming from strain hardening to strain softening. This again suggests that hydraulic history may be considered similar to the pre-consolidation pressure of an overconsolidated soil. However, the adopted methodology does not rule out the influence of other factors such as the effect of different compaction methods. For instance, dynamic compaction used by the Proctor method and compaction used by rollers in the field, more akin to static compaction, induce differences in pore structure which may influence macro behaviour (Li et al., 2023). Indeed, a greater dry density was observed in the field, however, no measurement was made to distinguish if this resulted from hydraulic history or differences in compaction method.

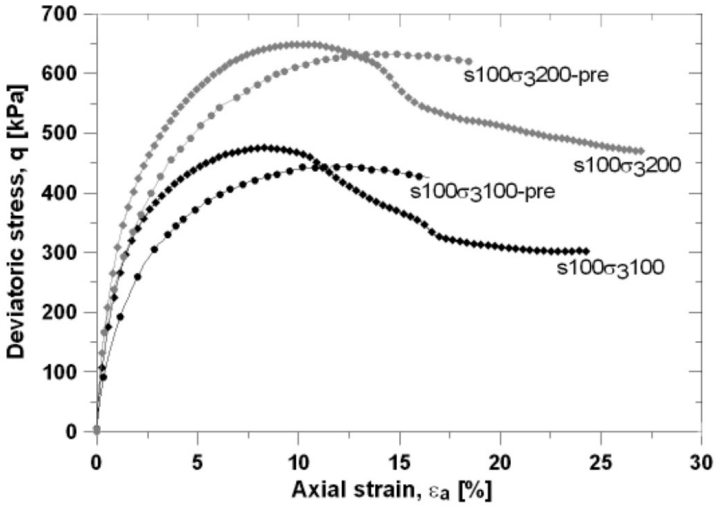


Figure 2-21 Stress-strain behaviour of compacted Po silt after Proctor compaction and post compacted embankment fill (Rojas et al., 2009).

This contrasts with results presented by Zhiming et al. (2023) who investigated the impact of up to three drying-wetting cycles (fully saturated on the wetting path) on both compacted kaolin clay (I_p 20%, W_L 47%) and Mercia Mudstone Clay (I_p 16% W_L 34%). During the application of drying-wetting cycles, constant vertical stresses (0 kPa, 25 kPa and 50 kPa) were applied to the specimens to simulate overburden. Upon saturated consolidated undrained (CU) shearing after one drying-wetting cycle at 25 kPa confining stress, strength was reduced for both the Kaolin clay (24% reduction) and Mercia Mudstone Clay (12% reduction) and thereafter to a lesser degree. However, when subjected to the same number of drying–wetting cycles, the peak shear strength of both soils increased with an increase in the vertical confining pressure applied during drying-wetting.

Similar results were also found by Stirling et al. (2020) for a glacial till (OMC 15%) (I_p 24%, W_L 44%) compacted wet of Optimum Moisture Content (OMC) at 22% water content following the application of up to six drying-wetting cycles (22%-15% water content). Consolidated drained (CID) triaxial testing was conducted at near or fully saturated conditions after the application of confining stress (25 kPa, 50 kPa and 100 kPa). The results showed that after three cycles an equilibrium was reached where an asymptotic reduction in peak deviator stress was observed (Figure 2-22). However, its noted that multistage testing was used to derive the deviator stress at failure and thus may have been impacted by the degree of straining.

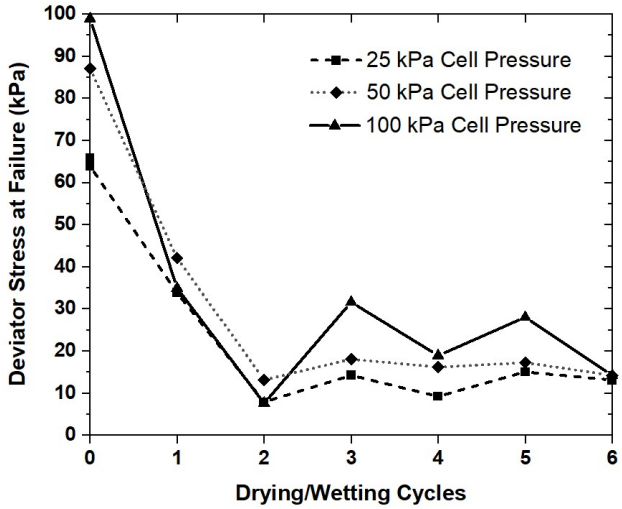


Figure 2-22 Relationship between deviator stress at failure and drying/wetting cycles (drying limit 15% water content and wetting to 22% water content) for a compacted sandy clay derived from the Durham Lower Boulder Clay, tested at different confining pressure levels (modified after Stirling et al. (2020)).

The response of the soil to this hydraulic history was attributed to the formation of micro-cracking (Figure 2-23). In unsaturated conditions the magnitude of suctions was shown to reduce depending on the density of the micro-cracking due to alteration of the pore structure. However, as the triaxial testing was conducted in near or fully saturated conditions this would suggest that the disaggregation of the soil also impacts the saturated macro behaviour.

For this behaviour it was theorised that an immediate increase in the permeability of the soil-atmosphere interface would occur, which is thought to thereafter continue at a slower rate. This would yield time-dependant changes to the rate of infiltration and evaporation experienced by a geostructure, important when considering the impacts of climate change.

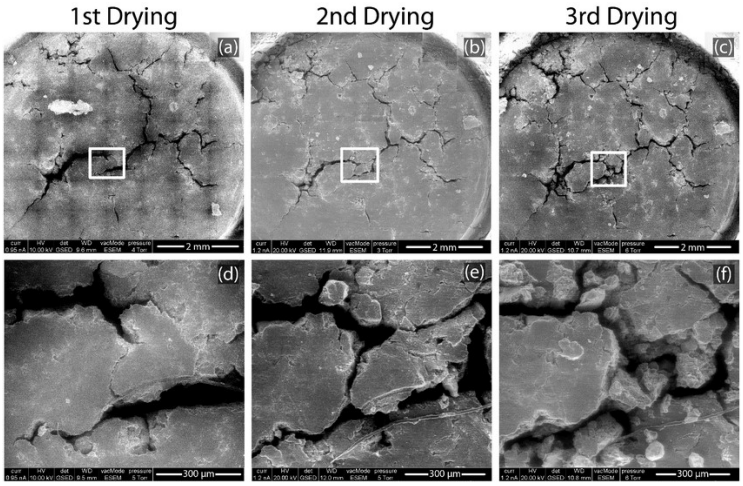


Figure 2-23 Environmental Scanning Electron Microscopy showing the development of micro cracking for three drying-wetting cycles: (a)-(c) x15 magnification and (d)-(f) x100 magnification (Stirling et al., 2020).

It was also observed that the compacted glacial till was sensitive to the degree of drying. Upon exceeding the maximum suction pressure experienced by the soil during drying-wetting cycles the scanning curve shifted downwards i.e. gravimetric water content reduced at constant suction (Figure 2-24). Nevertheless the impacts of the different drying-wetting boundaries, soil compositions and microstructure on macro behaviour remain less well understood. However, their consideration is key for effective management of the impacts of climate change by asset owners due to the complexity of new and to a greater degree existing geostructures. For instance, geostructures are composed of a range of differing soil types with differing mineralogy and soil pore architecture (depending on placement of the material). In addition, when compared to recent construction, historic structures have experienced a greater (but unknown) number of hydraulic cycles of unknown magnitude.

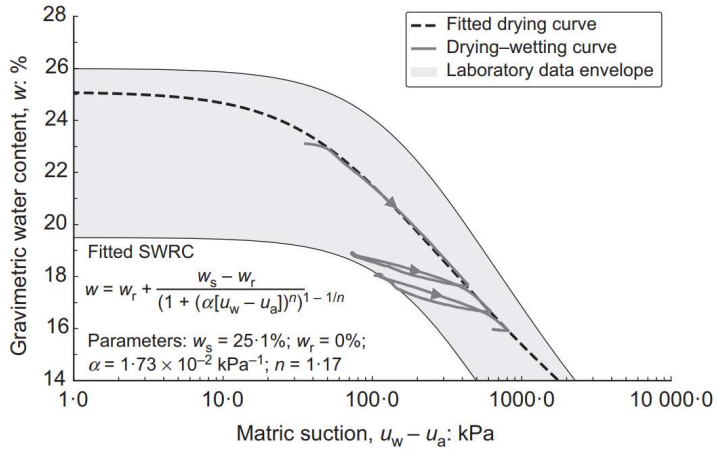


Figure 2-24 Drying-wetting pathways after the application of an increase in suction (Stirling et al., 2020).

2.7.4 Microstructure

The arrangement of a soils constituents (e.g. sands or gravel grains, aggregates and clay platelets) form the microstructure; sometimes referred to as the soil fabric. The fabric of compacted clay soils was initially investigated by Lambe (1958) and Seed and Chan (1959). These studies contributed to a conceptual model defining both a flocculated and dispersed soil microstructure depending on the moisture content during compaction. A flocculated structure consists of randomly oriented particles occurring when soils are compacted on the dry side of OMC due to the high concentration of electrolytes reducing the osmotic repulsion between particles. While on the wet side of OMC, the reduction of electrolytes results in a dispersed fabric of particles orientated in parallel. It's now understood that compacted clay soils also contain three scales of pores sizes, including: intra-platelet pores (micro), intra-aggregate (meso) and inter-aggregate (macro) pores

(Figure 2-25). The latter two groups of pores form the bimodal pore size distribution typically reported in porosimetry studies. These larger pores between platelets and aggregates are able to become unsaturated when sufficient suction is applied. In contrast, the water bound within the clay platelets themselves requires a significant degree of suction to be removed. Sharma (1998) estimates that larger intra-aggregate pores (several microns) require suctions exceeding 100 kPa for air to enter, whereas, intra-platelet pores require suctions greater than 10^5 kPa. Consequently, in general it is assumed that intra-platelet pores remain in saturated conditions.

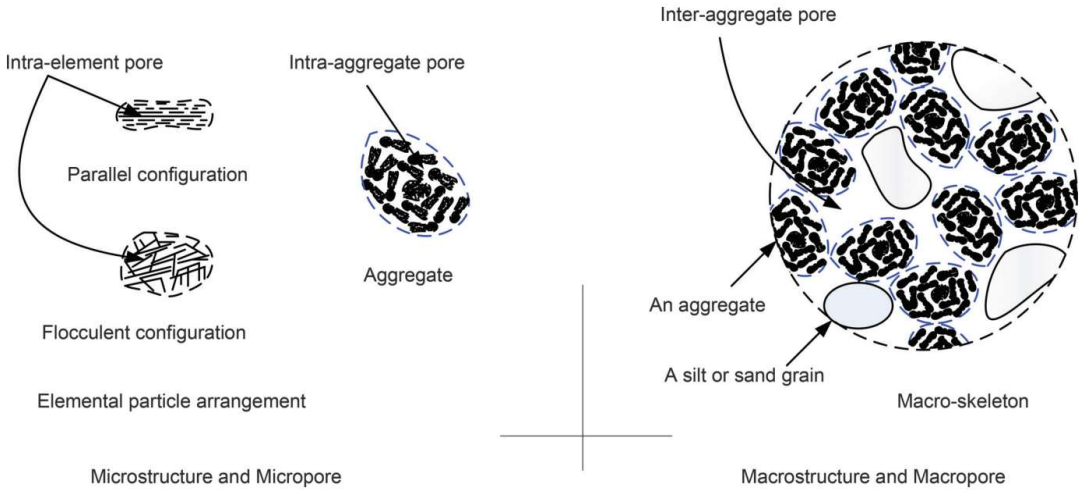


Figure 2-25 Conceptual model of the fabric of compacted clay (Wang and Wei, 2015)

Both compaction method and water content has been shown to impact the pore size distribution of a compacted soil. Indeed, Li et al. (2023) investigated this on a compacted silt using Mercury Intrusion Porosimetry (MIP) on 2-3 mm blocks of sub-sampled material. The results showed that when compared to the Proctor compaction method, static compaction pore size distribution density curve had an overall shift to the right with the maximum pore size distribution density increasing. Furthermore, in general the Proctor method showed greater variation in pore size when compacted dry or wet of OMC when compared to statically compacted specimens (Figure 2-26).

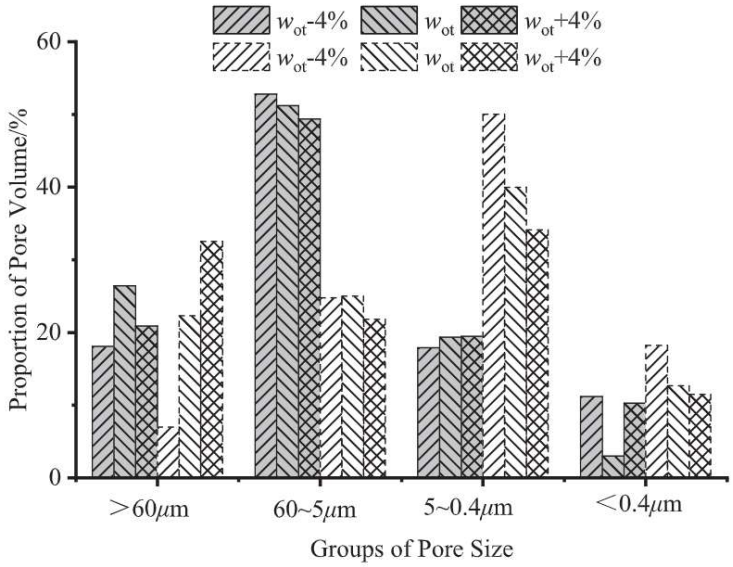


Figure 2-26 Pore size groups for Proctor compaction (white dashed boxes) and static compaction methods (grey solid boxes) (Li et al., 2023)

Following compaction, the evolution of the microstructure during changes in suction and external loading is also integral to understanding the unsaturated macro-mechanical behaviour of compacted soils, for instance in constitutive modelling. Indeed, Farulla et al. (2010) and Koliji et al. (2010) used both MIP/ESEM of a kaolinitic–illitic clay and neutron tomography of the Bioley silt respectively to observe aggregate volume changes in oedometer apparatus during changes in suction. As expected, both studies showed that during drying aggregates volume reduced, while during wetting aggregates increased due to swelling (Figure 2-27). Interestingly, the results also captured evidence of irreversible changes in deformation of the aggregates. For instance, upon a full cycle of wetting-drying Farulla et al. (2010) observed that aggregates on the drying path had greater volume compared to the wetting path.

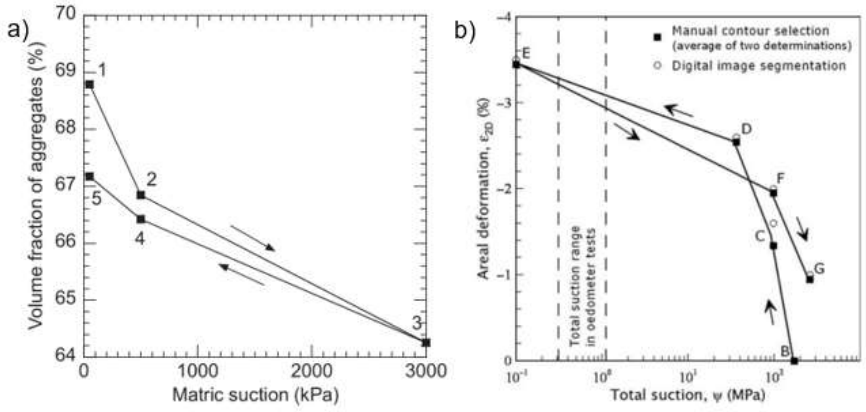


Figure 2-27 Variation of the aggregate volume for the (a) Bioley silt and (b) kaolinitic–illitic clay during drying-wetting cycle (Koliji et al., 2010; Farulla et al., 2010).

During drying and reduction in the volume of aggregates, Koliji et al. (2006) showed that for a silty soil a decrease in the inter-aggregate pores occurs (Zone 3) while simultaneously the volume of intra-aggregate pores increases (Zone 2), suggesting aggregation of the particles (Figure 2-28). Upon wetting at high suction, water is initially taken up by the intra-aggregate pores. Consequently, in this range Sivakumar et al. (2006) found that the compactive effort of a kaolin clay had little influence on the relationship between water content and matric suction. During wetting at lower suctions towards saturation, the aggregates continue to swell (Figure 2-29). In confined conditions swelling of the aggregates is correlated with a reduction in the inter-aggregate pores by several studies e.g. Sivakumar et al. (2006); Lloret et al. (2003); Koliji et al. (2010). However, changes in pore size distribution are known to be sensitive to confining conditions and initial compacted conditions due to their influence on the packing of the aggregates (Tang et al., 2023). For instance, for greater initial dry densities of kaolin clay Thom et al. (2007) observed a reduction in the available inter-aggregate pore space for expansion of the aggregates and therefore greater overall specimen volume changes. While at high confining stresses (1000 kPa) Koliji et al. (2010) found that the Bioley silt experienced a total loss of inter-aggregate pores after full saturation resulting in a unimodal pore size distribution.

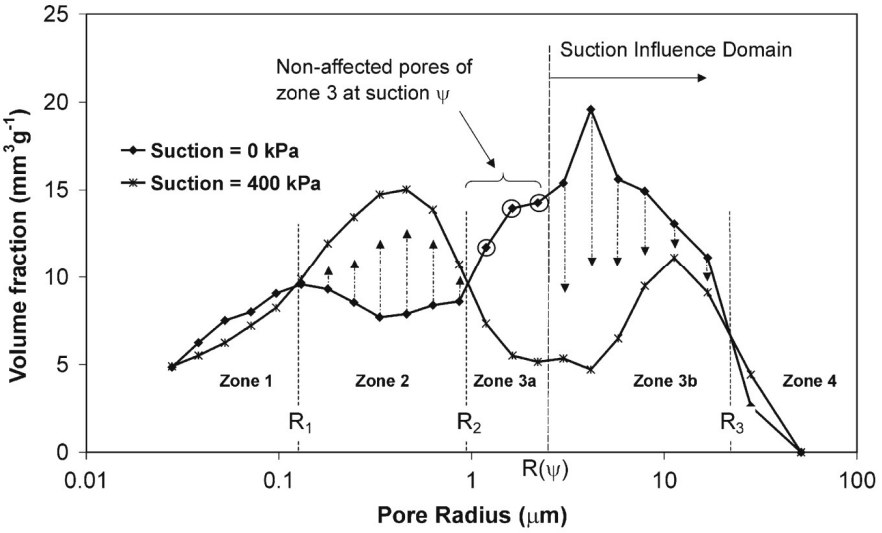


Figure 2-28 Evolution of silty soil microstructure drying (Koliji et al., 2006).

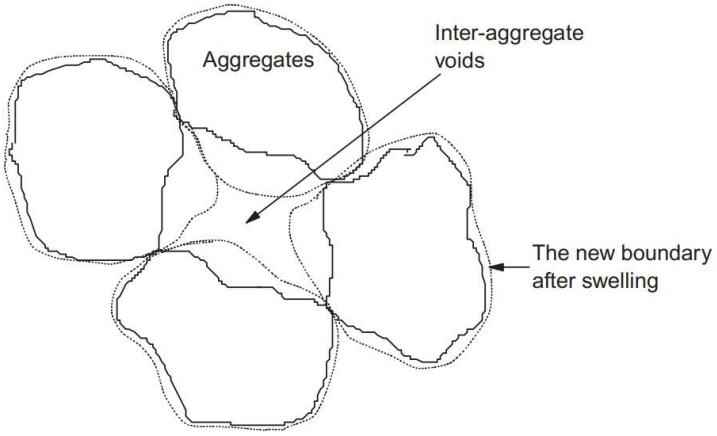


Figure 2-29 Conceptual model for swelling of aggregates into the inter-aggregate pore space during wetting (Sivakumar et al., 2006).

During the continued drying-wetting of compacted soils irreversible changes in structure may accumulate. This was demonstrated by Nowamooz and Masrouri (2010) on both densely (1.55 Mg/m^3) and loosely (1.27 Mg/m^3) compacted bentonite and silt mixtures (I_p 22%, W_L 88%) for four drying-wetting cycles between 0 MPa and 287.9 MPa. For this study wetting was conducted by submerging samples while suctions were imposed by osmotic techniques for suctions less than 8.5 MPa and vapour equilibrium or the salt solution techniques for suctions greater than 8.5 MPa. Observations of microstructure using MIP and nitrogen adsorption (BET) showed that for the dense specimens the diameter limit between the intra-aggregates and inter-aggregates decreased from 1.5 to 1 μm and inter-aggregates pore size increased. While for loose specimens, the diameter limit between the intra-aggregates and inter-aggregates increased from 0.15 to 1 μm and inter-aggregate pore size decreased. These changes in microstructure were also observed at the macroscale with the accumulation of swelling for dense specimens and shrinkage for loose specimens (Figure 2-30). Wang and Wei (2015) explains that during drying-wetting, expansive clays may rearrange the aggregate configuration to reach a stable equilibrium state which is approximately reversible. It was also suggested that this state is independent from the initial compacted density resulting in either accumulated shrink and swell depending on the degree of compaction.

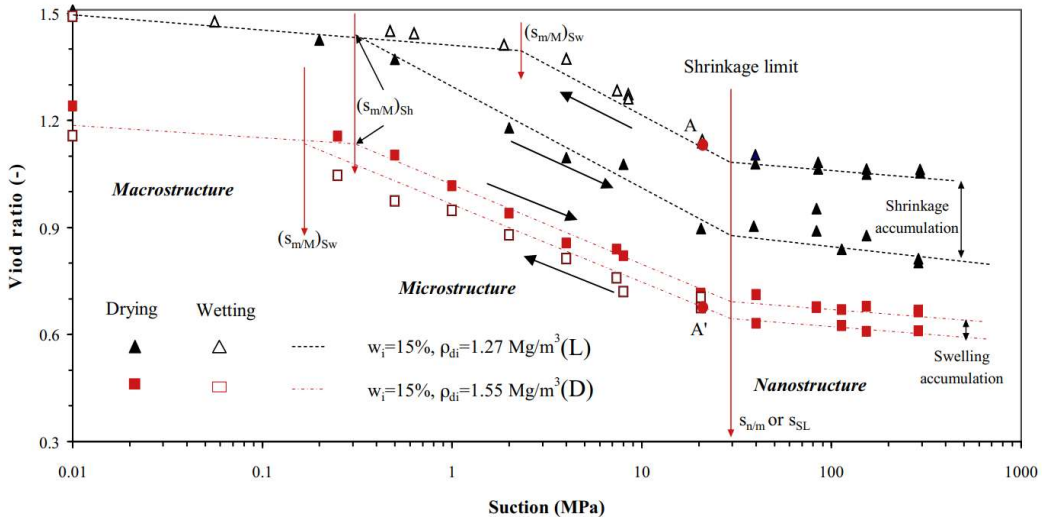


Figure 2-30 Change in void ratio for loosely and densely compacted mixtures of bentonite and silt during one wetting and drying cycle (Nowamooz and Masrouri, 2010).

However, this conceptual model does not fully capture the effect of the formation of micro-cracking on the change in pore size distribution reported by Stirling et al. (2020) and Azizi et al. (2019). For instance, Azizi et al. (2019) observed that during six drying-wetting cycles for a compacted clayey silt (I_p 8%, W_L 33%), micro cracking and breakdown of aggregates took place without any significant changes in overall volume (Figure 2-31). However, a loss in water retention capacity and increase in hydraulic conductivity took place. Indeed, MIP testing revealed that porosity of the aggregates reduced after the first cycle, however, the inter-aggregate porosity increased as the overall volume remained constant. These findings therefore suggest the mechanisms of micro-cracking differ to that of the pore structure changes observed during irreversible shrink/swell.

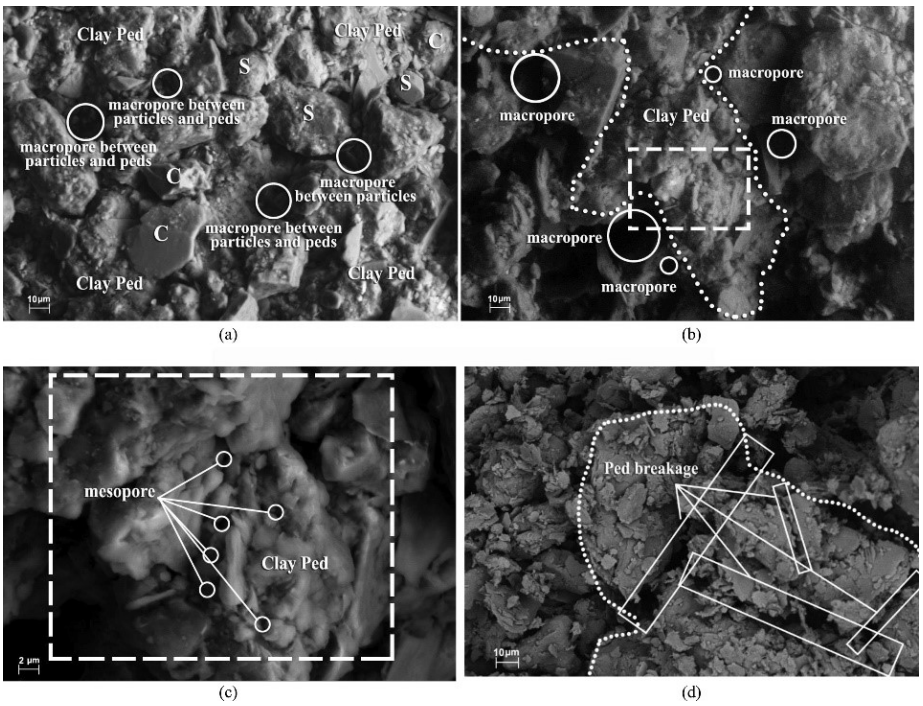


Figure 2-31 Environmental Scanning Electron Microscopy (ESEM) micrographs of a compacted low plasticity clayey silt, dried to a water content of 0.38% and wetted to the compacted water content (20%), where: (a) shows clay peds (aggregates), clay particles C, silt particles S, and macropores; (b) clays ped (aggregate) and macropores; (c) mesopores and; (d) ped (aggregate) breakage after undergoing drying and wetting cycles (reproduced from Azizi et al. (2019), © Canadian Science Publishing or its licensors).

2.8 Summary and contribution

Climate modelling using Representative Concentration Pathways (RCPs) show that the UK climate will experience increasingly high temperatures and widespread drought during summer, in conjunction with increasingly wetter winters due to growth in prolonged precipitation. Past studies suggest that this will have several negative impacts on transport geostructures which primarily relates to seasonal drying-wetting effects on the soils. For instance, the irreversible changes in soil structure including the formation of cracks and the increase shrink-swell of plastic soils. These impacts are particularly important for vulnerable structures, making them increasingly prone to performance shortfalls relating to their serviceability, and increases risk from several failure mechanisms (e.g. progressive failure). This vulnerability is also linked to the construction practices used in the formation of the UK transport network, which can be split between pre-regulation and post-regulation techniques.

Due to these encroaching climatic changes, research into the impacts of the variation in moisture (drying-wetting cycles) on the behaviour of unsaturated compacted soils has assumed greater importance when evaluating their performance. A review of both small

and large strain element testing studies after the application of hydraulic history showed a range of results for different soils and testing conditions. In both cases compacted soils presented evidence of hydraulic ageing and an increase in performance while also significant decrease in performance which was attributed to the formation of micro-cracking. However, in general the underlying mechanisms which drive this behaviour are not well understood. Indeed, these studies do not account for the impact of the amplitude of drying-wetting, mineralogy of compacted soils, compaction conditions and testing variables such as confinement. Furthermore, a review of the microstructure of compacted soils shows that evolution of the soil fabric is also significant during changes in water content however, little is presented linking this to the macro behaviour.

The main contribution of the research work included in this dissertation is therefore to address the research gap focussing on the evaluation of the role the amplitude of drying-wetting and soil characteristics (plasticity and particle size), on the unsaturated behaviour of compacted soils. This includes element testing for both unsaturated small strain (during drying-wetting cycles) and saturated large strain range, tested at the end of the selected drying-wetting cycle history.

Chapter 3
Laboratory Testing Programme

3.1 General

This chapter contains details which describe the procedures and apparatus adopted for laboratory testing (Figure 3-1). Initially it outlines the rationale for selection and preparation of soil samples representative of those present in the UK. Three soils with different plasticity were considered for studying the performance of compacted soils during drying-wetting cycles. Two soils (low to high plasticity) were selected on the basis that they represent typical soils incorporated in modern construction of transport infrastructure, whereas one soil was prepared to mimic high plasticity soils common for historic construction due to lack of regulation. The consideration of three soils is also important because transport infrastructure assets are linear and often composed of a range of compacted soil compositions/index properties owing to the differing depositional environments of the natural geology. A clearer understanding of the differences in their performance due to changes in seasonal moisture deficit resulting from climate change is therefore paramount for effective asset management on the transport network. This is then followed by a description of compaction methodology.

Following compaction at the OMC the soil remains in unsaturated conditions. Determination of unsaturated characteristics of compacted soils are integral for assessment of the continuity of water and air phases and associated changes in suction during drying-wetting. There are number of different techniques which can be selected to achieve this. For this study, the filter paper technique was selected to evaluate the SWRC, and was then used as a rationale to select appropriate and meaningful drying-wetting amplitudes for each soil.

In past studies several drying-wetting methods have been developed to apply hydraulic history to compacted soils. Most common of which, the axis translation technique, allows for control of the suction and has been used primarily for modelling purposes. For this study, a novel method was developed whereby water content was selected as an independent variable to simulate field conditions, where changes in suction take place as a result of a changes in water content. Consequently, for the water content levels considered, suction varies in accordance to the soil water retention behaviour and due to change in the fabric of the soil. A description of this method is also outlined in Section 3.4.

To evaluate the impact of the amplitude of drying-wetting the testing programme utilises both small strain stiffness and saturated stress-strain behaviour. In this study

determination of small strain stiffness was conducted using ultrasonic pulse transmission techniques (Pundit Lab). The use of ultrasonic testing is advantageous compared to more established small strain stiffness testing such as bender elements because they do not require penetration of specimens which may pose challenges due swelling or significant cracking. As bender elements have been used routinely for monitoring shear wave velocities in soil media, this chapter contains a benchmarking exercise to determine optimum testing conditions and validate the ultrasonic pulse transmission technique for soils by comparing the Pundit Lab to commercial bender elements.

As detailed in Chapter 2, the mechanisms that control the post compacted behaviour of compacted soils results from the structure of the soil skeleton. In past studies, both Environmental Scanning Electron Microscopy (ESEM) and Mercury Intrusion Porosimetry (MIP) have been widely used. However, these methods can cause disturbance to the compacted soil specimen pore structure; for example drying and associated shrinkage due to chamber conditions required for ESEM and soil disturbance induced by freeze-drying and the intrusion of mercury. This is of particular significance for this study due to the importance of maintaining the selected water content of specimens to accurately image the pore structure in unsaturated conditions. Consequently this chapter also outlines the procedure and apparatus used to capture micro X-ray computed tomography (Micro-CT) conducted at the Diamond Light Source synchrotron. This allowed the capture of micrographs at sufficient resolution to observe the fabric of the specimens without imparting specimen disturbance.

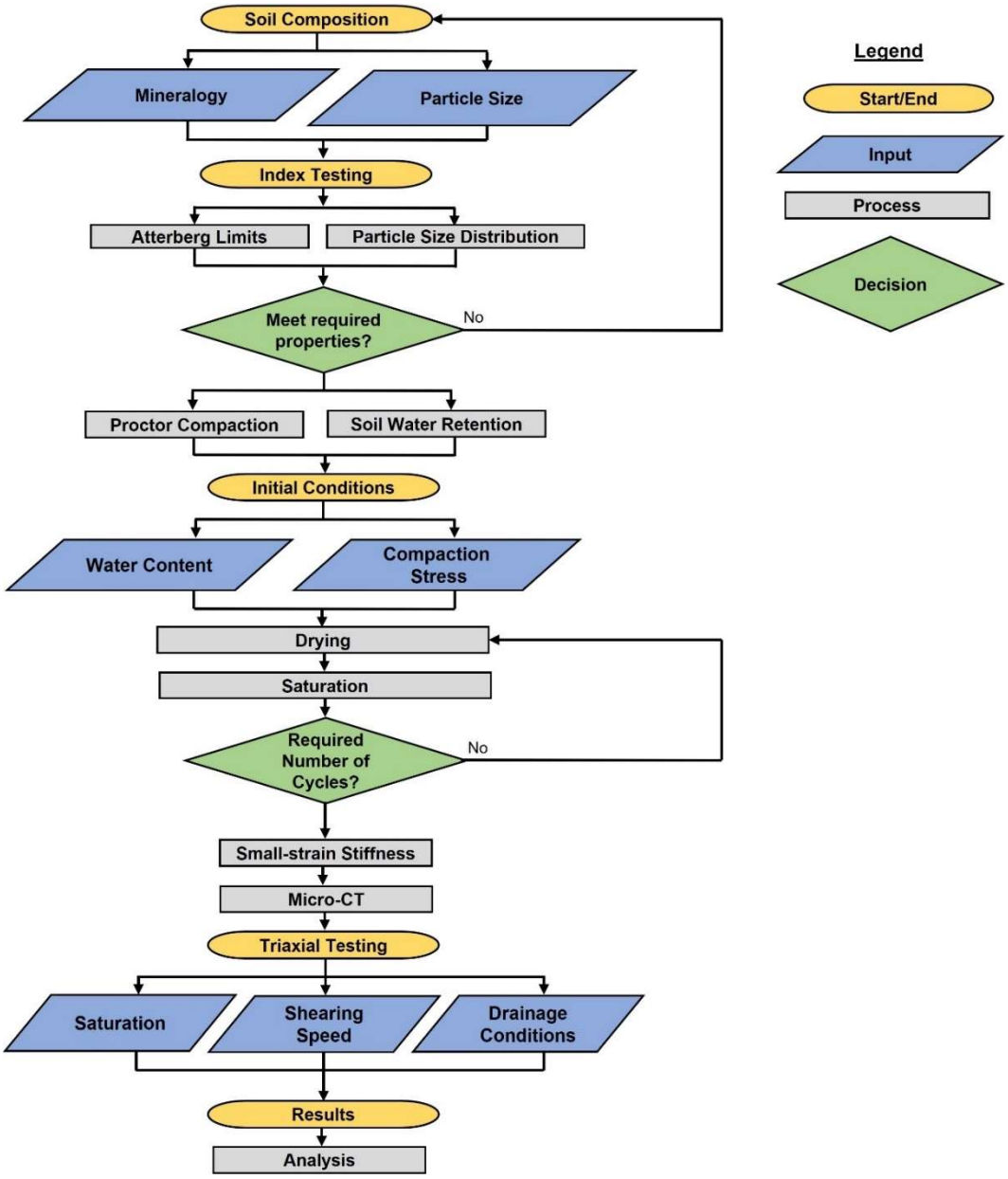


Figure 3-1 Summary of laboratory testing programme for compacted specimens.

3.2 Materials

The three soils tested in the study had differing plasticity and particle size distributions and were selected to be representative of soils in the UK (Table 3-1). Two 'synthetic soils' were created by combining differing quantities of sand fractions, silt fractions (composed of silica MIN-U-SIL acquired from U.S. Silica Inc), ball clay and bentonite. This was critical to ensure a high degree of repeatability between testing specimens. Kaolin clay procured from Imerys Ltd was used as a 'baseline' material from which behaviour could be compared to results presented in literature i.e. Hasan and Wheeler (2015), Vesga (2008), Thom et al. (2007) and Biglari et al. (2012). Ball clay was selected to constitute the clay sized potion of the other synthetic soil mixtures. It is a sedimentary clay which is primarily composed of kaolinite and consists of particles which are <2μm.

This allowed for a more accurate representation of the particle size of soils in the UK when compared to the kaolin clay (Imerys Ltd) which largely consists of silt sized particles.

The index properties of the low plasticity mixture was selected to represent typical coarser glacial tills in northern England deposited during the Devensian glaciation. It is noted that glacial tills in the UK contain significant particle size variability, however, for the purposes of discrete laboratory testing very coarse grained material was disregarded. The clayey sandy silt mixture (classified using BS 5930:2015+A1:2020) consists of 45% fine, medium and coarse sand particles, 36% silt sized particles and 19% clay sized particles (Figure 3-2) and was derived from the Vale of York glacial till formation reported by Culshaw et al. (2017).

For intermediate to high plasticity material, kaolin clay procured from Imerys Ltd was used without the addition of further minerals/particles. The commercial kaolin material is classified as a clayey silt mixture (using BS 5930:2015+A1:2020) and consists of 62% medium and fine silt and 38% clay sized particles (Figure 3-2).

The index properties of the final mixture were selected to reflect a silty London Clay, typical of stiff overconsolidated sedimented clays in Midlands and southern England known for their higher plasticity. The silty clay mixture (classified using BS 5930:2015+A1:2020) consists of 40% silt fraction and 60% clay fraction (Figure 3-2) derived from data reported by Eyles and Sladen (1981) and Freeborough et al. (2005).

The Atterberg limits of the materials are also given in Table 3-1 and shown in Figure 3-3. Representative plasticity was achieved by increasing or decreasing the proportion of bentonite by trial and error contingent on data taken from the literature presented in Appendix B, Table B-2. The Unified Soil Classification System (USCS) classifies the clayey sandy silt a clay of low-intermediate plasticity (CL) , the clayey silt as a silt of high plasticity (MH) and the silty clay a clay of very high plasticity (CV).

The results of x-ray diffraction analysis (XRD) are also presented in Figure 3-4. Expectedly, it shows that the clayey sandy silt is predominantly composed of quartz with small proportion of kaolinite, muscovite and sepiolite. The clayey silt also consists primarily of kaolinite, quartz and muscovite. While the silty clay consists of significant quartz, which can be attributed to the addition of silica MIN-U-SIL material, and kaolin with sepiolite and muscovite.

The proportion of the specific constituent components which form the discrete soil mixtures are presented in Appendix B, Table B-1. Mixtures were prepared by weight according to the ratio presented in Table B-1 and then thoroughly mixed in a dry state prior to the addition of water. Note that henceforth in the study the materials will be named by their classification, clayey sandy silt, clayey silt and silty clay.

Table 3-1 Summary of the index properties of the kaolin and target compaction conditions.

Geotechnical Properties	Clayey sandy silt	Clayey silt	Silty clay
Liquid Limit, W_L (%)	34	56	77
Plastic Limit, W_P (%)	14	33	23
Plasticity Index, I_P (%)	20	23	54
Specific gravity, G_s	2.64	2.61	2.62
Clay fraction (d< 2 μm) (%)	19	38	60
Maximum Proctor unit weight (kN/m³)	18.4	14.1	15.4
Optimum Water Content (OMC) (%)	13.5	28	22
Static Compaction Conditions			
Unit weight (kN/m³)*	17.8	13.2	14.9
Compaction water content (%)	13.5	28	22

**Unit weight achieved at static 1400 kPa stress*

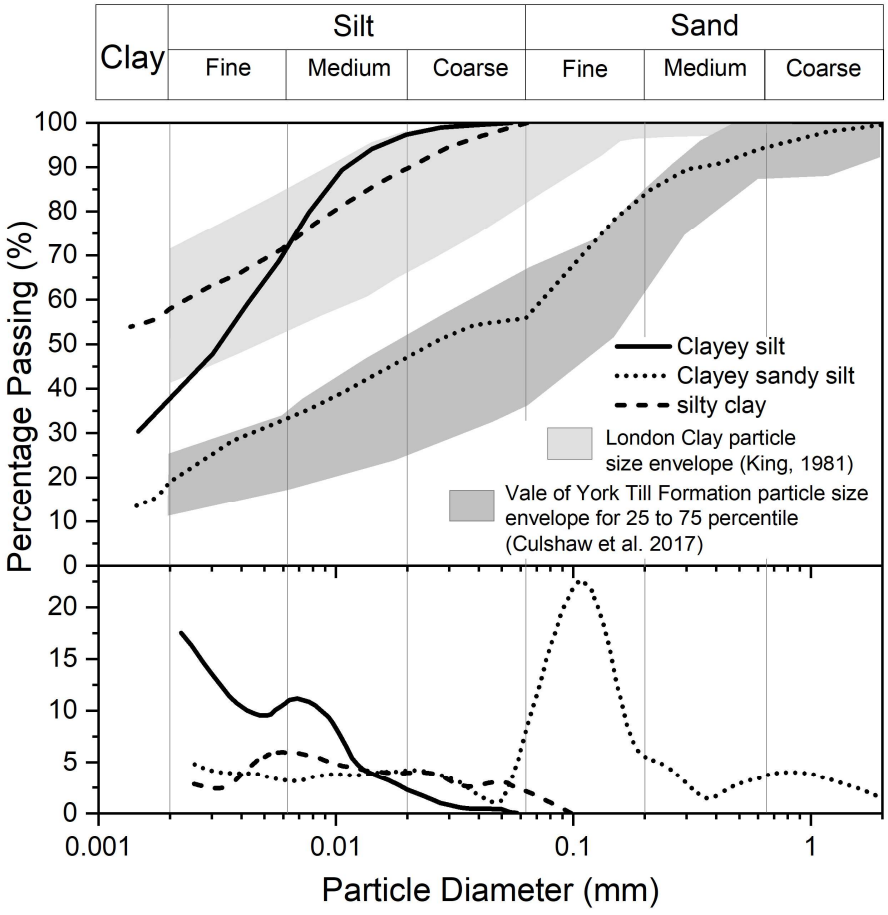


Figure 3-2 Particle size distribution of clayey sandy silt, clayey silt and silty clay used in this study.

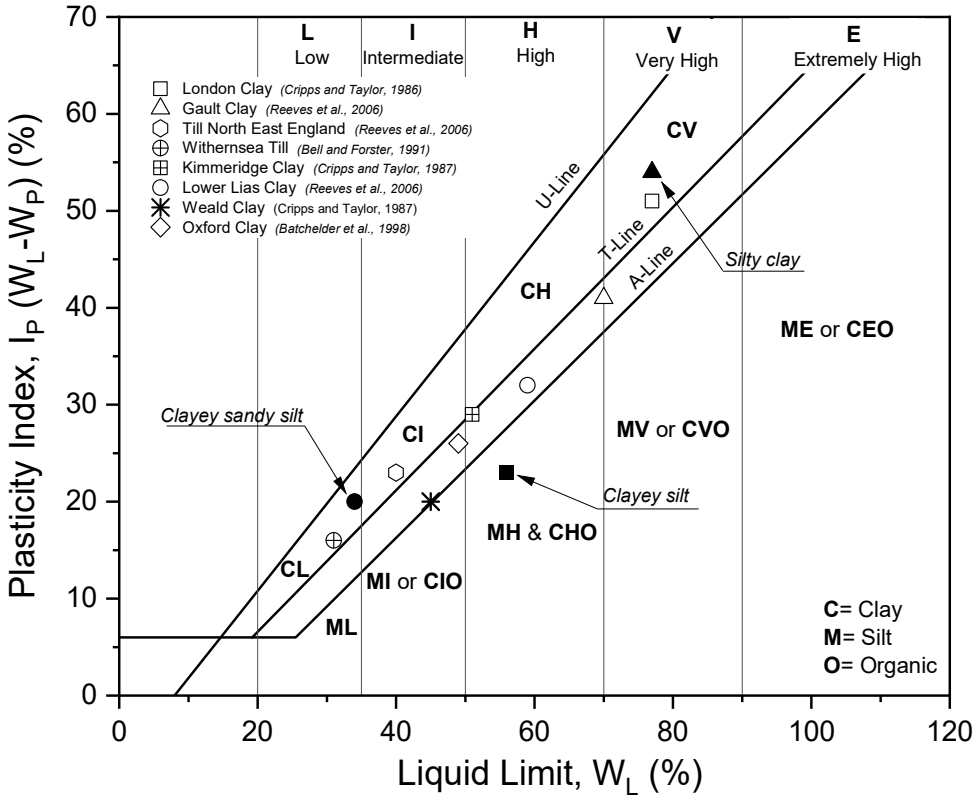


Figure 3-3 Casagrande chart showing the plasticity of three compacted soils in this study (solid) and different soils present in the UK (hollow).

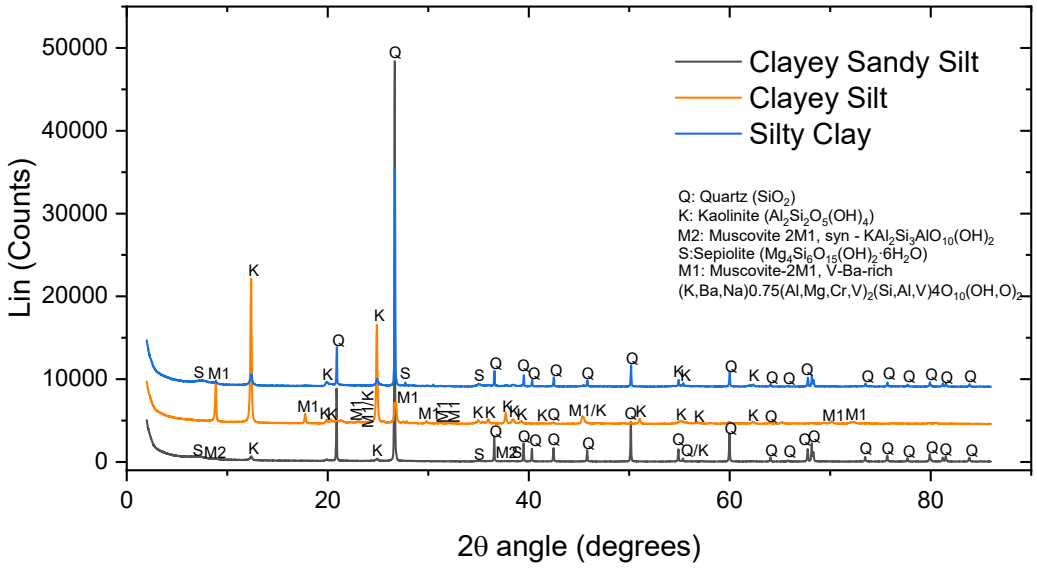


Figure 3-4 XRD analysis of clayey sandy silt, clayey silt and silty clay.

3.3 Compaction

The compaction characteristics for each of the soils were first established using Proctor compaction tests using standard 2.5 kg compaction hammer (BS 1377-2:2022). This was conducted as per end product specification (as specified in the Manual of Contract

Documents for Highway Works, MCHW series 600) to determine the maximum dry unit weight (MDUW) and corresponding OMC used in practice (Figure 3-5a). It's noted that historic structures on the transport network were not placed or indeed compacted at OMC however, for this study it was deemed a suitable benchmark to allow for comparison between the different soils. Furthermore, in practice dry or wet of optimum water content may be specified depending on the anticipated future behaviour of the soils which is further discussed in Section 6.2.

In this study, the specimens used for small strain stiffness and triaxial testing were prepared using static compaction in a split mould to a desired dry unit weight by applying a constant stress. Static compaction is favoured for its repeatability, ability to produce homogeneous specimens and resemblance to field compaction conditions (Serratrice, 2022). Similar procedures have been adopted in several past studies; for example Azizi et al. (2018); Reddy and Jagadish (1993); Tarantino (2009); Tarantino and Col (2008), among others.

Prior to compaction the dry powdered material was mixed with demineralised water to achieve the required water content. To emulate field conditions closely, the Proctor OMC water content was selected for compaction of the specimens.

The moist samples were sealed and kept at approximate constant temperature and humidity conditions for a minimum of 24 hours to ensure moisture equilibration. The material was then passed through a 2 mm aperture sieve to reduce the size of aggregated particles. All specimens were then statically compacted using a static stress level of 1400 kPa to a diameter of 38 mm and height of 76 mm. To minimise friction, dry Polytetrafluoroethylene (PTFE) was used to coat the split mould walls and soil was compacted in two layers. After placement of the first layer, the surface was scarified to ensure good adhesion between both layers.

Comparison between standard Proctor compaction and static compaction for each soil is presented in Figure 3-5b. The results are plotted using both water content (w) and water ratio (e_w). Water ratio is defined as the ratio of volume of water V_w to volume of solid V_s. As both void ratio and water ratio are normalized by the same quantity, the volume of solids, it allows for effective comparison between the different soil mixtures with different specific gravity values. It should be noted that in Figure 3-5a the different air void lines are represented considering a specific gravity value of 2.65, but in reality there were small differences in the specific gravity values obtained for the three soils (Table 3-1) and thus Figure 3-4b enables a better comparison between compaction data of the three soils. Results show that all materials achieve >90% Proctor conditions when statically compacted at 1400 kPa.

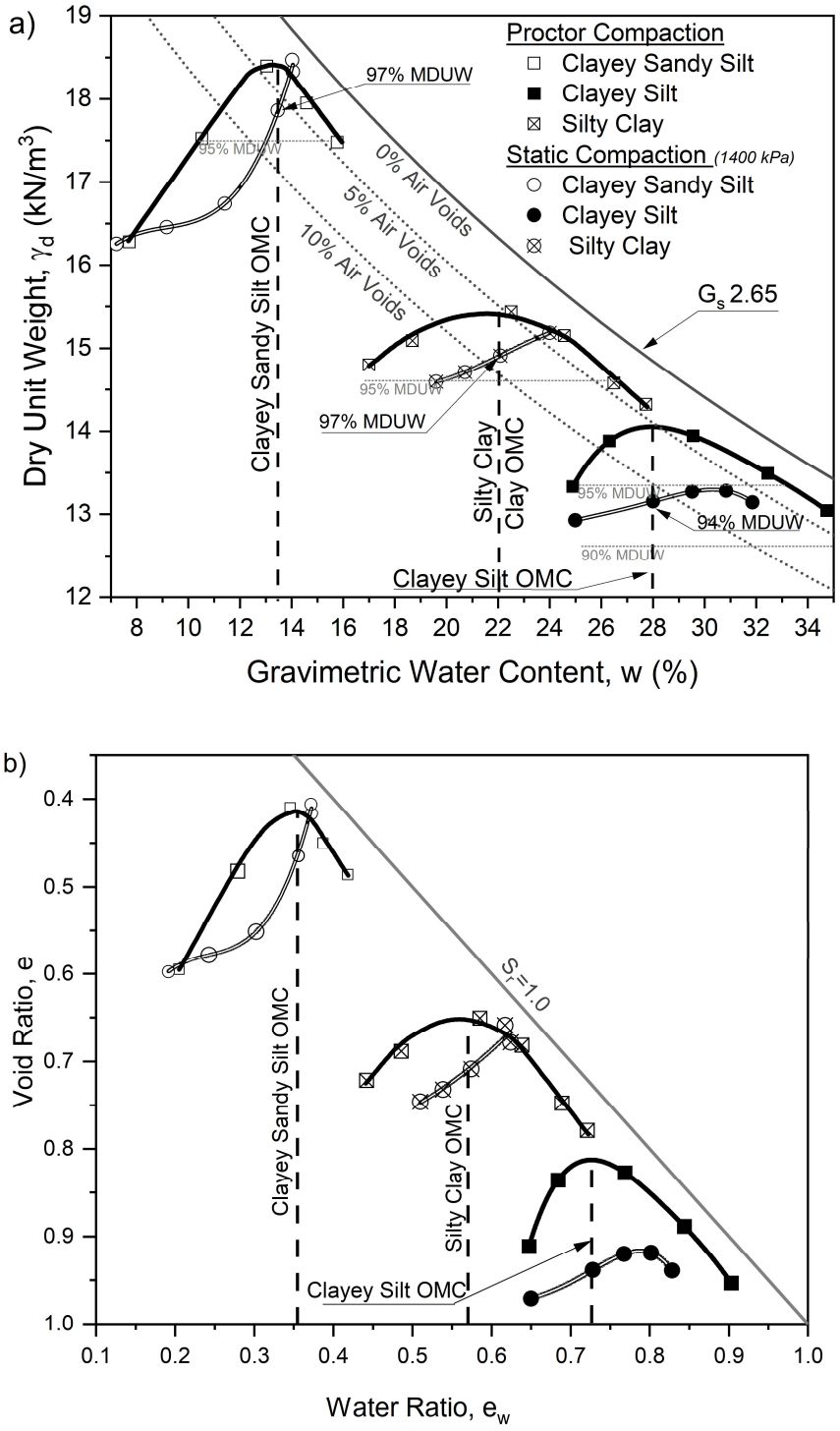


Figure 3-5 Comparison between standard Proctor compaction and static compaction (1400 kPa) for a) dry unit weight and b) void ratio.

3.4 Drying and wetting

Compacted samples were subjected to drying and wetting to evaluate the effect of different hydraulic states on the small strain stiffness behaviour of the three soils. Drying-wetting was controlled using gravimetric water content as an independent variable. To achieve full saturation specimens were submerged in demineralised water under vacuum for 24 hours. Figure 3-6 shows the novel setup developed to achieve full saturation which allows water ingress while maintaining their integrity.

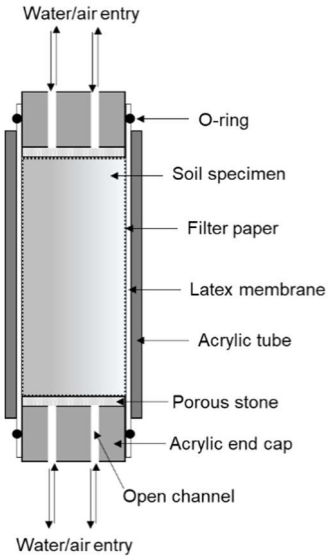


Figure 3-6 Schematic diagram showing the configuration used during wetting specimens.

Drying and wetting to target water contents was achieved by considering the mass of the solids was constant (Mendes, 2011; Dong and Lu, 2016). For instance, for a given target water content ($w_{initial}$) the corresponding weight (m_{final}) was calculated using the initial mass ($m_{initial}$) and water content ($w_{initial}$), as follows:

$$m_{final} = \frac{m_{initial} \times (1 + w_{final})}{(1 + w_{initial})} \quad (3.1)$$

Wetting to selected water contents was achieved by adding water towards the target weight while the specimens were contained in the setup shown in Figure 3-6. Air-drying at a constant 40℃ (<1℃ variation) using the Genlab soil drying ovens was selected to expedite the time required to reduce moisture of the specimens. When specimens were placed in the oven their weight was closely monitored to ensure target weights were met. Once the a change in moisture is achieved, an equilibration period is required to ensure that there is an homogeneous distribution of moisture within the specimen. For instance, without equilibration small strain stiffness has been shown to be underestimated (Ngoc et al., 2020). To validate the adopted drying-wetting methodology, the distribution of moisture was measured both horizontally and vertically by subsampling the specimens

(Figure 3-7). During equilibration specimens were kept at a relatively constant temperature and humidity conditions. The results for the clayey sandy silt, clayey silt, and silty clay for selected water contents are shown in Figure 3-8, Figure 3-9 and Figure 3-10 respectively.

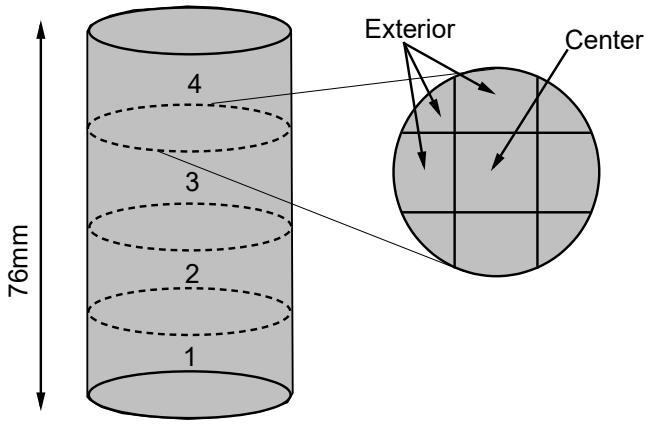


Figure 3-7 Illustration of subsampling method to determine distribution of water content following drying-wetting.

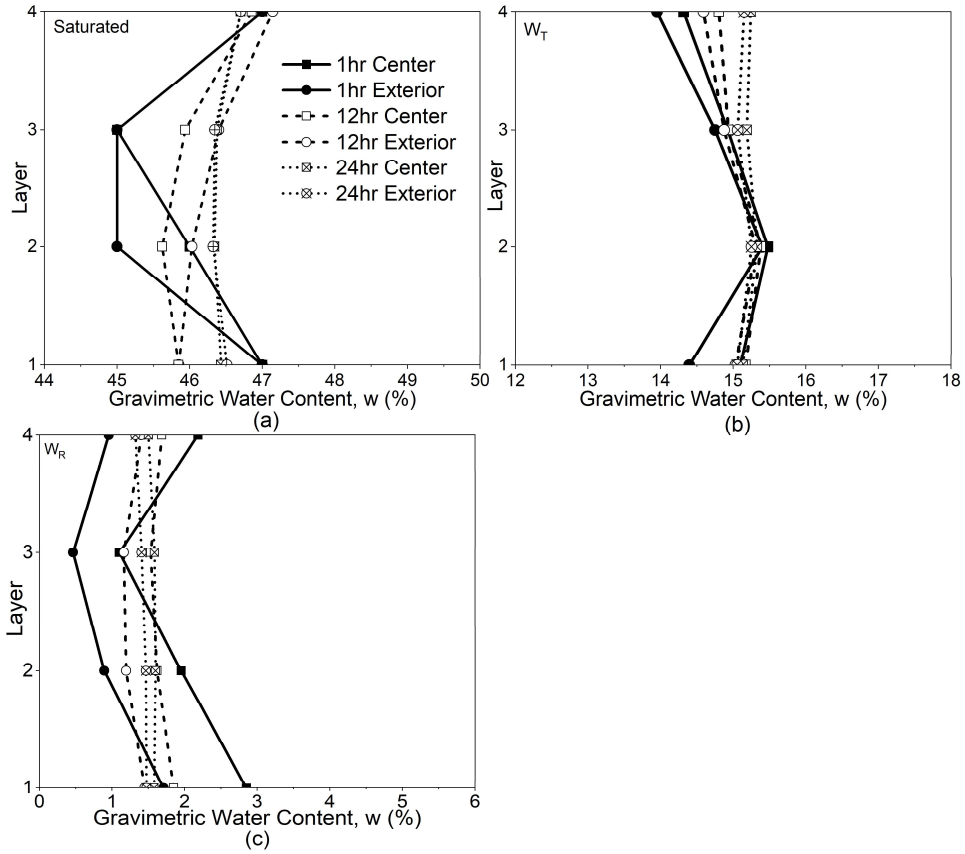


Figure 3-8 Compacted clayey silt specimen water content distribution after 1hr, 12hr and 24hr equilibration time for a) full saturation, b) drying to 15% water content (w_T), c) drying to 1% water content (w_R).

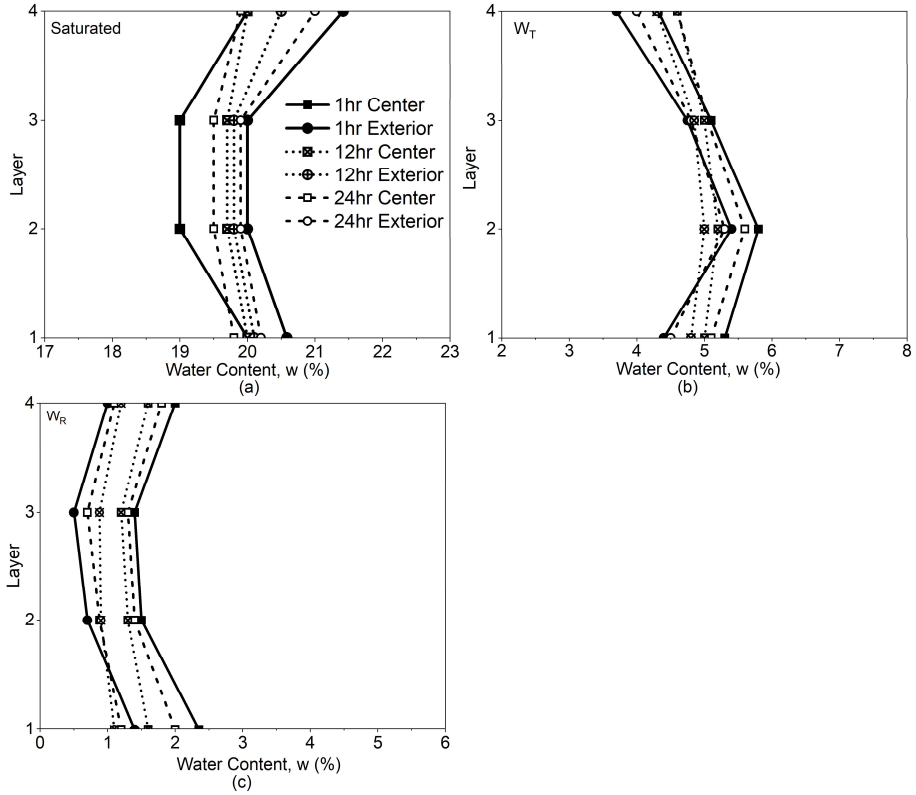


Figure 3-9 Compacted clayey sandy silt specimen water content distribution after 1hr, 12hr and 24hr equilibration time for a) full saturation, b) drying to 5% water content (w_T), c) drying to 1% water content (w_R).

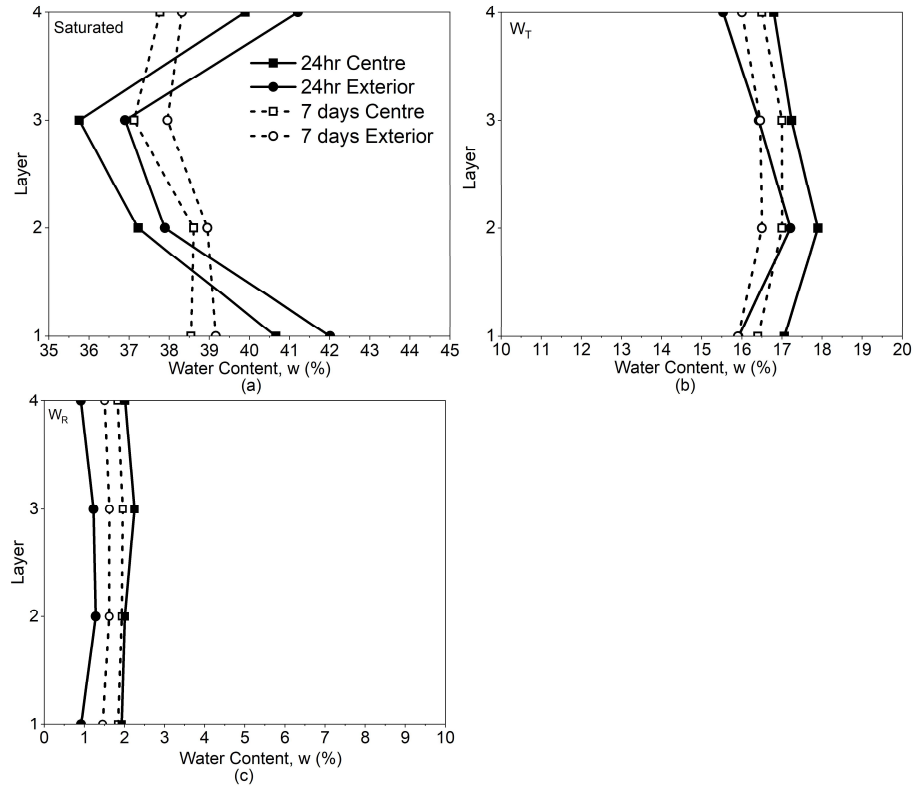


Figure 3-10 Compacted silty clay specimen water content distribution after 24hr and 7 days equilibration time for a) full saturation, b) drying to17% water content (w_T), c) drying to 1.5% water content (w_R).

The results show that initially following air-drying a greater loss of moisture is evident at the specimen boundaries inducing a hydraulic gradient between the centre and boundaries of the specimen. A similar effect also occurs at the ends of the specimens due to the increased surface area for evaporation of moisture, resulting in a vertical hydraulic gradient. During wetting the inverse trend is observed due to infiltration of water from the exterior of the specimens. To achieve a homogenous distribution of water content across the specimens a difference in water content of <0.5% both vertically and laterally was targeted. Results show that both the clayey silt and the clayey sandy silt required a minimum of 24 hours of equilibration time to achieve adequate homogeneity at all selected water contents. As expected, the silty clay required significantly more equilibration time due to the decrease in hydraulic conductivity and thus rate of water flow. Results show that a minimum of 7 days achieved adequate homogeneity for all conditions.

3.5 Determination of water retention behaviour

3.5.1 Suction

Suction underpins the determination of unsaturated behaviour and characterisation of unsaturated soil. In the laboratory, suction can be measured and controlled using several different methods and commercially available apparatus depending on the target suction ranges (Figure 3-11). Among those, the filter paper (contact method) can cover an extensive range of measurements of matric suction and is relatively well established. For that reason, in this thesis the filter paper method was selected as the preferred method and will be further discussed.

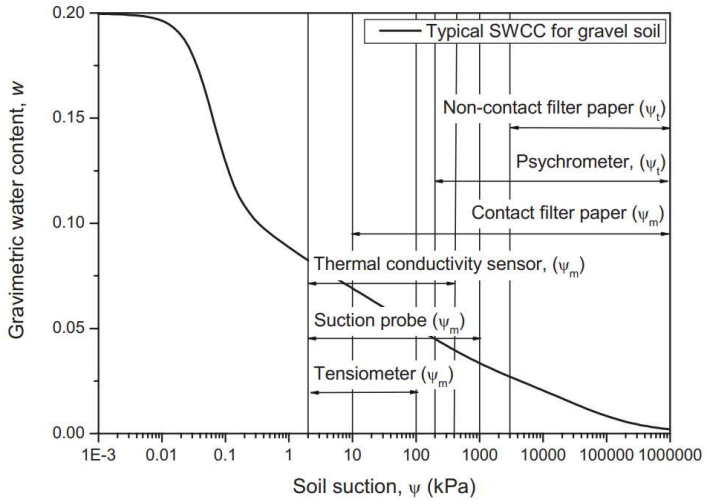


Figure 3-11 Methods for both total (Ψ_t) and matric suction (Ψ_m) measurements in soils (Li et al., 2009).

3.5.1.1 Filter paper method

Filter paper testing has been widely adopted for the determination of suction due to it being cost effective, relatively simple while having the ability to measure a large target suction range. Testing was conducted in accordance with ASTM D5298-10 using Whatman No.42 filter paper, while adopting more recent calibration curves published in past studies (e.g. Leong and Rahardjo (2002)). Both matric suction and total suction was measured to determine the main drying curve and drying-wetting suctions. In most cases matric suction measurements were primarily used and total suction taken as precaution in cases where matric suction measurements were lost i.e. contamination or recording errors. In this case it was assumed that the contribution of osmotic suction to the total suction of the soils was low due negligible amounts of salts.

For measurement of matric suction the filter paper was placed in contact with the specimen. To prevent contamination of the filter paper by the soils it was placed between two sacrificial filter papers with a larger diameter. Two contact measurements were made for each specimen to allow for the determination of an average value of matric suction to ensure precision (Figure 3-12 and Figure 3-13). Good contact between the filter paper and the specimen was ensured by wrapping it with electrical tape. For measurement of total suction, the filter paper was separated from the specimen using a plastic grid (Figure 3-12 and Figure 3-13). Two filter papers where then placed on top of the grid and the container was sealed using electrical tape. After placement of the filter paper specimens were left for equilibration. According to ASTM D5298-10 equilibration should be allowed for a minimum of 7 days. During this period the specimens were stored in an insulated cooler to minimise thermal variation and prevent the formation of condensation. Upon the completion of equilibration the central (contact) and two loose (non-contact) filter papers were removed to determine their water content. Following their removal from the specimen container they were quickly moved to an aluminium cup and their weight was swiftly determined using precision scales (0.00001g) to minimise loss of moisture by evaporation.

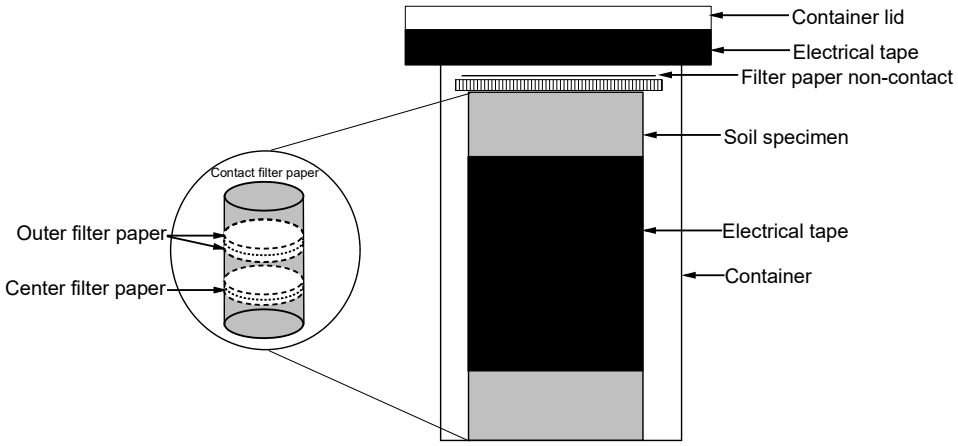


Figure 3-12 Filter paper configuration during measurement of both contact and non-contact suctions.



Figure 3-13 Filter paper precision weight scales and accessories (left) and filter paper configuration (right).

Once the water content of the filter paper was determined suction was calculated using bi-linear calibration curves for Whatman No. 42 filter paper reported by Leong and Rahardjo (2002):

Matric Suction

$$log_{10}\Psi = 2.909 - 0.0229\left(wc_{fp}\right) \text{ where } wc_{fp} > 47\% \quad (3.2)$$

$$log_{10}\Psi = 4.945 - 0.0673\left(wc_{fp}\right) \text{ where } wc_{fp} \leq 47\% \quad (3.3)$$

Total suction

$$log_{10}\Psi = 8.778 - 0.222\left(wc_{fp}\right) \text{ where } wc_{fp} > 26\% \quad (3.4)$$

$$log_{10}\Psi = 5.31 - 0.0879\left(wc_{fp}\right) \text{ where } wc_{fp} \leq 26\% \quad (3.5)$$

The relationship between filter paper water content (wc_{fp}) and suction is presented in Figure 3-14 for matric suction expressed in Eq. (3.2) and Eq. (3.3) and total suction expressed in Eq. (3.4) and Eq. (3.5). The curves are also compared with ASTM D5298-10 standard curve which does not distinguish between total and matric suctions.

The degree of saturation of the specimens for determination of the saturation-suction relationship was calculated by measuring their volume and determining their water content following equilibration. Volume was determined using vernier callipers and taking measurements at several locations in the specimens. More details are included in Section 3.6.

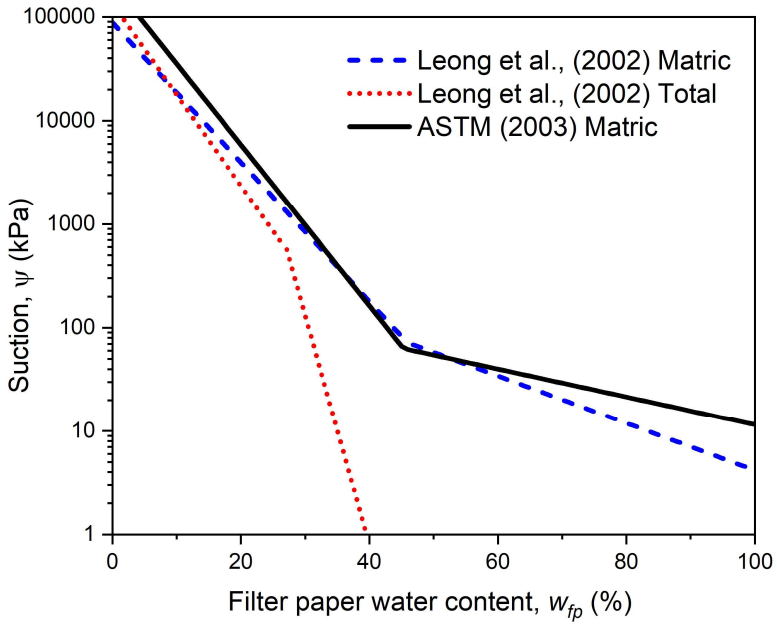


Figure 3-14 Whatman No. 42 filter paper calibration curves for Leong and Rahardjo (2002) and ASTM D5298-10.

The suctions determined for specimens on the main drying path was then used to determine the SWRC. To interpolate the SWRC, the closed form relationship proposed by Van Genuchten (1980) expressed in Eq. (3.6) and Eq. (3.7) was adopted and best fit parameters (*a, m* and *n*) determined using the least square method (Table 3-2).

$$s_r = \left[\frac{1}{1+(a\Psi)^n}\right]^m \qquad (3.6)$$

$$m = (1 - 1/n) \qquad (3.7)$$

Table 3-2 Summary of Van Genuchten (1980) fitting parameters used to derive the main drying water retention curves for kaolin clay clayey sandy silt and silty clay.

	Soil Type	*α*	*m*	*n*
Gravimetric Water Content	Clayey silt	0.0021	0.4920	1.9686
	Clayey Sandy Silt	0.0012	0.4945	1.9783
	Silty Clay	0.0019	0.3027	1.4341
Degree of Saturation	Clayey silt	0.0016	0.5190	2.0790
	Clayey Sandy Silt	0.0012	0.4870	1.9492
	Silty Clay	0.0026	0.4048	1.6802

3.5.2 Drying-wetting extents

Climate change is expected to alter the amplitude of hydraulic cycles experienced by compacted soils used in transport infrastructure in the UK (Walker et al., 2022). UKCP18 predicts increases in future surface temperatures and the frequency and intensity of rainfall and flooding (Lowe et al., 2019). Modelling by Clarke and Smethurst (2010) (using UKCP09 medium high emission scenario data) showed that predicted increases in the UK summer temperatures will result in a corresponding increase in soil moisture deficits by 2080 in compacted London Clay fills. However, the impact of this predicted change on compacted soils behaviour has not been reported. Therefore in this study, the extent of the hydraulic cycle (i.e. range of drying and wetting) forms the independent variable from which the change in small strain behaviour was measured.

The initial dimensions, compaction stress and water content were maintained as constant variables for each specimen and soil composition. The extent of the applied hydraulic cycles (drying and wetting) was controlled using target gravimetric water content levels rather than adopting constant suction levels via the axis translation technique. This approach allowed for saturation and suction to remain dependent variables during application of hydraulic cycles. The method is advantageous as it simulates field conditions more closely while also simplifying testing apparatus and testing times requisite for a large testing programme.

During a singular drying-wetting cycle the small strain stiffness, water content and volume was measured at five discrete points. These measurements took place during the 1st (D/W1), 3rd (D/W3), 6th (D/W6) and 10th (D/W10) cycle. Table 2-3 in Chapter 2 shows that in general drying-wetting cycles have only been conducted on a few cycles. Consequently, 10 cycles will allow for comprehensive investigation into the impact of drying-wetting on the unsaturated behaviour of the selected compacted soils. Following

small strain stiffness testing for each discreet drying-wetting cycle specimens were sheared to failure in saturated conditions (more details included in Section 3.7.4).

For each soil four drying-wetting testing conditions were investigated, including drying-wetting between: full saturation (S_r=1.0) and transition zone (w_T) (abbreviation FT), compacted OMC (w_{OMC}) and transition zone (w_T) (abbreviation CT), full saturation (S_r=1.0) and residual conditions (w_R) (abbreviation FR) and compacted OMC (w_{OMC}) and residual conditions (w_R) (abbreviation CR). To ensure suitable comparison between each soil mixture these drying wetting boundaries were selected using the SWRC. As a consequence, despite differences in saturation and gravimetric water content, the continuity of water phases and air phases were comparable. For each soil graphical construction using the SWRC in a semi-logarithmic space was conducted to determine the AEV and residual conditions. The AEV and residual point are shown in Figure 3-15. By distinguishing these regimes, drying to the 'transition zone boundary' (i.e. FT and CT conditions) was defined as the straight portion of the SWRC within the transition zone prior to transition to residual conditions (Figure 3-15). Drying to the 'residual conditions boundary' (i.e. FR and CR conditions) was defined as the residual water content (Figure 3-15). By distinguishing these novel boundaries the effect of the degree of drying on soil behaviour was evaluated for each soil.

Wetting boundaries were constrained to fully saturated conditions S_r=1.0 (i.e. FT and FR) and the Proctor compacted water content (i.e. CT and CR). This allows for the evaluation of the impact of full saturation during drying-wetting on soil behaviour which has not been previously reported. Note that following compaction at the OMC, specimens were initially dried to their respective drying boundary prior to wetting. The water contents corresponding to the selected drying and wetting boundaries for each soil mixture are presented in Table 3-3.

Table 3-3 Drying and wetting boundaries water content.

Drying-wetting boundaries		Clayey silt	Clayey sandy silt	Silty clay
Wetting boundaries	Full saturation (S_r=1.0)	46.0	20.0	39.0
	Optimum moisture content (w_{OMC}) (%)	28.0	13.5	22.0
Drying boundaries	Transition zone (w_T) (%)	15.0	5.0	17.0
	Residual water content (w_R) (%)	1.5	1.0	2.0

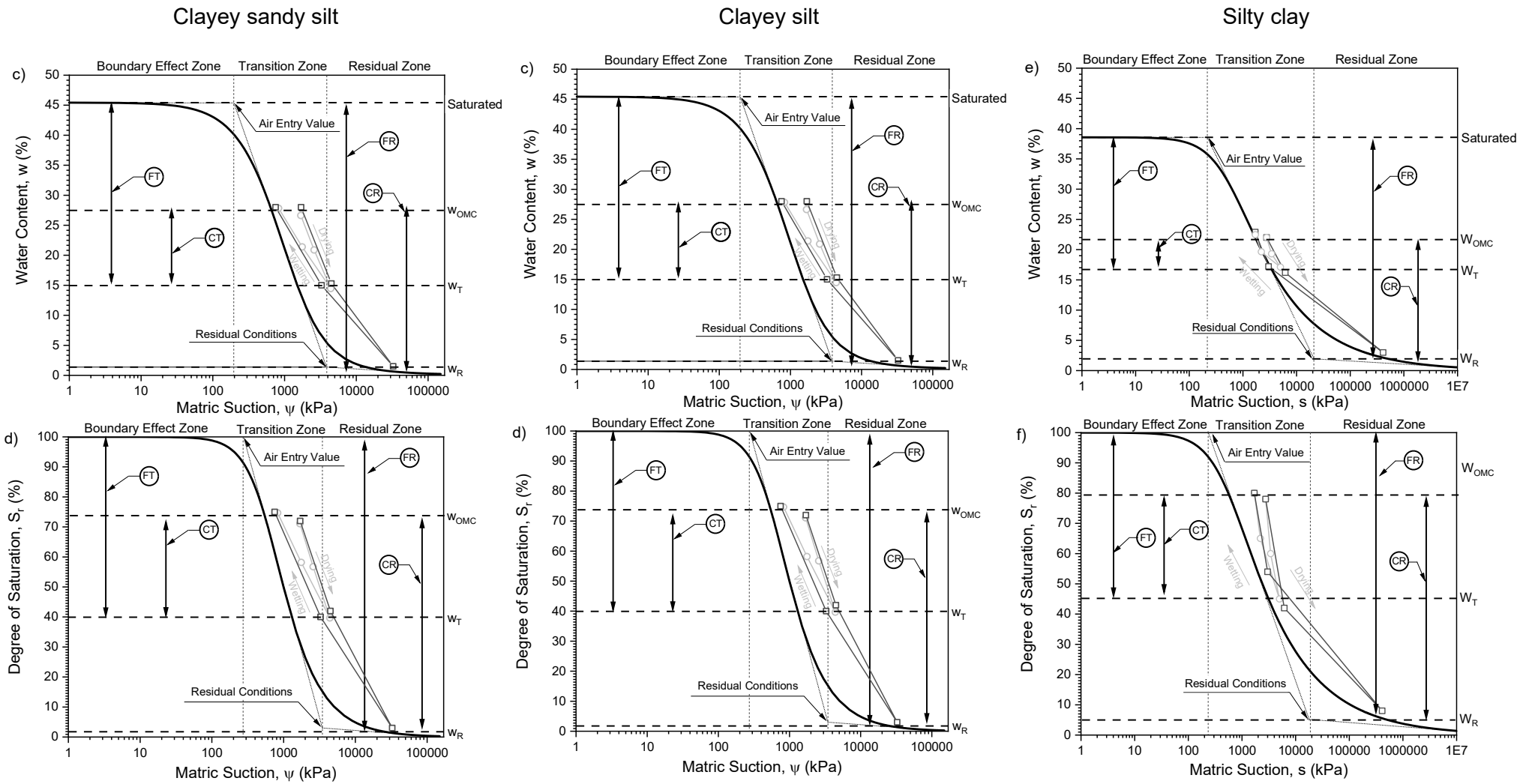


Figure 3-15 The van Genuchten (1980) SWRC, drying-wetting boundaries and the 1st drying-wetting suction measurements for the clayey sandy silt (figures a and b), clayey silt (figures c and d) and the silty clay (figure e and f).

3.6 Determination of volume

Volume changes during drying-wetting were recorded using vernier callipers (0.001mm) according to the procedure suggested by Head (1996) for cylindrical specimens. Three measurements were made of the length, evenly spaced on the face of the specimens (L1-L3). Two perpendicular measurements of the diameter were made at the ends and mid-point of the specimens (D1-D6) (Figure 3-16). Care was taken to ensure the callipers were perpendicular to the surface measured. This was achieved by visual inspection for the skew of the callipers while simultaneously taking measurements and checking for the lowest value. Due care was taken to ensure the callipers did not deform the specimens during measurements. Consequently only a small amount of pressure was applied when closing the jaws. After recording the measurements the average values were taken for length and diameter to determine volume.

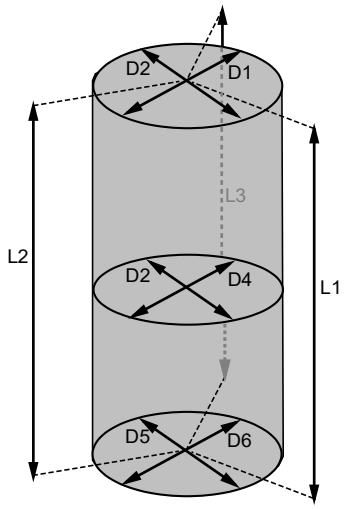


Figure 3-16 Illustration showing measurements made to determine volume of specimens.

3.7 Determination of small strain stiffness

In past studies, small strain stiffness properties have been evaluated using a range of different approaches, i.e. resonant column (Vassallo et al., 2007; Khosravi and McCartney, 2012), bender elements (Dyvik and Madshus, 1985; Viggiani and Atkinson, 1995; Brignoli et al., 1996; Arulnathan et al., 1998; Jovicic et al., 1996; Nakagawa et al., 1996; Ng et al., 2009; Heitor et al., 2015; Gajo et al., 1997; Clariá and Rinaldi, 2007; Blewett et al., 2000; Pennington et al., 2001), ultrasonic pulse transmission (Stephenson, 1978; Prasad and Meissner, 1992; Leong et al., 2004; Nakagawa et al., 1996; Cheng and Leong, 2014) and acoustic measurements (George et al., 2009).

The main advantage that pulse transmission tests (bender elements and ultrasonic pulse) have over other methods for estimating wave velocities is associated with its

versatile construction, simple test procedure as well as the ease in which they can be integrated into a wide range of apparatus and used in different testing conditions (triaxial and oedometers cells, direct and simple shear i.e. Dyvik and Madshus (1985) and Arroyo et al. (2003). Nevertheless, there are some disadvantages, that is, the installation of bender elements causes local disturbance to the sample in the area the elements are embedded, and when it is used in very slender specimens the derived flexural modes of propagation may impede the detection of shear waves (Rio, 2006). In contrast, the ultrasonic pulse tests overcome these limitations and developments in data acquisition technology now enable reliable measurements to be obtained (Leong et al., 2004). However, since the procedure for selecting an appropriate set of testing variables and determining the time the waves travel has not been standardised for both bender elements and ultrasonic pulse tests, interpreting the results may prove difficult at times. It is therefore critical to benchmark these two approaches for a wide range of testing conditions. Therefore, in this section, the bender elements (more established) and ultrasonic pulse testing methods are compared and evaluated to monitor the changes in small strain behaviour of two compacted soils during a drying and wetting cycle. It should be noted that the benchmark comparison was conducted to largely verify the accuracy of the ultrasonic pulse testing, as this testing method is not very well established for soils. In subsequent chapters, the ultrasonic pulse testing was the preferred testing method for the assessment of shear wave velocity and small strain stiffness in the compacted specimens.

3.7.1 Bender element system

Bender elements, or bimorphs, consist of two piezoelectric ceramic elements joined to each side of an intermediate conduction shim (Santamarina et al., 2001). When a voltage differential is applied, one of the elements elongates and the other shortens, which in turn causes the bimorph to bend, hence the name. Bender element transducers are usually used in pairs, which means that one acts as a transmitter and the other as a receiver. The tip of the transmitting bender element is embedded in one end of a specimen of soil while the receiving tip is aligned with the transmitter and embedded at the opposite end. The element acting as a transmitter converts the input electric signal in terms of voltage, into a mechanical energy that generates waves. Some of the components of these waves travel through the specimens and reach the other end where the element is acting as a receiver (Figure 3-17). Wave components travelling to the tip of the receiving transducer force it to bend, and consequently, generate an electric signal. In this study the signal generation was controlled by Clisp software (VJ Tech) while the data acquisition system had 2 input channels each with 16-bit resolution.

Another important aspect when dealing with digital signal processing in bender element systems is the selection of the correct sampling frequency because it determines the accuracy of the results. In this study a sampling rate of 1000 kHz was used to test frequencies from 0.5 to 15.0 kHz to ensure there would be an adequate resolution of the time and voltage for the input and output signals.

3.7.1.1 Bender element tests

The bender elements are 11.25 mm long by 1.80 mm wide and have a protruding thickness or l_b of 3.20 mm. The compacted specimens were carefully protruded, and the bender elements were embedded in the specimens for each of the wetting and drying states considered. It should be noted that there were some small volume changes during wetting branches that caused the soil indentations to close. Subsequent testing therefore caused some additional disturbance in the specimens.

3.7.2 Ultrasonic pulse system

Ultrasonic transducers differ from bender elements as the piezoelectric ceramic elements are bonded to a circular platen consisting of low acoustic impedance material (e.g. impedance equal to stiff materials such as metals). The singular piezoelectric ceramic is also sandwiched between two electrodes which generate the ultrasonic wave excited at frequencies greater than 20 kHz thus above the audible range. Excitation to produce compressional waves is achieved when polarisation of the element is perpendicular direction to the electrode while shear waves are generated due to polarisation parallel to the electrode (Suwal and Kuwano, 2013). Similarly to bender elements, ultrasonic transducers come in pairs whereby the excited wave travels from the piezoelectric element and passes through both the platens and specimen to an opposing element which records the received wave with a data acquisition system. Figure 3-17 shows a schematic diagram illustrating the main differences in wave propagation when using ultrasonic pulse transmission systems for generating shear and compressional waves. In this study the ultrasonic signal was generated by a Pundit Lab system while data acquisition was achieved using a digital oscilloscope. The data acquisition has a 12 bit resolution and 6250 kHz sampling rate to ensure resolution in the time domain was adequate.

As ultrasonic piezoelectric elements do not penetrate the specimens, disturbance due to the insertion of tip of the bender elements can therefore be mitigated. However, good contact between the platen and the specimen must be ensured for reliable measurements. The air present between the platen and the specimen is displaced by a thin layer of acoustic couplant such as water, petroleum jelly or glycerine. For

transmission of shear waves the viscosity of the couplant is important i.e. couplant must have shear strength to transmit the wave. A study by Leong et al. (2004) showed that the signal to noise ratio (SNR) was significantly improved with the addition of acoustic couplant for both compression and shear waves.

Ultrasonic testing systems have been implemented into the investigation of soils to a lesser extent in the literature when compared to bender element systems (Table 3-4). The determination of small strain properties using ultrasonic techniques have been reported primarily for compacted kaolin but also some results reported for residual mudstone, Toyoura sand and compacted silts (Slavova et al., 2010; Weidinger, 2008; Mulmi et al., 2008; Nakagawa et al., 1996; Leong et al., 2004). Furthermore, the use of hybrid systems (both bender elements and ultrasonic) have also been reported by Cheng and Leong (2014). Despite the considerable difference in methods of wave propagation between the bender elements and ultrasonic systems little information has been presented for optimum testing variables for ultrasonic systems. This is especially true for different unsaturated specimen conditions pertinent to field conditions, for instance post compacted soil-atmosphere interactions experienced by most transport infrastructure.

Table 3-4. Summary of literature testing conditions used in ultrasonic and acoustic pulse transmission techniques.

	Materials	Dimensions (diameter × length; mm)	Confining stress (kPa)	Testing frequency
Leong et al., 2004	Kaolin clay	70 × 60	800	P wave: 90 kHz S wave: 76 kHz
	Compacted residual mudstone (S_r 1.0 and S_r 0.6)	70 × 105-118	800	
Brignoli et al., 1996	Saturated Ticino sand	50 × 100	30-500	P wave: 100 kHz S wave: 3 – 10 kHz
	Reconstituted saturated Pontida silty clay	50 × 100	50-500	
	Undisturbed offshore clay	50 × 100	30-100	
Cheng and Leong, 2014	Saturated kaolin	60 × 100-140	-	P wave: 100 kHz S wave: 49 kHz
	Changi sand (S_r 0.5)	60 × 100-140	-	
Mulmi et al., 2008	Dry Toyoura sand	50 × 100	50, 100, 200, 400	P wave: 4 – 16 kHz S wave: 4 – 16 kHz
Miturski et al., 2021	Compacted stabilized clay	80 × 80	Unconfined	P wave: 54 kHz
Slavova et al., 2010	Low plasticity silt	70 × 50	Unconfined	P wave: 46 kHz S wave: 39 kHz
Nakagawa et al., 1996	Saturated kaolin Saturated fine sand	- × 101	98 -490	P wave:200 kHz S wave: 3-5 kHz
George, 2009	Bonny silt Heterogeneous mixture of sand, silt and clay	100 × 125	Unconfined	P wave: 20 kHz S wave: 20 kHz

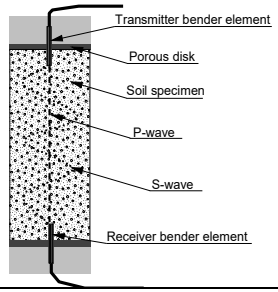
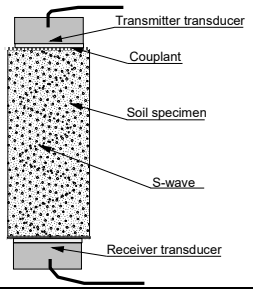
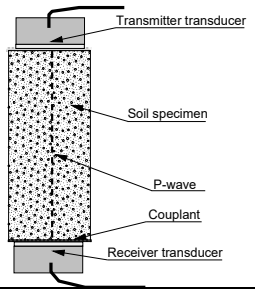
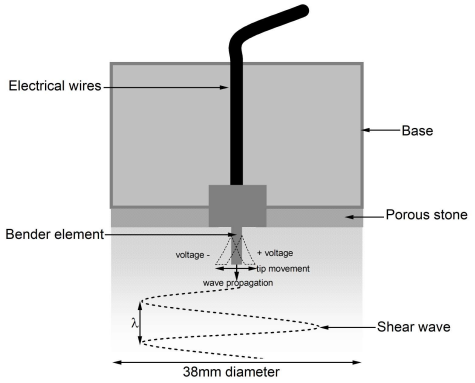
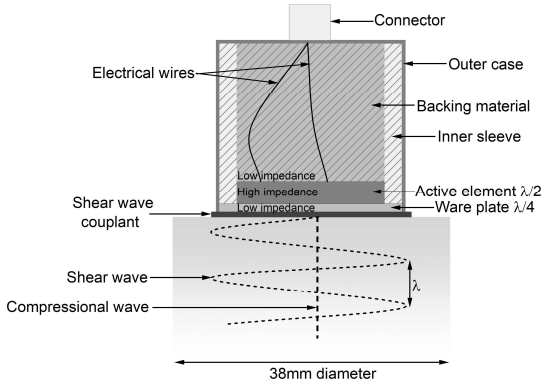
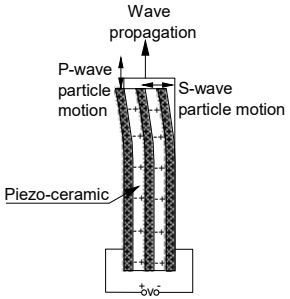
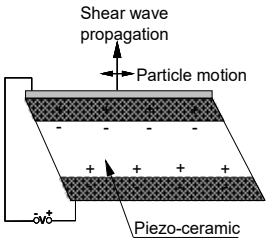
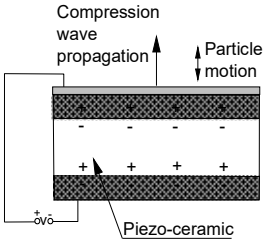
Configuration	BE System	Ultrasonic System	
	Shear and compressional wave	Shear wave	Compressional wave
Pulse transmission			
Transducers			
Piezoelectric element			

Figure 3-17 Schematic diagram showing a comparison between wave propagation in soils using bender elements and ultrasonic shear wave transducers and ultrasonic compression wave transducers (modified after Mulmi et al., 2008).

3.7.2.1 Ultrasonic pulse test system

A Pundit Lab system was used to measure ultrasonic pulse velocities. The Pundit Lab system consist of portable pulse generation instrument with a resolution of 0.1 μs and two 1.5 m transducer cables. Two Olympus normal incidence shear wave transducers (V150-RB) were employed to measure shear wave response using through transmission. The transducers consist of a single piezoelectric crystal attached to a ceramic platen with approximately 25 mm diameter element size. This transducer is highly damped and thus produces a large frequency range. This allows for greater axial resolution (pulse echo techniques) and improved signal to noise ratio in attenuating or scattering materials.

To ensure adequate contact between the soil specimens and transducers a thin layer of Olympus shear wave acoustic couplant (SWC-2) was placed prior to any measurements and small amount of pressure applied to the contact area. After measurements were made all excess couplant was removed from the specimens using a dry cloth.

It is important to note that as the wave passes through the ceramic platen a delay is produced in the received wave. Several testing methods can be used to determine the delay time including face-to-face tests, measurement of a calibration rod of known velocity, or determination of travel time for different rod length (y-axis intercept). In this study a comparison between face-to-face tests and a calibration rod was made at both 24 kHz and 200 kHz input frequencies. The calibration rod consists of an acrylic tube with a known compression wave travel time of 25.4 μs. The calibration rod was thus used to determine the delay time of the shear wave transducers by measuring the compression wave component of the signal rather than the shear wave directly. The results of the tests are presented in Figure 3-18 and show that both methods produced similar delay times with a slight discrepancy of 0.4 μs. However, this is likely a consequence of the determination of the travel time using the compressional wave component of the shear wave, which is likely less accurate. Despite this, the results demonstrate relatively high accuracy for both testing methods. Furthermore, despite the large difference in chosen input frequency (f_{in}) there was no effect on the delay time of the transducers. Therefore, it was assumed that the final delay times were valid for all chosen input frequencies. To ensure the true travel time was calculated a 2.4 μs delay for the shear wave were accounted for in subsequent measurements.

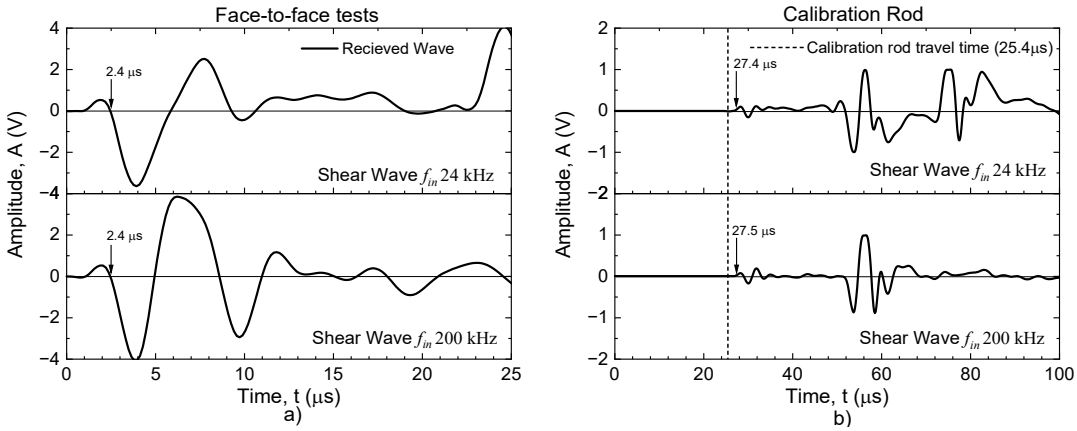


Figure 3-18 Measurement of ultrasonic shear wave and compression wave transducer delay using a) shear wave face-to-face tests, b) shear wave calibration rod (known compression wave 25.4 μs travel time).

3.7.3 Benchmarking ultrasonic pulse transmission

The Pundit Lab ultrasonic pulse test system is less well established for geotechnical engineering applications compared to bender elements owing to the high damping characteristics of soil. As a consequence the following sections describe a comparative exercise between commercial bender elements and the Pundit Lab system. This will validate the use of the Pundit Lab system for different soil compositions during changes in water content used in the remainder of this study. For this exercise both the clayey silt and clayey sandy silt mixtures were considered. These soil mixtures were selected as they have the greatest difference in stiffness, particles size and water content, which impact the propagation of shear waves during drying-wetting and must be considered to select appropriate testing variables. The soil mixtures were compacted at the OMC with a static force of 1400 kPa according to the methodology outlined in Chapter 3.3. Identical specimens were prepared for each system to allow for the comparison of wave transmission techniques.

Note that novel measurement of the attenuation of the waves for the clayey silt and clayey sandy silt using the Pundit Lab during this exercise are also presented in Appendix B, Section B.2.

During testing, specimens were dried and wet according to CT/FT target water contents shown in Figure 3-15 and Figure 3-19. The extent of drying was determined from the main drying SWRC. For this exercise, specimens were dried and wetted within the transition zone (i.e. linear section between air entry and residual suction). As a consequence, both soils were subject to comparable water regimes i.e. continuity of water and air phases. While the adoption of these conditions results in different ranges in water content and matric suction for the two soils, the majority of volume change

occurs within these boundaries and so too the microstructural changes. Consequently, the soil also undergoes significant stiffness changes, which allow for effective comparison between both pulse transmission methods in different states.

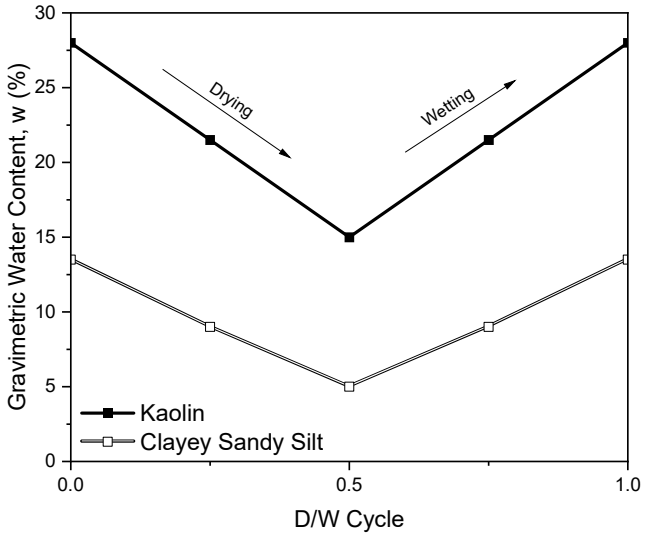


Figure 3-19 Target water contents during drying and wetting for statically compacted kaolin clay and clayey sandy silt.

3.7.3.1 Waveforms

The most common waveform used for testing with transmission pulse tests is the impulse or pulse signal (Shirley, 1978), because the signal in the time and frequency domain are easy to interpret. Of the different waveform pulse signals available, the sinusoidal and square signals (Dyvik and Madshus, 1985) are the two types generally adopted for testing. The square signal has a very well-defined start, which is typically the point from when the wave travel time is measured. While this signal was one of the first used in bender element testing, issues relating to its sharp initial rise and very broad frequency have gradually resulted in it being used less often. This sharp initial rise may prove to be difficult for mechanical devices to reproduce whereas its broad frequency may cause problems in the interpretation the output signals because the near field effects (dispersion phenomena) and modal wave propagation cannot be avoided (Jovicic et al., 1996). Nevertheless, the Pundit Lab is limited to the use of a square pulse to generate both compression and shear waves. This type has been used successfully by several researchers for example Leong et al. (2005); Díaz-Rodríguez et al. (2001) and Pincus et al. (1995). Moreover, the resonant frequency of a system has shown to depend on the stiffness of material which the wave passes (Lee and Santamarina, 2005). In this regard, as a square wave contains a wider range of frequencies a clear response is produced

regardless (Suits et al., 2005). This may be of importance for drying-wetting conditions where soil specimens undergo significant changes in stiffness. Furthermore, as ultrasonic pulse testing takes place at much higher frequencies when compared to bender elements, square waves are better suited as the impact of the near field effect is less prominent.

In contrast, for bender elements sinusoidal signals overcome some of the limitations of the square wave by generating a well-defined signal, although near field components may still be detected (Jovicic et al., 1996). For these reasons, a sinusoidal type of input wave was selected for bender element testing. Other types of waveforms such as continuous wave signals and sweep signals have been explored for bender element systems in past studies e.g. Rio (2006); Da Fonseca et al. (2009); Bonal et al. (2012). However, the impact of these type of waveforms in the bender elements response was not examined in this study.

3.7.3.2 Testing frequency

One of the difficulties involved with measuring the shear wave velocity using transmission pulse tests is selection of adequate testing variables, including the frequency (Viggiani and Atkinson, 1995; Brignoli et al., 1996; Jovicic et al., 1996; Leong et al., 2005). Figure 3-20 shows the time domain traces of the shear wave velocity obtained using the bender elements in a clayey silt specimen (static stress 1400 kPa) tested with different input frequencies. For this system, input frequencies (f_{in}) above 4 kHz yielded approximately the same travel time (i.e. time to the first deflection and bump maximum), whereas lower values of 1 kHz and 2 kHz led to much larger values and consequently underestimation of the shear wave velocity. It is noted that as the frequency of the waveform increases beyond 4 kHz, the strength of the signal reduced significantly.

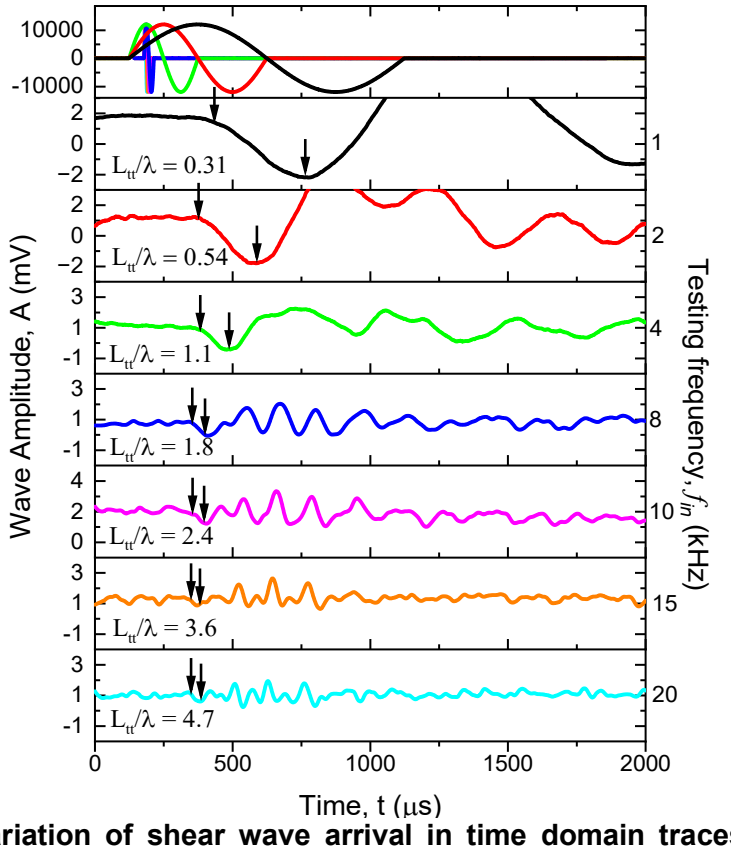


Figure 3-20 Variation of shear wave arrival in time domain traces (compacted clayey silt) for bender elements testing method (first deflection and first bump for frequencies ranging from 1-20 kHz).

These results are consistent with the findings by Arulnathan et al. (1998), who demonstrated that a decrease in wavelength to length of the bender element (λ/L_b) ratio leads to a deterioration of the received signals. The ratio between the length of the wave path (tip to tip L_{tt} or platen to platen L_{pp}) and length of the wave (λ) also indicates that the chosen testing frequency is adequate. The L_{tt}/λ can be obtained from the tests as follows:

$$L_{tt} / \lambda = (L_{tt} / V_s)\, f_{in} = f_{in}\, \Delta t \qquad (3.8)$$

where, f represents the frequency and Δt the wave travel time. By considering the traces of the shear wave in Figure 3-20 we obtain an L_{tt}/λ between 0.3 and 4.7 for the bender element system. A sufficiently large value is desirable to avoid the influence of the near field effects (i.e. Sanchez-Salinero et al. (1986) suggests $L_{tt}/\lambda>2$, Pennington et al. (2001) $2<L_{tt}/\lambda<10$ and Arroyo et al. (2003) $L_{tt}/\lambda>2$). For the bender element system used in this study it was found that a testing frequency of between f_{in} 8 kHz and f_{in} 10 kHz successfully minimised the effect of the near field component and warrant the strength of the received signal at various water contents. Furthermore, although the near field effects strongly influence the estimated travel times in time domain methods, the frequency domain methods are relatively unaffected (Lee and Santamarina, 2005). Notably the strongest output was detected when the input wave is 1 kHz (Figure 3-20),

which indicates that this may be the approximate natural resonant frequency of the soil and bender element system.

The ultrasonic transducer configuration produces unique wave propagation whereby the frequency of the traducer is dependent on the thickness of the piezoelectric element (resonant frequency wave length of an ultrasonic element is equal to twice its thickness). As a result, unlike the bender element system the frequency cannot be dynamically selected for a set of transducers. Therefore, the selection of suitable transducers is important when conducting ultrasonic testing. The frequency spectra of the ultrasonic system can be simply understood using face-to-face tests. The frequency spectra of the ultrasonic shear wave transducers for f_{in} 24 kHz and f_{in} 200 kHz square wave used in this study are presented in Figure 3-21. As expected, the results show that both input frequencies produced similar output frequency (f_{out}) distributions. The frequency spectra for the shear wave test for f_{in} 200 kHz shows the presence of three prominent peaks at f_{out} 131 kHz, 175 kHz and 321 kHz. Notably, the f_{in} 24 kHz input shows increased magnitude at lower frequencies. However, when compared with the wave trace these frequencies arrive later, which is a likely result of the presence of two arrivals; one caused by the negative step of the square wave and another of opposite polarity resulting from the approximately 20 μs later positive step. The frequency distribution can be attributed to the characteristics of the transducer. For instance the Olympus shear wave transducers selected have increased damping (backing material with similar impedance to the element, commonly a tungsten polymer composite). As a result, the transducer has higher sensitivity and broader frequency range (Figure 3-21).

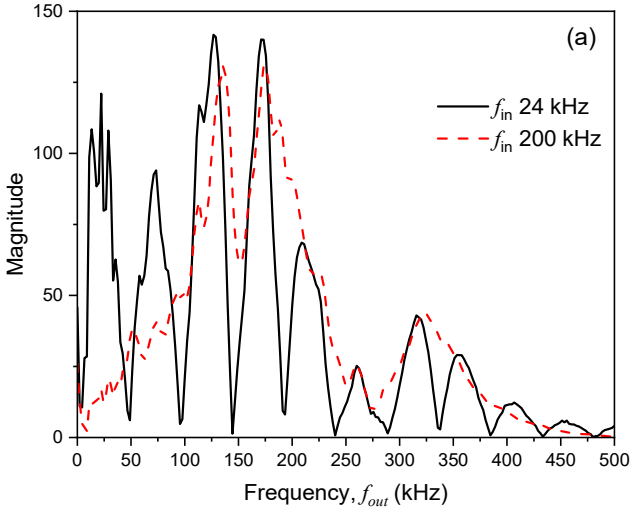


Figure 3-21 Frequency spectra of ultrasonic system during face-to-face tests with acoustic couplant for shear wave transducers at both f_{in} 24 kHz and f_{in} 200 kHz.

A comparable test was also conducted using the ultrasonic shear wave transducers on compacted clayey silt (static stress 1400 kPa) for frequencies ranging from f_{in} 24-200 kHz, shown in Figure 3-22. The waveforms show that the testing frequencies (f_{in}) results in L_{pp}/λ between 6.5 and 53.9. However, the strongest response is received between f_{in} 24 kHz and f_{in} 37 kHz. This suggests that the natural frequency of the ultrasonic-soil system is lower than the resonant frequency of the transducers (Lee and Santamarina, 2005). Similar reduction in the frequency of the received wave (f_{out}) is reported by both Leong et al. (2009) and Brignoli et al. (1996) and attributed to damping properties of the soil and the interaction of transducers and the soil specimens. Furthermore, it's important to note that the broad range of frequency content generated by the shear wave transducers may not allow for full mitigation of the near field effect. However, the f_{out} frequency spectra of the ultrasonic-soil system for the first cycle of the received waveform, considered to be the shear wave arrival, shows a relatively narrow frequency range between 8 kHz and 33 kHz with prominent a peak at 17 kHz at all testing frequencies. The L_{pp}/λ ratio using this output frequency equals 5.9. Thus, due to the comparably large L_{pp}/λ ratio generated by the natural resonant frequency ultrasonic system the impact of the near field effect is not likely present at the initial shear wave arrival. For completeness, the bender element system f_{out} spectra was also checked, however the frequency content approximately equals the f_{in} therefore calculation of L_{tt}/λ using the input frequency is suitable.

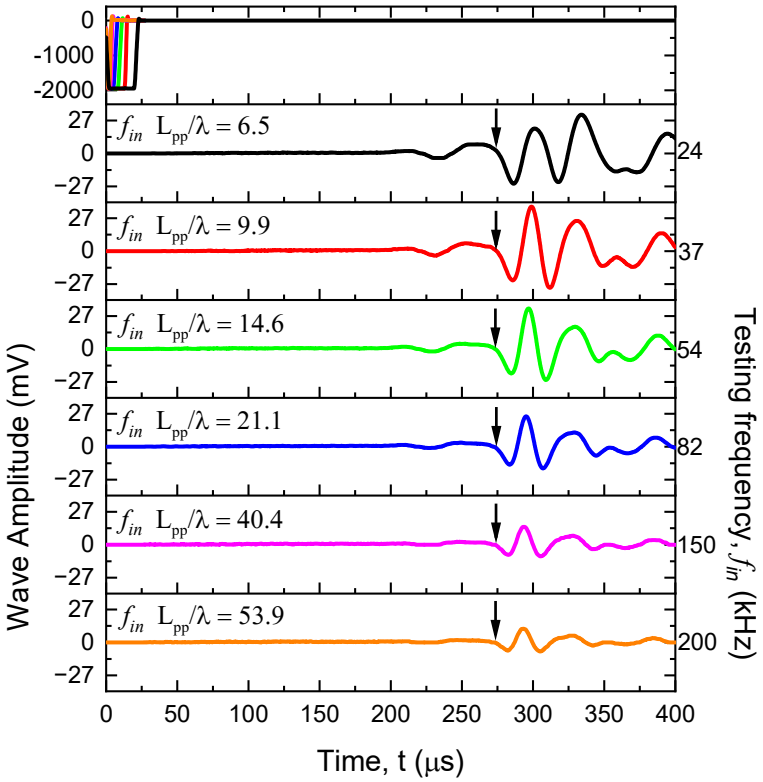


Figure 3-22 Variation of shear wave arrival in time domain traces (compacted clayey silt) for ultrasonic testing method (first deflection for frequencies ranging from 24-200 kHz).

For the reliable measurement of compression waves using ultrasonic techniques the ASTM D2845 (2008) for ultrasonic testing in rock suggests that the sample diameter (D) should be at least five times the wavelength ($D/\lambda_p > 5$). This restriction is necessary due to the dispersion of the compressional wave caused by the interaction with the boundary of the specimen and its conversion to a slower one-dimensional wave velocity as a function of Poisson's ratio. However, Leong et al. (2004) showed that this does not apply to shear waves.

3.7.3.3 Signal to noise ratio and wave amplitude

Testing with transmission pulse methods deals with electrical signals and thus the systems are potentially capable of picking up noisy electrical sources and other sorts of residual vibration other than the vibration intended by the excitation of the pulse transmitters. This means that different sources of noise can be present during laboratory testing, such as background emissions from electro-magnetic noise in the electrical systems and residual vibrations from nearby roads, railways or any other sounds. These sources of noise are random in nature and its influence can be minimised or even eliminated by sampling a larger number of signals and consistently averaging the results. In the bender element system this process is known as stacking. In this study, for the

bender element testing, 20 signals were collected and averaged and a double amplitude of 10V was sufficient to produce a strong signal. A similar method was employed for the ultrasonic testing system whereby between 10 and 50 signals were collected and averaged for each specimen, depending on the quality of the received waveforms.

3.7.3.4 Bender element and ultrasonic system comparison

The wave velocities in pulse transmission methods can be determined as a function of the wave travel path (L_{tt} *and* L_{pp}) and the wave arrival time (t), as follows:

$$V_s = \frac{L_{tt/pp}}{t} \tag{3.9}$$

where V_s represent the shear wave velocity. It should be noted that the L_{tt} value for bender element systems represents the tip-to-tip distance between the transducers, whereas in ultrasonic testing L_{pp} represents mthe length of the specimen between the platens. This was determined using vernier callipers to measure the length of the specimens. The small strain shear modulus can then be evaluated using:

$$G_{max} = \frac{\gamma_b}{g} V_s^2 \tag{3.10}$$

where, γ_b is the bulk unit weight (kN/m³), g is acceleration due to gravity (m/s^2) and V_s is the measured shear wave velocity (m/s).

In this study, time domain signals were used for determining the arrival time by visual picking. In this case the quality of the wave is important as identification of wave arrival is dependent on distortion of the received wave. For ultrasonic testing, travel time was taken from between the drop in the square wave and the first deflection of the received wave (Figure 3-23 A-A'). In this case, the shear wave trace is only produced by the initial square wave voltage drop. When using this method, it's important to note that the accuracy of first detection is significantly impacted by distortion due to the near field effect.

Use of a sinusoidal input wave in the bender element system allows for a greater range of possible methods, for example Figure 3-23 shows first deflection (A-A'), first bump (A-D), first rise and characteristic peaks (B-B') (C-C'). For first bump, first rise, and characteristic peaks, dispersion of the received wave can reduce the confidence in the selected arrival time (Chan, 2010; Yamashita et al., 2009). However, for suitable comparison between both the bender elements and ultrasonic systems the first deflection was also selected. In this case, the travel time was taken from the initial rise of the input wave and initial drop of the first bump of the received wave.

Figure 3-23 shows an example of received shear and compressional wave for the

compacted clayey silt tested at a frequency of 24 kHz for the ultrasonic system and 10 kHz for the bender element system. For the ultrasonic waveform the presence of a higher velocity compressional wave is clearly visible. However, this compression wave component arrives at a significantly reduced amplitude when compared to the shear wave. The significant sharp defined drop in shear wave amplitude confirms the suitability of first deflection method for the ultrasonic system.

The bender element trace contains more ambiguity for the selection of the first deflection resulting from greater noise and the less defined nature of the wave. However, the arrival of first deflection is relatively clear and no distortion of the wave is visible due to the near field effect at 10 kHz. It should be noted that the shear wave arrival time using first deflection are different for the bender elements and ultrasonic systems. This results from the difference in wave paths length of the two systems. The bender elements are embedded in the soil specimen and thus travel over a shorter distance (tip-to-tip) and arrive earlier than in the ultrasonic system (platen-to-platen) despite both specimens having the same size.

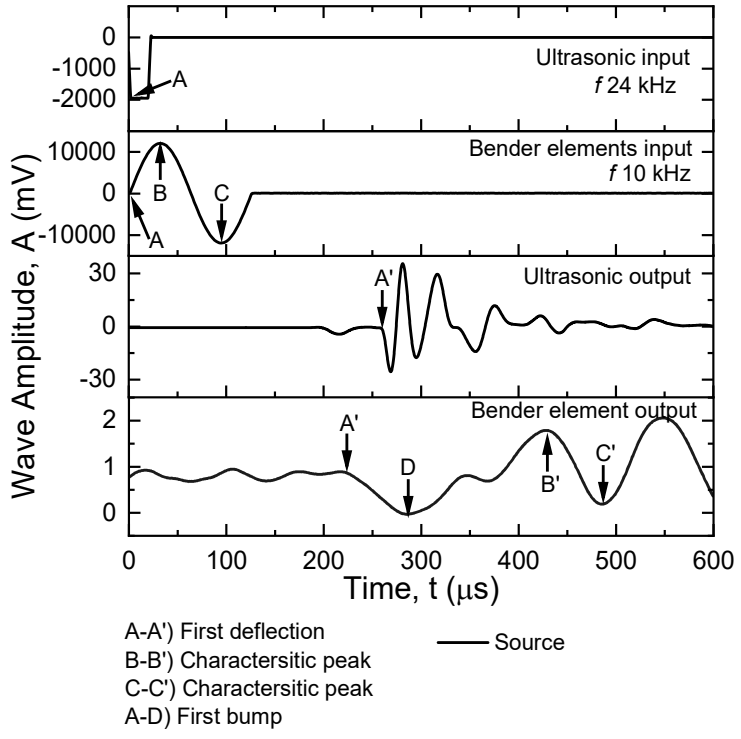


Figure 3-23 Typical received wave forms in the time domain generated using ultrasonic shear wave transducers and bender elements on compacted clayey silt highlighting their characteristics used for visual picking.

In total, two sets of identical compacted clayey silt and clayey sandy silt specimens were tested by both the ultrasonic and bender element systems. The tests were conducted at approximately equal target water contents during drying and wetting while shear wave was monitored for the ultrasonic system and the bender elements. For suitable comparison of measured velocities between both systems the first deflection method

was used to determine the wave arrival. The received waveforms are shown in Figure 3-24 and Figure 3-25. Note, for completeness an example of captured waveforms for the silty clay using the ultrasonic system for identical amplitude of drying-wetting are also presented in Appendix B, Figure B-4.

For ultrasonic testing the L_{pp}/λ values were measured using the f_{out} received frequency spectra to account decrease in resonant frequency of the system. However, for both the ultrasonic and bender element systems the ratio of wave path to wavelength decreases during drying and increases during wetting. This is particularly important to consider for the bender element system due to its lower operating frequencies. As a result, higher frequencies were used at drier states (>10 kHz) to avoid the near field effect.

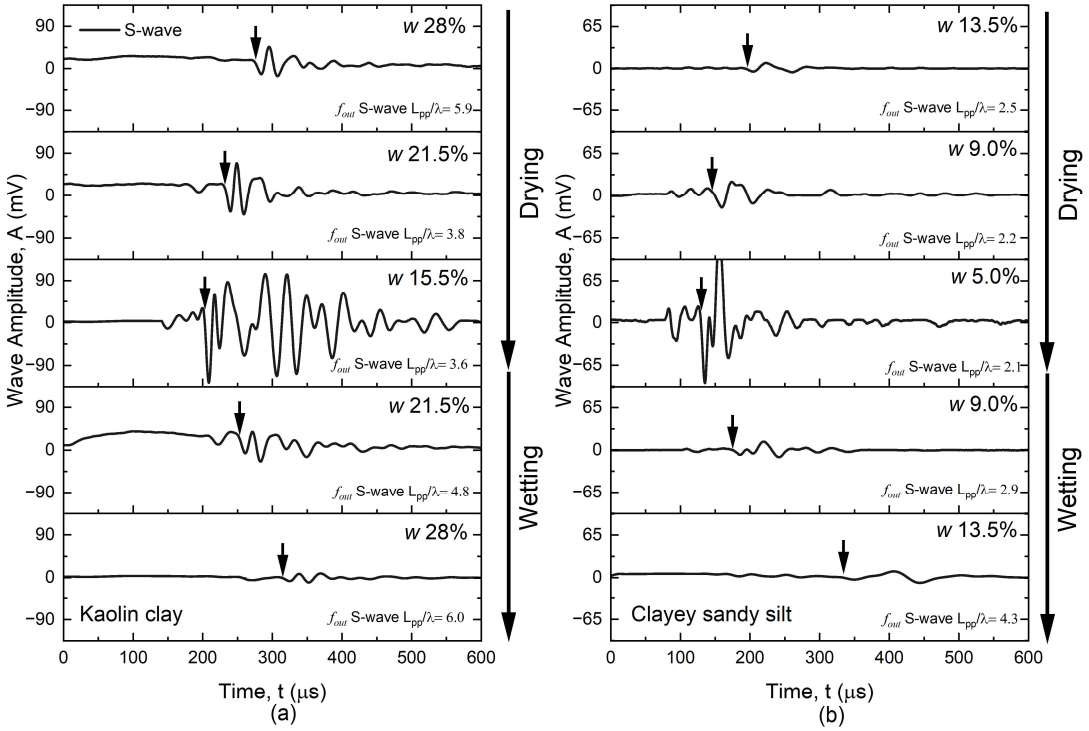


Figure 3-24 Ultrasonic time domain shear wave drying and wetting wave forms for a) clayey silt and b) clayey sandy silt (arrows indicate wave arrival).

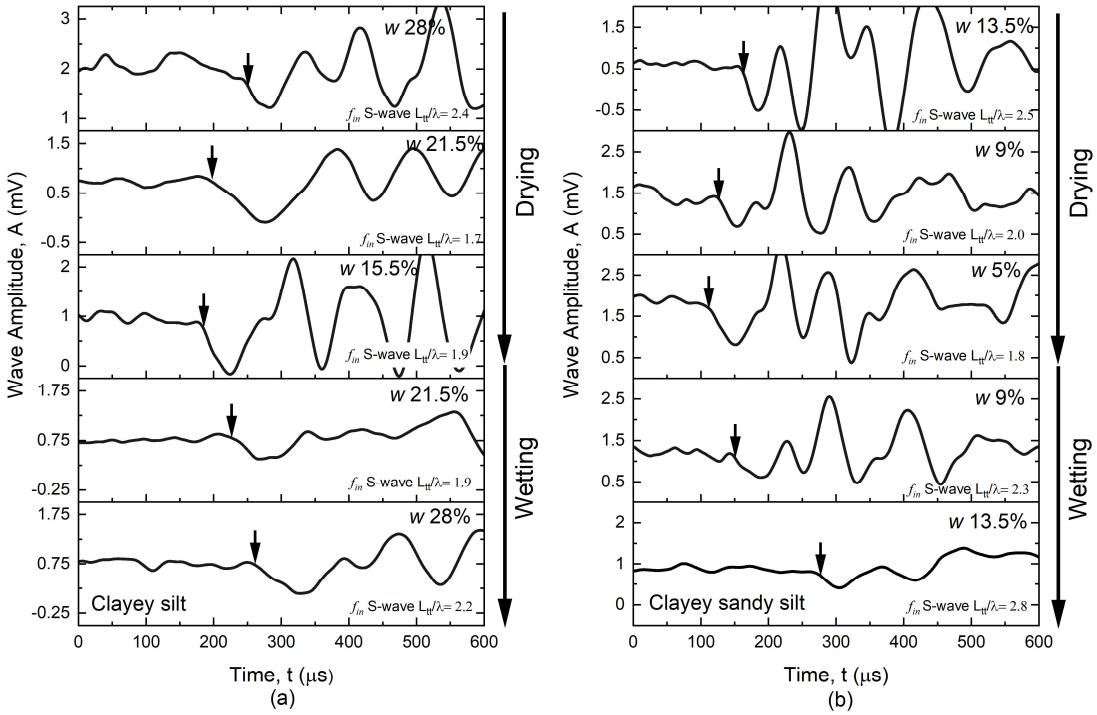


Figure 3-25 Bender elements time domain shear wave drying and wetting wave forms for a) clayey silt and b) clayey sandy silt (arrows indicate wave arrival).

The variation in small strain response of compacted soil specimens obtained for a drying-wetting cycle is shown in Figure 3-26 for both bender elements and ultrasonic systems. It can be observed that for both systems similar shear wave velocities were obtained. In addition, the wave velocities during a drying-wetting cycle exhibit lower values when following the wetting paths which is further discussed in section 3.7.3.6.

The compacted clayey sandy silt (Figure 3-26c) also presents a larger range in shear wave velocities and increased hysteresis during drying-wetting when compared to clayey silt. This is expected when comparing the measured suction variation which exhibit similar behaviour (Figure 3-14).

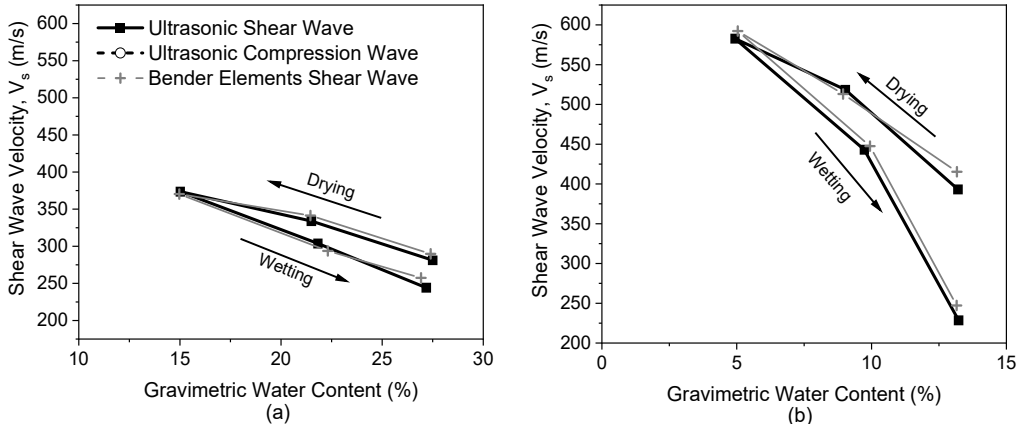


Figure 3-26 Ultrasonic and bender element wave velocity data during drying and wetting for: a) clayey silt shear wave and b) clayey sandy silt shear wave.

Figure 3-27 presents a comparison between measured shear wave velocities using the bender element and ultrasonic systems. The results show good agreement between both systems for both soils over the range of water contents tested. The small amount of variation observed can be accounted for by interpretation of waveform arrivals in the time domain. However, the results show that ultrasonic system is suitable for measuring shear wave velocities during drying-wetting of soils which consist of a range of particle sizes (mixtures of clay, silts and sands) and unsaturated conditions (saturations between 0.87 and 0.32).

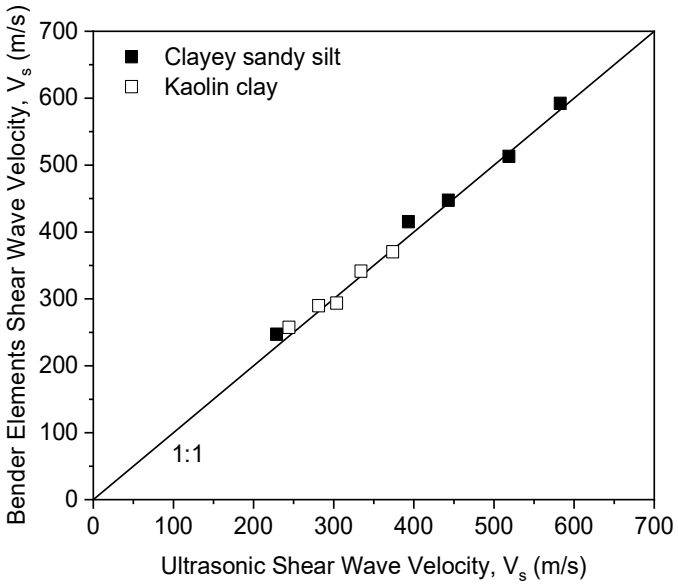


Figure 3-27 Shear wave velocity comparison between ultrasonic and bender element pulse transmission techniques for clayey silt and clayey sandy silt.

3.7.3.5 Ultrasonic testing repeatability

The shear wave response of the ultrasonic system and specimens was also checked for repeatability to ensure suitability of the compaction procedure. Four identical clayey silt specimens were statically compacted (1400 kPa) at the OMC (w 28%) and then the small strain stiffness measured in unconfined conditions. Shear wave traces presented in Figure 3-28 shows a small amount of variation in wave traces which is attributed to the random variation in soil fabric. However, the arrival times of the specimens is very comparable showing similar wave traces and a small 8μs range.

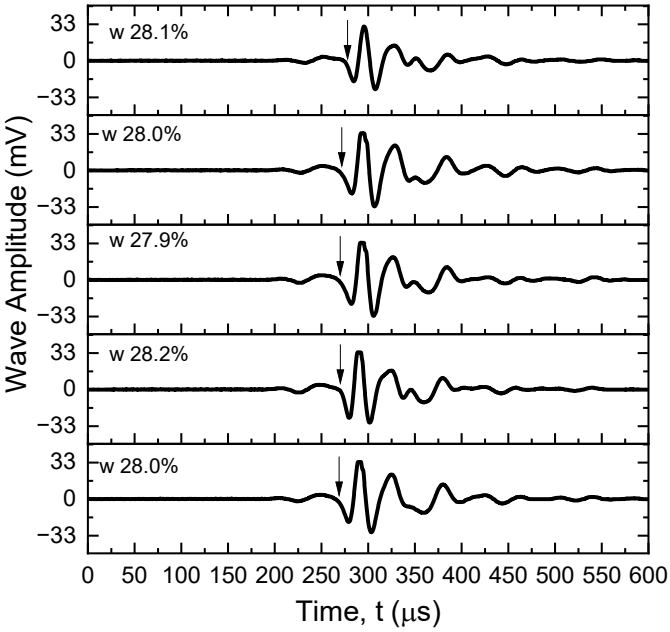


Figure 3-28 Ultrasonic shear wave traces measured on identical clayey silt specimens compacted at OMC.

3.7.3.6 Drying-wetting hysteresis

During drying and wetting to selected water content levels, shear wave data was collected at discrete points. Figure 3-29 shows an example of the typical shear wave evolution for clayey silt during the first drying-wetting cycle between the compacted water content and the transition zone (CT). It can be observed during initial drying from a water content of w_{OMC}= 28% to the driest point w_T= 15%, the shear wave arrival time decreases by 72 μs. However, upon wetting back to the compacted water content (w_{OMC}= 28%) the shear wave arrival time was delayed by 113 μs. This represents a 41 μs decrease in arrival time at the compacted water content on the wetting path as a result of hysteresis of capillary water (Dong and Lu, 2016). Notably this is contrary to suction controlled testing where arrival times on the drying path are slower when compared to wetting paths.

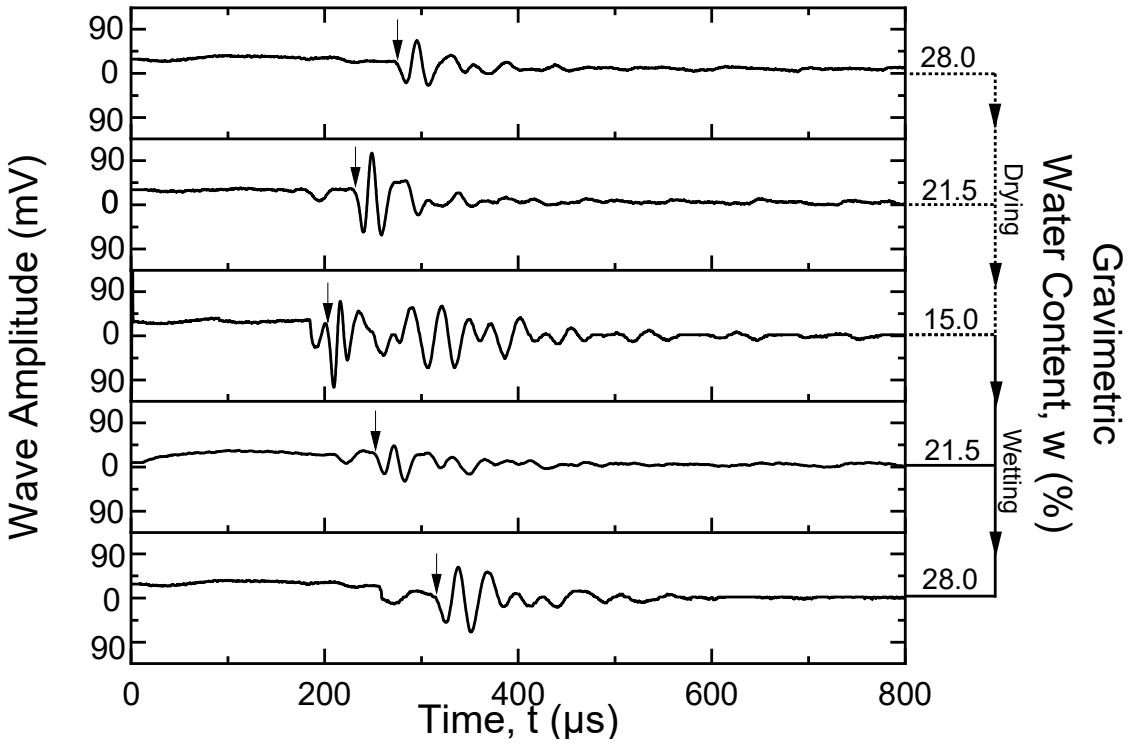


Figure 3-29 Typical ultrasonic shear wave trace evolution in time domain during drying and wetting cycle, arrows indicate interpretation of shear wave arrival time.

Figure 3-30 presents the shear wave velocity data for the first drying-wetting cycle (CT). Figure 3-30a confirms that when the data is plotted using gravimetric water content, the drying path exhibits greater shear wave velocity at the water content levels considered. However, when the data is again plotted using suction values (Figure 3-30b) the trend is inverted (i.e. higher shear wave velocity on the wetting path) as reported in previous studies (Khosravi and McCartney, 2012; Ngoc et al., 2019; Ng et al., 2009; Heitor et al., 2015).

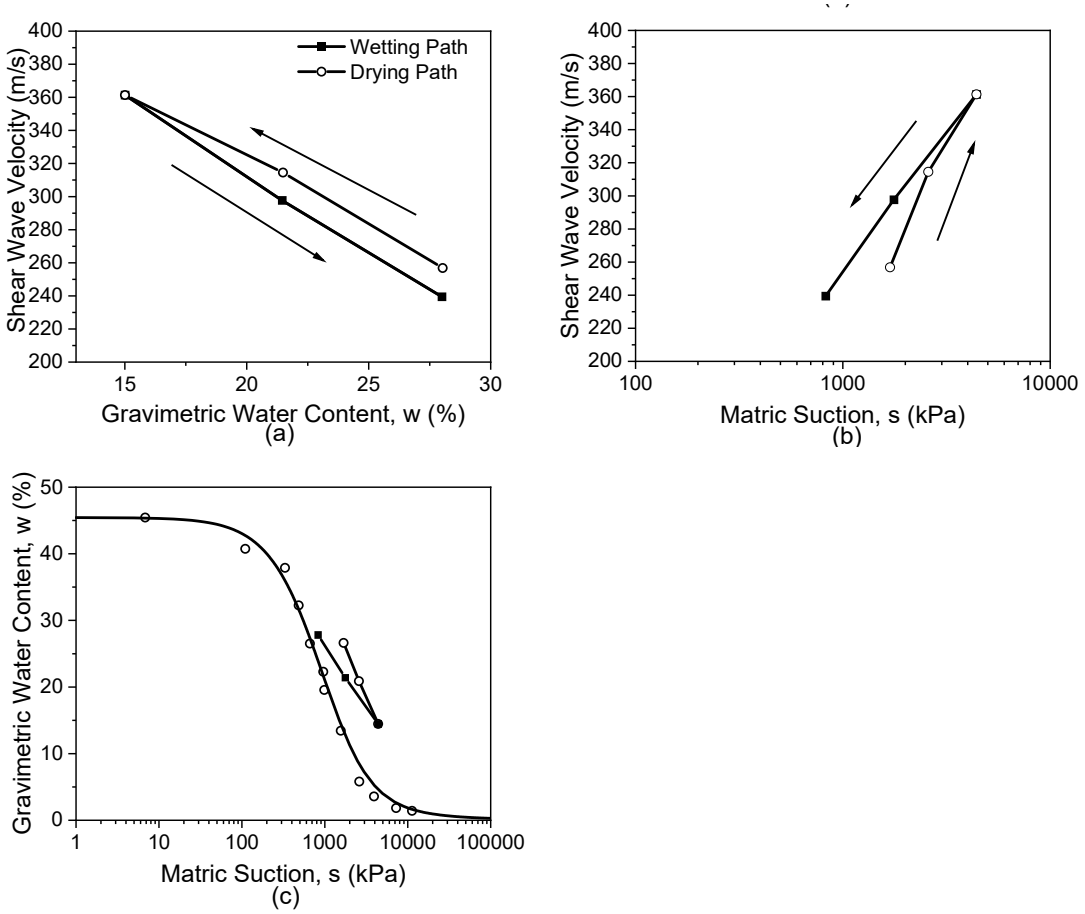


Figure 3-30 Shear wave velocity data for single drying-wetting path (CT) measured at constant water content, presented using variables a) gravimetric water content, b) matric suction and c) suction data and main drying SWRC

As expected, Figure 3-30c also shows that drying-wetting cycles controlled by gravimetric water content levels induce differences in suction values upon rewetting. This is associated with the soil pore structure, i.e. water re-enters the macropores first and is affected by contact angle and entrapped air (Hillel, 2003). The decreased suction on the wetting path in combination with the reduction of shear wave velocity, inverts the hysteresis cycle in the small strain stiffness-suction space. This is further exemplified when the data is plotted in the gravimetric water content-suction space (Figure 3-30c). In this case the hysteresis loop again shows the equivalent behaviour to Figure 3-30a. The discrepancy in hysteresis loop configuration between water content and suction approaches is thus a consequence of the representation of data in the suction-small strain stiffness space, as the control of suction is generally requisite of the axis translation technique. The axis translation approach generally requires saturation to be reduced (coupled with water content) on the wetting path to reach a selected suction level. However, when this is presented in a water content-small strain stiffness space, the behaviour is consistent with Figure 3-30a. The distinction between the configurations of hysteresis loops is important when considering behaviour of material in practice. In this

case, matric suction changes are commonly a consequence of changes in water content resulting from soil-atmosphere interactions including evaporation, evapotranspiration and infiltration. Furthermore, the consideration of water content has additional advantages in light of recent advancement in satellite imagery using L-band Synthetic Aperture Radar (Ahlmer et al., 2018) that enable the determination of water content non-destructively.

3.7.4 Determination of saturated stress-strain behaviour

The testing procedure described in this section relates to evaluation of the saturated stress-strain behaviour of specimens following the application of hydraulic history using a VJ Tech effective stress triaxial system. The system consists of 170 mm diameter triaxial cell, 38 mm diameter base pedestal and top cap, S-beam external load cell (20 kN capacity and <0.03% measurement accuracy), linear variable differential transformer displacement transducer (LVDT) (accuracy <0.1% of full 25 mm scale), pressure transducer (range 0-20 bar and accuracy of 0.25% of full scale), dual automatic pressure controller (maximum pressure of 3500 kPa with a pressure accuracy 0.1% and volume capacity of 250 cm^3 with an accuracy of 0.25%) mounted on a TriSCAN 50 kN load frame. During saturation, consolidation and shearing stages, data acquisition was controlled by Clisp Studio Triaxial Software (VJT-csTRIAX). The configuration of the triaxial system and specimens is shown in Figure 3-31. In this setup the pore pressure transducer measures from the base of the specimen while the back pressure is applied through the top cap.

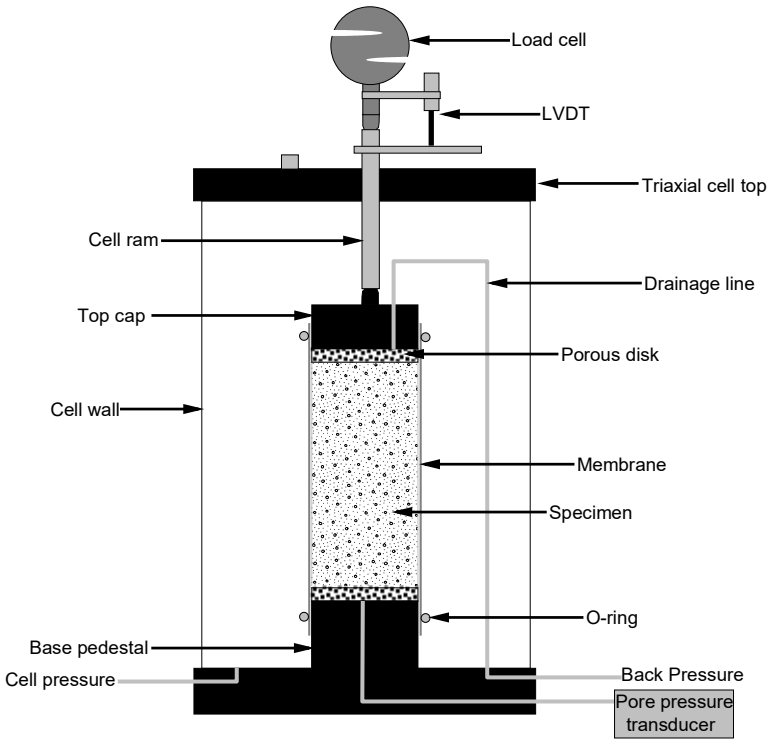


Figure 3-31 Illustration of VJ Tech triaxial setup.

Preparation and checks were conducted according to BS 1377-8-1990. Specimens were mounted on the base pedestal with saturated porous disks, membrane, O-rings, and top cap, always ensuring trapped air was removed. Following this, the saturation of the specimen was conducted in steps of 50 kPa with a differential pressure of 10 kPa. After an increase in cell pressure, a B check (Eq. 3.11) was conducted when equilibrium of the pore pressure was reached:

$$B = \frac{\delta u}{\delta \sigma_3} \qquad 3.11$$

If a minimum B value of 0.95 was not achieved, then the back pressure and cell pressure were ramped further to assist with the dissolution of any trapped air. Consolidation was conducted by applying a 50 kPa confining pressure (equivalent to approximately 2 m depth). This was consolidation pressure was considered as a conservative representative depth where water content changes are likely to occur in older embankment fills. In general, the depth of seasonal hydraulic stress changes depends on the initial compaction and age of the fill. For well compacted embankment fills this depth has been shown to range from 0.3 to 0.6 m whereas for poorly compacted ageing fill between 2.0 to 3.0 m depth (Briggs et al., 2023). Consolidation was conducted until a minimum of 95% of the excess pore pressure had been dissipated. Shearing was performed in drained conditions allowing the measurement of volume change of the specimens. The rate of axial displacement for the shearing stage was calculated using

the square root method and checked during shearing to ensure fully drained conditions. Shearing was conducted until 25% axial strain of the specimen. A membrane correction was applied to account for the restraining effect of the membrane using the membrane correction curve for 38 mm diameter specimens and 0.2 mm thick membranes reported by Head and Epps (2014). Each membrane was measured using vernier callipers and thickness greater than 0.2 mm were accounted for by multiplying the correction by:

$$\frac{38}{D_o} \times \frac{t}{0.2} \qquad 3.12$$

where the initial specimen diameter (D_o) and membrane thickness (t) are required. The presence of a slip plane was corrected by considering curves for 50 kPa pressure reported by La Rochelle (1967) and Head and Epps (2014). This correction is appropriate for a shear plane inclined at 35° to the axis of a standard 38 mm by 76 mm specimen. For membranes greater than 0.2 mm thick the correction was multiplied by:

$$\sqrt{\frac{38}{D_o} \times \frac{t}{0.2} \times \frac{L}{2D}} \qquad 3.13$$

which also requires the inclusion of the length of the specimen (L). A barrelling correction to account for the change in area was also applied considering the change in volume during drained shearing, as follows:

$$(\sigma_1 - \sigma_3) = \frac{P\ (100 - \varepsilon\%)}{A_c(1 - \frac{\Delta V}{V_c})} \qquad 3.14$$

where the deviator stress (σ_1-σ_3) is calculated using the axial force (P), the initial area of the consolidated specimen (A_c) axial strain ($\varepsilon\%$), and the volumetric strain from the initial area of the consolidated specimen (V_c).

Due to the difference in the composition of the three soil mixtures testing conditions during triaxial shearing differed. For suitable drained conditions the change in pore water pressure during shearing must be less than 5% of the effective confining conditions. The change in pore water pressure and associated strain rate is summarised in Figure 3-32 for specimens statically compacted at 1400 kPa and prepared at the OMC. The silty clay required the slowest shearing rate due to its high plasticity and low permeability. As a consequence, these specimens were fitted with filter drains to more rapidly allow volume changes to occur and pore pressures to dissipate. However, care was taken during the saturation stage to ensure the pore water pressure within the specimen had equalised due to the 'short circuit' effect of the side drains. A side drain correction was also applied to account for the additional constraint applied by the filter paper. For 38 mm diameter specimens an additional 10 kPa was added to the membrane correction when strains were greater than 2%. To maintain consistency between specimens of the same

composition the initial strain rate was maintained in subsequent tests and pore pressures monitored to ensure drained conditions (Quinn and Brown, 2011).

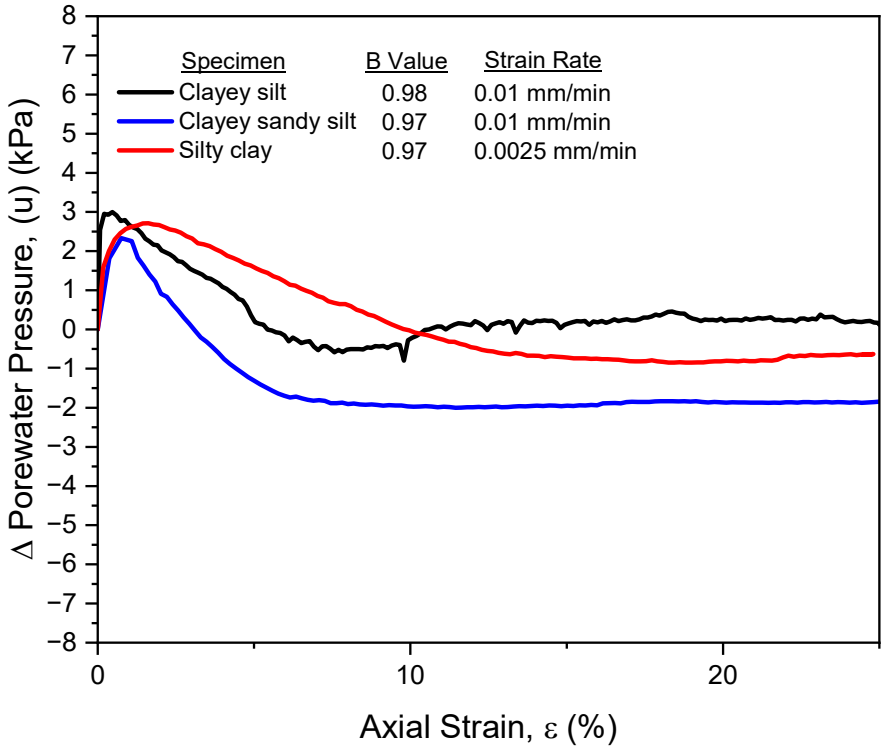


Figure 3-32 Change in pore water pressure during drained shearing for specimens statically compacted at OMC.

3.7.5 Micro X-ray CT scan

X-ray computed tomography (CT) was used to visualise cross sections of the compacted specimens to understand the change in microstructure following drying-wetting. Micro X-ray CT data was acquired at the Diamond Light Source 3 GeV synchrotron situated at the Harwell Science and Innovation Campus in Oxfordshire. A synchrotron source produces radiation by the movement of charged particles through magnetic fields which is orders of magnitude greater in flux than laboratory sources. The testing was performed using the I12 Joint Engineering, Environmental and Processing (JEEP) beamline which uses the high photon energies and intensity of the beam (53 keV and 150 keV) to penetrate through large dense samples of engineering materials. The increase in image quality allowed for larger specimen sizes and reduction in potential disturbance due to sampling. Specimens were subsampled from compacted specimens identical to those used for small strain stiffness and triaxial testing. Subsampling was conducted by penetrating specimens with an acrylic tube with an internal diameter of 10 mm. The tube was sharpened to reduce disturbance to the exterior of the sample during insertion. Specimens where then sealed with epoxy resin to maintain their water content. Care was

taken to remove air bubbles using a syringe to mitigate potential loss of moisture. Specimens were kept in a insulated cooler to minimise thermal variation prior to testing. Their tomography was captured in experimental hutch 1 where specimens were placed on sample table 1 within the beamline. They were positioned in the centre of a goniometer and held in place with double sided tape to ensure no movement during rotation of the stage (Figure 3-33).

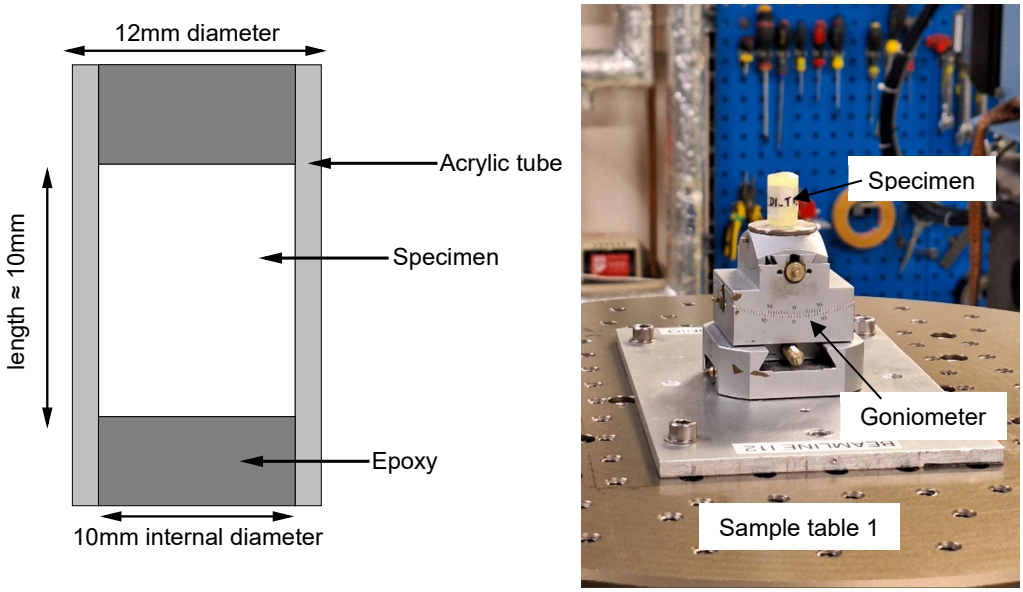


Figure 3-33 Schematic illustration of specimen configuration during testing (left) and specimen arrangement on sample table 1 (right).

Figure 3-34 shows the imaging detector and monochromatic beam used to capture projections. It consist of four modules with differing field of view and pixel size. To capture images a scintillator converts the incident X-ray beam into visible light, mirrors then reflect the visible light out of the X-ray beam path to visible light optics to magnify the scintillator image onto the camera's sensor. Optical module 3 was used to capture a field of view of 8.0 mm by 7.0 mm comprising of pixels of 3.24 µm. The ratio of field of view/mean particle diameter using this module was therefore 2,667 for the clayey silt, 133 for the clayey sandy silt and >4,000 for the silty clay. Use of this module therefore allowed for the imaging of a sufficient representative element volume (REV) while allowing for identification of macro pores and development of cracking.

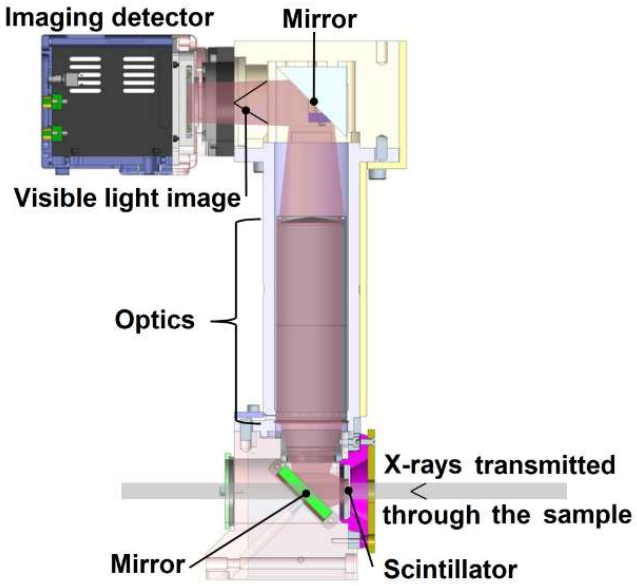


Figure 3-34 Configuration of the imaging detector at I12 beamline (Drakopoulos et al., 2015).

Table 3-5 presents a summary of conditions reported in the literature for micro X-ray CT testing in compacted soils using laboratory derived X-ray sources. It shows that achieving sufficient contrast to distinguish microstructure of compacted soils at high magnifications can be difficult due to attenuation of the X-rays as they pass through large soil samples. As a consequence many researchers reduce the specimen diameter which makes it less representative of the overall soil mass and may increase disturbance i.e. Takahashi and Tachi, 2018 used 0.5 mm specimen diameter. For this investigation the tomography was captured using the synchrotron monochromatic beam with a selected energy of 112 KeV and exposure for a time of 0.0130 seconds. The monochromatic beam improves signal-to-noise ratio and reduces artifacts compared to laboratory sources. Furthermore, the monochromatic beam also creates a slight phase shift enhancement between the interface of surfaces, increasing their contrast, which can allow for easier identification of cracking (Bhreasail et al., 2012). In total 3000 projection were captured (180° in 0.01° steps) in approximately 10 minutes. During their capture the tomography was visualised in DAWN, a scientific visualisation and processing suite, to check the quality of projections.

Table 3-5 Summary of literature using Micro X-ray CT testing in compacted soils.

Authors	Material	X-ray CT	Sample Size	Temperature	Voltage	Current	Steps	Resolution
Takahashi and Tachi (2019)	Compacted montmorillonite	SkyScan-2011 nanofocus X-ray CT system	Subsampled with an internal diameter 0.5 mm	20–25 °C and ~40% relative humidity	30 keV	200 μA	360° in steps of 0.6° (130mins for total test)	0.36 μm
Pires et al. (2020)	Clay (53%), sand (30%)and silt (17%)	G.E. V-Tomex-M X-ray	50mm diameter 50mm height	Not given	180 keV	160 μA	2520 projections	35.00 μm
Al Mahbub and Haque (2016)	Compacted sand	Zeiss Xradia XRM520 Versa	8mm diameter 4mm height	Not given	140 keV	Not given	810 projection	14.00 μm
Li and Shao (2020)	Loess clay	ZEISS Xradia 520 Versa	39.1 mm diameter 80 mm in height	Not given	Not given	Not given	1015 projections	40.00 μm 10.00 μm
Mirzababaei et al. (2020)	Compacted clay	Zeiss Xradia XRM520 Versa	10mm diameter 20 mm height	Not given	140 keV	Not given	801 projections	12.00 μm
Smith (2015)	Compacted clay	XRadia/Zeiss XRM 410 XRCT	12mm diameter	Not given	Not given	Not given	Not given	2.70 μm 4.60 μm

3.8 Summary

The material characterisation and laboratory testing programme were summarised in this chapter. The composition, index properties and compaction characteristics (both Proctor and static compaction) for three representative UK soils were presented. A novel methodology to apply hydraulic history to compacted specimens was outlined. The filter paper method was adopted to measure the SWRC and determine changes in suction at selected target water content levels. Using this, four drying wetting boundaries were defined to evaluate the effect of amplitudes of drying-wetting on soil behaviour.

An exercise was also conducted to benchmark pulse transmission tests to validate the Pundit Lab ultrasonic system against bender elements. For both soils tested, the ratio of L_{tt}/λ and L_{pp}/λ decreased during drying and increased during wetting. The bender elements were able to account for the near field effect by the increasing testing frequency (>10 kHz) at the driest point. The ultrasonic system showed a reduction in natural resonant frequency compared to transducer resonance, resulting from the variation of the damping properties of the soil and the interaction of transducers and specimen. However, the output signal frequency showed that L_{pp}/λ was maintained above 2 during drying and wetting for both soils.

During drying and wetting lower velocities were recorded on the wetting path compared to drying path for select water content levels, the inverse of the small strain stiffness trend measured at constant suction. However, this is intuitive when considering changes in suction when controlled at target water content levels compared with the changes in saturation when controlled at target suction levels. The results showed that for both soils the shear wave velocities measured using both the bender elements and ultrasonic systems show good agreement during a drying and wetting cycle.

Details of the triaxial system used to determine the stress strain behaviour of compacted specimens was also given. This includes the method used to saturate the specimen and justification for the chosen 50 kPa confining stress. The corrections adopted to account for the change in specimen area during shearing and confining effect of the membrane and filter paper drains were also established.

Finally, a description was given of the Diamond Light Source synchrotron I12 Joint Engineering, Environmental and Processing (JEEP) beamline used to capture micro X-ray computed tomography. The methodology developed to subsample specimens and beamline characteristics used to capture tomography were also presented.

Chapter 4
Small Strain Behaviour

4.1 General

In this chapter the small strain stiffness results of three compacted soils representative of low to very high plasticity soils in the UK are presented for selected drying-wetting amplitudes. Ultrasonic small strain stiffness testing is used as a non-destructive method to monitor compacted soil performance during drying-wetting for the 1st (D/W1), 3rd (D/W3), 6th (D/W6) and 10th (D/W10) cycle. This is conducted for drying-wetting amplitudes FT, FR, CT and CR according to the methodology set out in Chapter 3. For consistency all laboratory small strain stiffness data is presented using shear modulus (G_{max}) which is calculated using the shear wave velocity (Vs) and the bulk unit weight (γ_b). The post compacted relationship between shear modulus and the number and amplitude of drying-wetting cycles is evaluated for each soil mixture. Volume changes during drying-wetting cycles, presented using void ratio (e) and volumetric strain (ε_{vs}), are also reported in a similar manner.

Testing was conducted in unconfined conditions, as a consequence total stress was zero (e.g. no confinement in excess of atmospheric pressure) and effective stress is represented by the suction pressure. This was selected to allow for simple comparison between the specimens for the chosen independent variables. However, it should be noted that specimens behaviour during drying-wetting would likely be different for increasing confining stresses. For instance, higher confining stresses would reduce volume changes during drying-wetting which would inhibit the formation of cracking. In practice, unconfined conditions are representative of shallow surface stresses where desiccation cracks form at local stress concentrations due to loss of moisture and shrinkage of a soil mass. Increasing depth both increases confining stresses and generally reduces seasonal fluctuations in moisture, restricting the formation of cracking due to tensile stresses. Indeed Dyer et al. (2009) showed that in compacted fill up to approximately 500 mm depth (the observed depth of cracking) water contents were close to the shrinkage limit whereas, at greater depths water content varied between the shrinkage limit and plastic limit.

A total of 36 statically compacted specimens prepared at the OMC were tested using the ultrasonic Pundit Lab to evaluate changes in shear modulus during drying-wetting. For the clayey silt and clayey sandy silt an individual specimen was prepared for each drying-wetting cycle. This allowed the stress-strain behaviour to be evaluated for each of four selected drying-wetting cycles following small strain stiffness testing. This was conducted for each of the four drying-wetting amplitudes thus requiring a total of 16

specimens for the clayey silt and clayey sandy silt respectively. Additional specimens of clayey silt were prepared to check the repeatability (Section 3.7.3.5). The silty clay experienced significant cracking and loss of integrity between 2 and 6 drying-wetting cycles dependent on the amplitude. Due to this, a total of 7 specimens were tested for all drying-wetting amplitudes.

In this study the clayey silt was used as a 'baseline material' to compare with previous studies and thus is presented first in Section 4.2. This section therefore provides a more in-depth discussion with regards to the behaviour of the clayey silt during drying-wetting. Following this, the data for the low plasticity clayey sandy silt (Section 4.3) and very high plasticity silty clay (Section 4.4) is presented in the same fashion for consistency. In these sections however their respective behaviour is discussed in a brief manner to reduce repetition. Section 4.5 then aims to then provide a comprehensive comparison between the behaviour of the three soils.

4.2 Unsaturated small strain behaviour: clayey silt (high plasticity)

The initial compacted conditions for the clayey silt specimens used in the study are shown in Table 4-1. The consistency between all 16 specimens is high with a 1% variation in the dry unit weight. This can be attributed to small variations in procedure such as small difference in the compaction water content. The hydraulic pathways of the clayey silt specimens is also shown in Figure 4-1. The statically compacted clayey silt specimens were subject to the four selected drying and wetting domains presented in Figure 3-15, while the small strain stiffness and volume was monitored. Measurements were made at the selected water content levels (solid symbols) to allow for the evaluation of the evolution of soil behaviour during the drying-wetting cycles. No measurements were made at full saturation as specimens were very soft. Thus, to minimise specimen disturbance measurements were conducted at the compacted water content (w_{OMC}=28%) which correlated to an increase in stiffness suitable for testing while allowing for comparison with initial compacted conditions. Measurement of small strain stiffness was also conducted at boundary water content (w_T=15% and w_R=1.5%) and intermediate water content (w=21.5%) to provide increased definition of drying-wetting cycle. It's important to note that there were no visible macroscopic cracks observed during drying-wetting which could have impacted the integrity of the specimens.

Table 4-1 Summary of initial compacted conditions for clayey silt specimens.

Test ID	Water Content, w: %	Bulk Unit Weight, γ_b: kN/m^3	Dry Unit Weight γ_b: kN/m^3	Platen to Platen distance, L_{pp}: mm	Void Ratio, e	Water Ratio, e_w	Degree of Saturation, S_r
FT-D/W1	28.0	16.91	13.20	38.2	0.93	0.73	0.79
FT-D/W3	28.3	16.82	13.11	38.3	0.95	0.74	0.78
FT-DW6	28.2	16.83	13.13	38.2	0.94	0.73	0.79
FT-D/W10	28.1	16.91	13.20	38.1	0.93	0.73	0.78
FR-D/W1	28.2	16.88	13.17	38.2	0.94	0.73	0.78
FR-D/W3	28.1	16.80	13.11	38.3	0.94	0.73	0.78
FR-D/W6	28.3	16.87	13.13	38.2	0.94	0.74	0.79
FR-D/W10	28.0	16.87	13.18	38.2	0.93	0.73	0.78
CT-D/W1	28.0	16.94	13.23	38.2	0.93	0.73	0.79
CT-D/W3	27.8	16.92	13.24	38.1	0.93	0.72	0.78
CT-D/W6	27.8	16.92	13.24	38.1	0.93	0.72	0.78
CT-D/W10	28.0	16.92	13.22	38.1	0.93	0.73	0.78
CR-D/W1	28.2	16.88	13.17	38.2	0.94	0.73	0.78
CR-D/W3	28.3	16.94	13.16	38.2	0.94	0.74	0.79
CR-D/W6	28.0	16.94	13.13	38.2	0.94	0.73	0.78
CR-D/W10	27.9	16.87	13.18	38.1	0.94	0.73	0.78

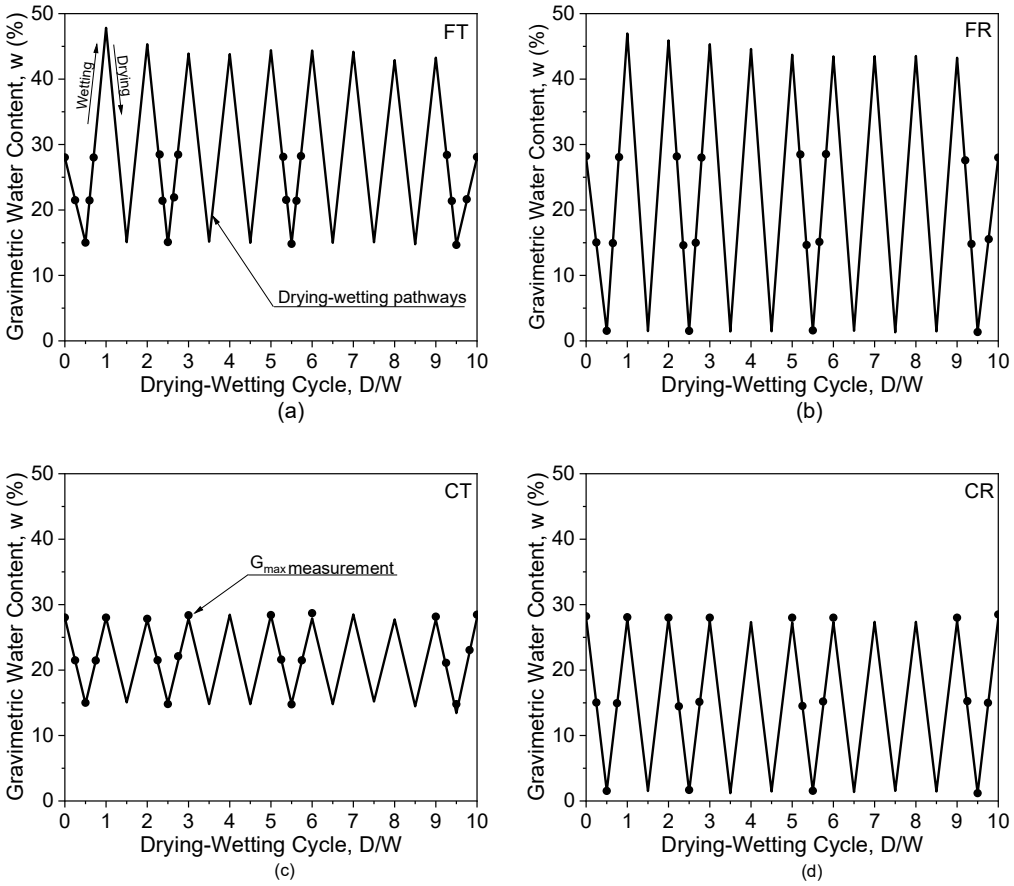


Figure 4-1 Clayey silt drying-wetting pathway and discrete G_{max} measurement points (solid symbol) for a) FT conditions, b) FR conditions, c) CT conditions and d) CR conditions.

4.2.1 Shear modulus variation with water content

The evolution of small strain shear modulus during for FT/FR/CT/CR hydraulic pathways at selected water content levels are presented in Figure 4-2 for drying-wetting cycles 1, 3, 6 and 10. It shows that small strain shear modulus values measured for the different drying-wetting cycles are inversely correlated to water content, i.e. at low water contents a higher shear modulus is measured, whereas shear modulus decreases as the water content increases. This is not surprising as the matric suction levels in the specimens are quite different, with approximately 2,500 kPa increase in matric suction between w_{OMC}=28% and w_T=15% water contents on the first drying path (Figure 3-30). Equally, the range of water content values during drying influences the small strain shear modulus for an increment of water content. For instance, during drying within the transition zone (FT and CT), an approximately linear increase in small strain shear modulus is reported for an increment of water content (Figure 4-2a,c). However, drying to the residual range (FR and CR) between w_T= 15% and w_R= 1.5% on the first drying-wetting cycle yields a comparative reduction in the rate of small strain shear modulus increase (Figure 4-2b,d).

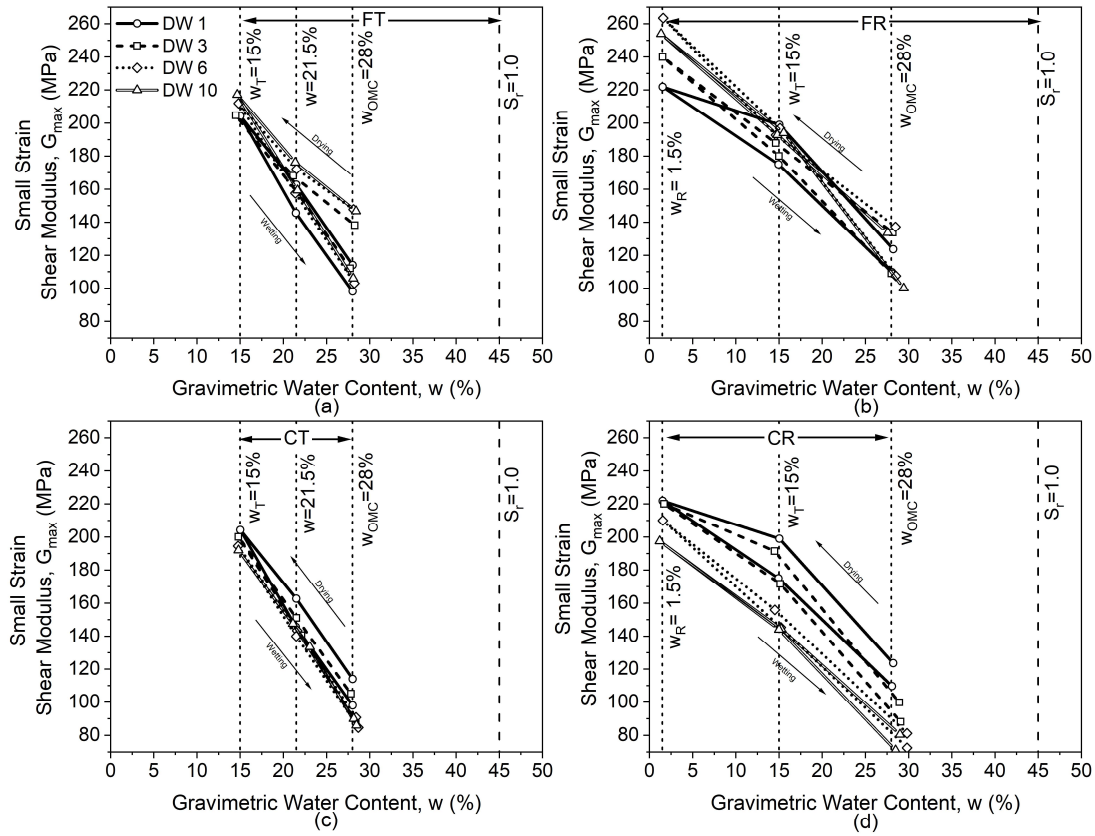


Figure 4-2 Small strain shear modulus of compacted clayey silt specimens subjected to D/W 1, 3, 6, and 10 for a) FT – full saturation to transition zone, b) FR – full saturation to residual conditions, c) CT – compacted OMC to transition zone and d) CR – compacted OMC to residual conditions (note the horizontal arrows indicate the extent of drying-wetting cycles).

Within the transition zone (FT and CT) a pendular state develops and the meniscus effect dominates the increase in normal force between particles (Dong et al., 2017). Figure 4-2a,c shows that in this range the increase in suction is approximately linear when compared to water content. Thus, the increase in stiffness and small strain shear modulus of the clayey silt essentially reflects the SWRC. However, at the lower water content range within residual conditions (FR and CR) the formation of the partial pendular state has been observed to reduce the meniscus radius and Equivalent Effective Stress (EES) σ'_{eq} (Cho and Santamarina, 2001). The EES accounts for the total resultant forces acting between particles of soil beyond capillary forces, including physiochemical forces such as Van der Waal attraction, double layer repulsion and Coulomb electrostatic forces. For instance, Vesga (2008) showed that for kaolin clay a decrease in the EES was present at low water contents (determined from unconfined direct shear tests when considering the coefficient of friction between the particles and cohesion intercept of the soil). This contrasted with the soil water retention curve where matric suction asymptotically increased at low water contents, suggesting that suction was not transmitted effectively to the soil skeleton. Furthermore, upon drying physiochemical

forces such as Van der Waals attractions and electric double layer repulsions also develop and may dominate at these residual conditions (Lu, 2016). However, these forces are proportional to particle size and pore size, influencing clays sized particles to greater extent compared to silts (Ngoc et al., 2019). Although difficult to validate, these observations align with the shear modulus behaviour of the clayey silt at residual conditions. Highlighting the novelty and complexity of interparticle forces in unsaturated soils and their potential impact on small strain shear modulus.

The evolution of small strain shear modulus data for FT/FR/CT/CR pathways against the number of drying-wetting cycles is shown in Figure 4-3. The data shows that within the first 6 drying-wetting cycles a decrease in hysteresis loop amplitude between drying and wetting paths for the CT and CR conditions is present (Figure 11c,d). This is corroborated by measurement of void ratio for these pathways which show smaller volumetric changes. Similar observations have also been reported by Farulla et al. (2010) and Liu et al. (2020) for drying-wetting paths, e.g. reduction in the difference of suction between hysteresis loops after application of hydraulic cycles. This was also exemplified by Stirling et al. (2020) for results of continuous suction and water content on statically compacted glacial till during three drying and wetting cycles. It was shown that repeated drying between saturated conditions and 500 kPa suction resulted in a 50 kPa decrease on the drying path at constant 22% water content.

Curiously, both hydraulic pathways FT and FR generally exhibit increases in small strain shear modulus during the drying path for the first 6 cycles at their compacted water content (w_{OMC}= 28%), but approximately constant shear modulus during wetting (Figure 4-3a,b). These changes are not surprising and can be related to the associated changes in microstructure (Section 4.5.3). Hydraulic path FR also shows a significant increase in the small strain shear modulus within the residual state at w_R= 1.5% water content (Figure 11b). These increases also suggest a change within the micro pore structure as both suction and other inter particle forces within this state are dependent on pore diameters.

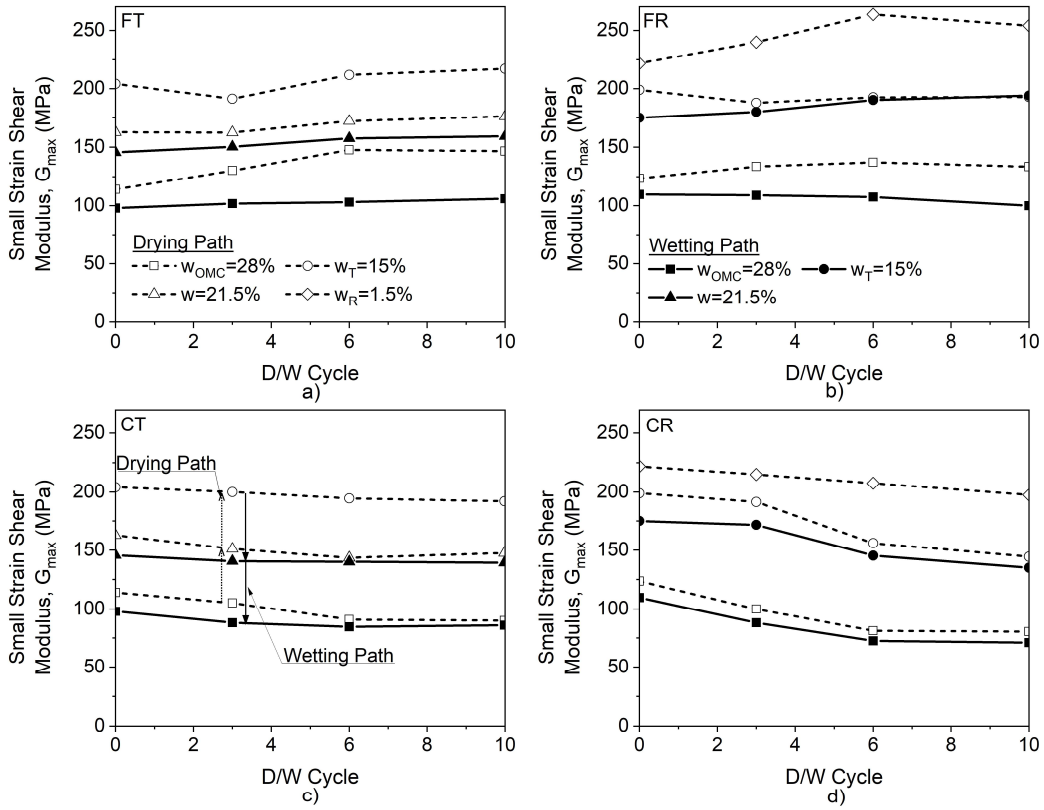


Figure 4-3 Small strain shear modulus of compacted clayey silt specimens subjected to D/W 1, 3, 6, and 10 for a) FT – full saturation to transition zone, b) FR – full saturation to residual conditions, c) CT – compacted OMC to transition zone and d) CR – compacted OMC to residual conditions.

4.2.2 Void ratio variation with drying-wetting

Changes in void ratio directly affect the properties of the soil such as porosity, density and degree of saturation, which are critical to compacted soils performance. In this study volume changes were measured using Vernier callipers for nine discrete points to allow for calculation of volume using average dimensions to ensure accuracy (Head, 1996). Volume change of the specimens is presented using the water ratio, defined as the ratio of the volume of water to the volume of solids, against void ratio. Both variables are normalized against the volume of solids thus indicative of the volume change of the specimen with respect to the volume of water (i.e. equal void and water ratios indicate full saturation). The variation in computed void ratio (e) and water ratio (e_w) for all specimens and their associated hydraulic pathways are shown in Figure 4-4.

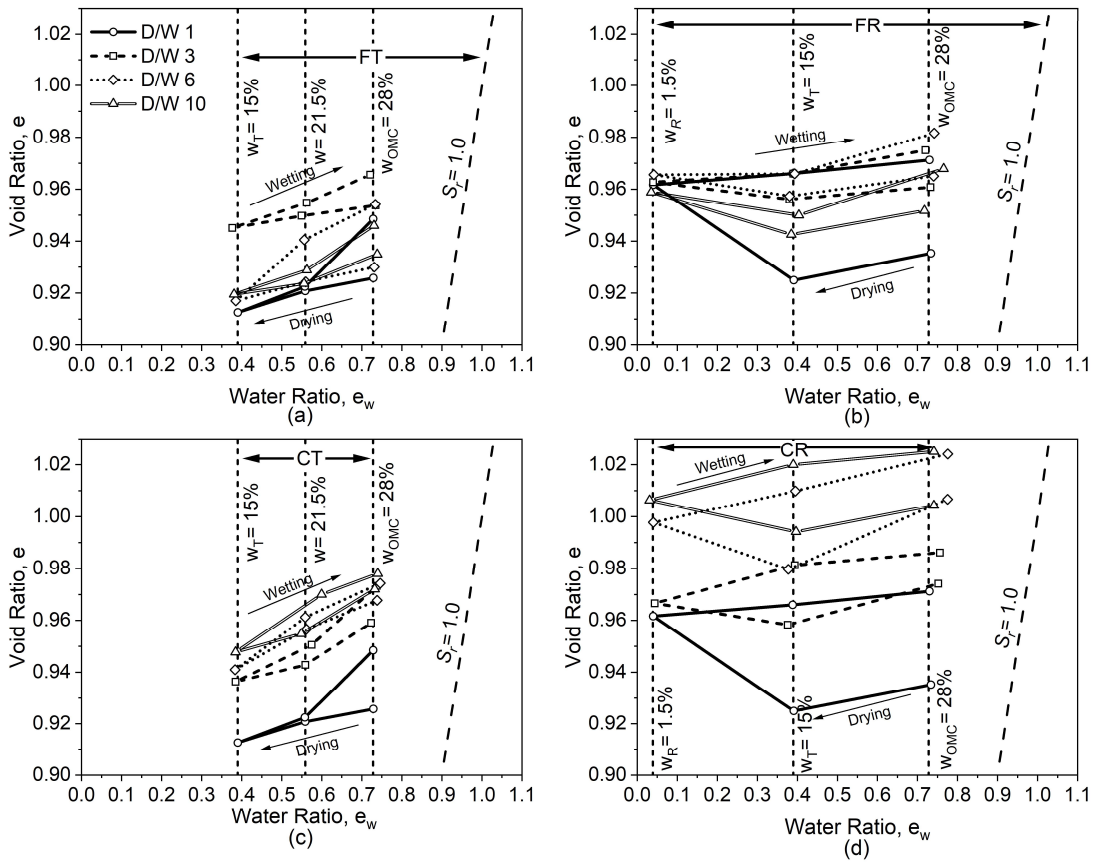


Figure 4-4 Volume change of compacted clayey silt specimens subjected to D/W 1, 3, 6, and 10 for a) FT – full saturation to transition zone, b) FR – full saturation to residual conditions, c) CT – compacted OMC to transition zone, d) CR – compacted OMC to residual conditions (note the horizontal arrows indicate the extent of drying-wetting cycles).

Data reveals that all clayey silt specimens exhibit hysteric behaviour between drying and wetting paths, where at selected water content levels during a wetting pathway, swelling is greater than on the drying path. This coincides with the reduction in matric suction during wetting due to SWRC hysteresis (Figure 3-30). When comparing these changes in void ratio with the corresponding results for small strain shear modulus, common trends are visible. Most noticeably, small strain shear modulus is inversely proportional to void ratio data, where increases in void ratio yields a decrease in shear modulus during drying-wetting.

It's also evident that the amplitude of drying and wetting paths had a significant impact on changes in volume during the 10 drying-wetting cycles. For instance, specimens dried to the residual conditions (CR) showed a larger increase in void ratio from 0.930 to 0.971 at the compacted water content (w_{OMC}= 28%) after the first drying and wetting cycle (Figure 4-5d). However, specimens dried to the transition zone (CT) showed a smaller void ratio increase after the first cycle from 0.926 to 0.953 (w_{OMC}= 28%) (Figure 4-4c).

These increases were also observed for kaolin clay by Suits et al. (2009) to occur

simultaneously for when a decrease in the EES was measured during drying at residual conditions. For this study, the first drying-wetting cycle of the FR pathway between w_T= 15% water content and w_R= 1.5 % water content showed an increases in void ratio of 0.925 to 0.962 (Figure 4-4 b) which corresponds well with this observation.

However interestingly, as wetting and drying continued these changes in structure were maintained, particularly when full saturation was not reached, and continued to allow for an increase in void ratio. This is shown in Figure 4-4d (CR) where void ratio increases from 0.961(D/W1) to 1.01 (D/W10) at w_R= 1.5 % water content after 10 drying-wetting cycles. Furthermore, when compared with the equivalent saturated pathway (FR) in Figure 4-4b it's clear that saturation has an effect on the kaolin producing a decrease in void ratio after 10 drying-wetting cycles at the same water content level despite the initial large void ratio increase.

These changes in volume during drying-wetting indicate changes in the pore structure of the specimens (Thom et al., 2007; Nowamooz et al., 2016) (see Section 4.5.3). For instance, this can observed when comparing specimens both dried to residual conditions (FR) and dried to the transition zone (FT). During the first wetting cycle of FT, the void ratio increases from 0.913 to 0.949 when wetting between w_T=15% and w_{OMC}=28% (Figure 4-4(a)). Whereas, the first wetting cycle of FR, the void ratio only increases from 0.961 to 0.971 between w_R=1.5% and w_{OMC}=28% despite the larger change in water content (Figure 4-4b). This is likely due to difference in packing of the aggregates resulting from the prior volume changes during drying.

4.2.3 The effects of hydraulic pathway on small strain shear modulus

Figure 4-5 shows the normalized change in small strain shear modulus from compacted conditions at selected water content levels for both drying and wetting paths. A clear distinction is observed between the fully saturated boundary (FT/FR) and compacted water content wetting boundary (w_{OMC}=28%) (CT/CR). In general, specimens brought to full saturation during drying-wetting (FT/FR) exhibit increases in small strain shear modulus for increasing drying wetting cycles (Figure 4-5a-g). In contrast, specimens wetted to the compacted water content (CT/CR) during drying-wetting experienced a decrease in small strain shear modulus (Figure 4-5a-g). It should be noted that this trend is reflected on both drying and wetting pathways irrespectively of the water content level represented. Notably, the data also shows that drying to residual conditions produces a decrease (Figure 4-5a,b,e,f and g for FR conditions) or increase (Figure 4-5a,b,e,f and g for CR conditions) in the rate of shear modulus change at all water contents, of which

w_{OMC}=28% (Figure 4-5a) shows the largest variation. For instance, the drying CR pathway at w_{OMC}=28% (Figure 4-5 b) resulted in a 35% reduction in shear modulus compared to compacted conditions after 10 drying-wetting cycles ($G_{max}/G_{max\text{-}initial}$ =0.65), whereas, comparable CT conditions yielded a smaller 21% reduction ($G_{max}/G_{max\text{-}initial}$ =0.79). Conversely, the FT pathway at w_{OMC}=28% (Figure 4-5a) showed a 29% increase in shear modulus after 10 drying-wetting cycles ($G_{max}/G_{max\text{-}initial}$ = 1.29), while the drying FR pathway produced a smaller 8% increase ($G_{max}/G_{max\text{-}initial}$ = 1.08).

These results indicate that the for the clayey silt the wetting boundary has a significant influence on the behaviour of the specimens. In this study, only fully saturated and compaction water content boundaries were considered and a reversal in the shear modulus behaviour was observed. In addition, this reversal behaviour seems to be far more significant at the wetter end (w_{OMC}=28%) (Figure 4-5a,b). The recorded trends further suggest that drying boundaries influence the magnitude of the change observed, e.g. similar variations were observed between the increase in shear modulus for FT and FR and the decrease in shear modulus for CT and CR. This is not surprising and can be attributed to the changes in microstructure specimens exhibit at the drying boundaries (see Section 4.5.3).

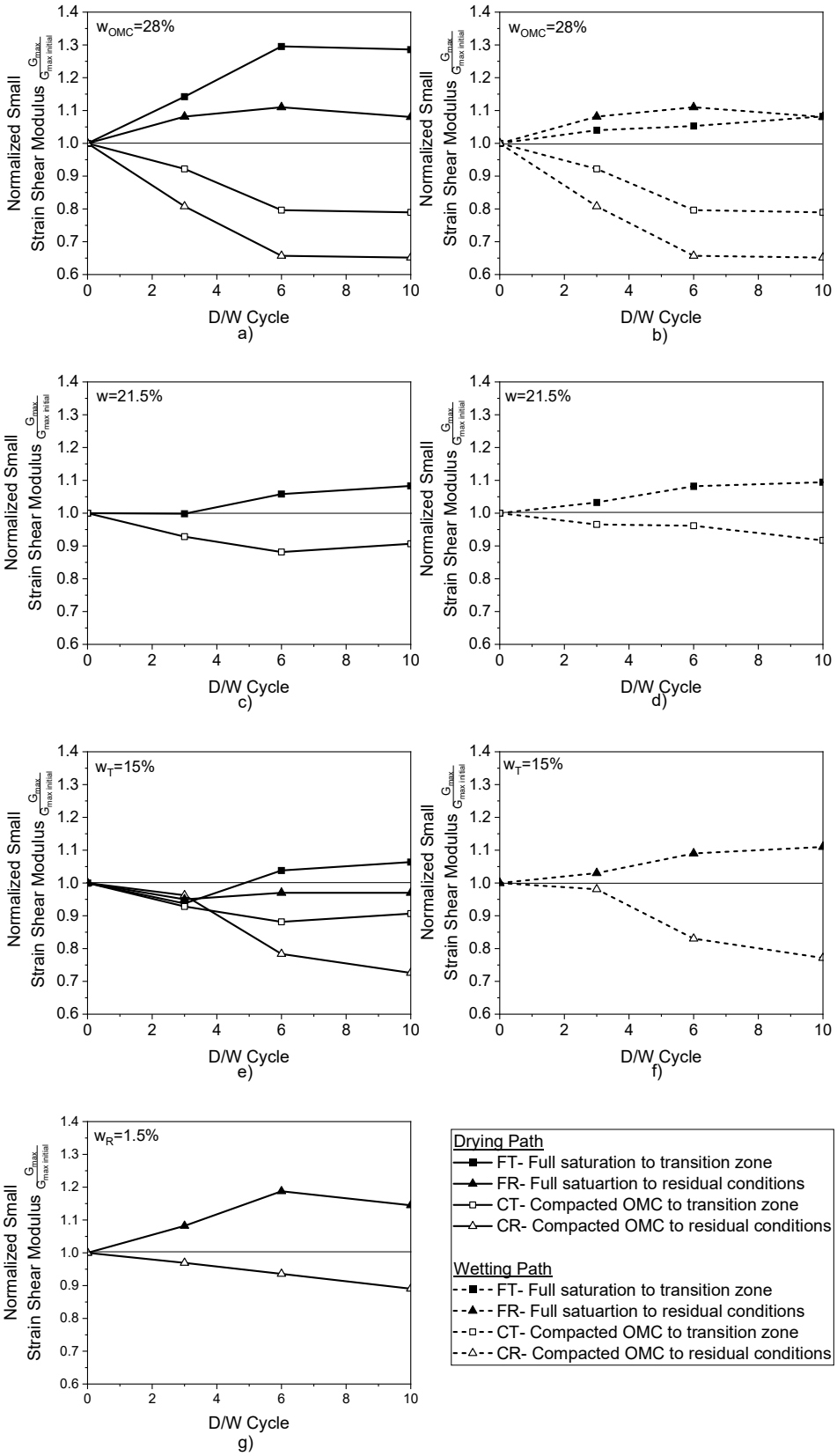


Figure 4-5 Normalized small strain shear modulus of compacted clayey silt specimens at constant water content levels during drying-wetting cycles, for amplitudes: a) FT – full saturation to transition zone, b) FR – full saturation to residual conditions, CT – compacted OMC to transition zone and d) CR – compacted OMC to residual conditions.

Figure 4-6 further explores this by presenting recorded volumetric strain data at the boundaries of drying-wetting cycles for all pathways. The volumetric strain is determined considering the ratio between the variation volume and the initial compacted volume, shown as a percentage. It shows that both fully saturated pathways exhibit large swelling strains when brought to full saturation (Figure 4-6a shows FT pathway produced ε_{vs} of 13% after first full saturation). While specimens brought to compacted water content experienced smaller degrees of volumetric strain variation (Figure 4-6c shows CT pathway produced ε_{vs} of 1% after first wetting to 28% water content). Furthermore, fully saturated pathways (Figure 4-6a,b) are dominated by an irreversible shrinkage strain component with asymptotic behaviour. In contrast, specimens brought to compacted water content (Figure 4-6c,d) exhibit a similar asymptotic irreversible swelling strain. The reversal observed for small strain shear modulus measurements strongly correlates with this behaviour.

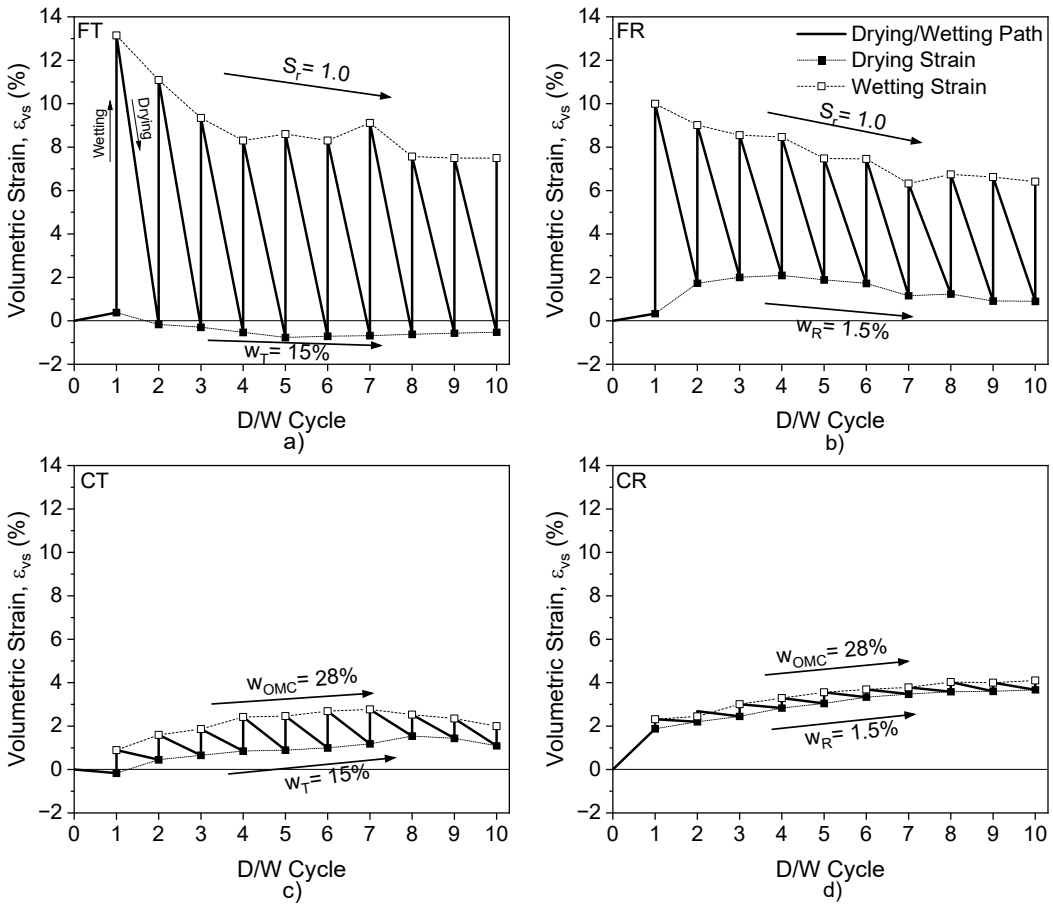


Figure 4-6 Volumetric strain at drying and wetting boundaries during the application of 10 cycles for a) FT – full saturation to transition zone, b) FR – full saturation to residual conditions, c) CT - compacted OMC to transition zone and d) CR – compacted OMC to residual conditions (compressive strains considered negative).

Interestingly, Figure 4-6b pathway FR, also shows evidence of irreversible swelling at the drying boundary (w_R=1.5% water content) within the first three cycles, while also presenting subsequent irreversible shrinkage. This contrasts with the equivalent CR pathway (Figure 4-6d) which shows continuous irreversible swelling at this drying boundary. This therefore confirms the presence of interactions between both wetting and drying boundaries. Wang and Wei (2015) suggests that the deformation of compacted soils results from both the rearrangement of the skeleton of the aggregates and the deformation of the aggregates. Irreversible swelling/shrinkage represents rearrangement of the pore structure in this respect. While attainment of equilibrium represents the reversible deformation of aggregates during changes in water content. These accumulated irreversible changes in volumetric strain have been characterized, for a small number of cycles only, by several researchers including Koliji et al. (2010); Nowamooz et al. (2016); Farulla et al. (2010); Ma et al. (2015); Sun and Cui (2018) corresponding with significant changes in the pore structure of the soil. These findings corroborate the empirically supported presupposition of irreversible structural changes and demonstrate for the first time that the associated observed changes in small strain stiffness are highly dependent on hydraulic loading conditions.

4.3 Unsaturated small strain behaviour: clayey sandy silt (Low plasticity)

The initial compacted conditions for the clayey sandy silt specimens are presented in Table 4-2. The hydraulic pathways of the clayey sandy silt specimens are presented in Figure 4-7. Monitoring of small strain stiffness was conducted in an identical manner to the clayey silt. Measurement of small strain stiffness and volume was made at the selected discrete water content levels shown by the solid symbols in Figure 4-7. No measurements were made at saturated conditions as specimens were soft. Consequently, to minimise disturbance and allow suitable comparison between hydraulic pathways, the compacted water content (w_{OMC}= 13.5%) was selected to observe changes in small strain stiffness. Similarly, no visible macroscopic cracking was observed during drying-wetting that impacted the integrity of the specimens.

Table 4-2 Summary of initial compacted conditions for clayey sandy silt specimens.

Test ID	Water Content, w: %	Bulk Unit Weight, γ_b: kN/m^3	Dry Unit Weight γ_b: kN/m^3	Platen to Platen distance, L_{pp}: mm	Void Ratio, e	Water Ratio, e_w	Degree of Saturation, S_r
FT-D/W1	13.5	20.03	17.65	38.1	0.45	0.351	0.79
FT-D/W3	13.3	20.03	17.68	38.1	0.44	0.346	0.78
FT-DW6	13.6	19.92	17.54	38.1	0.45	0.354	0.78
FT-D/W10	13.3	19.98	17.63	38.1	0.45	0.346	0.78
FR-D/W1	13.7	20.02	17.61	38.1	0.45	0.356	0.80
FR-D/W3	13.5	20.00	17.62	38.1	0.45	0.351	0.79
FR-D/W6	13.4	20.03	17.67	38.1	0.44	0.348	0.79
FR-D/W10	13.4	20.07	17.70	38.1	0.44	0.348	0.79
CT-D/W1	13.5	20.03	17.65	38.1	0.45	0.351	0.79
CT-D/W3	13.2	19.97	17.64	38.1	0.45	0.346	0.77
CT-D/W6	13.3	20.01	17.66	38.1	0.44	0.346	0.78
CT-D/W10	13.3	20.03	17.70	38.1	0.44	0.346	0.78
CR-D/W1	13.4	20.07	17.86	38.1	0.44	0.348	0.79
CR-D/W3	13.7	20.10	17.68	38.1	0.44	0.356	0.80
CR-D/W6	13.6	20.07	17.66	38.1	0.44	0.354	0.80
CR-D/W10	13.3	19.92	17.60	38.1	0.45	0.346	0.78

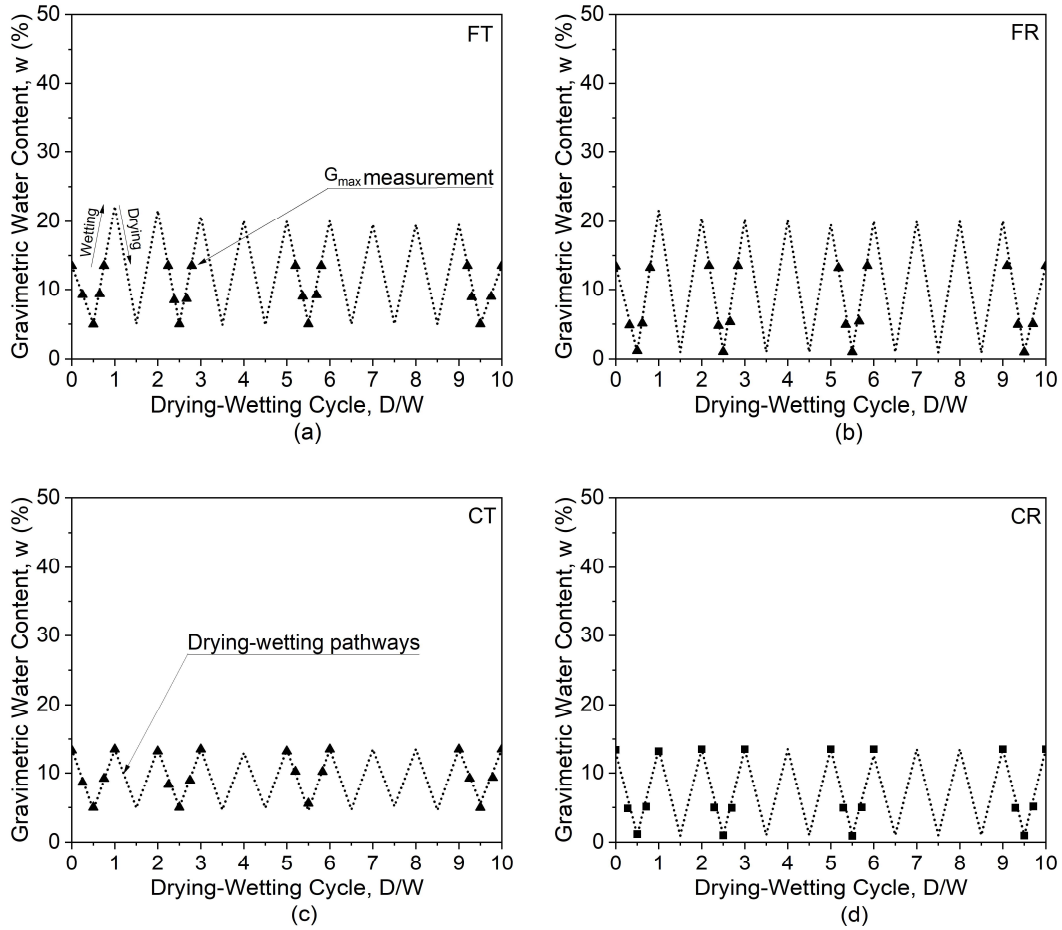


Figure 4-7 Clayey sandy silt drying-wetting pathway and discrete G_{max} measurement points (solid symbol) for a) FT, b) FR, c) CT and d) CR conditions.

4.3.1 Drying-wetting behaviour

The relationship between small strain shear modulus and gravimetric water content for the clayey sandy silt at selected drying-wetting cycles is presented in Figure 4-8. The results again clearly illustrate the approximate inverse relationship between small strain shear modulus and water content and the hysteretic response of small strain shear modulus during drying-wetting.

Similarly, the void ratio results presented in Figure 4-9 show a hysteretic response whereby void ratio is greater on the wetting path than the drying path at a given water content. Upon drying greater than the transition zone water content (w_T=5%) to residual conditions (w_R=1%) (Figure 4-9b,d) no further volume change was recorded. This behaviour is expected as the shrinkage limit of the material was exceeded. The rate of shear modulus change is also significantly influenced by the domain in which water content is changed. For instance, within the transition zone (w_{OMC}=13.5% to w_T=5%) a slower rate of shear modulus change is observed (Figure 4-8a,c), when compared to drying to residual conditions (w_T=5% to w_R=1%) (Figure 4-8b,d).

Upon the application of repeated drying-wetting cycles, Figure 4-10 shows that in general the small strain shear modulus of the clayey sandy silt also experiences inverse behaviour. For instance, hydraulic pathway FT (Figure 4-10a) shows a slight increase in shear modulus after 10 D/W cycles. Whereas, FR, CT and CR pathways (Figure 4-10b,c,d) experienced a decrease in shear modulus.

When results are presented using normalised change in small strain shear modulus at select constant water content levels, shown in Figure 4-11, a clear trend is visible between the different pathways. At all water contents during both drying and wetting, specimens brought to full saturation (S_r=1.0) and dried to the transition zone (w_T=5%) (FT) show an asymptotic increase in normalised shear modulus. For instance, drying at the compacted water content (w_{OMC}=13.5%) an 6% increase in shear modulus ($G_{max}/G_{max\text{-}initial}$=1.06) was experienced after 10 D/W cycles (Figure 4-11a). In contrast specimens on both the FR and CT pathways show slight decrease in shear modulus. At the same water content level (w_{OMC}=13.5%) both FR and CR experienced a 9% decreases in shear modulus ($G_{max}/G_{max\text{-}initial}$=0.91) after 10 D/W cycles. While specimens on the CR pathways experienced the largest decrease in shear modulus of 16% ($G_{max}/G_{max\text{-}initial}$=0.84) after 10 D/W cycles.

Figure 4-12 presents the volumetric strains during drying-wetting. Results show swelling of approximately ε_{vs} 8% upon full saturation owing to the clay portion of the soil mixture. Upon continued drying-wetting of specimens on the FT and FR pathways irreversible shrinkage strains were recorded (Figure 4-12a,b). While specimens on the CT and CR pathways experienced small amount of irreversible swelling strains (Figure 4-12c,d). Furthermore, when comparing CT and CR pathways the impact of the drying boundary can be discerned. For instance, following the initial drying-wetting specimens on the CT pathway a 0.5% ε_{vs} increase was recorded after 10 drying-wetting cycles while CR pathway experienced approximately 1% ε_{vs} increase.

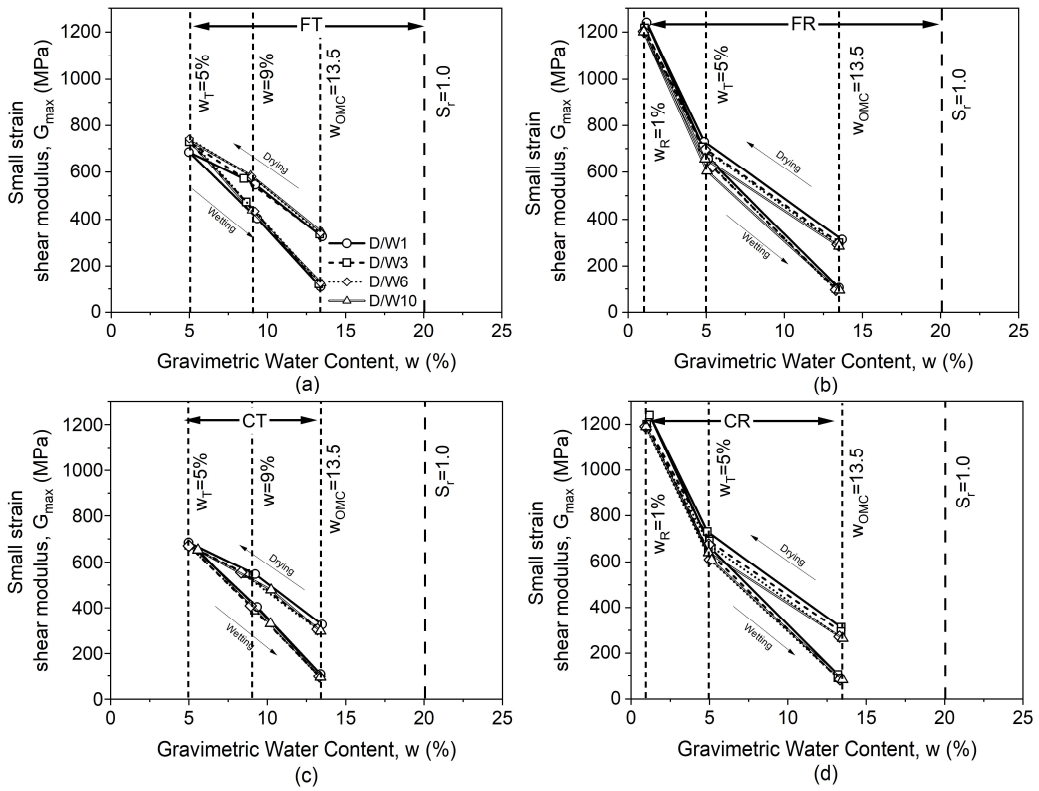


Figure 4-8 Small strain shear modulus of compacted clayey sandy silt specimens subjected to D/W 1, 3, 6, and 10 for a) FT, b) FR, c) CT and d) CR conditions (note the horizontal arrows indicate the extent of drying-wetting cycles).

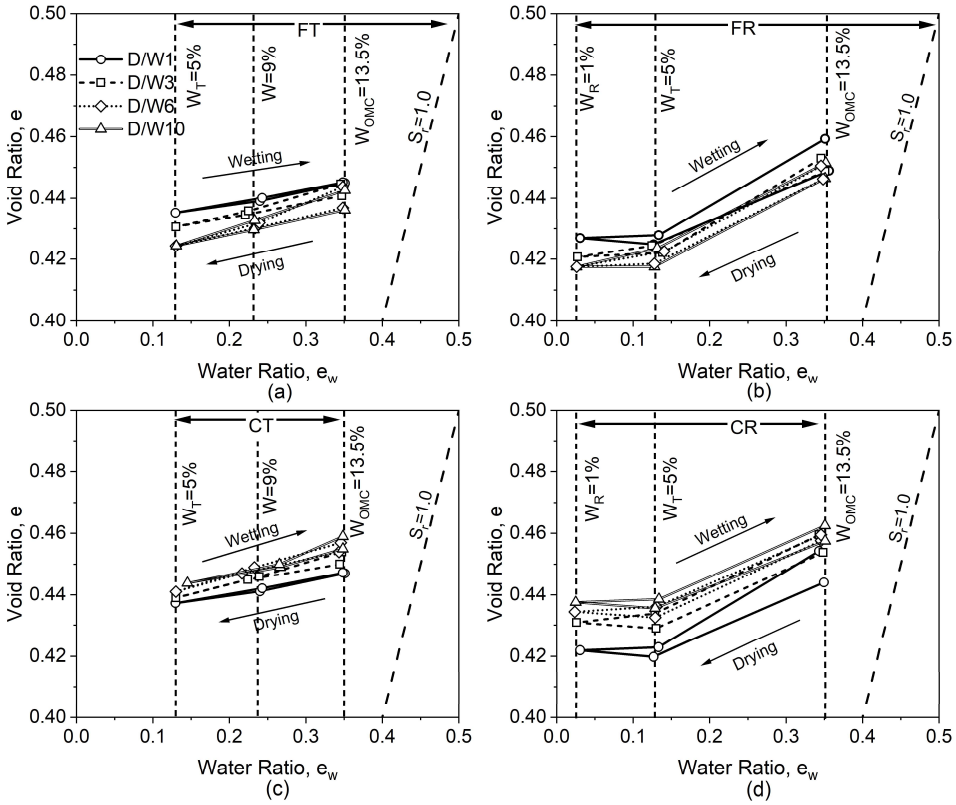


Figure 4-9 Volume change of compacted clayey sandy silt specimens subjected to D/W 1, 3, 6, and 10 for a) FT, b) FR, c) CT and d) CR (note the horizontal arrows indicate the extent of drying-wetting cycles).

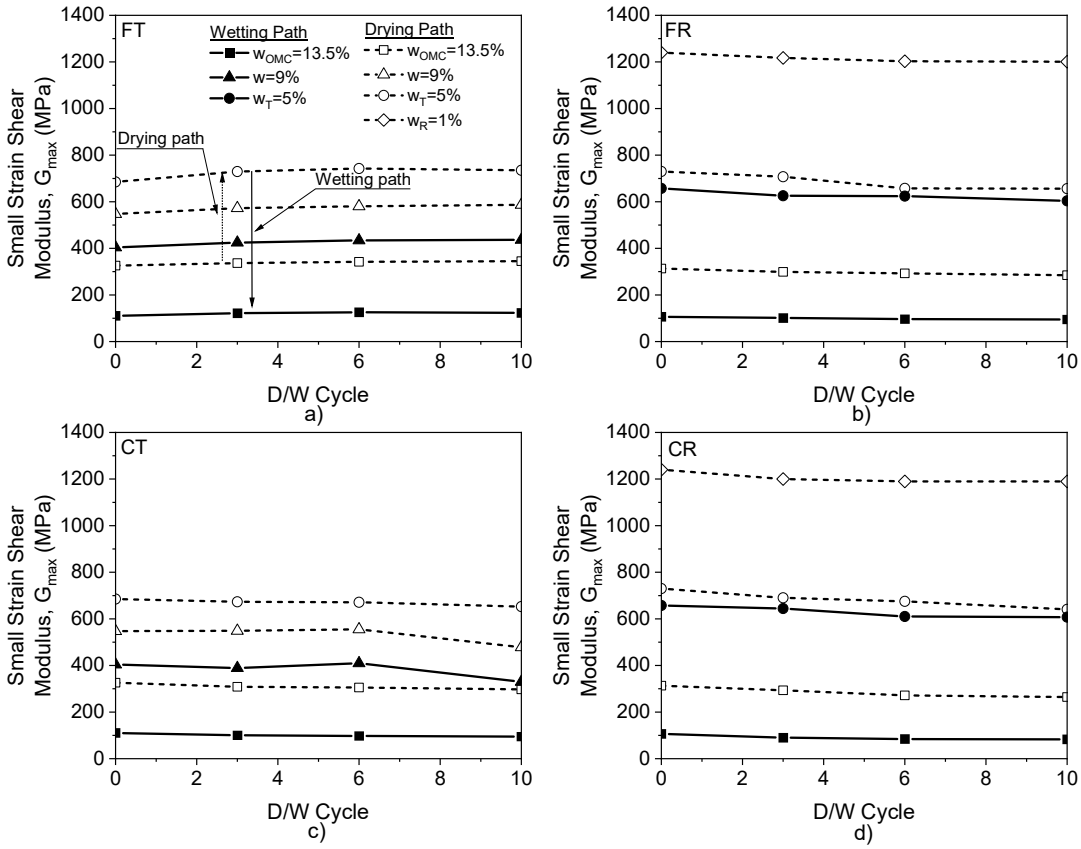


Figure 4-10 Small strain shear modulus of compacted clayey sandy silt specimens subjected to D/W 1, 3, 6, and 10 for a) FT, b) FR, c) CT and d) CR conditions.

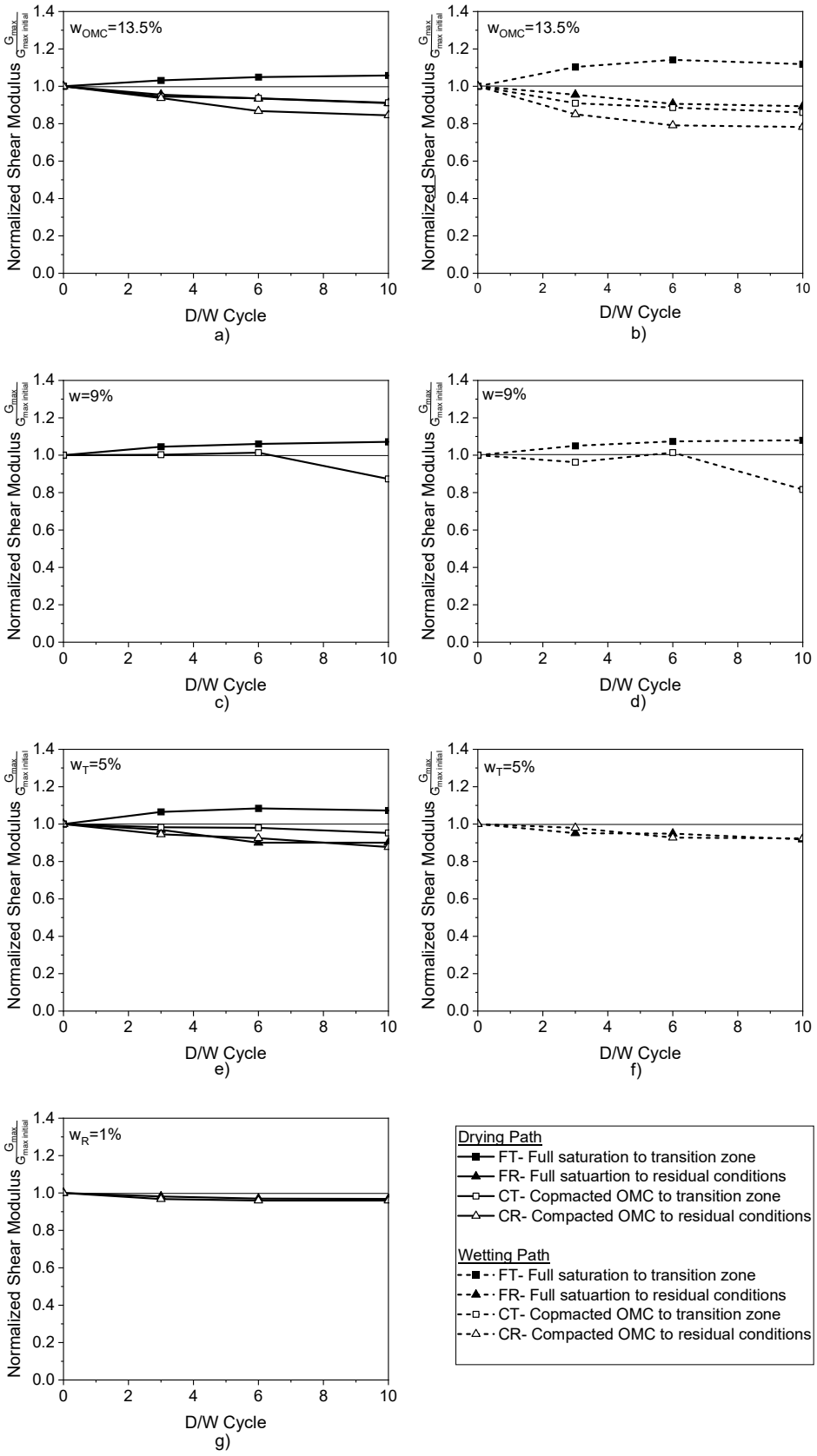


Figure 4-11 Normalized small strain shear modulus for compacted clayey sandy silt specimens at selected water content levels during drying-wetting.

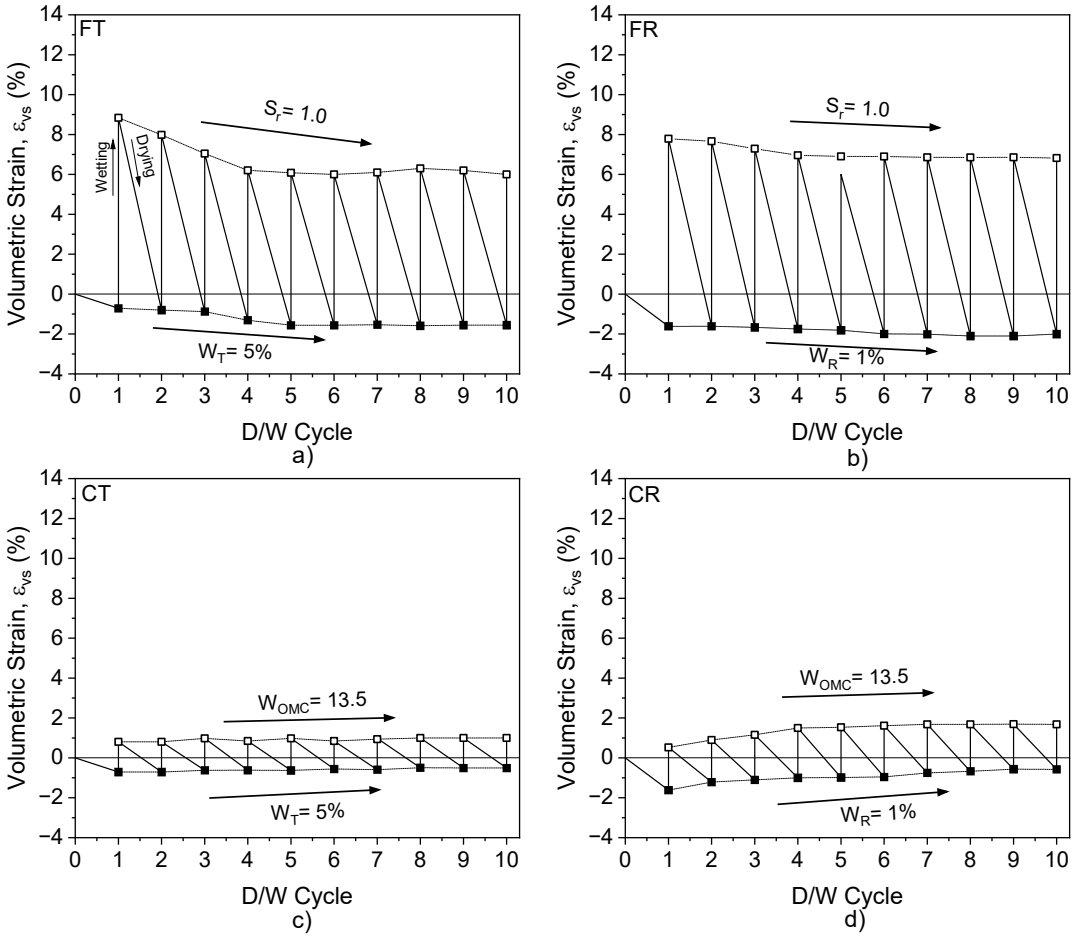


Figure 4-12 Volumetric strain at drying and wetting boundaries for the clayey sandy silt during the application of 10 cycles for a) FT, b) FR, c) CT and d) CR conditions (compressive strains considered negative).

4.4 Unsaturated small strain behaviour: silty clay (very high plasticity)

The initial compacted conditions of the silty clay is presented in Table 4-3 and shows good repeatability between specimens. Fewer specimens were prepared as FR, CT and CR pathways resulted in significant cracking and loss of integrity of the specimens prior to reaching 6th D/W cycles. As a consequence, a further three specimens were added to measure the small strain stiffness during the 2nd drying-wetting cycle and increase the number of measured points prior to specimen failure.

The hydraulic pathways applied to the silty clay specimens and discrete water contents at which small strain stiffness was measured are also shown in Figure 4-13. Notably, due to failure of specimen as a consequence of severe cracking, the hydraulic pathways end prior to 10 drying-wetting cycles. Corresponding images of the final failed specimens, presented in Figure 4-14, show configuration of cracking and failure of specimens. The specimens experienced macroscopic cracking both perpendicular and parallel to their vertical axis. Interestingly, it appears that the density of cracking was greater for specimens which were wet to the compacted water content (w_{OMC}=22%) and dried to residual conditions (w_R=1.5%) (CT/CR). This suggests that saturation of specimens (FT/FR) results in a closure of cracks and a degree of 'self-healing' due saturation.

Table 4-3 Summary of initial compacted conditions for silty clay specimens.

Test ID	Water Content, w: %	Bulk Unit Weight, γ_b: kN/m^3	Dry Unit Weight γ_b: kN/m^3	Platen to Platen distance, L_{pp}: mm	Void Ratio, e	Water Ratio, e_w	Degree of Saturation, S_r
FT-D/W1,3,6	22.0	17.92	14.69	38.0	0.73	0.572	0.78
FR- D/W1,3	22.3	17.98	14.70	38.1	0.73	0.579	0.79
FR-D/W2	22.1	17.92	14.69	38.1	0.73	0.574	0.78
CT- D/W1,3	22.4	18.16	14.84	38.0	0.72	0.582	0.81
CT-D/W2	22.1	17.87	14.64	38.1	0.74	0.574	0.77
CR- D/W1,3	22.1	18.06	14.78	38.0	0.72	0.574	0.80
CR-D/W2	22.3	17.82	14.57	38.2	0.74	0.579	0.77

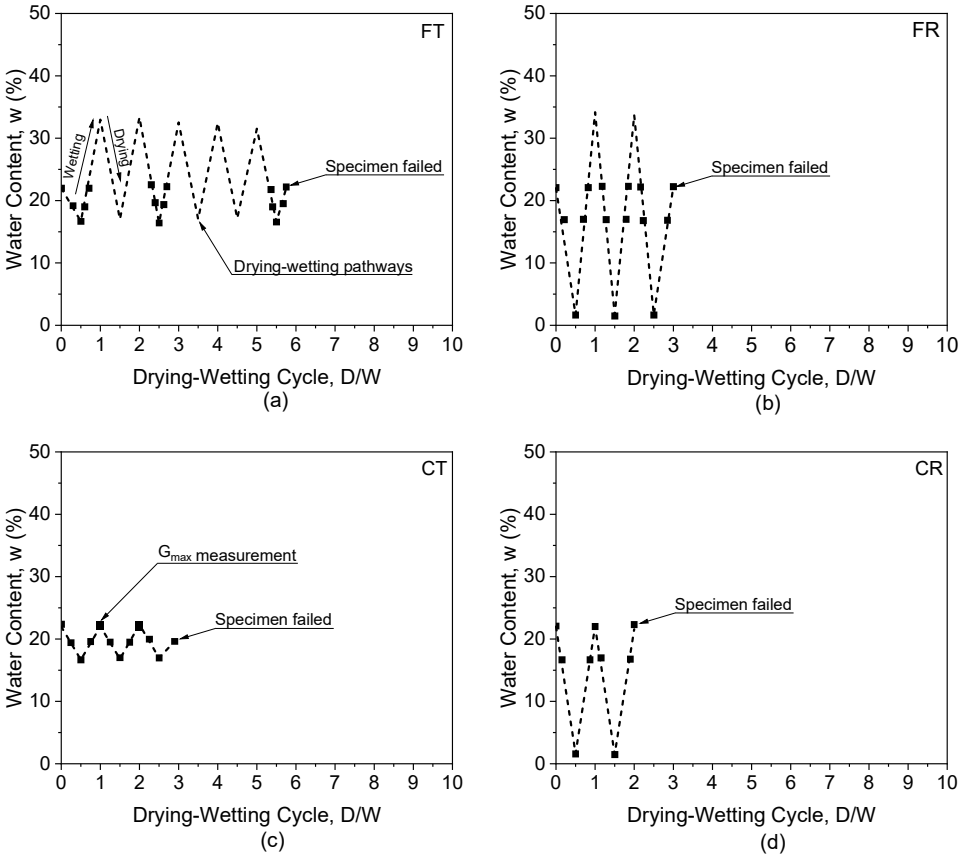


Figure 4-13 Silty clay drying-wetting pathway and discrete G_{max} measurement points (solid symbol) for a) FT, b) FR, c) CT and d) CR conditions.

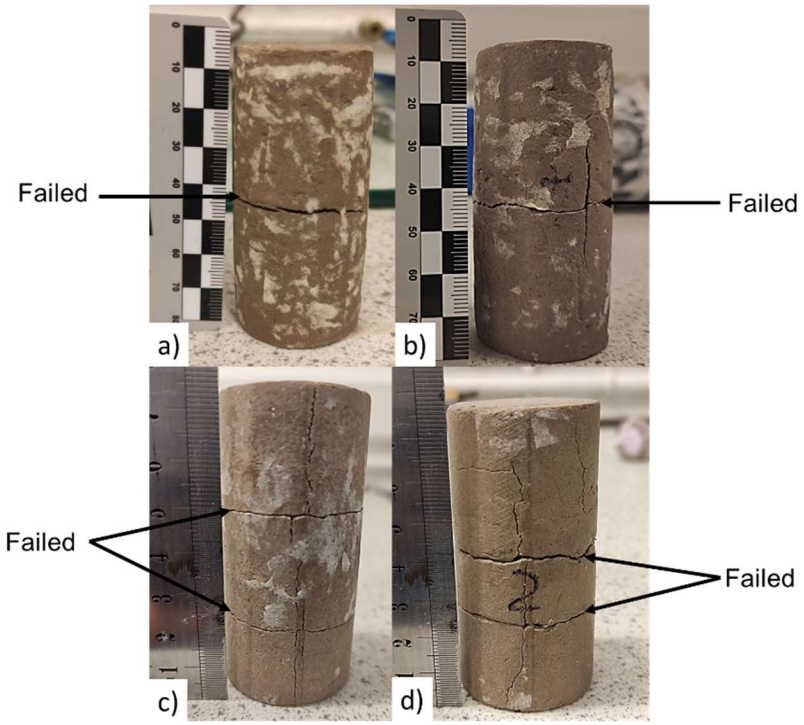


Figure 4-14 Images showing the final failed specimens of silty clay for: a) FT – 6th D/W cycle on wetting path at w_{OMC}=22%, b) FR – 3rd D/W cycle on wetting path at w_{OMC}=22%, c) CT – 3rd D/W cycle on wetting path at w=19% and d) CR – 2nd D/W cycle on wetting path at w_{OMC}=22%.

4.4.1 Drying-wetting behaviour

The relationship between small strain shear modulus and gravimetric water content for the silty clay during drying-wetting is shown in Figure 4-15. The results show a consistent trend of drying-wetting behaviour (i.e. configuration of drying-wetting loop) with the previously tested soils. Albeit, the silty clay shows a more linear trend for small strain shear modulus in different domains during drying-wetting. Conversely, the void ratio results, presented in Figure 4-16, show the expected nonlinear trend when dried to residual conditions (w_R=1.5%). Interestingly, despite the small reduction in volume on FT and FR pathways (Figure 4-16a,b) a reduction in shear modulus was also recorded (Figure 4-15a,b). However, this is intuitive when considering the formation of cracking (Figure 4-14). Its noted that due to the macroscopic method at which volume was determined, volume change owing to microstructural changes cannot be distinguished from the formation of macroscopic cracking. For instance, the increase in void ratio for CT and CR pathways may be attributed to the significant density of macroscopic cracking shown in Figure 4-14.

The evolution of small strain shear modulus during drying-wetting of the silty clay for the selected water content levels is presented in Figure 4-17. In general, all hydraulic pathways resulted in a reduction in small strain shear modulus and the degree of hysteresis during drying-wetting. For instance, at the compacted water content (w_{OMC}=22%) drying-wetting on the FT pathway (Figure 4-17a) resulted in a reduction hysteresis amplitude of 51 MPa, while at w_T=17% a reduction of 59 MPa was observed after 3 drying-wetting cycles. Furthermore, when comparing the different hydraulic pathways, presented in Figure 4-18, it's clear that specimens subjected to full saturation (FT and FR) during drying-wetting have a smaller reduction in small strain shear modulus when compared to specimens brought to the compacted water content during wetting (CT and CR). While specimens dried to residual conditions (w_R=1.5%) (FR and CR) exhibit a greater loss of in shear modulus compared to specimens dried within the transition zone (w_T=17%) (FT and CT). This behaviour is clearly illustrated on the drying path at the compacted water content (Figure 4-18a) after three drying-wetting cycles. In this instance, the FT pathway experienced 24% reduction in small strain shear modulus ($G_{max}/G_{max\text{-}initial}$=0.76), the lowest reduction when considering all pathways. In comparison the FR pathway experienced a greater 40% reduction in shear modulus ($G_{max}/G_{max\text{-}initial}$=0.60) as a consequence of increased drying boundary water content. The CT pathway experienced a 57% decreases in shear modulus ($G_{max}/G_{max\text{-}initial}$=0.43), which is significantly greater than the corresponding full saturated FT pathway. Finally, CR pathways experienced the greatest loss in shear modulus of 72% ($G_{max}/G_{max\text{-}initial}$=0.28). Notably, this trend is present on both drying and wetting pathways. Moreover, this

reduction in stiffness intuitively corresponds with the empirical visual observations of the density of macroscopic cracking shown in Figure 4-14, highlighting the impact of self-healing of cracks on performance.

Considering these observations when viewing the volumetric strain data in Figure 4-19 a similar distinction can be made between FT/FR and CT/CR pathways. As expected the silty clay experienced significant volumetric strains during drying-wetting owing to its very high plasticity. However both FT and FR specimens experienced irreversible shrinkage at both the fully saturated (S_r=1.0) and drying boundaries (w_T=17% and w_R=1.5%) (Figure 4-19a,b). As a consequence it's probable that microstructural changes are occurring similar to the previously tested soils. This behaviour may explain the self-healing cracks observed for saturated specimens (Figure 4-14) however, the mechanism driving this novel observation remains unexplored. In contrast, specimens subject to CT and CR pathways experienced irreversible volume increase (Figure 4-19c,d), likely owing to the increased density of macroscopic cracking shown in Figure 4-14. Nevertheless, this observation confirms the significant influence of the wetting and drying amplitudes on the behaviour of very high plasticity soils.

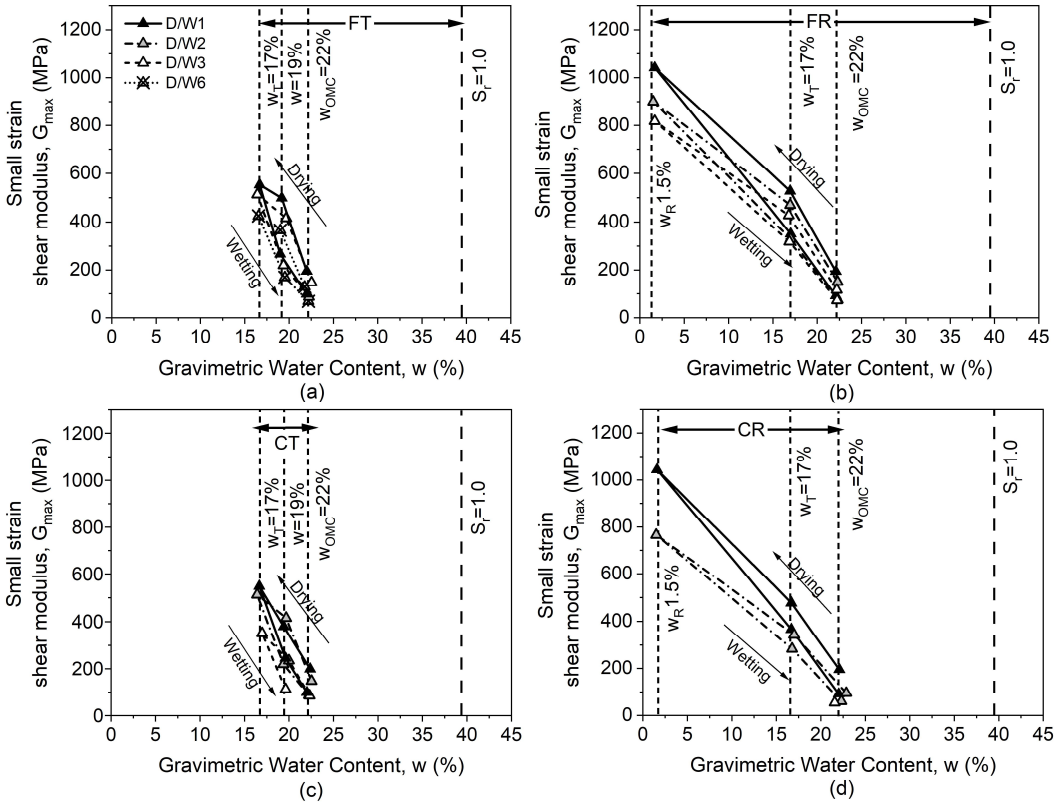


Figure 4-15 Small strain shear modulus of compacted silty clay specimens subjected to D/W 1, 3, 6, and 10 for a) FT, b) FR, c) CT and d) CR (note the horizontal arrows indicate the extent of drying-wetting cycles).

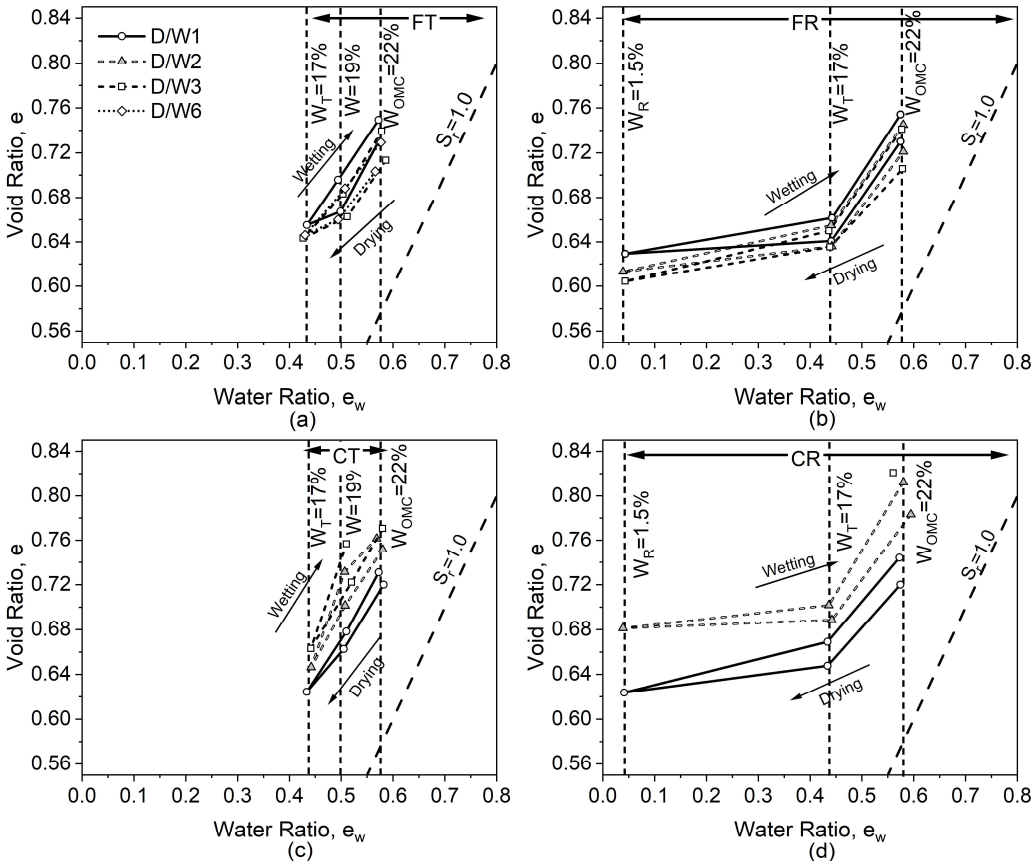


Figure 4-16 Volume change of compacted silty clay specimens subjected to D/W 1, 3, 6, and 10 for a) FT, b) FR, c) CT and d) CR (note the horizontal arrows indicate the extent of drying-wetting cycles).

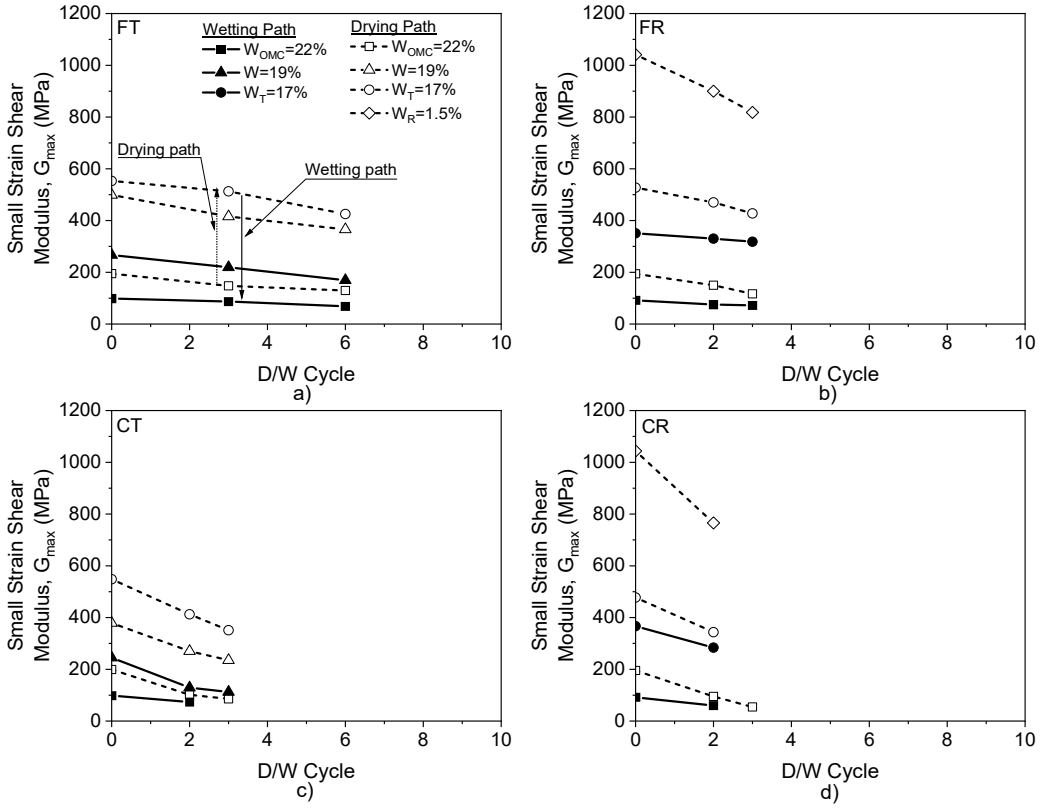


Figure 4-17 Small strain shear modulus of compacted silty clay specimens subjected to D/W 1, 3, 6, and 10 for a) FT, b) FR, c) CT and d) CR conditions.

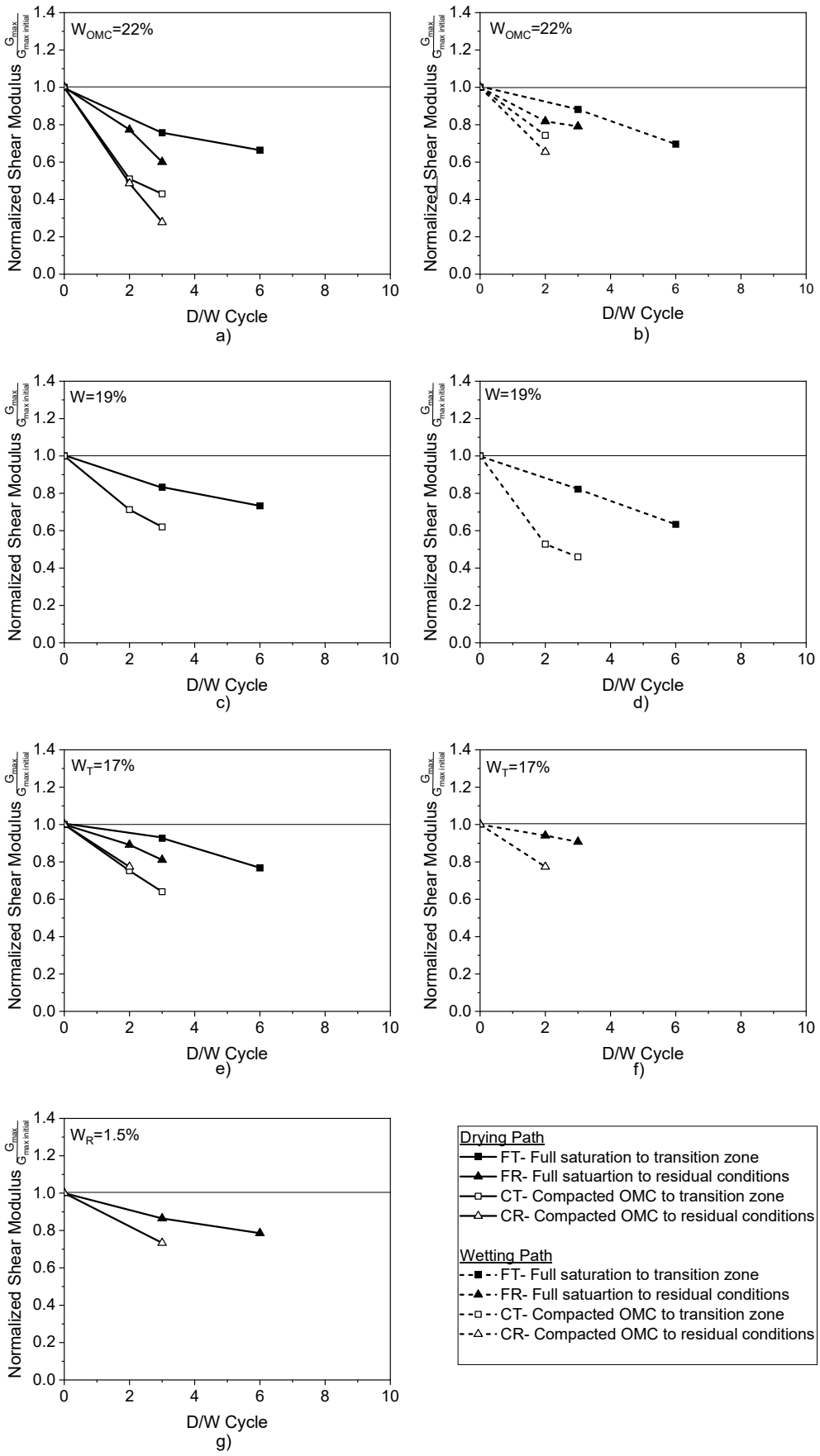


Figure 4-18 Normalized small strain shear modulus for compacted silty clay specimens at selected water content levels during drying-wetting.

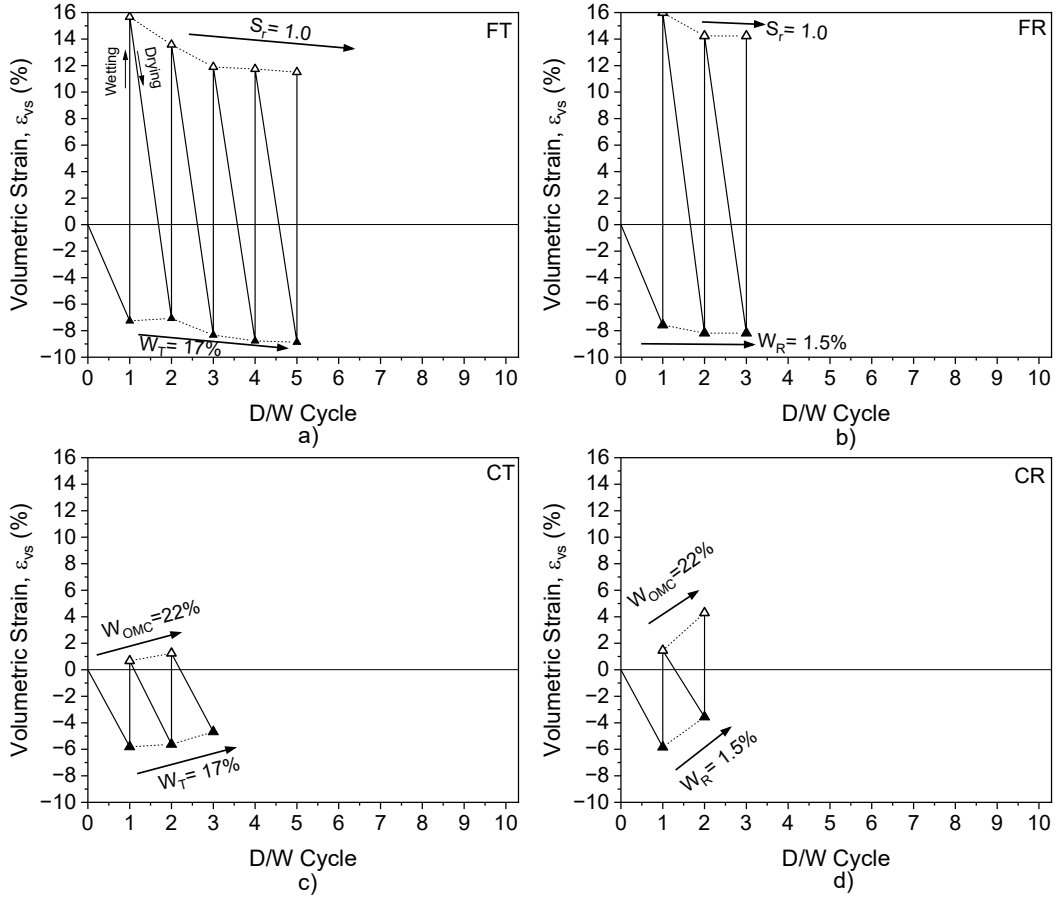


Figure 4-19 Volumetric strain at drying and wetting boundaries during the application of 10 cycles for a) FT, b) FR, c) CT and d) CR (compressive strains considered negative).

4.5 Small stain stiffness comparison

4.5.1 Initial drying-wetting cycle behaviour

The small strain shear modulus (G_{max}) and void ratio (e) of the clayey sandy silt, clayey silt and silty clay during the initial drying-wetting to the transition zone (w_T) and residual conditions (w_R) is compared in Figure 4-20a,b. The data is also normalised to allow for comparison against the initial compacted conditions (Figure 4-20c,d). The results show that the compacted small strain shear modulus is smallest for the clayey silt (124 MPa), silty clay (199 MPa) and the greatest for the clayey sandy silt (313 MPa), which is expected when comparing the void ratio following compaction (Figure 4-20b). When normalised against the initial compacted conditions the rate of small strain shear modulus change during drying-wetting to the transition zone (w_T) is significantly greater for the silty clay despite having the smallest change in water content. In this range both the clayey silt and clayey sandy silt have similar rates of change in small strain shear modulus which is reflected by the recorded volume changes (Figure 4-20d). Upon drying to residual conditions (w_R) the silty clay has the greatest change in shear modulus from the compacted state. Comparatively, the clayey sandy silt has the has a significant increase in shear modulus compared to the clayey silt. Similar behaviour was also reported by Dong and Lu (2016) for small strain shear modulus of coarse soils during drying-wetting. For instance, Esperance sand showed a similar, but more pronounced, 'S' shaped evolution of shear modulus during drying-wetting compared to linear increases in small strain shear modulus for clays i.e. Denver claystone.

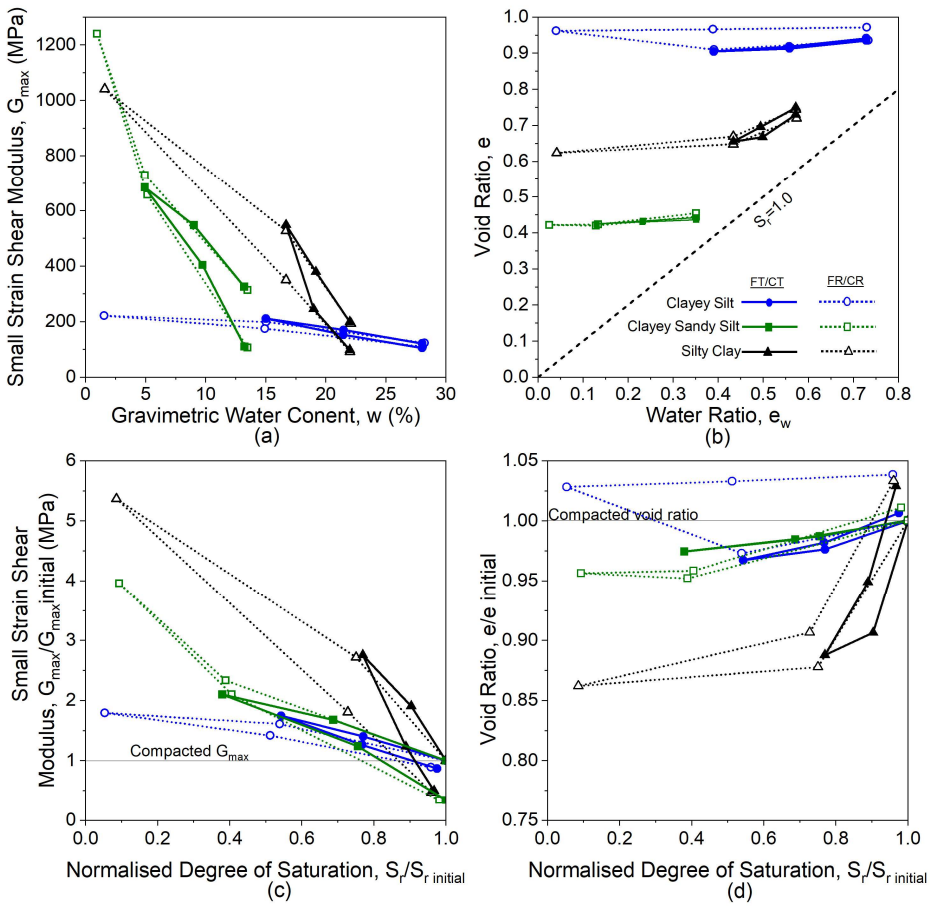


Figure 4-20 Comparison of clayey sandy silt, clayey silt and silty clay for initial drying-wetting cycle showing: a) small strain shear modulus, b) void ratio, c) normalised small strain shear modulus and d) normalised void ratio.

4.5.2 Cyclic drying-wetting behaviour

Figure 4-21 and Figure 4-22 shows the small strain shear modulus and void ratio for all measured dying-wetting cycles for each of the soils. While all soils displayed a decrease in small strain stiffness for for CT and CR drying-wetting pathways, the silty clay experienced the greatest overall decrease for fewest number of drying-wetting cycles (between 2 and 6 D/W) prior to loss of sample integrity. Similarly, both the clayey silt and silty clay show the greatest range of void ratio change during drying-wetting compared to the clayey sandy silt.

Not surprisingly, the comparison of volumetric strains (Figure 4-23) shows the silty clay also experiences the greatest volumetric strains at drying-wetting boundaries. For instance, upon drying the silty clay specimens experienced between - 6 and - 8% ε_{vs}, while upon wetting to fully saturated conditions a 16% ε_{vs} was recorded. During cumulative drying-wetting cycles all soils also experience irreversible reduction in volume

in saturated conditions for FT and FR pathways. However uniquely, the clayey silt shows significant swelling strains at the drying boundary (w_R) for the FR pathway. The volumetric strains measured for CT and CR differ from fully saturated pathways (FT and FR) for all soils where asymptotic swelling strains are present at both the drying and wetting boundaries. This behaviour is most prominent in for the CR pathway. In these conditions the silty clay and clayey silt exhibits ε_{vs} 4% increase at the compacted water content (w_{OMC}) for 2 and 10 drying-wetting cycles, respectively. In contrast, the clayey sandy silt experienced ε_{vs} 2% after 10 drying-wetting cycles. It's also notable that similar behaviour was exhibited for CT pathways but smaller swelling strains were recorded for all soils.

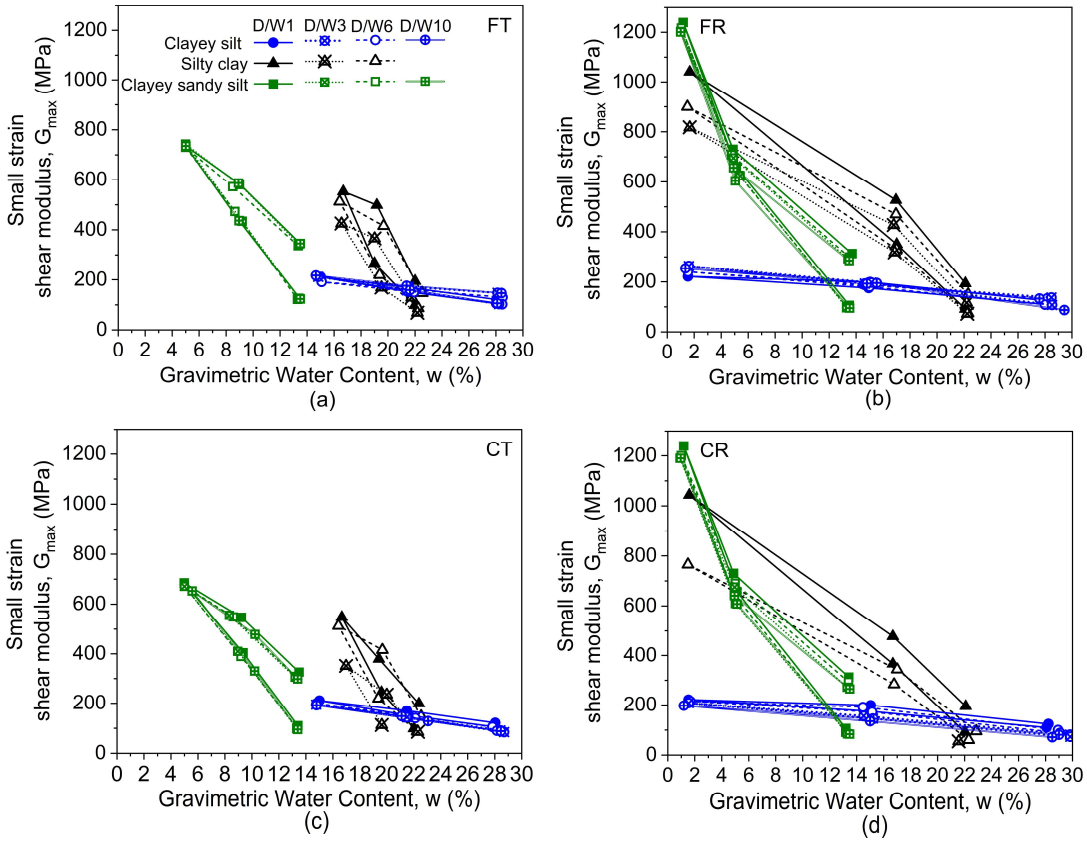


Figure 4-21 Small strain shear modulus comparison of clayey sandy silt, clayey silt and silty clay during the application of 10 drying-wetting cycles for: a) FT, b) FR, c) CT and d) CR conditions.

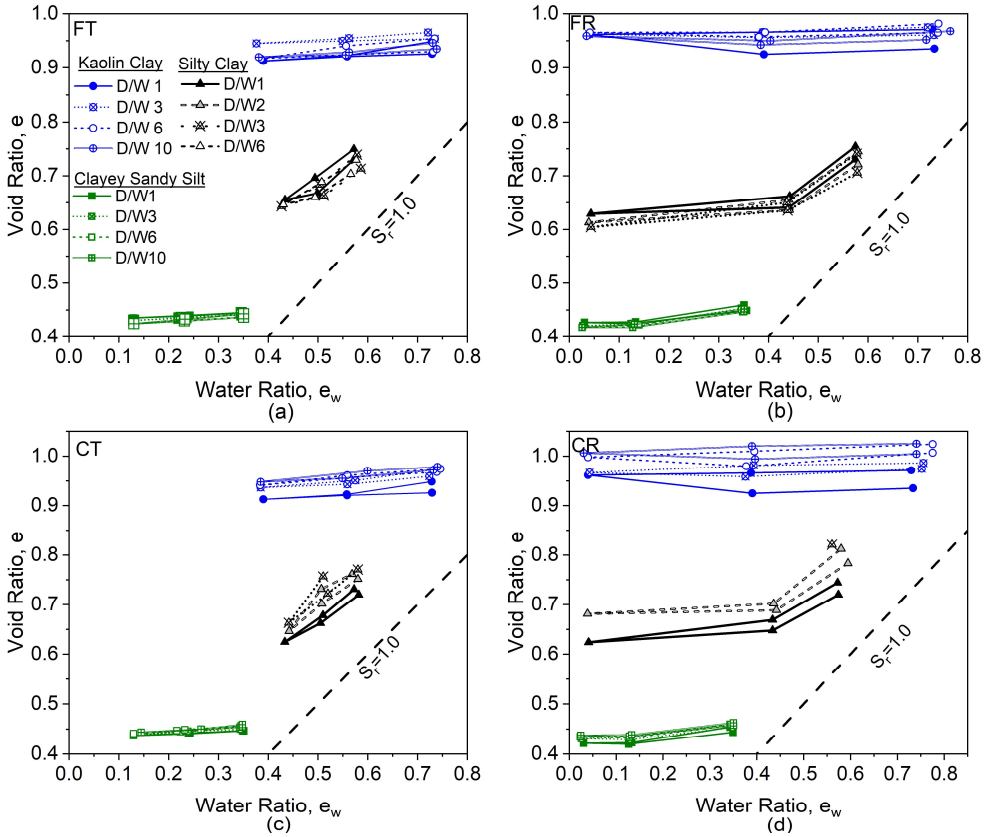


Figure 4-22 Void ratio comparison for the clayey sandy silt, clayey silt and silty clay during the application of 10 drying-wetting cycles for: a) FT, b) FR, c) CT and d) CR conditions.

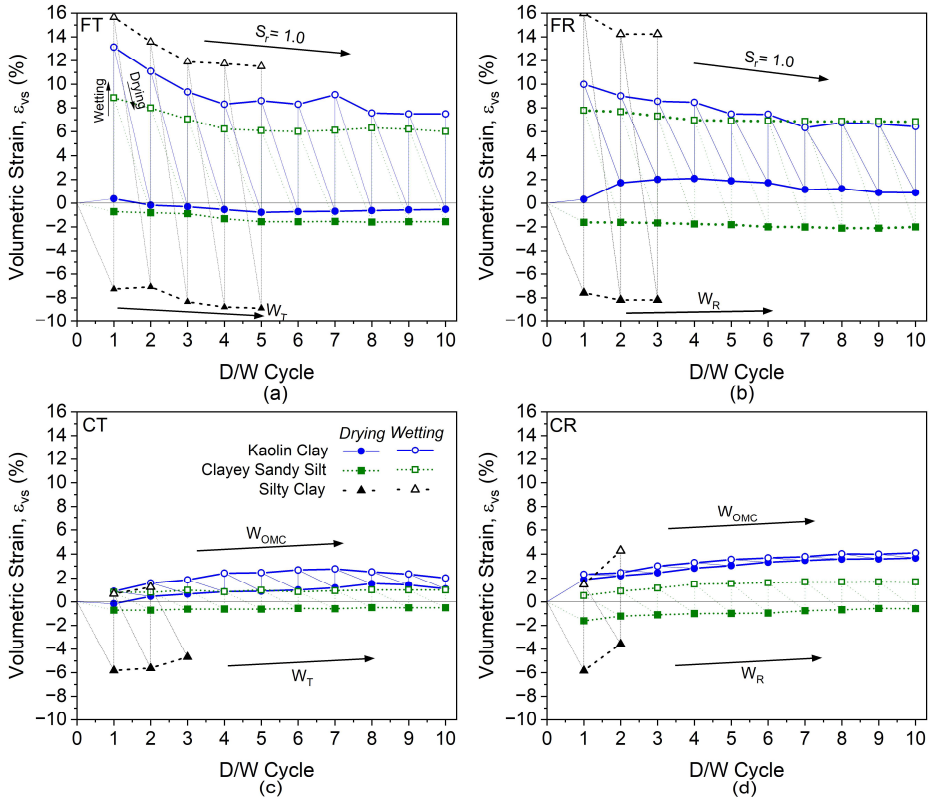


Figure 4-23 Volumetric strain comparison for the clayey sandy silt, clayey silt and silty clay during the application of 10 cycles for: a) FT, b) FR, c) CT and d) CR conditions (compressive strains considered negative).

Figure 4-24 presents a comparison of the final normalised small strain shear modulus values at compacted water content (w_{OMC}). Note that this data was taken from the 10th drying-wetting cycle for the clayey silt and clayey sandy silt, whereas the final measurement prior to loss of specimen integrity was taken for the silty clay. The compacted water content (w_{OMC}) was also chosen as a common point to allow for comparison between the three soils for all hydraulic pathways. This was deemed suitable as behaviour of the soils appears generally consistent at all selected water content levels. However the compacted water content allows for quantification of changes in normalised small strain stiffness behaviour from the initial compacted conditions.

The results show clearly that clayey sandy silt had the best performance with the least deviation from the compacted condition for all selected hydraulic pathways. Comparatively, the silty clay had the worst performance showing the greatest loss of small strain shear modulus from the compacted condition. Most strikingly, a decrease in the normalised small strain shear modulus from FT to CR conditions (left to right) for each soil is observed, relating to selected drying-wetting boundaries.

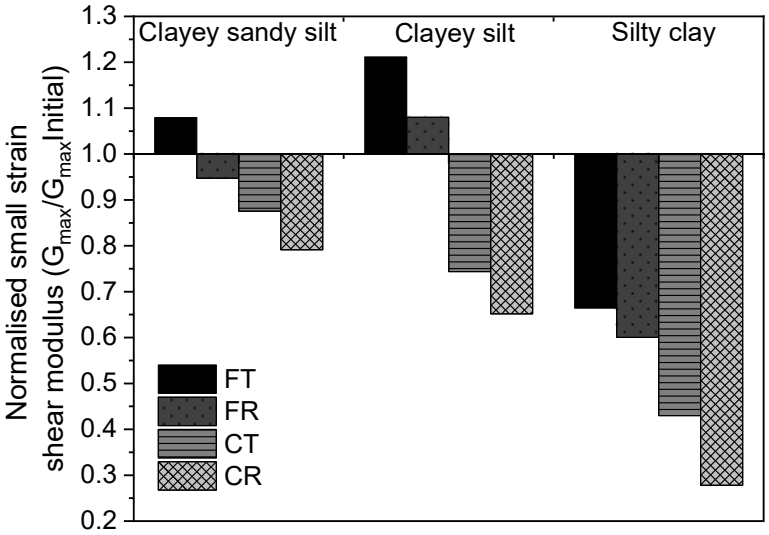


Figure 4-24 Change in normalised small strain stiffness for the clayey sandy silt (10 D/W cycles), clayey silt (10 D/W cycles)and silty clay (2-6 D/W cycles) after application of all drying-wetting cycles at the compacted water content (W_{OMC}).

This finding is further explored in Figure 4-25 which compares the normalised small strain shear modulus during drying-wetting for the selected hydraulic pathways at the compacted water content. Figure 4-25a (CT and FT) and Figure 4-25b (CR and FR) compare the effect of wetting boundaries by plotting data such that constant drying boundaries are maintained. Comparatively, Figure 4-25c (FT and FR) and Figure 4-25d (CR and CT) compare the effect of the drying boundaries as constant wetting boundaries are selected. The results show common behaviour for all soils. For instance, in general it appears that the majority of change in small strain shear modulus is complete after 6

drying-wetting cycles for all hydraulic pathways. Furthermore, specimens brought to full saturation (FT and FR) show an increase in performance when compared to equivalent wetting boundary (CT and CR) (Figure 4-25a and Figure 4-25b). This behaviour was present for all soils irrespective of the degree of drying. In contrast, the comparison between the drying boundaries (FT/FR) in Figure 4-25c shows that an increase in the degree of drying resulted in an overall decrease in small strain shear modulus. This behaviour was also found for (CT/CR) boundaries in Figure 4-25d. The results therefore suggest that the degree of drying or wetting produces inverse behaviour where an increase in the wetting boundary results in hydraulic ageing and increase in small strain shear modulus, while an increase in the drying boundary results in a decrease in performance.

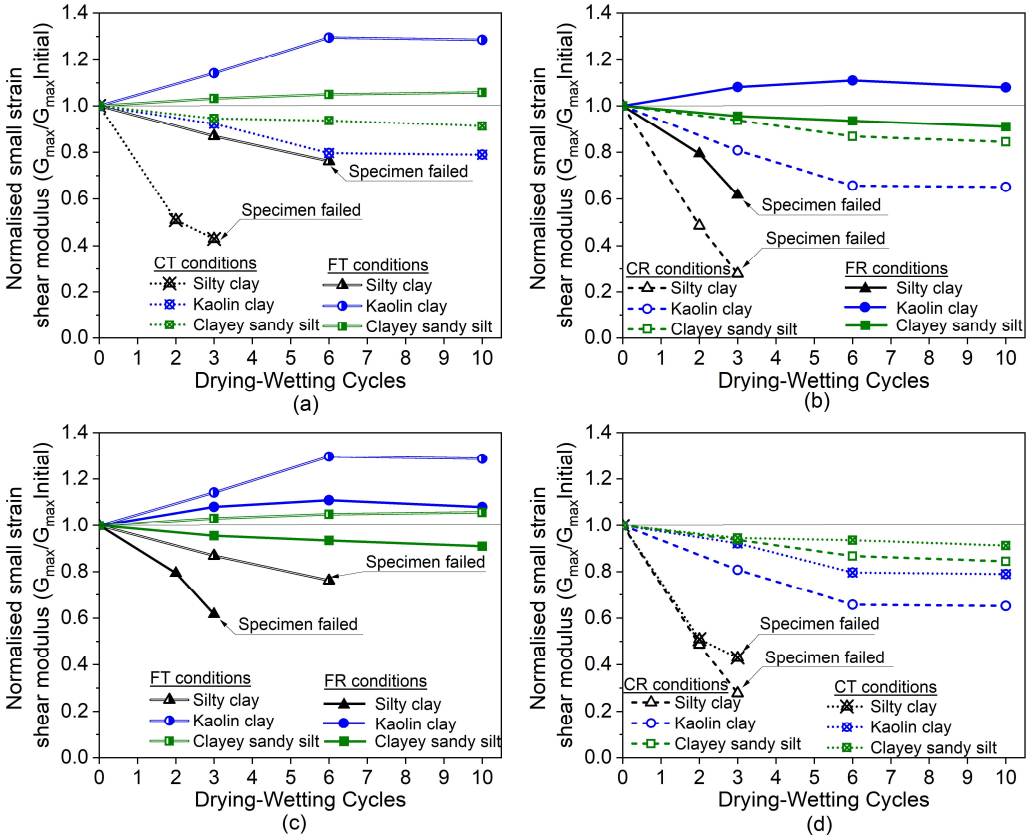


Figure 4-25 Normalised small strain shear modulus at compacted water content for clayey sandy silt (W_{OMC}=13.5%), clayey silt (W_{OMC}=28%), and silty clay (W_{OMC}=22%) comparing: a) CT/FT, b) CR/FR, c) FT/FR and d) CR/CT pathways.

The amplitude of the variation in small strain shear modulus is presented in Figure 4-26 following the application of all drying wetting cycles and is normalised by the compacted water content to allow comparison between soils, as follows:

$$G_{\max} normalised = G_{max}xx - G_{max}yy/G_{max}Initial \qquad (4.1)$$

where G_{max}xx and G_{max}yy represent the different paired drying-wetting pathways considered. Pairings include FT-CT, FR-CR, FT-FR and CT-CR and were selected to

compare the variation in behaviour between a change in drying and wetting boundary respectively. The results show that change in the wetting boundaries (FT-CT and FR-CR) yields the largest difference in small strain shear modulus after drying-wetting for both the clayey silt and silty clay, when compared with counterpart drying boundaries (FT-FR and CT-CR). The significant variation exhibited by the clayey silt likely results from the reduced MDUW during static compaction. In comparison, the clayey sandy silt shows a similar difference between both drying and wetting boundaries. It is also evident that compacted clays are susceptible to larger range of behaviour during drying-wetting when compared to predominantly sandy soils. This is intuitive when considering irreversible volumetric strains reported in Figure 4-23. This therefore suggests that compacted clay fills present a greater challenge for asset management due to greater seasonal variation in behaviour.

Interestingly, the difference between small strain shear modulus for drying boundaries FT-FR and CT-CR is generally similar between all soils which suggests that the mechanism which results in the reduction in small strain shear modulus when the soils were dried to residual conditions is effective despite hydraulic ageing due to full saturation.

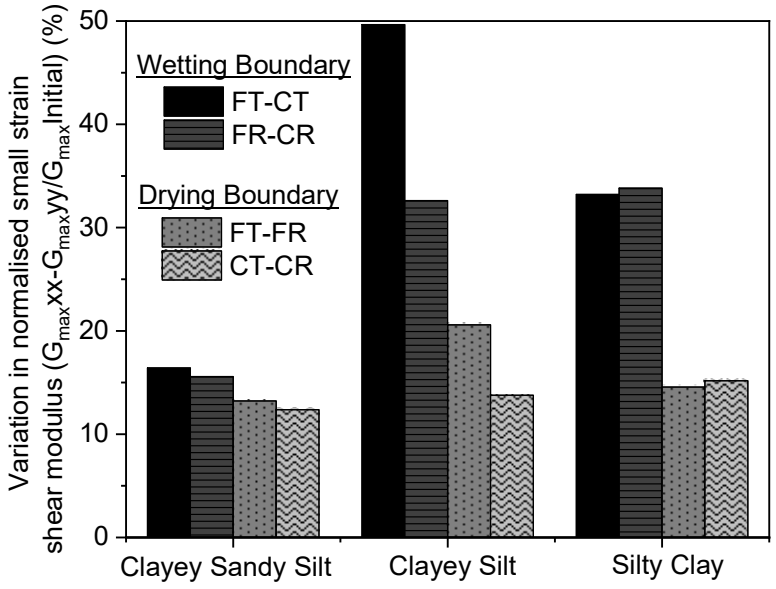


Figure 4-26 Difference in normalised small strain shear modulus between wetting boundaries (FT/CT and FR/CR) and drying boundaries (FT/FR and CT/CR) after application of all drying-wetting cycles at the compacted water content (W_{OMC}).

4.5.3 Drying-wetting microstructure

To investigate the microstructure of the compacted soils during drying-wetting, micro X-ray computed tomography (CT) was conducted at selected water content levels comparable to those measured for small strain stiffness testing. The soil conditions used during testing and presented in this study are shown in Table 4-4. Micrographs were captured at a resolution of 3.24 μm × 3.24 μm/pixel, allowing for changes in soil structure to be evaluated primarily in terms of inter-aggregate pores. In this study, specimen fabric was examined for different magnification by selecting micrographs representative of the soil structure, considering the representative element volume (REV). This allows for comparison between micrographs taken following the application of drying-wetting cycles and the compacted microstructure.

Table 4-4 Conditions of micro X-ray CT imaging

Test Conditions/Test ID	Water Content, *w*: %		
	Clayey Sandy Silt	Clayey Silt	Silty Clay
Compacted conditions (com_w_{OMC})	13.7	28.2	21.9
Initial drying (initial_w_R)	1.0	1.6	1.4
FT_10D/W_w_{OMC}_d (clayey silt 6 D/W)	13.5	28.3	22.3
FR_10D/W_w_{OMC}_d (clayey silt 3 D/W)	13.6	28.0	22.2
CT_10D/W_w_{OMC}_d (clayey silt 3 D/W)	13.1	27.9	22.1
CR_10D/W_w_{OMC}_d (clayey silt 2 D/W)	13.7	28.1	22.0

Where abbreviation 'd' refers to the drying path

The initial compacted conditions (com_w_{OMC}) for the clayey sandy silt, clayey silt and silty clay are presented Figure 4-27 for several levels of magnification, showing characteristic soil structure and inter-aggregate pores. As expected, the results show that inter-aggregate pores are the largest diameter for the clayey sandy silt which ranges from <15μm-160μm. While the clayey silt and silty clay have a similar range approximately between <15μm-60μm. Notably, the clayey sandy silt fabric is shown to consist of sand particles which are surrounded by a silt and clay matrix. Based on these observations it is likely that the water retention behaviour of clayey sand silt is primarily controlled by the finer portion of the soil. Interestingly, the largest inter-aggregate pores are located against the larger coarse sand particles and appear to form due to the aggregation of finer sand particles. In contrast, the clayey silt has a uniform fabric with a uniform distribution of inter-aggregate pores. The silty clay also exhibits a similar fabric, however,

lighter coloured angular medium and coarse silt particles are also present.

Figure 4-28 presents micrographs of the specimens following initial drying at residual conditions (initial_w_R). The results show a decrease in inter-aggregate pore diameter for all soils. For instance, the prevalence of smaller inter-aggregate pores within the clay matrix of the clayey sandy silt appear to reduce. Interestingly, the clayey silt experiences a significant decrease in inter-aggregate pore frequency, with most pores no longer visible at 3.24 µm pixel resolution. This observation is surprising considering the increase in macro volume following drying to residual conditions (see Figure 4-23). This suggests that macroscopic change in volume recorded is related to changes in pore volume at the micro pore scale. Indeed, this observation is also supported by Pedrotti et al. (2024) which reported that upon desaturation at low water contents the micro pores rebound. The silty clay also appears to exhibit a small reduction in the prevalence of inter-aggregate pores accompanied by the formation of cracking. For example, in Figure 4-28(l) the largest crack developed measured 661µm in length and 15µm in width, while smaller cracks are also presented measuring <80µm.

The remaining micrographs for FT, FR, CT and CR conditions are presented in Figure 4-29, Figure 4-30, Figure 4-31 and Figure 4-32. These conditions, allow for an evaluation on the impact of drying and wetting boundaries on the changes to the soil fabric and support the small strain stiffness findings reported in the previous sections. Upon initial qualitative observation the greatest difference in soil fabric is present between FT/CT and FR/CR conditions. This finding is not surprising given these conditions resulted in the largest variation in macro behaviour in terms of small strain shear modulus (see Figure 4-21).

For instance, the clayey silt exhibited a reduction in inter-aggregate pore diameter following 10 D/W cycles on the FT pathway. For this condition, the maximum pore diameter reduced to approximately 40µm. In comparison, after 10 D/W cycles for CT and CR conditions the initial open structure following compaction appears to remain. Its therefore probable that significant swelling of the clay minerals occur upon full saturation and allows for rearrangement of the fabric surrounding sand particles reducing the macroscopic volume.

For the clayey silt the results show less extreme inter-aggregate fabric changes for all pathways. From observation of FT and FR conditions after 10 D/W cycles, there is an apparent reduction in the size and prevalence of inter-aggregate pores. With maximum pore diameter slightly reducing to <40µm. By comparison, after 10 D/W cycles for CT and CR conditions the fabric remain similar to compacted conditions. This result again confirm that changes in the macroscopic behaviour of the clayey silt are a result of changes at the micro pore scale which cannot be imaged at the resolution tested.

In contrast, the silty clay exhibited significant cracking for all pathways. Strikingly, the size and diameter of cracking in all cases is greater than the cracking shown following drying to residual conditions. Suggesting that cracks develop further during subsequent drying-wetting cycles. Furthermore, nuanced differences in the configuration of cracking can be distinguished for the different drying boundary conditions. For instance, when comparing FT and CR conditions, CR conditions appear to contain a higher frequency of larger and branching micro-cracks, with the largest measuring 5.52mm in length and 78μm in diameter (Figure 4-32i-l). In comparison, in the micrograph representing FT conditions cracking appears less branching and slightly smaller, approximately measuring 4mm in length and 45μm in diameter (Figure 4-29i-l). Similarly, when comparing the micrographs representing the CT and CR pathways it's clear that the width and frequency of cracking for CR conditions is much greater than CT conditions. This somewhat can also be observed when comparing FT and FR conditions. These observations are in agreement with small strain stiffness shear modulus measurements (see for instance Figure 4-18). This confirms that the formation of cracking for very high plasticity clays is influenced by drying-wetting boundaries. This is intuitive considering that increased drying results in greater shrinkage to occur. It also suggests that certain cracks persist and develop during drying-wetting, while full saturation results in a certain degree of self-healing of certain cracking which can be visually observed in Figure 4-14.

The results also demonstrate the impact of plasticity, showing that very high plasticity soils experience larger changes in soil fabric for all amplitudes of drying wetting due to formation of micro and macro cracks. While, for lower plasticity materials fabric changes during drying-wetting may occur at a significantly smaller scale (micro pore scale), albeit still impacting the macro scale behaviour.

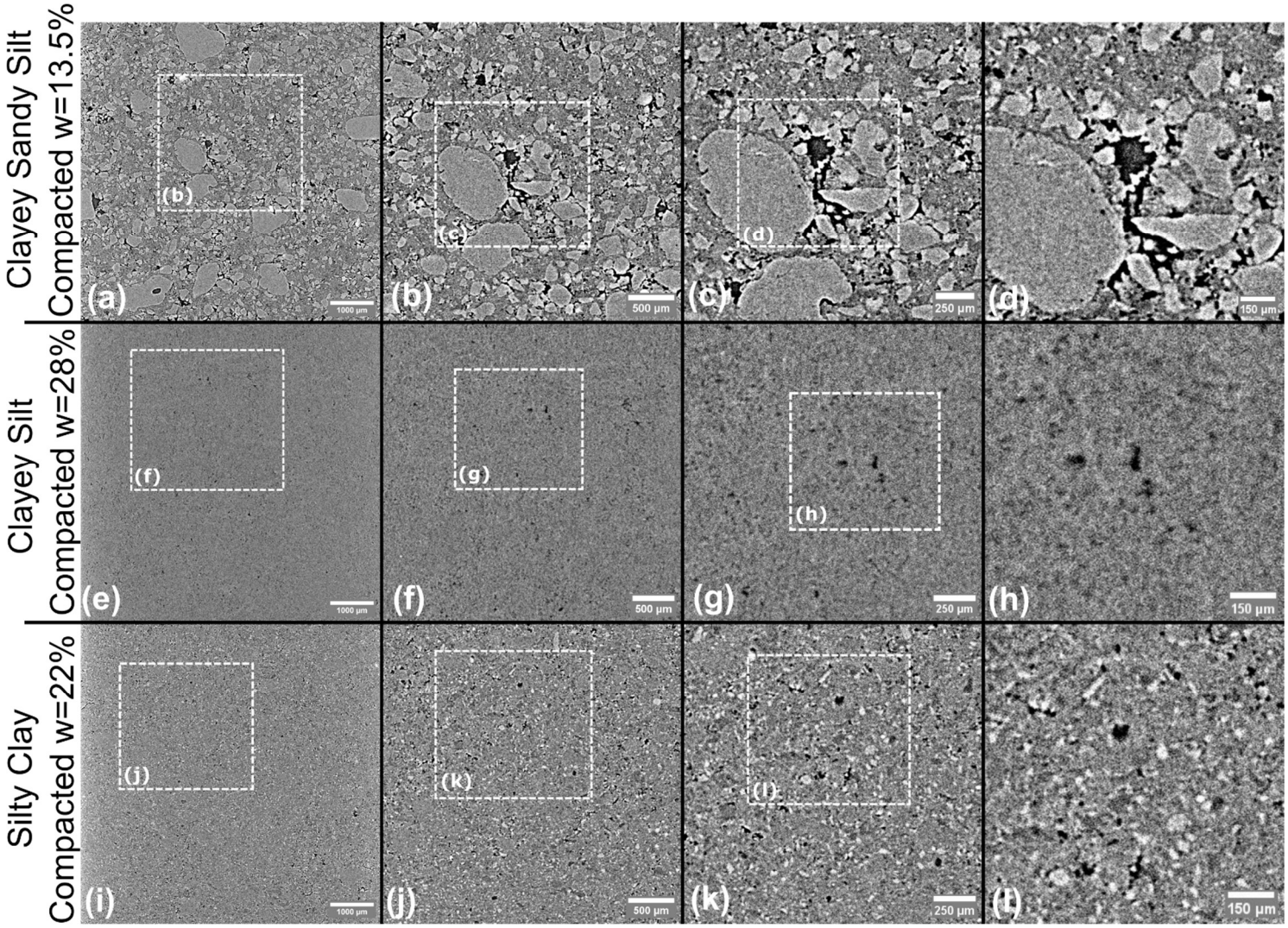


Figure 4-27 Micro X-ray CT micrographs (com_w_{OMC}) of the compacted clayey sandy silt, clayey silt and silty clay with marked regions indicating positions of zoomed images.

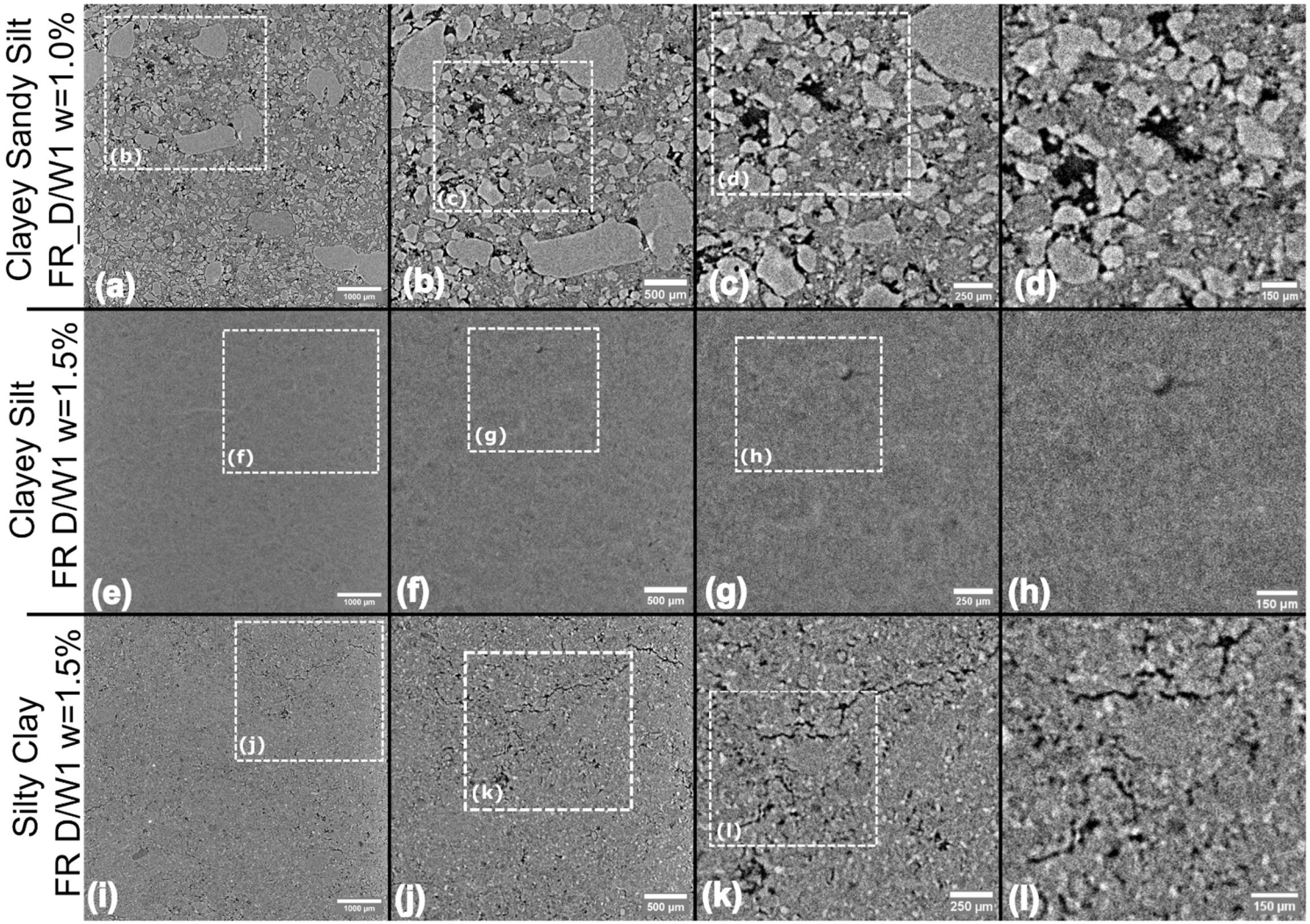


Figure 4-28 Micro X-ray CT micrographs of clayey sandy silt, clayey silt and silty clay at residual conditions (initial_w_R), with marked regions indicating positions of zoomed images.

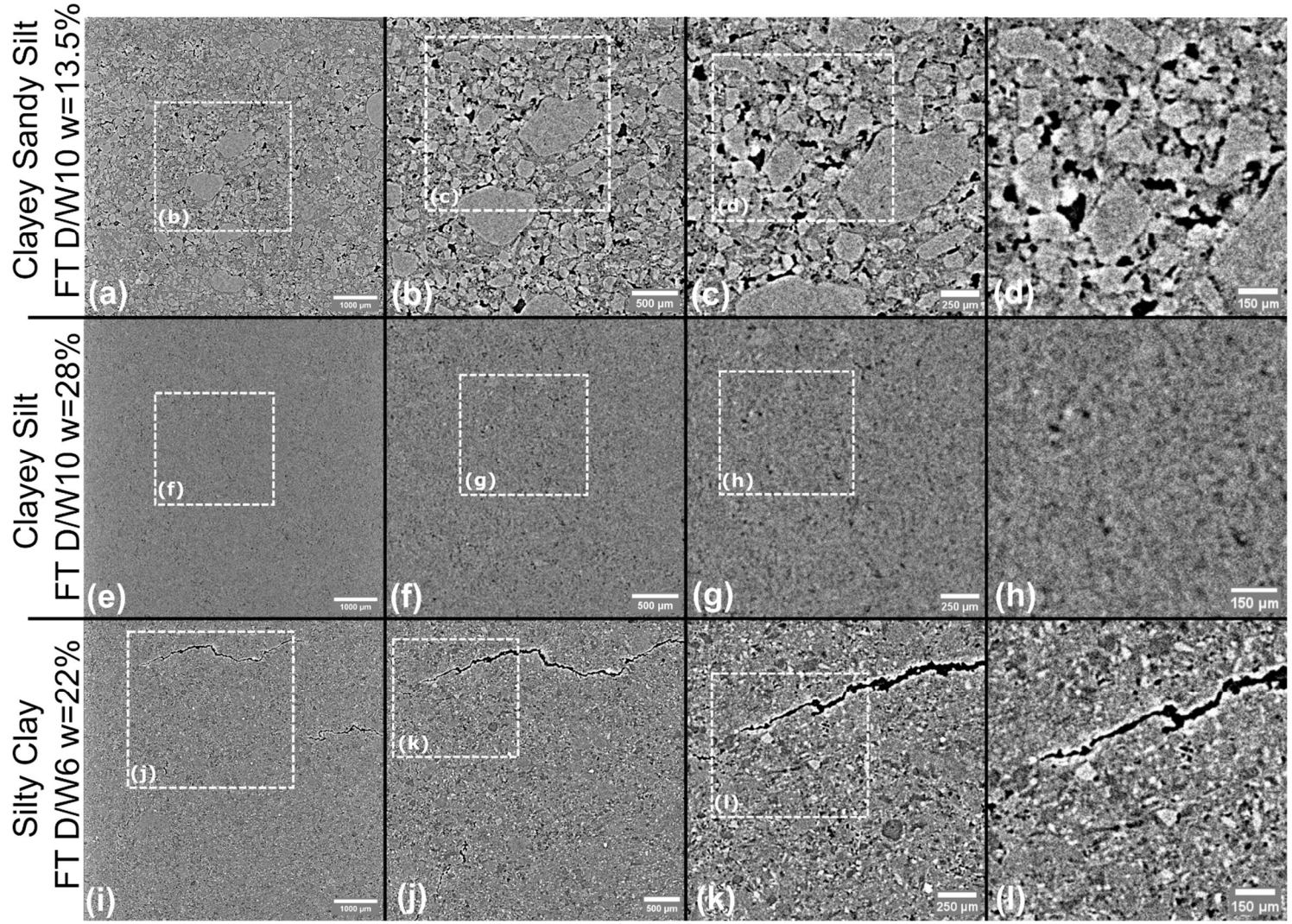


Figure 4-29 Micro X-ray CT micrographs of clayey sandy silt, clayey silt and silty clay after FT (FT_10D/W_w_{OMC}_d) drying-wetting, with marked regions indicating positions of zoomed images.

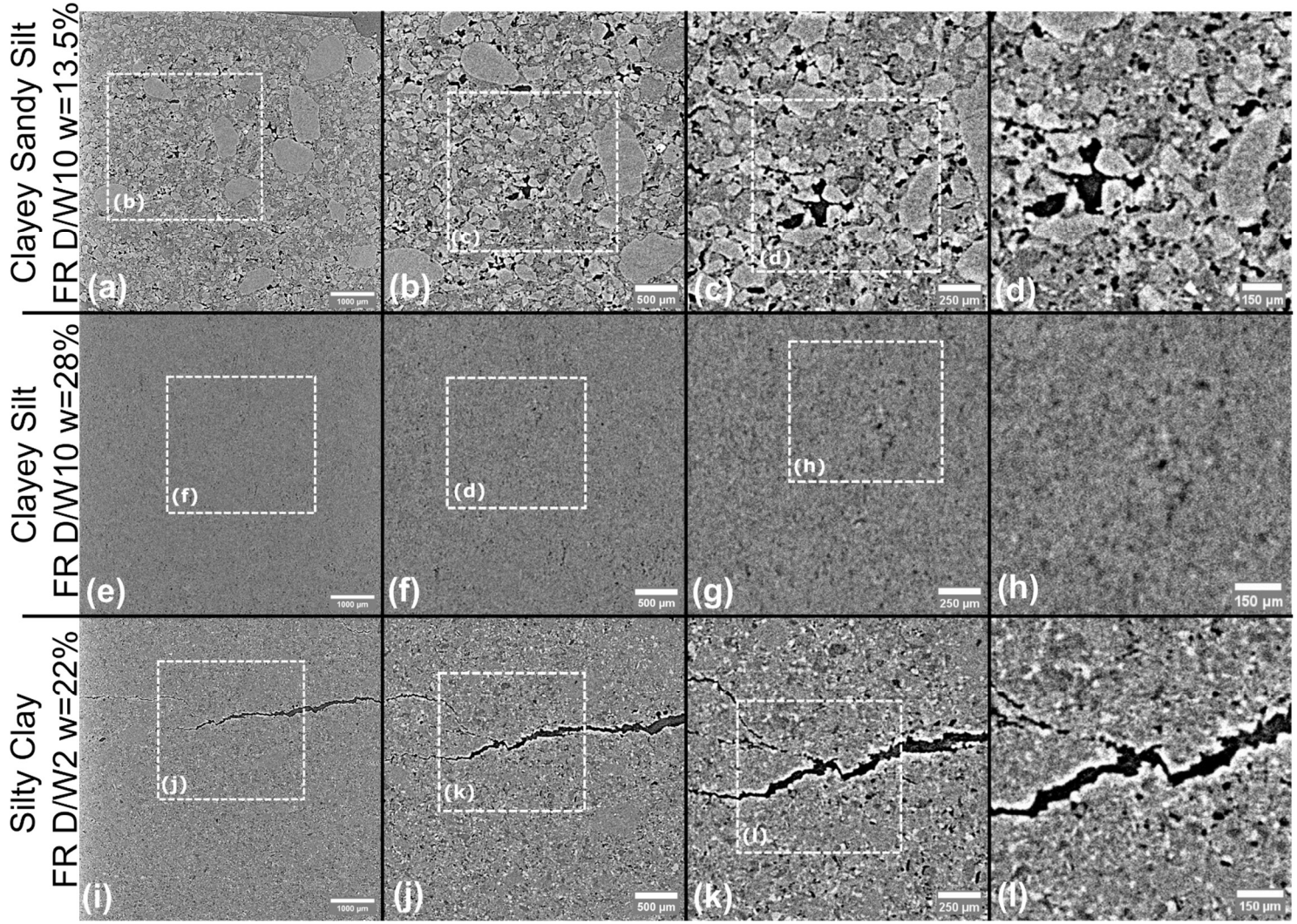


Figure 4-30 Micro X-ray CT micrographs of clayey sandy silt, clayey silt and silty clay after FR (FR_10D/W_w_{OMC}_d) drying-wetting, with marked regions indicating positions of zoomed images.

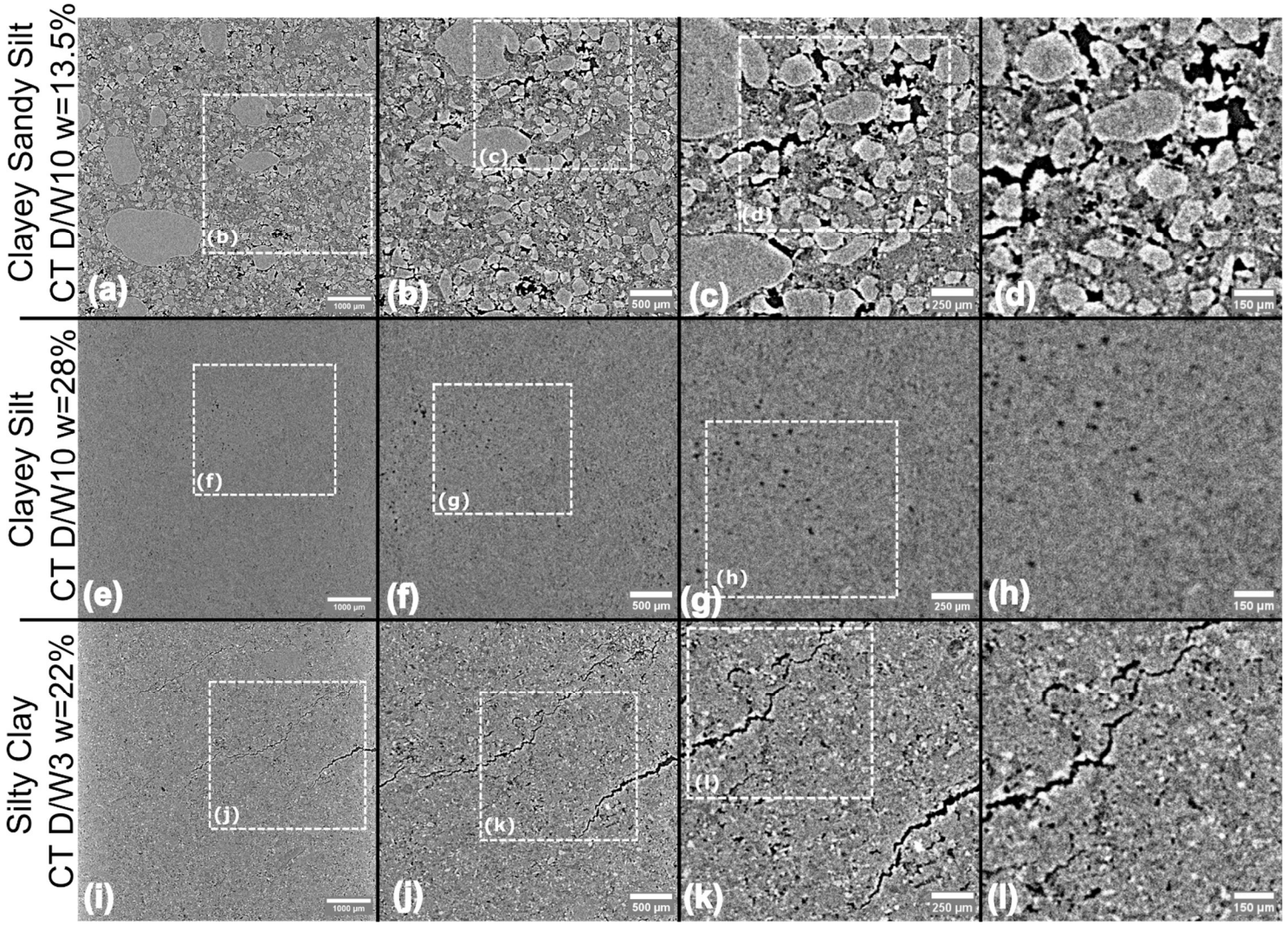


Figure 4-31 Micro X-ray CT micrographs of clayey sandy silt, clayey silt and silty clay after CT (CT_10D/W_w_{OMC}_d) drying-wetting, with marked regions indicating positions of zoomed images.

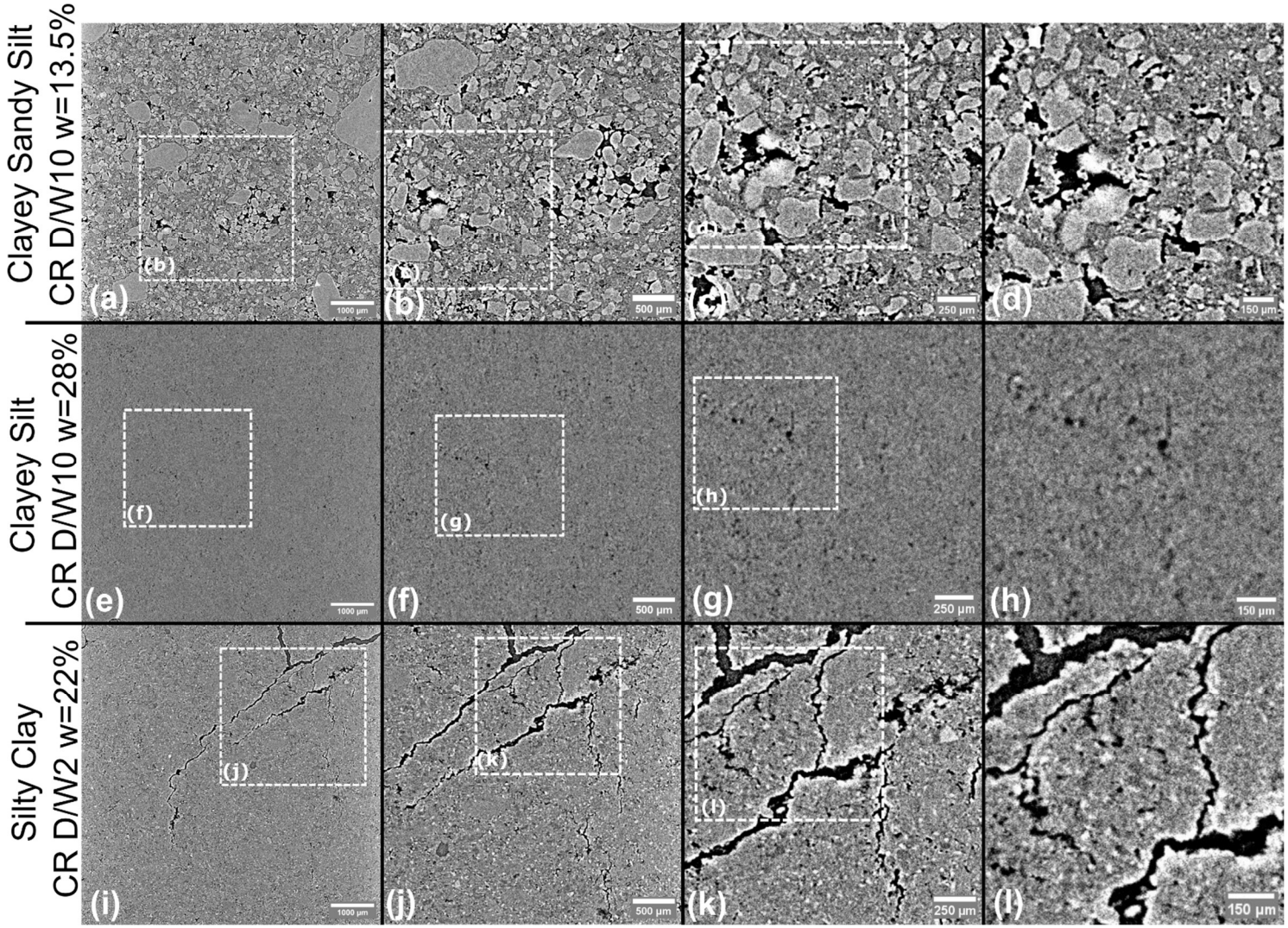


Figure 4-32 Micro X-ray CT micrographs of clayey sandy silt, clayey silt and silty clay after CR (CR_10D/W_w_{OMC}_d) drying-wetting, with marked regions indicating positions of zoomed images.

4.6 Summary

In this chapter, the small strain stiffness (G_{max}) and void ratio (e) results (monitored during the application of 10 drying-wetting cycles for FT/FR/CT/CR pathways) for the clayey silt, clayey sandy silt and silty clay were presented. Upon drying, the rate of small strain stiffness change for an increment of water content for the clayey silt reduced at residual water content (w_R). However, the silty clay and clayey sandy silt experienced an increase in the rate of small strain stiffness change at residual water contents respectively.

When G_{max} normalised against compacted conditions was plotted for drying-wetting cycles, the very high plasticity silty clay displayed the largest decrease in small strain stiffness for all hydraulic pathways. This is not surprising considering the large volume change during drying-wetting and the presence of macroscopic cracking, resulting in the eventual loss of specimen integrity between 2 and 6 D/W cycles. In comparison, the clayey sandy silt showed the smallest deviation in small strain stiffness from the compacted state, while also the smallest changes in volume for all hydraulic pathways. The clayey silt exhibited a novel increase in volume upon drying to residual conditions, previously attributed to reduction in the EES.

When the small strain stiffness data was normalised using the compacted state and presented against the number of drying-wetting cycles, it showed that FT/FR conditions resulted in an increase in small strain stiffness compared to their CT/CR counterparts. Furthermore, CR conditions exhibited the greatest reduction in small strain stiffness for each soil compared to other hydraulic pathways. While FT conditions resulted in an increase in small strain stiffness for the silty clay and clayey sandy silt. When data was presented using normalised variation in small strain stiffness (i.e. difference in shear modulus between FT-CT, FT-CR and FT-FR, CT-CR) the compacted clays (clayey silt and silty clay) were observed to have the greatest variation in small strain stiffness.

The chapter also included micro X-ray CT micrographs for the compacted soils allowing for observation of changes in inter-aggreate pores during drying-wetting cycles. The compacted pore structure of the soils showed that the clayey sandy silt has the greatest range in pore diameter compared to the clayey silt and silty clay. Upon initial drying to the residual conditions a reduction in interaggregate pores was observed for all soils, while micro-cracking was also exhibited by the silty clay. The reduction in inter-aggregate pores for the clayey silt suggests that the observed macro behaviour (i.e. increase in volume) results from change in the micropore structure. Following the application of drying-wetting cycles changes in pore structure were generally in agreement with observations made for small strain stiffness testing. Indeed, FT/FR pathways generally experienced a decrease in the prevalence of inter-aggregate pores, while CT conditions

generally maintained the original pore structure for the clayey silt and clayey sandy silt. Finally, significant cracking was also observed for the silty clay. The frequency and prevalence of cracks generally agreed with the small strain stiffness testing. Following drying wetting in CR conditions the silty clay experienced the largest reduction in small strain stiffness in 2 D/W cycles while also exhibiting the greatest frequency and largest branching cracking compared to other conditions. The results also highlight the different ranges that pore structure changes occur, suggesting that higher plasticity materials experience inter-aggregate pore structure changes while the lower plasticity materials experience changes predominantly in micropore scale.

Chapter 5
Saturated Drained Triaxial Testing

5.1 General

In this chapter the saturated isotopically consolidated drained tests (CID) for the three selected soils are presented. Following the application of drying-wetting cycles and measurement of small strain stiffness, specimens were sheared in saturated conditions. This therefore allows for stress-strain behaviour of specimens to be evaluated for identical drying-wetting conditions to small strain stiffness testing i.e. FT/FR/CT/CR drying-wetting amplitudes. For each drying-wetting amplitude shearing was conducted at compacted conditions, 3 D/W, 6 D/W and 10 D/W cycles. Note, that due to cracking and loss of integrity of the silty clay between 2-6 drying-wetting cycles, shearing was conducted at the last D/W cycle possible. The chapter initially examines the stress-strain behaviour in terms of peak stress (q_{peak}) and initial tangent modulus (E_i) following drying-wetting. During shearing, volume change was also monitored by the back pressure line. Therefore, change in volume behaviour during drying-wetting, relative to the compacted condition, is also examined in terms of the dilatancy ratio (d_g).

5.2 Triaxial shearing in drained conditions

To investigate the role of hydraulic history on the stress-strain behaviour of the selected compacted soils for different drying-wetting amplitudes, saturated drained shearing was performed. Saturated conditions were considered so that hydraulic history associated the different drying-wetting boundaries and number of cycles could be compared in a systematic manner for all soils. Their initial compacted conditions are thus presented in Table 4-1, Table 4-2 and Table 4-3. Specimens were initially saturated and consolidated to 50 kPa effective confining pressure, equivalent to approximately 2m depth for a typical embankment. This corresponds to a conservative estimate for the greatest depth where pronounced water content changes occur (Glendinning et al., 2014). Table 5-1,

Table 5-2 and Table 5-3 shows the summary of the isotopically consolidated drained tests (CID). This includes the initial void ratio (e), peak deviator stress (q_{peak}) and the peak mean effective stress (p'_{peak}). Furthermore, the stress-strain (q-ε_1) and volumetric strain (ε_{vs}) response obtained in the series of the drained triaxial tests are plotted in Figure 5-1, Figure 5-2 and Figure 5-3.

Volumetric strains during shearing were monitored for all specimens. The volumetric strain is defined as negative in compression. Shearing was conducted to a maximum

axial strain of 25%, with the aim of reaching the critical state. However, its apparent that upon application of drying-wetting cycles the strain required to achieve critical state increased. Initially, compacted specimens experienced compression followed by dilation. Notably the clayey silt and silty clay showed small degrees of dilation at higher strains. However, at lower strains following compression, the clayey silt showed the greatest degree of dilation.

Generally all specimens tested displayed predominantly strain softening behaviour although some differences were observed for different soils subjected to different hydraulic history, i.e. drying-wetting boundaries and number of cycles. For instance, Figure 5-1a-d shows the stress-strain response of the clayey silt. It can be observed that as the number of drying-wetting cycles increases, higher peak shear stresses are achieved which suggests specimens are undergoing hydraulic ageing which is in agreement with the observations made at small strain (e.g. Figure 4-5). However, difference are more evident for the FT and FR conditions, while small changes were observed for the CT and CR pathways. Interestingly, small strain stiffness decreases with the number of cycles in CT and CR conditions, but the behaviour in Figure 5-1c and Figure 5-1d seems to indicate that when these specimens were brought to saturated conditions microstructural changes may have taken place and therefore performance approaches that of compacted saturated specimens (i.e. FR and FT). The volumetric strains results shown in Figure 5-1e-h, exhibit a substantial increase in dilation with the number of cycles for FT and FR pathways compared to CT and CR. These results are in agreement with stress-strain response and indicate specimens are undergoing hydraulic ageing but the degree of ageing is related to the hydraulic history more specifically the drying-wetting boundaries. Similar observations were also obtained for the clayey sandy silt specimens, albeit the strain softening and dilation are less pronounced. It should be noted that silty clay specimens experienced severe cracking prior to shearing, but were nonetheless placed in the triaxial and saturated. Interestingly, for the silty clay the conditions displaying greater performance are FR and CR. While this is contradictory to the small strain stiffness results, the changes in microstructure derived from specimens upon full saturation may explain why these conditions are exhibiting better performance. This illustrates the importance of evaluating performance within the ranges of water content likely experienced by the soil during its service life.

Table 5-1 Summary of clayey silt peak state for drained triaxial tests

	D/W cycle	Specimen ID	Void Ratio, *e*	p'_{peak}	q_{peak}	$(q/p')_{peak}$	Axial strain failure (%)
Compacted			0.929	87	108	1.24	8.3
FT	3	K-FT3	0.932	92	119	1.29	7.5
	6	K-FT6	0.927	95	130	1.37	6.9
	10	K-FT10	0.926	98	135	1.38	6.9
FR	3	K-FR3	0.952	94	121	1.29	6.7
	6	K-FR6	0.948	97	131	1.35	6.3
	10	K-FR10	0.946	95	129	1.36	6.6
CT	3	K-CT3	0.939	90	112	1.24	7.5
	6	K-CT6	0.943	91	116	1.27	7.7
	10	K-CT10	0.944	93	118	127	8.0
CR	3	K-CR3	0.955	94	123	1.31	6.7
	6	K-CR6	0.958	92	120	1.30	7.2
	10	K-CR10	0.960	88	117	1.31	7.4

Table 5-2 Summary of clayey sandy silt peak state for drained triaxial tests

	D/W cycle	Specimen ID	Void Ratio, *e*	p'_{peak}	q_{peak}	$(q/p')_{peak}$	Axial strain failure (%)
Compacted			0.432	78	99	1.27	6.9
FT	3	CSS-FT3	0.424	87	109	1.25	5.5
	6	CSS-FT6	0.420	92	126	1.37	5.2
	10	CSS-FT10	0.418	93	130	1.40	4.6
FR	3	CSS-FR3	0.429	99	140	1.41	2.9
	6	CSS-FR6	0.426	99	141	1.42	4.5
	10	CSS-FR10	0.426	96	138	1.43	5.4
CT	3	CSS-CT3	0.439	88	110	1.25	6.1
	6	CSS-CT6	0.441	91	120	1.32	3.7
	10	CSS-CT10	0.443	94	128	1.36	3.6

Table 5-2 continued

	D/W cycle	Specimen ID	Void Ratio, *e*	p'_{peak}	q_{peak}	$(q/p')_{peak}$	Axial strain failure (%)
CR	3	CSS-CR3	0.442	92	123	1.34	3.5
	6	CSS-CR6	0.447	89	121	1.36	4.0
	10	CSS-CR10	0.447	92	125	1.36	4.8

Table 5-3 Summary of silty clay peak state for drained triaxial tests

	D/W cycle	Specimen ID	Void Ratio, *e*	p'_{peak}	q_{peak}	$(q/p')_{peak}$	Axial strain failure (%)
Compacted			0.726	69	73	1.06	11.3
FT	6	SC-FT6	0.713	62	81	1.31	11.5
FR	3	SC-FR3	0.732	74	111	1.50	6.7
CT	3	SC-CT3	0.735	60	76	1.26	10.7
CR	2	SC-CR2	0.746	75	101	1.35	6.4

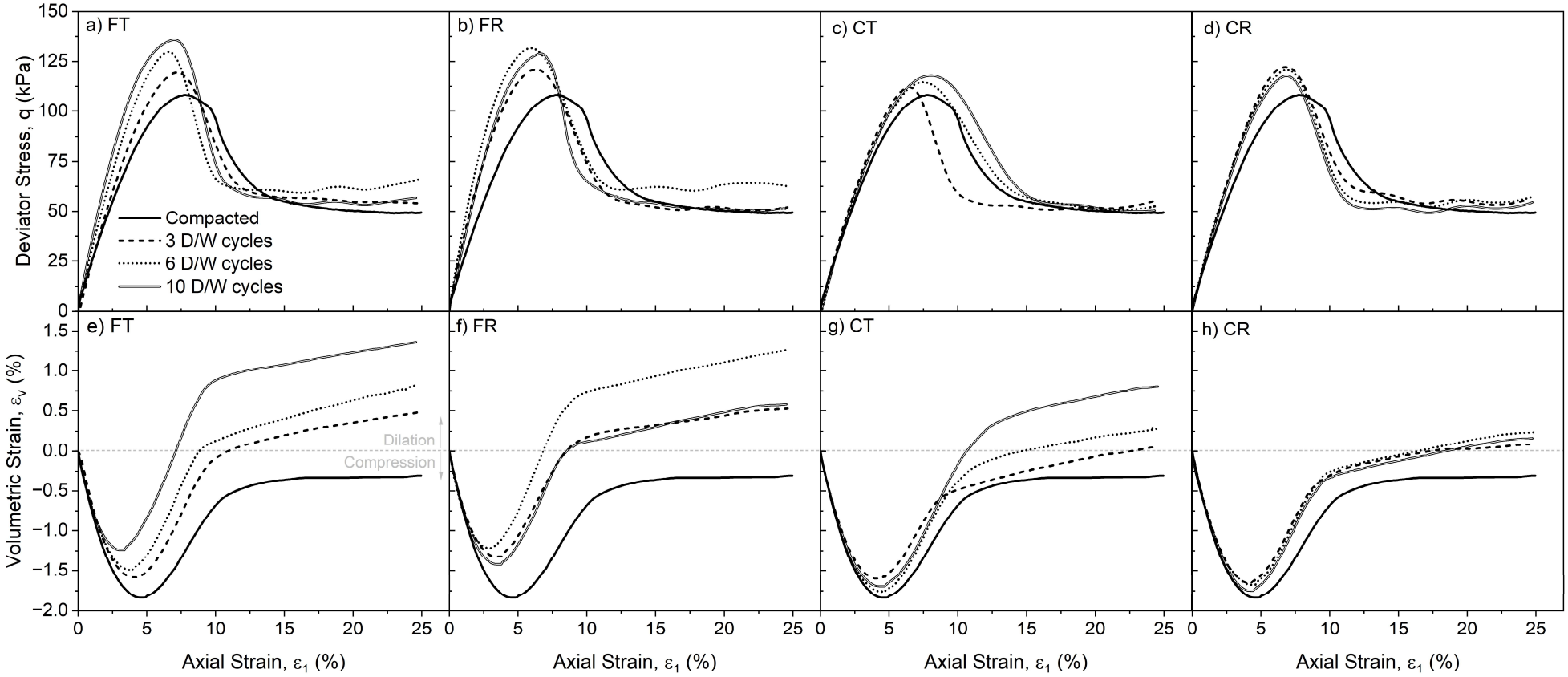


Figure 5-1 Clayey silt stress-strain relationship (a-d) and corresponding volumetric strains (e-f) for compacted, 3rd, 6th and 10th drying-wetting cycle at 50 kPa confining stress.

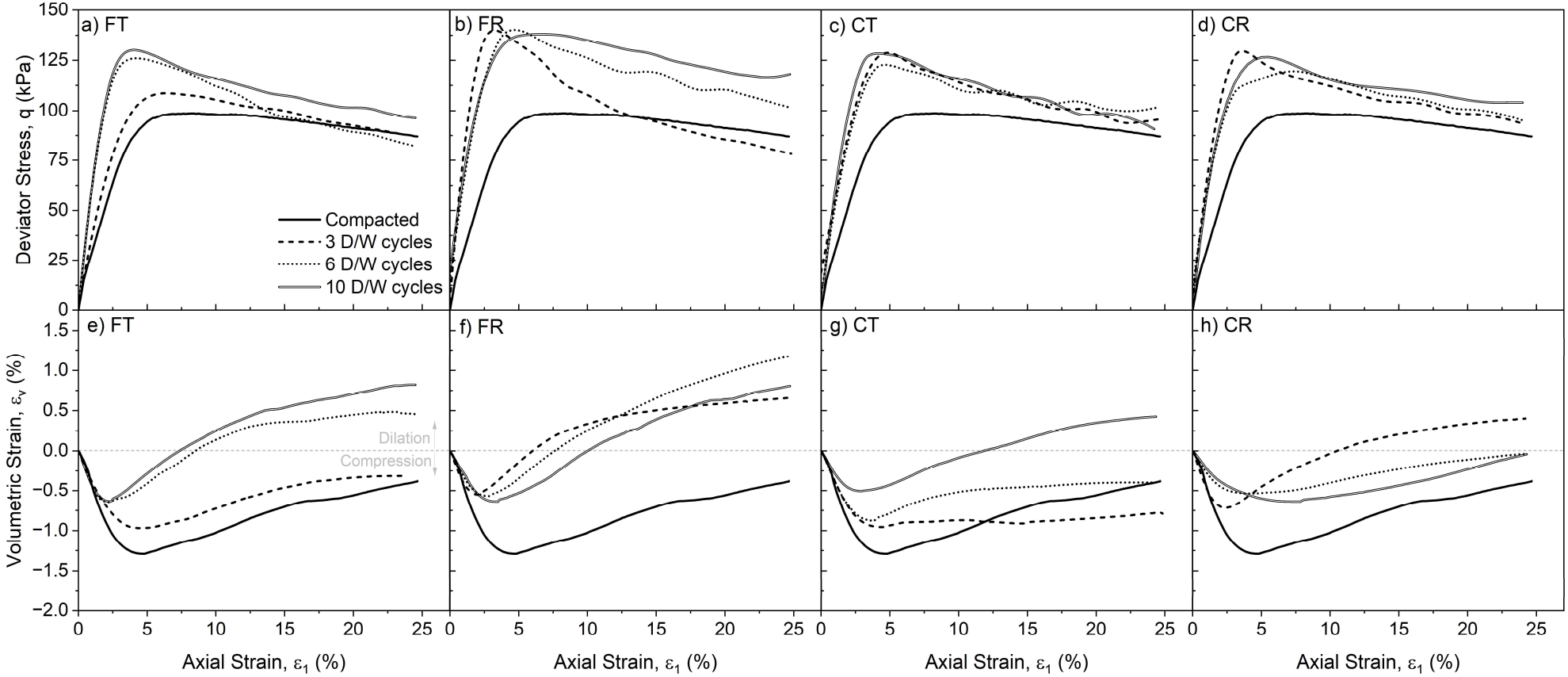


Figure 5-2 Clayey sandy silt stress-strain relationship (a-d) and corresponding volumetric strain (e-h) for compacted, 3rd, 6th and 10th drying-wetting cycle at 50 kPa confining stress.

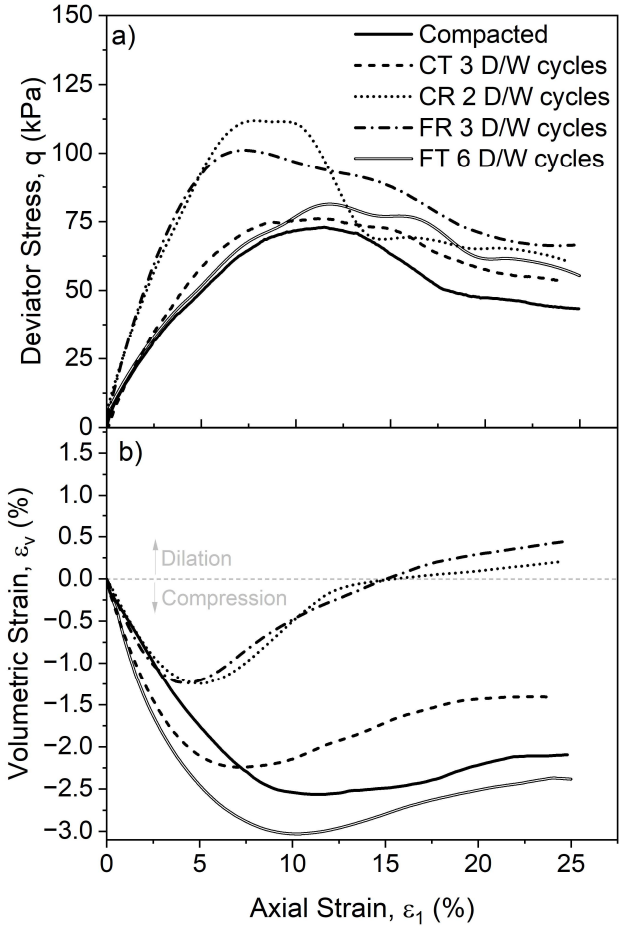


Figure 5-3 Silty clay stress-strain relationship (a) and corresponding volumetric strains (b) for drying-wetting cycle at 50 kPa confining stress.

5.2.1 Stress-strain relationship

The peak strength (q_{peak}) and initial tangent modulus (E_i) are presented against the number of drying-wetting cycles in Figure 5-4. In general, the initial compacted specimens show more ductile behaviour when compared to the specimens that underwent several drying-wetting cycles prior to shearing. Generally, following the application of drying-wetting cycles all soils show a progressive increase in the stiffness (E_i) and brittle response characterised by an increase in peak strength (q_{peak}) at lower axial strains followed by strain softening. Its therefore likely that is a result of changes in pore structure following drying wetting cycles. Importantly, in the field this behaviour increases the vulnerability of embankments to the progressive failures (Rojas et al., 2009).

For the clayey silt both FR and FT pathways result in the greatest increase in peak deviator stress and initial tangent modulus, while CT and CR pathways exhibited lesser changes from initial compacted conditions. Interestingly, after 6 drying-wetting cycles smaller changes in peak strength and initial tangent modulus occurred. Similar observation are also applicable to the clayey sandy silt, however, the FR pathway

showed the greatest overall change in in both peak strength and initial tangent modulus. Despite loss of integrity of the silty clay, the specimens also showed an increase in initial tangent modulus and peak shear strength during shearing. Furthermore, at the end of shearing, it could be observed the specimens were intact. This suggests that 'self healing' of the specimens took place. In particular, its notable that despite cracking and loss of integrity of the specimens following drying-wetting testing, during shearing specimens behaviour exceeded that of compaction conditions. The results also show a significant increase in initial tangent modulus and peak stress for both FR/CR pathways compared to FT/CT pathways.

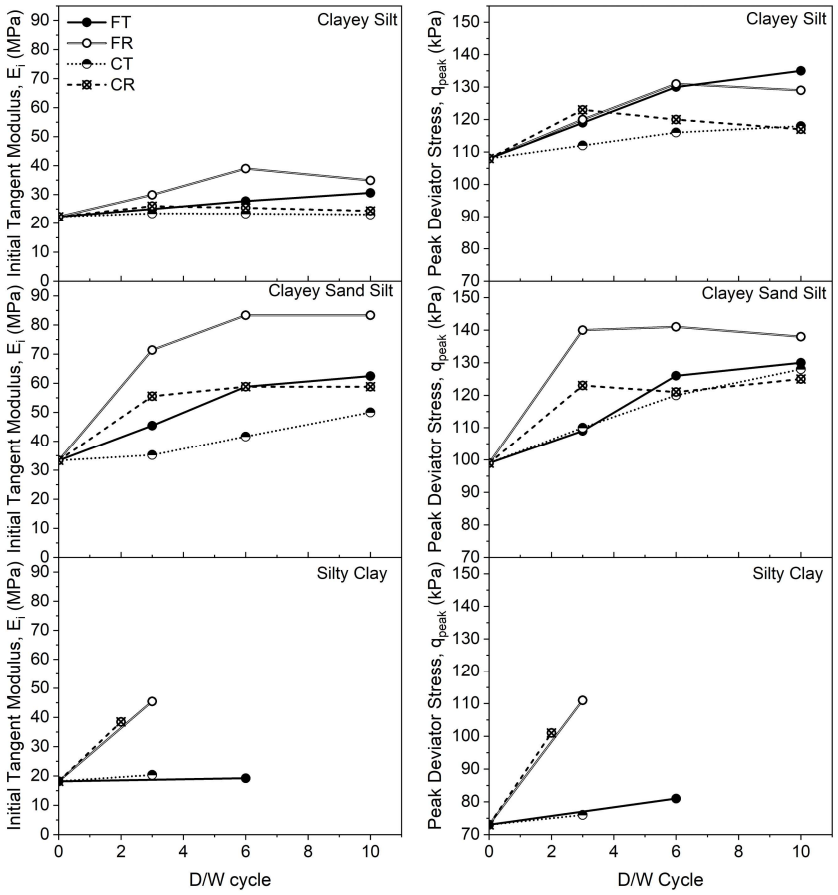


Figure 5-4 Clayey sandy silt and clayey silt initial tangent modulus and peak deviator stress during drying wetting for different drying-wetting amplitudes.

As expected, the results therefore suggest that behaviour of compacted material following drying-wetting is dependent on the hydraulic history, strain range and saturation. Notably it appears that the impact of drying-wetting is maintained when specimens are fully saturated and suction influence minimised. The recorded behaviour is intuitive for FT and FR pathways of the clayey sandy silt and clayey silt, due to the formation of irrecoverable shrinkage during drying-wetting. However, CT and CR pathways which did not experience shrinkage also appear to exhibit equivalent, albeit lesser, changes in behaviour i.e. an increase in peak deviator stress and tangent

modulus, despite loss of small strain stiffness. This difference can be attributed to saturation of the specimen. For unsaturated small strain stiffness it's likely that the changes in pore structure during drying (see Section 4.5.3) cause a reduction in small strain stiffness due to corresponding reduction of suction. However, upon reduction of suction due to saturation, this is mitigated and the behaviour is no longer equivalent to unsaturated conditions. Furthermore the significant difference in strain range is also expected to impact behaviour.

Similar increases in stiffness in triaxial conditions are often attributed to an increase in the over consolidation ratio (OCR). Likewise for unsaturated conditions, during drying the increase in suction increases unsaturated effective stress (Bishop, 1959), as follows:

$$\sigma' = \sigma - u_a + \chi(u_a - u_w) \quad (5.1)$$

Indeed, for normal geological processes an increase in net stress occurs (and thus maximum effective stress and generally OCR) due to an increase in vertical stress and dissipation of positive pore water pressure. However during drying-wetting the matric suction component (u_a-u_w) in Eq. (5.1) contributes to an increase in effective stress. This behaviour has previously been captured by Ng and Xu (2012) by using the Current Suction Ratio (CSR), as follows:

$$CSR = \Psi_{max}/\Psi_{current} \quad (5.2)$$

Where Ψ_{max} is the maximum suction experienced by the soil and is divided by $\Psi_{current}$ the current suction. It was shown that for small strain conditions the magnitude of suction during drying-wetting, thus suction history, significantly impacted the behaviour of compacted soils. It was observed by Ng and Xu (2012) and Heitor et al. (2015) that for a given suction, small strain shear modulus was greater for specimens with a higher CSR.

As all soils in this study experience the same drying boundaries, comparative the SWRC, this may explain similarities in the behaviour between FT/FR and CT/CR despite difference amplitude of drying-wetting i.e. for FT/CT or FR/CR conditions following saturation the CSR is the same. For instance, following compaction at 1400 kPa static stress, filter paper measurements show the clayey silt experienced 4500 kPa matric suction at the FT/CT drying boundary and 32,000 kPa at the FR/CR boundary. Therefore, both boundaries significantly exceed the previous maximum stress (Ψ_{max}) for the soil at the compacted condition. As a result CSR increases for both conditions, but CSR is greater for specimens brought to residual conditions (FR/CR).

Silty clay results further suggest that the drying boundary contributes to an increase in initial tangent modulus and peak stress in saturated conditions. The silty clay experienced a large difference in Ψ_{max} of 400,000 kPa between FT/CT and FR/CR

pathway. This is significantly greater than the 27,500 kPa difference for the clayey silt and 24,000 kPa difference for the clayey sandy silt. As a consequence the difference in CSR in saturated conditions is also the greatest for the silty clay. Upon review of Figure 5-4 it can be observed that the silty clay also experienced the largest difference in initial tangent modulus and peak stress for FT/CT and FR/CR conditions. The results thus reveal the significance of plasticity on saturated stress-strain behaviour. Suggesting that the behaviour of very high plasticity soils, which experience increased suctions, are dominated by the drying boundary. While the wetting boundary appears to have lesser impact on the behaviour.

5.2.2 Shear-induced volume changes

The stress paths in the *e-p'* space are presented in Figure 5-5, Figure 5-6 and Figure 5-7. The results generally show that with larger number of drying-wetting cycles specimens approach critical state at larger void ratios and display predominantly dilation behaviour. Its noted that further testing to greater axial strains, reaching true critical state conditions, while applying several confining stresses may allow for the identification of a critical state line for different drying-wetting cycles and conditions. In this study that was not possible because the specimens tested were those used to monitor the small strain stiffness behaviour during drying-wetting cycles.

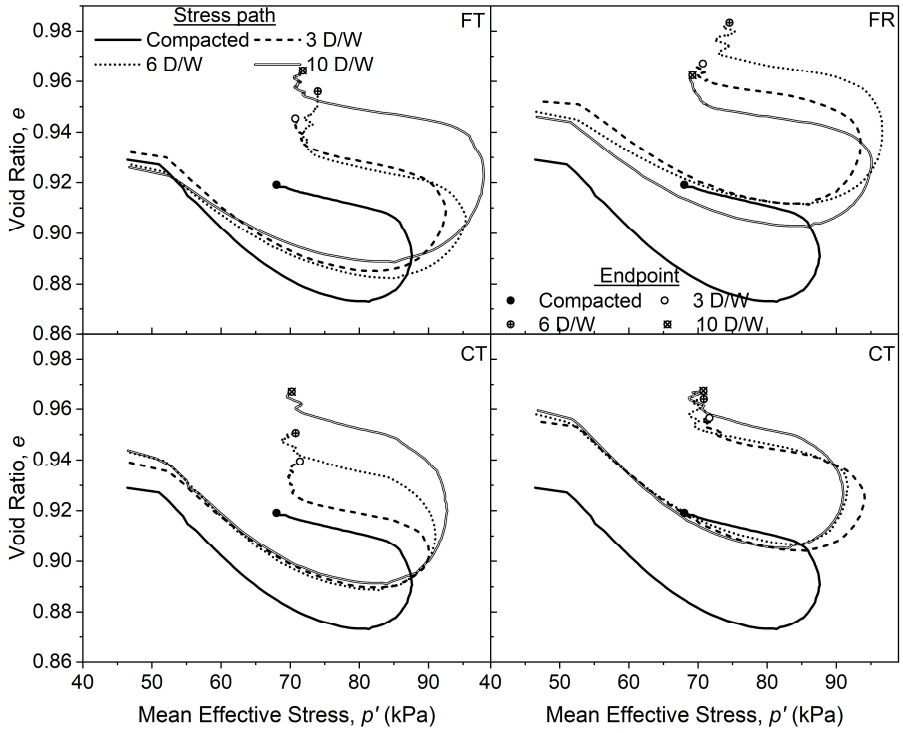


Figure 5-5 Clayey silt stress path in *e-p'* space.

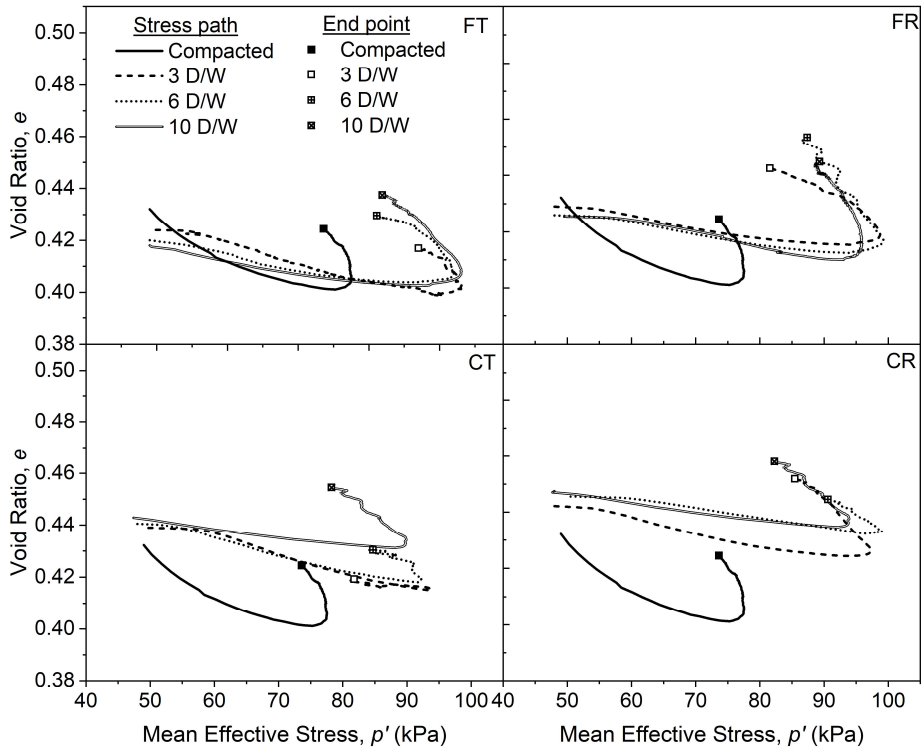


Figure 5-6 Clayey sandy silt stress path in *e-p'* space.

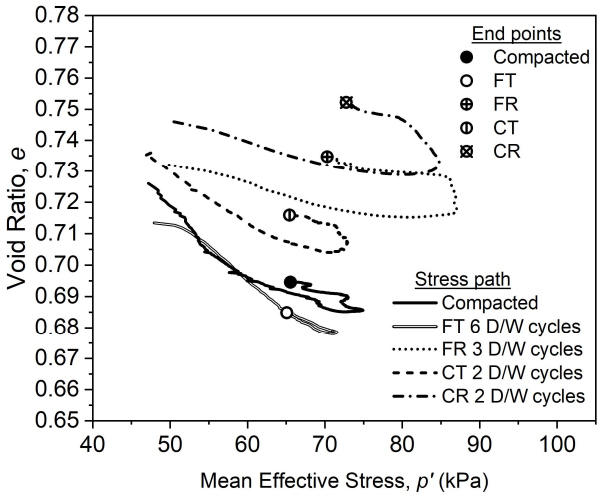


Figure 5-7 Silty clay stress path in *e-p'* space.

In this study, the dilatancy ratio (d_g), defined in Eq. (5.3), is used to examine the effect of drying-wetting cycles on saturated stress-dilatancy response

$$d_g = \delta\varepsilon_{vs}/\delta\varepsilon_1 \tag{5.3}$$

The stress-dilatancy response of the clayey silt, clayey sandy silt and silty clay are presented in Figure 5-8, Figure 5-9 and Figure 5-10, respectively.

The compacted clayey silt specimen demonstrates an initial consistent decrease in the degree of contraction and development of dilation until 1.23 *q/p'*, achieving a maximum dilation ratio of 0.29 d_g. This approximately corresponds to the attainment of peak stress,

whereafter dilation decreases towards the critical state. Subsequent specimens show similar behaviour, however, FT, FR and CR conditions show a small variation in compression for a given stress ratio. Furthermore, FT and FR conditions show a clear progressive increase in the maximum dilation ratio following the application of drying-wetting cycles. For instance, FT conditions show an increase in the maximum dilation ratio to d_g=0.37 at *q/p'*=1.28 after 3 D/W, d_g=0.42 at *q/p'*=1.35 after 6 D/W and d_g=0.45 at *q/p'*=1.38 after 10 D/W cycles. Interestingly, CT and CR conditions have smaller differences in dilatancy increases during drying-wetting. This may possibly be attributed to the wetting boundary and the resultant change in structure due to saturation (exhibited in Figure 4-29 and Figure 4-30) during drying-wetting for FT/FR conditions.

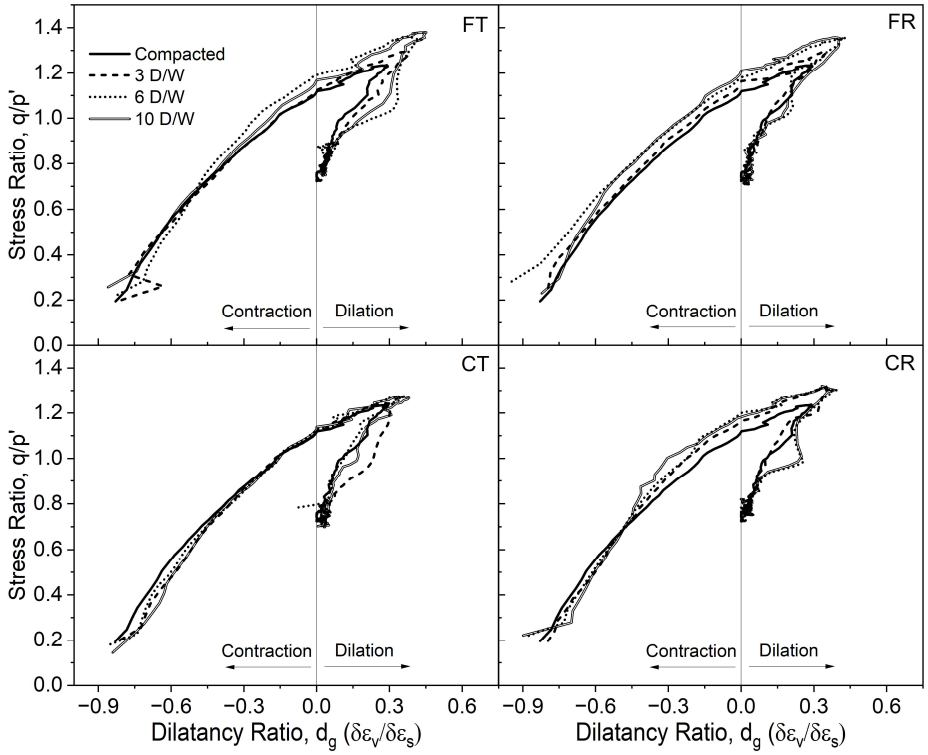


Figure 5-8 Influence of drying-wetting cycles on the stress-dilatancy response of clayey silt for different drying-wetting amplitudes.

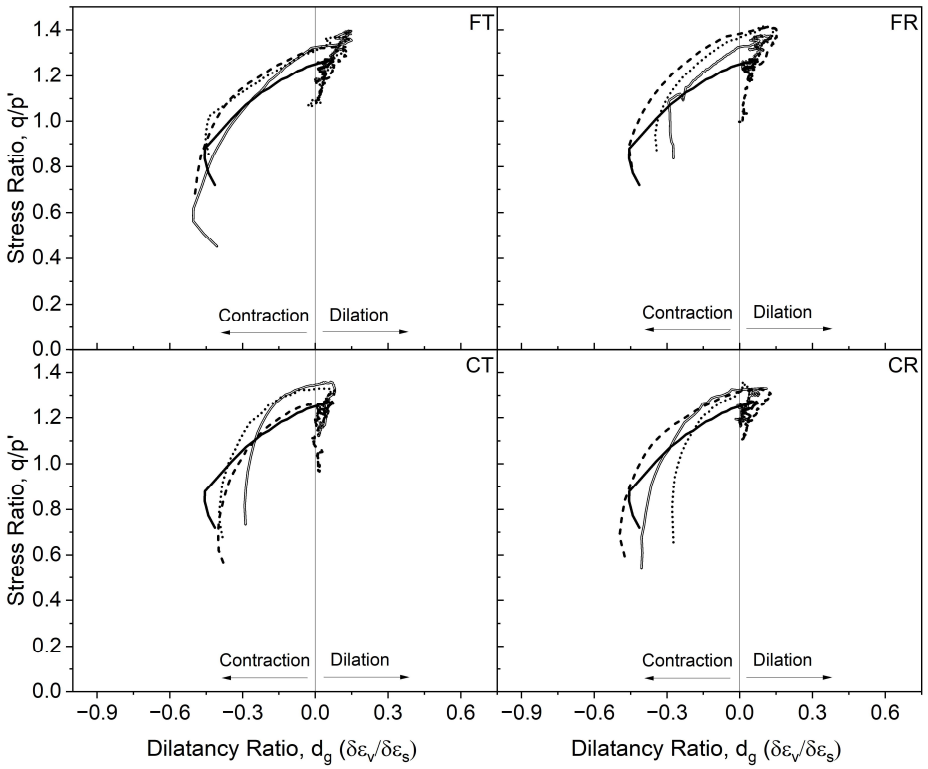


Figure 5-9 Influence of drying-wetting cycles on the stress-dilatancy response of clayey sandy silt for different drying-wetting amplitudes.

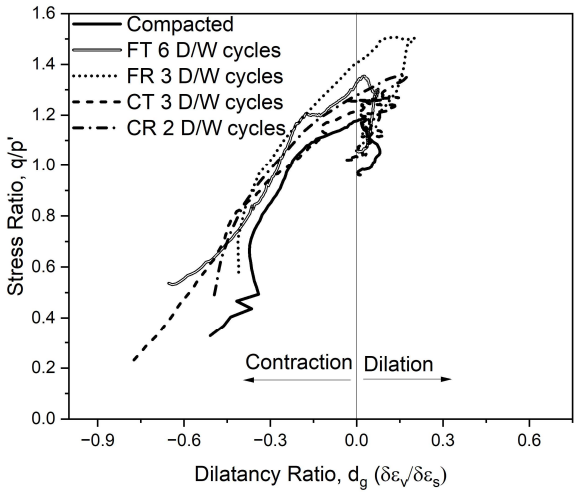


Figure 5-10 Influence of drying-wetting cycles on the stress-dilatancy response of silty clay for different drying-wetting amplitudes.

The clayey sandy silt exhibited similar behaviour to the clayey silt with an initial, but smaller, decrease in contraction followed by a small amount of dilation. For this material, the compacted specimens experienced maximum dilatancy of 0.07 d_g at 1.27 *q/p'*. However, following drying-wetting specimens showed initially smaller degrees of contraction and a steeper relationship between *q/p'* and d_g, while also experiencing an increase in maximum dilatancy. For instance, in FR conditions the clayey sandy silt experienced an increased maximum dilatancy of 0.14 d_g. Furthermore, there is a trend of increasing dilatancy during drying-wetting for FT, CT and CR pathways.

The silty clay also showed similar trend in terms of dilatancy. Achieving an initial maximum dilatancy of 0.08 d_g at 1.05 *q/p'* in compacted conditions, which increased upon drying-wetting. Interestingly, both FR and CR showed the greatest dilatancy of 0.20 d_g and 0.17 d_g, respectively. While FT and CT pathways achieved a maximum dilatancy of 0.14 d_g. This again highlights for a higher plasticity material, the influence of the drying boundary in saturated drained triaxial conditions.

This volume change response is not surprising when considering the change in initial tangent modulus of the materials following drying-wetting. However, the results indicate drying-wetting has a significant impact on the dilative behaviour of compacted soils during shearing. This is intuitive as dilatancy strongly relates to the pore structure of clay soils. For instance, Gao et al. (2020) showed that drained shearing of over consolidated kaolin resulted in tortuosity of the particle arrangements and increase in dilatancy. Furthermore, Hattab (2011) showed that microcracks (defined as two highly parallel-oriented face-to-face particle groups) form preferential points where larger cracks are generated. Gao et al. (2020) also showed that these micro-cracks propagate to the meso and macro scales during shearing in over consolidated soils. Thus, changes in the micropore structure of specimens during drying-wetting may account for a greater degree of dilatancy. However, further investigation is required to confirm the mechanism of this behaviour for drying-wetting soils is required.

5.3 Summary

This section presented the saturated isotopically consolidated drained tests (CID). Testing was conducted with the application of identical drying-wetting history (FT/FR/CT/CR) as small strain stiffness tests. All three selected soils showed predominantly strain softening behaviour and increase in dilation following drying-wetting. The behaviour was quantified using initial tangent modulus (E_i) and peak deviator stress (q_{peak}) against drying-wetting cycles, generally showing an asymptotic increase during drying-wetting. When compared to the unsaturated small strain stiffness results the saturated stress-strain behaviour highlights that compacted soil behaviour during drying-wetting is dependent on the hydraulic history, strain range and saturation. The observed behaviour was attributed to an increase in effective stress during drying which was interpreted using the CSR. The significant difference in CSR between FT/CT and FR/CR pathways for silty clay and significant increase in E_i and q_{peak} for FR/CR behaviour was consistent with this. The dilation ratio (d_g) was also used to quantify the saturated stress-dilatancy response. In general soils showed an increase in dilation following drying-wetting. This is not surprising following the increase in E_i and q_{peak} and changes in pore structure.

Chapter 6
Engineering Application

6.1 General

Geostructures on the transport network consist of a range of soils. This is particularly pertinent to the UK due to the contrast between northern Devensian glacial tills and older sedimented clays in the south. Thus, an understanding the type of soil and their associated performance when subject to drying-wetting processes is key for formulating asset management strategies to mitigate the impact of climate change in future decades. In this chapter, the small strain shear modulus is examined considering the soil plasticity. Following this the small strain stiffness results of all selected amplitudes of drying-wetting are further analysed in the G_{max}-e space at constant water content levels, for each soil. This analysis was conducted to allow for a deeper understanding of the relationship between different drying-wetting amplitudes.

6.2 Effect of plasticity small strain stiffness during drying-wetting

In the UK Volume Change Potential (VCP) is classified using the modified plasticity index (I_p') which accounts for all particles constituting the specimen rather than just the fine fraction which is usually used in the determination of plasticity index (BS 1377-2:2022). The modified plasticity index is defined by:

$$I_p' = I_p \times \frac{\%425\mu m}{100} \tag{6.1}$$

where I_p represents the plasticity index and %425μm represents the fraction of soil particles finer than 425μm. The BRE (1993) also distinguishes different categories of the Volume Change Potential based on the modified plasticity index according to Table 6-1, as follows.

Table 6-1 Classification of soil shrink–swell VCP (BRE, 1993).

I_p'	VCP
1-20	Low
20-40	Medium
40-60	High
>60	Very high

Using this classification system the clayey sandy silt has low VCP (I_p'=18), clayey silt

medium VCP (I_p'=23) and silty clay high VCP (I_p'=55).

The influence of plasticity on the void ratio amplitude of a single drying-wetting cycle is quantitively presented in Figure 6-1. In this case, the amplitude refers to the change in volume considering the compacted water content specimen volume as a benchmark, at both the drying boundary and upon re-wetting back to the compacted water content. The role of plasticity with respect to volume is well established whereby the sorption of water causes intraparticle and interparticle swelling/shrinkage of certain clay minerals, for example smectites (montmorillonites) and vermiculites (Reeves et al., 2006). Shrinkage measured when drying to transition zone boundary (w_T) is consistent with this, as an increase in weighted plasticity index (I_p') resulted in a trend of increasing shrinkage (Figure 6-1), presenting a clear relationship between I_p' and volumetric stability. Strikingly, following the rewetting path back to the compacted water content (w_{OMC}), a similar trend is also present. In this case, an increase in volume compared to the initial compacted volume was observed, relative to I_p', despite being brought to the same water content upon wetting. These observations are consistent with a reduction in suction and the microstructural changes that take place upon wetting. Several studies show that changes in soil structure when specimens are saturated result in changes at both at macroporosity range, due to shrink/swell of the aggregates, and at the microporosity range, and the magnitude of those changes are typically associated with the specimen density (Monroy et al., 2010; Thom et al., 2007; Cuisinier and Laloui, 2004; Farulla et al., 2010).

Upon drying to residual conditions (w_R), the trend is less consistent due to the behaviour of the clayey silt which experienced a significant volume increase both at the drying and wetting boundaries, resulting in no trend among the three soils. The results therefore suggest that there is no obvious relationship between volume change and modified plasticity index considering the residual state boundary, because some soils may experience significant swelling upon drying beyond residual suctions. Nonetheless, both the silty clay and clayey sandy silt experienced the expected behaviour with a further reduction normalised void ratio at the w_R boundary compared to w_T boundary. While small increases in normalised void ratio with comparison to drying to the w_T boundary at the compacted water content (w_{OMC}), suggesting further microstructural changes have taken place (i.e. Figure 4-28).

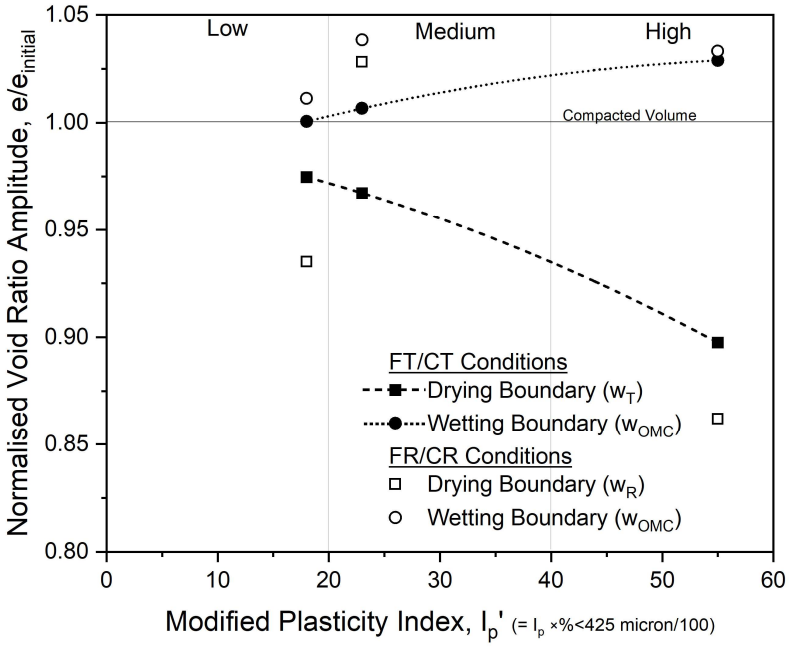


Figure 6-1 Normalised change in void ratio (from initial compacted state) against modified plasticity index.

The correlation between clay activity (ratio between clay fraction under 2μm and plasticity index) and the amplitude of small strain shear modulus is also presented in Figure 6-2. Amplitude refers to the difference in small strain shear modulus from the compacted state and at the same water content on the wetting path For this comparison, the compacted water content (w_{OMC}) was chosen as a suitable comparable state between the soils. Results show a nonlinear exponential trend between the two variables i.e. as the activity of the clay fraction increases so too does the small strain shear modulus or G_{max} amplitude. Interestingly, the clayey sandy silt shows the largest range in small strain shear modulus amplitude despite being classified as a soil of low plasticity. However, the clay activity (A) is able to account for the increased proportion of swelling clay minerals relative to the total clay fraction for the clayey sandy silt compared to the silty clay. Clariá and Rinaldi (2007) reported that in similar clayey silts the clay minerals form buttresses around the contact of the sand and silt particles and thus the capillary forces in the clay control the stiffness of the soil. This is clearly visible in Figure 4-27 as sand particles can be observed to be suspended in a clay matrix. As a consequence, it's probable the clay particles control the unsaturated behaviour. It noted that the recorded change in small strain shear modulus represents a change in the stiffness of the soil skeleton which primarily relates to effective stress but also particle size and void ratio. Indeed, the observed trend likely relates to hysteresis of matric suction which is primarily due to ink bottle effect in this suction range. Intuitively, due to the differences in mineral structure between montmorillonite and kaolinite, the difference in geometric nonuniformity of individual pores is significant and has been noted in the literature (i.e. Ng and Peprah-

Manu (2023); Anandarajah and Amarasinghe (2012)). The mineralogy also influences other factors which impact the degree of hysteresis including swelling and shrinkage effect which may impact the microstructure during drying and wetting. The result is therefore unsurprising when observing differences in suction shown in Figure 3-15. The findings thus highlight the importance of considering activity of the clay minerals for clear understanding of the unsaturated behaviour of soils. As a consequence, the determination of the proportion of particle constituting <0.002mm, albeit not routinely evaluated, is indeed critical particularly for soils which contain sand sized particles. Santamarina et al. (2002) notes that even small amount of fines can impact the behaviour of coarse grained soils as fines fill larger pore spaces and control permeability.

Figure 6-2 also presents the change in amplitude at the compacted water content after application of all drying-wetting cycles for FT/FR/CT/CR conditions. It clearly demonstrates that the silty clay experiences the greatest reduction in hysteresis between drying-wetting pathways and is likely attributed microstructural changes such as cracking. Indeed, for the clayey silt and silty clay CT/CR conditions results in the largest reduction in hysteresis amplitude at the compacted state. This is supported by the presences of larger more frequent cracking for the silty clay in these conditions i.e. Figure 4-31 and Figure 4-32.

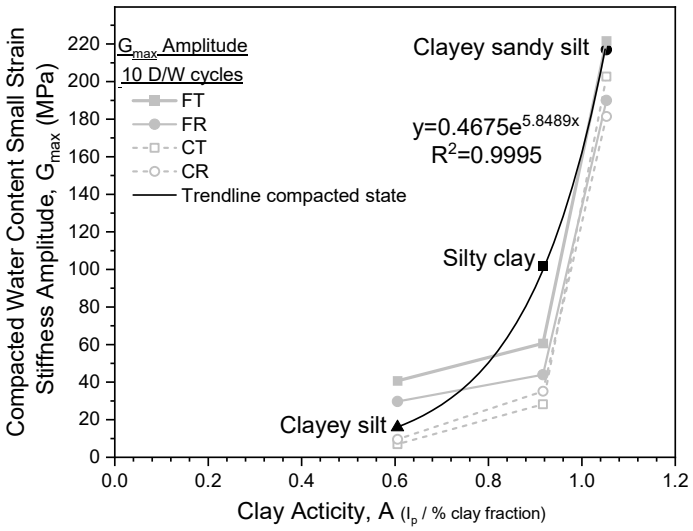


Figure 6-2 Shear wave velocity amplitude at w_{OMC} against clay activity (A) for the compacted state (black) and for FT/FR/CT/CR conditions (grey) following 10 D/W cycles for the clayey silt and clayey sandy silt and between 2-6 D/W cycles for the silty clay.

Figure 6-3 shows the relationship between normalised small strain shear modulus and modified plasticity index at the compacted water content. Its noted that the data presents the small strain shear modulus after 10 drying-wetting cycles for the clayey sandy silt and clayey silt and between 2-6 cycles for the silt clay. For CT and CR pathways a clear trend is evident whereby an increase in modified plasticity index resulted in the reduction

of small strain shear modulus. The trend is less evident for the FT and FR pathways due to the significant increase in small strain shear modulus of the clayey silt following full saturation. However, in both cases drying to residual conditions (w_R) resulted in a comparative reduction in small strain shear modulus. Therefore the results show a lower bound and upper bound, delineated by CR and FT conditions respectively.

These results can also be compared to the swelling and shrinking potential map reported by the British Geological Survey, presented in Figure 6-4 (left) (Jones and Hobbs, 2004). The map was created using a large data set of index tests for the UK and determined using the VCP classification by the BRE (1993). Consequently, it can be directly compared to the results presented in Figure 6-3 using modified plasticity index. In this case 'significant' is equal to high VPC and 'moderate' medium VCP. As expected, it shows that the high VCP soils, equivalent to the silty clay, are present in midlands and south east England in stiff overconsolidated sedimented clays, while also present in north east England. Medium VCP soils, equivalent to the clayey silt, are also distributed in a similar manner, albeit more widespread. The results therefore suggests that geostructures built using these materials have higher potential for post compacted performance change. Furthermore, high VCP materials are particularly vulnerable to the effects of cracking. By comparison northern and western areas of the UK are less susceptible to reduction of performance, although results suggest some reduction in performance may occur.

The nuance in the results can be considered further by comparing them to the prevailing weather conditions in the UK, presented in Figure 6-4 (right). It shows that significantly more precipitation is experienced in the west regions of the UK compared to the east from Atlantic weather systems. This is particularly evident for mountainous regions which force prevailing westerly winds to higher elevations cooling the air and generating clouds. If the ground becomes saturated more frequently in these regions, they may also experience smaller reduction in performance compared to the east. This indicates that the impacts of climate change on the performance of compacted soils may be exacerbated in the eastern region of the UK compared to the west.

UKCP18 data is also presented Figure 6-5 showing the summer and winter mean temperature and precipitation changes for the UK. Data is derived from RCP 4.5 and was selected as a conservative future outcome by 2070. When comparing this to Figure 6-4, it can be seen that the high VCP soils in the south of England will potentially experience deviations from mean rainfall which are greater than previous years, (reduction summer and increase in winter) and relative increase in summer temperatures (90^{th} and 10^{th} percentiles).

This increase in surface temperatures is likely to increase the degree of drying during

summer and soil moisture deficit. The results presented in Figure 6-3 suggest that historic geostructures which are constructed of high VCP material would experience a reduction in performance due to increased degree of drying, irrespective of achieving full saturation i.e. difference between FT/FR. If rainfall intensity is significant, the reduction in surface permeability may result in a further reduction, i.e. CR conditions. However, further analysis is required to fully capture the behaviour, as data was derived from 10 or fewer drying-wetting cycles. Nonetheless, the results highlight that the contrast of soil behavior between the northern and southern regions will likely be exacerbated due to the impacts of climate change.

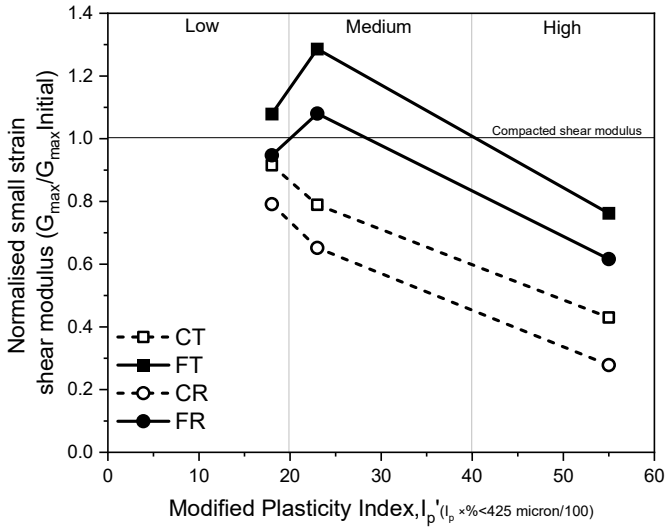


Figure 6-3 The relationship between normalised small strain shear modulus at w_{OMC} and weighted plasticity index after all drying drying-wetting cycles for the clayey sandy silt (10 D/W cycles), kaolin clay (10 D/W cycles) and silty clay(2-6 D/W cycles).

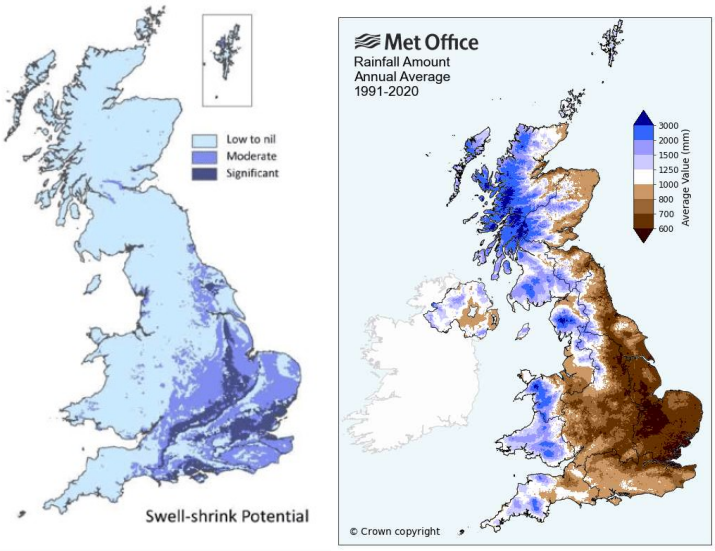


Figure 6-4 UK shrink-swell potential map, based on VCP (left) (Jones and Hobbs, 2004) and annual average rainfall between 1991-2020 (right) (Met Office, 2020).

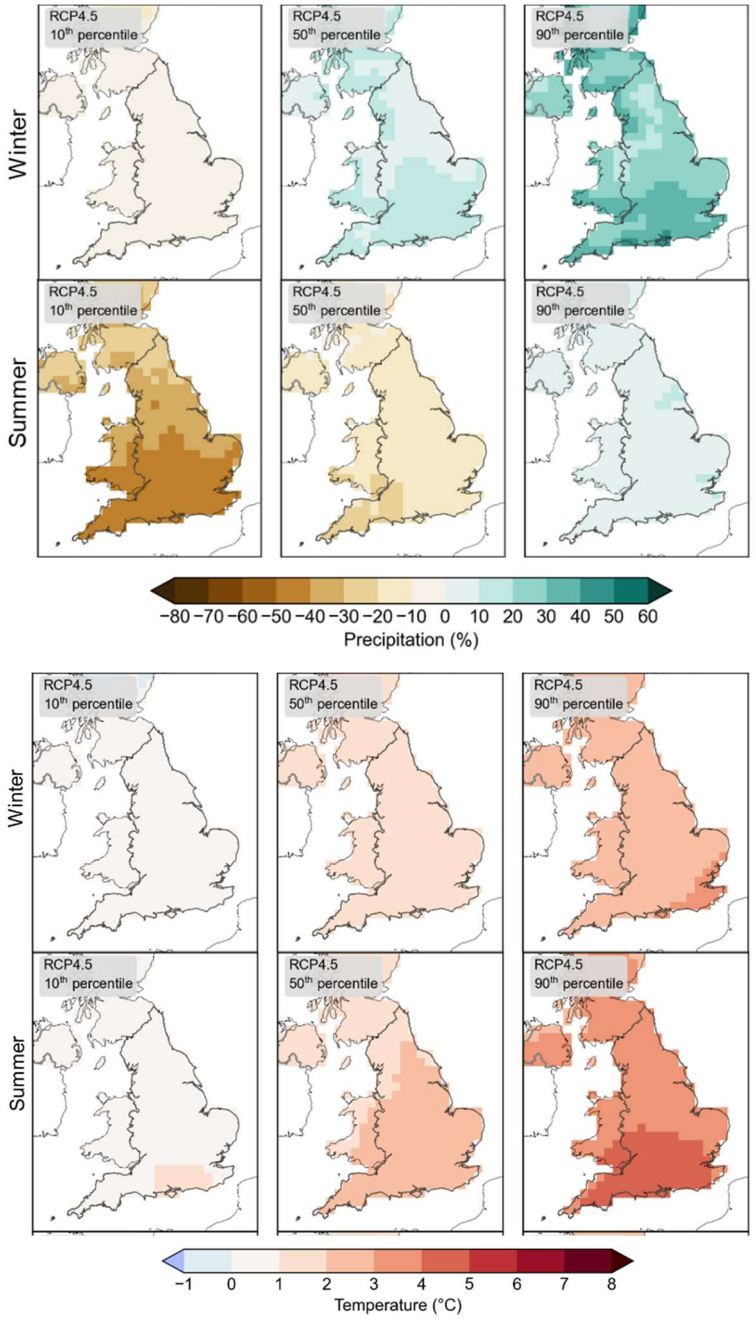


Figure 6-5 UKCP18 RCP 4.5 probabilistic projections for changes in rainfall (top) and temperature (bottom) in 2070 for 1981-2000 baseline (Met Office, 2024).

In practice the UK national annex of Eurocode 0 requires the working design life of category 5 structures to be 120 years. Consequently, modern embankments will likely experience significant changes in climate during their design life which highlights the need to account for future climate scenarios in design and construction. When considering these climate changes, the results suggest that plasticity can provide and indicator for performance when soils are subject to drying-wetting. Therefore, during the initial desk study, the determination of plasticity along the alignment of an infrastructure project may be useful for identifying soils at risk from the impacts of

climate change. In the Design Manual for Roads and Bridges (DMRB) MCHW Series 600, clays with a liquid limit exceeding 90% and plasticity index exceeding 65% as designated unacceptable, therefore higher plasticity materials similar to the silty clay may be incorporated into a newly constructed embankment. Indeed, for large projects reuse of excavated material may necessitate the incorporation of higher plasticity soils. However, the results show that lower plasticity materials perform better during changes in water content which are most prevalent at depths up to 1-2 m. This suggests that lower plasticity material could be specified for placement on the exterior of the embankment during compaction ensuring that higher plasticity materials at the centre are exposed to fewer water content changes reducing the likelihood of future deterioration i.e. the formation of desiccation cracking.

Furthermore, a testing regime which initially includes the determination of plasticity and unsaturated characteristic (i.e. SWRC) followed targeted establishment of the impact of drying-wetting extents, adopting similar methodology than presented in this thesis, could be used to determine the range of behaviour of the soils for design work which considers post compacted behaviour. For a larger scheme which includes a range of soils this may also aid in the establishment of an empirical relationship between plasticity and performance of compacted soils.

Compaction water content should also be considered as the difference in fabric between soils compacted at dry and wet of optimum water content may result in differences in behaviour during drying-wetting, however, this requires further investigation For example, a designer may want to specify compaction of earth works slightly wet of optimum water content as a precaution, as this has been found to reduce permeability compared to compaction at OMC (Zhongzhi et al., 2020), which may reduce the impact of climate change on the performance of compacted soils due to the reduction in ability for water content to change i.e. reduce drying-wetting amplitude and therefore potentially increase resilience.

The management of historic rail embankments in UK practice involves greater complexity as following their construction the subsequent >100 years of soil-atmosphere interactions and loading conditions (cyclic loading and rotation of principal stresses from traffic during service) results in a unique soil structure (i.e. soil memory) which is expressed in the behaviour of the soil but difficult to assess for asset managers. At a macro scale the results confirm the potential for plasticity to be used as general indicator for a risk-based prioritisation for the management of embankments to climate change. However, for these historic embankments it would be advantageous to capture the history of the soils as this will be unique to a given embankment depending on its age, construction materials, location (prevailing weather conditions) and traffic conditions. For instance, element testing of samples obtained from the field consisting

of end tipped fill could be used to simulate the impact of extreme drying based on the SWRC, thus both capturing the unique history of the soils and impact of future climate on behaviour.

6.2.1 Small strain stiffness drying-wetting behaviour in the G_{max}-e space

Figure 6-6, Figure 6-7 and Figure 6-8 shows the relationship between void ratio and shear modulus during drying-wetting grouped by constant water content for the clayey silt, clayey sandy silt and silty clay. Upon initial observation it's clear that when grouped by different water content levels the clayey silt and clayey sandy silt can be fitted with a moderately strong linear relationship. The results show that for the clayey sandy silt a distinct difference between drying and wetting pathways is present and has been plotted as independent trends. In this case for an equal water content the drying pathway exhibited greater small strain shear modulus for a given void ratio. However, the clayey silt shows similar trend between both drying and wetting pathways, consequently, a single trend was fitted to both pathways. These results are not surprising considering the amplitude difference between both soils shown in Figure 6-2. However, its noted that a singular trend for the clayey silt does not fully reflect the suction changes during drying-wetting. The results also present the initial drying-wetting pathways for FT/CT and FR/CR. It shows that data for all chosen boundaries lie on the same linear trends in spite of difference in drying-wetting amplitude. The trends thus appear independent of the number of cycles and drying and wetting boundaries. Its noted that the silty clay displays significantly more scatted data points, showing no strong trend, due to the formation of macroscopic cracking. However, at the compacted water content a similar distinction between drying and wetting pathways may also be made. This is because the cracks reduced in width upon an increase in water content and thus slightly reduced scatter.

For the clayey silt the gradient of the observed trends are approximately the same at all recorded water contents, which is notable due to the large difference in water content. However, as measurements were made at constant water content levels, changes in void ratio results in equal changes in saturation i.e. an increase in void ratio produces an equivalent decrease in saturation. These changes result in nonlinear changes in suction according to the SWRC in the Ψ-S_r space. However, it can be ascertained from Figure 6-6 and Figure 6-7 that differences in void ratio and saturation at constant water content levels are relatively small over the 10 drying-wetting cycles. For instance, for the clayey silt at constant w_{OMC}= 28% water content the minimum void ratio equals 0.926 resulting in a small strain shear modulus 114 MPa and saturation of 78.7%. While the corresponding maximum value of void ratio equals 1.025 for a small strain shear modulus

of 71 MPa and saturation of 74.9%. Thus, changes in suction due to the difference in saturation are likely to be relatively small, which may explain why the trend appears linear across the range or recorded void ratios.

Finally, Figure 6-9 presents the data normalised against initial compacted state. When comparing the trends for the clayey sandy silt and clayey silt, the rate of small strain stiffness change for a given increment of void ratio appears approximately similar. This is not surprising considering that both soils are lower plasticity and have similar SWRC. The silty clay data shows a much greater range of data points compared to the clayey silt and clayey sandy silt. However when normalised, the changes in small strain shear modulus at the compacted water content appears similar but the trend is much weaker due to cracking.

The constant water content conditions employed in this study therefore show that unconfined compacted soils show an approximate linear change in small strain shear modulus for an increment of void ratio change over 10 drying-wetting cycles. The existence of such relationship is very encouraging as there is a great uncertainty currently in relation to the role of different wetting and drying boundaries and their impact on performance of existing transport infrastructure assets. In practice, this understanding is also beneficial when estimating the range of variation of performance and volume changes likely to be expected for soils of different plasticity. This may be particularly important when consideringthe performance of high-speed rail which is sensitive to rail deflections when the critical speed is reached i.e. when train speed approximates the minimum wave propagating speed of the track-ground system and amplifies ground displacements. (Shih et al., 2017). Dynamic loading and resultant ground borne vibration emitted at the critical speed (determined by the speed of Rayleigh waves) results in increased strains according to the non-linearity small strain conditions (Costa et al., 2020).

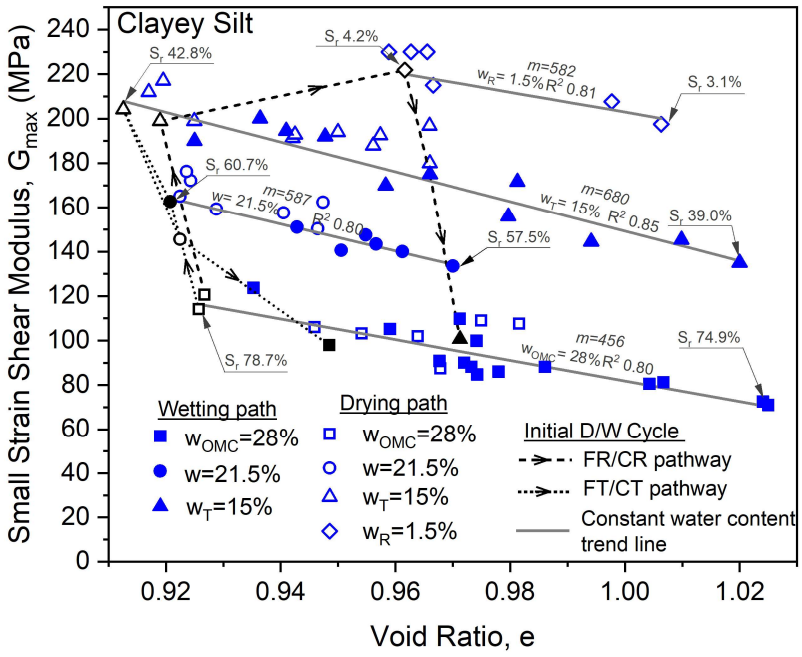


Figure 6-6 Relationship between void ratio and small strain shear modulus at constant water content for compacted clayey silt subject to 10 drying and wetting cycles for all boundary conditions (FT/FR/CT/CR).

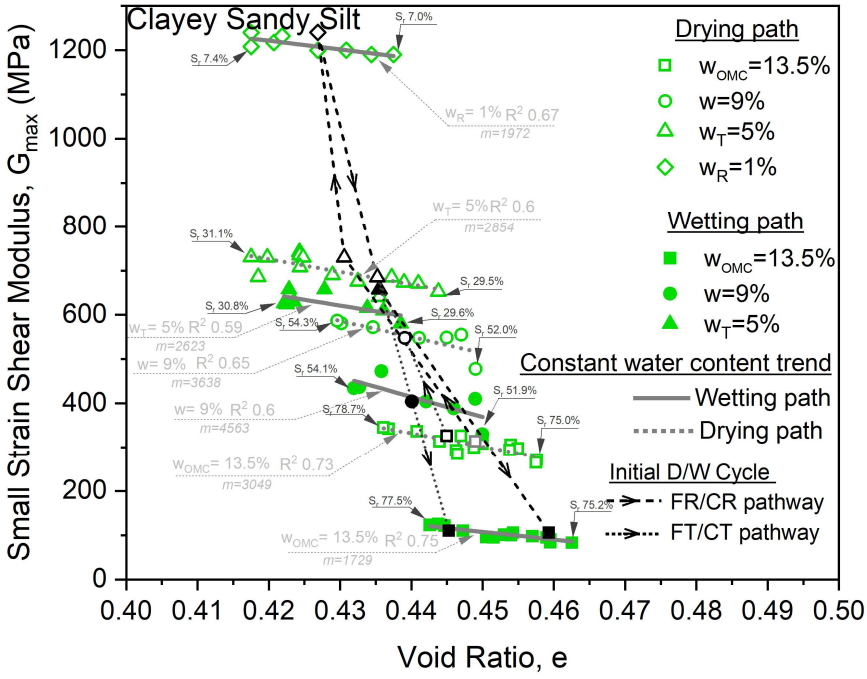


Figure 6-7 Relationship between void ratio and small strain shear modulus at constant water content for compacted clayey sandy silt subject to 10 drying and wetting cycles for all boundary conditions (FT/FR/CT/CR).

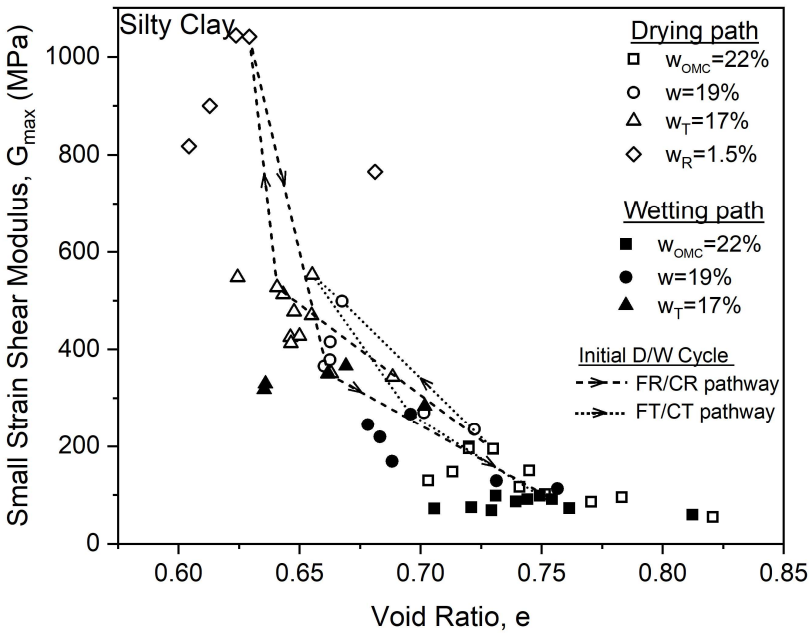


Figure 6-8 Relationship between void ratio and small strain shear modulus at constant water content for compacted silty clay subject drying and wetting cycles for all boundary conditions (FT 6D/W cycles, FR 3 D/W cycles, CT 3 D/W cycles and CR 2 D/W cycles).

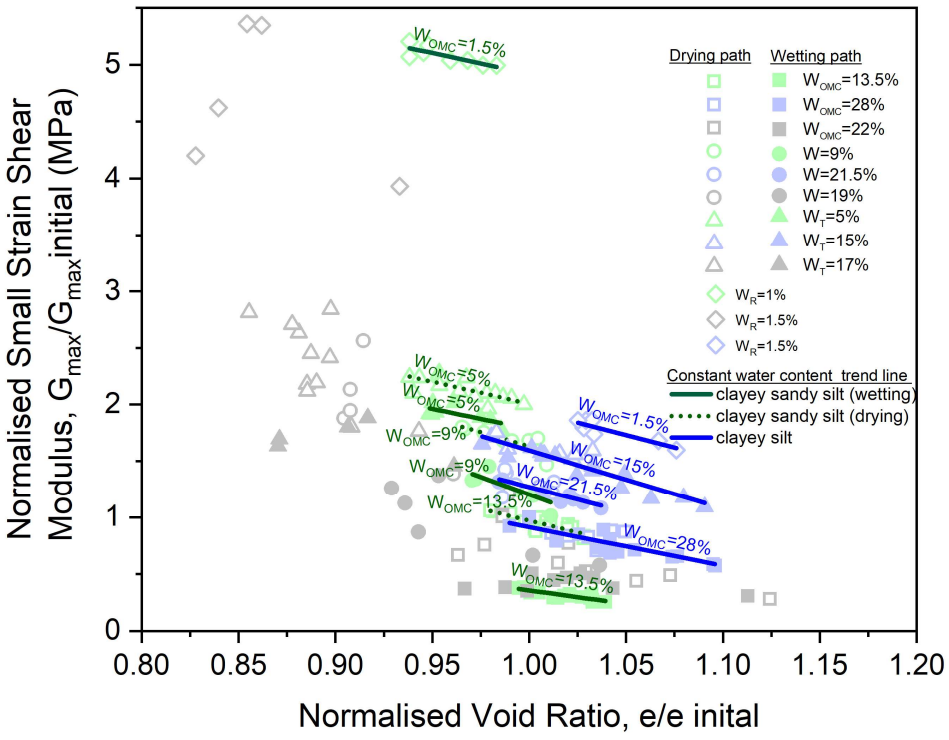


Figure 6-9 Comparison between the relationship between normalised void ratio and normalised small strain shear modulus for the compacted clayey sandy silt (green), clayey silt (blue) and silty clay (grey) during drying-wetting.

6.3 Summary

The small strain stiffness and volume change behaviour for the clayey sandy silt, clayey silt and silty clay were analysed using modified plasticity index (I_p') and clay activity. The results showed an expected trend of increasing volume change at the drying boundary (w_T and w_R) when plotted against I_p'. While upon wetting back to the compacted water content an increase in volume was captured, which again increased for an increase in I_p'. However, for the clayey silt drying to w_R water content resulted in significant volume increase contrary to the trend of the other selected soils.

The amplitude of small strain stiffness during drying-wetting at the compacted water content also exhibited a trend of increasing amplitude when plotted against clay activity (A). The largest amplitude was found for the clayey sandy silt, highlighting the importance of determining the proportion of particle constituting <0.002mm for sandy soils. The final small strain stiffness values following drying-wetting boundaries at the compacted water content were also plotted against I_p'. Results showed a trend of a reduction in small strain stiffness with increasing I_p'. When compared to the distribution of high VCP soils in the UK, prevailing weather and future climate change its clear that the difference in performance of geostructure in southern England and northern England will likely be exacerbated.

Drying-wetting small strain stiffness data was also plotted in the G_{max}-e space. An approximately linear trend is present at the selected water content levels for both the clayey sandy silt and clayey silt. This is likely due to small changes in saturation during drying-wetting relative to the SWRC in the Ψ-S_r space. Macroscopic cracking during drying-wetting for the silty clay resulted in significant scatter of the data. However the trend is encouraging, showing potential for allowing estimation of the range in performance of compacted soils.

Chapter 7
Conclusions and Recommendations

7.1 General summary

Climate modelling estimates that the UK climate will likely experience increasingly high temperatures and widespread drought during summer, in conjunction with increasingly wetter winters due to growth in prolonged precipitation. Previous studies indicate that that post-compacted changes in moisture and suction significantly influence the small strain response. However, in general experimentation investigating the impact of drying-wetting on compacted soils has been carried out on low to intermediate plasticity soils as they are primarily incorporated in modern construction of transport infrastructure. Nonetheless, it's common for historic construction to include soils with higher plasticity due to lack of regulation. For instance, in the UK during construction of the railway network in the late 19th century and early 20th century, no exceptions were made for material which would now be deemed unsuitable for use in embankments. In addition, transport infrastructure are linear assets that are often composed of a range of compacted soil compositions/index properties owing to the differing depositional environments of the natural geology.

This study therefore examined the behaviour of three compacted soils representative of those incorporated in the UK transport network. This included a low plasticity clayey sandy silt similar to Devensian glacial tills, high plasticity clayey silt and very high plasticity silty clay similar to the London Clay. The specimens' behaviour following 10 drying-wetting cycles were characterised in unsaturated conditions, in terms of small strain stiffness, and saturated stress-strain behaviour during consolidated drained shearing (CID). Micro X-ray computed tomography (CT) was also employed to observe changes in the pore structure during drying-wetting.

Chapter 3 outlined the basic characteristics of the selected soils, methodology for drying-wetting and rationale for the four drying-wetting amplitudes. A brief explanation of the equipment and methodology for triaxial testing and X-ray computed tomography (CT) was also included. To validate the use of ultrasonic pulse transmission testing for determination of small strain stiffness during drying-wetting, an exercise was conducted comparing the Pundit lab and bender elements. Chapter 4 then described the results of small strain stiffness testing for each soil. This chapter also presented the micro X-ray computed tomography micrographs captured during drying-wetting to complement small strain stiffness testing. The stress-strain behaviour during saturated drained triaxial shearing following drying-wetting were presented and discussed. An analysis of the selected compacted soils was also presented in terms of plasticity and compared to the

their presence in the UK. Finally, observed trends at constant water content in the G_{max}-e space were also presented.

7.1.1 Key Findings

Key findings of the work show that that the amplitude of drying-wetting impacts the behaviour of compacted soils. Most strikingly, the results showed that an increase in drying boundary resulted in a loss of performance, which has not been retrospectively considered when analysing failures on the transport network due to climate. Furthermore, it was shown that higher plasticity compacted soils experienced greater loss of performance during drying-wetting highlighting the difference in the impacts of climate change between Devensian glacial tills and high plasticity overconsolidated sedimented clays in the UK. Finally, this behaviour was linked to changes in microstructure during drying-wetting.

7.2 Ultrasonic pulse transmission testing

Ultrasonic testing is an attractive non-destructive technique as the transducers do not penetrate the specimen, thus eliminating disturbance produced by bender elements. This is especially beneficial upon repeated disturbance due to volume changes during drying-wetting. To check the suitability of ultrasonic transducers for shear wave pulse transmission testing in soils, a comparison was conducted between bender elements and the Pundit lab ultrasonic system. Testing was performed on two compacted soils during a drying-wetting cycle. Ultrasonic testing requires the consideration of several additional variables, for example the calibration time accounting for the waves as they pass through the platens, requirement of adequate contact between platens and specimens (couplant) and transducer resonant frequency (i.e. transducer characteristics).

For both soils, the ratio of L_{tt}/λ and L_{pp}/λ decreased during drying and increased during wetting. The bender elements were able to account for the near field effect by the increasing testing frequency (>10 kHz) at the driest point. The ultrasonic system showed a reduction in natural resonant frequency compared to transducer resonance, resulting from the variation of the damping properties of the soil and the interaction of transducers and specimen. However, the output signal frequency showed that Lpp/λ was maintained above 2 during drying and wetting for both soils. The results showed that for both soils the shear wave velocities measured using both the bender elements and ultrasonic systems show good agreement during a drying and wetting cycle.

7.3 Drying-wetting small strain shear modulus behaviour

The results of a series for non-destructive small strain stiffness tests carried out for three soils during 10 drying-wetting cycles were presented in Chapter 4. Three soils were selected to be representative of soils in the UK which have a range of plasticity. A novel method was also employed to determine four amplitudes of drying-wetting from the soi water reterntion curve (SWRC) to allow suitable comparison between the soils. This included water content levels corresponding to drying to within the transition zone (w_T) and drying to residual conditions (w_R), while also wetting to compacted conditions (w_{OMC}) and wetting to full saturation (S_r=1.0). This approach therefore allowed for a comparison between saturation and the degree of drying on the performance of the soils (i.e. comparison of FT/FR/CT/CR conditions). Small strain stiffness testing was conducted in unsaturated conditions at the selected water content levels to mimic field conditions. This approach revealed that when small strain stiffness observed during drying-wetting is presented using water content on abscissa the small strain stiffness on drying path is greater than the wetting path. However, when the same data is presented against suction this trend is inverted, which corresponds with data collected at constant suction levels using axis translation technique.

For the three soils, drying-wetting exhibited a range of behaviour. For instance, the clayey silt exhibited a nonlinear increase in small strain shear modulus due to changes in water content, where the rate of increase in shear modulus reduces at residual conditions. This contrasts with the clayey sandy silt which experienced a significant increase in shear modulus at residual conditions, while the silty clay showed a more linear trend during drying-wetting.

Notably, drying to residual conditions resulted in a significant increase in void ratio for the clayey silt. Evidence suggests that this occurs due to the development of the partial pendular state where capillary contacts break and the Equivalent Effective Stress (EES) decreases. The measured changes in small strain shear modulus are consistent with these changes in void ratio. By comparison, the clayey sandy silt experienced greater volumetric stability and thus a smaller change in small strain stiffness during drying-wetting, while the silty clay exhibited significant macroscopic cracking for all selected drying-wetting amplitudes. Integrity of the specimens was therefore lost between 2-6 cycles. This resulted in the greatest reduction in small strain shear modulus from compacted conditions.

Further insight was also determined from drying-wetting amplitudes. For the clayey silt and clayey sandy silt a reversal of both small strain shear modulus and volume change was observed for the drying-wetting boundaries considered. For instance for the clayey silt, fully saturated boundary conditions (FT/FR) resulted in the increase in small strain

shear modulus and comparative reduction in void ratio. While at the compacted water content, wetting (CT/CR) boundary conditions resulted in an asymptotic decrease in small strain shear modulus and increase in void ratio. The results also showed a decrease in performance for all soils when the drying amplitude was increased to residual conditions, with CR conditions resulting in the greatest reduction in small strain stiffness overall. Interestingly, both the clayey silt and silty clay showed the greatest variation between all selected hydraulic amplitudes. This suggests that compacted clays exhibit the greatest range in behaviour. The results therefore show significant nuance in soil behaviour during drying-wetting dependent on the degree of drying-wetting and composition of the compacted soil.

7.4 Microstructure following drying-wetting

The results presented both microstructural observations and inferred microstructural behaviours during drying-wetting. Microstructural observation were made by comparing micro X-ray computed tomography (CT) micrographs, shown in Chapter 4. The study allowed for investigation of change in inter-aggregate pore structure and was generally in agreement with small strain stiffness testing. It showed that the compacted structure of the clayey silt and silty clay were similar with a more uniform fabric. Whereas, the clayey sandy silt exhibited the greatest range in inter-aggregate pore size due to voids forming between sand particles and within the finer matrix. Upon initially drying to residual conditions (w_R) the soils experienced a reduction in the inter-aggregate pore frequency while the silty clay experienced the formation of micro-cracking. The results highlight significant differences in microstructural mechanisms which impact macro behaviour i.e. small strain stiffness. For instance, the clayey silt was observed to undergo significant increase in volume upon drying to residual conditions. This increase coincided with a reduction in small strain shear modulus which was surmised to result from fabric changes at a microscopic level. The higher plasticity silty clay also experienced a reduction in shear modulus in the same conditions, however, observations confirmed the development of larger inter-aggregate cracking.

For the selected drying-wetting amplitudes the microstructure observation further complements the small strain stiffness testing. For instance, specimens brought to full saturation (FT/FR) experience a reduction in the frequency and diameter of inter-aggregate pores, whereas the original compacted fabric is maintained for CT and CR conditions. Similarly the silty clay shows a higher frequency of larger and branching micro cracks for CT/CR conditions when compared to fully saturated conditions (FT/FR), suggesting that full saturation results in ‘self healing’ of some smaller cracking. The results therefore highlight the significance of both drying and plasticity on the

performance of compacted soils, showing that the 'damage' to the pore structure due to these factors results in an observable decrease in small strain stiffness. In practice, these observations also suggest a decrease in the performance of compacted soils due changes in the unsaturated behaviour, for instance due to loss of suction and mechanical strength.

7.5 Saturated stress strain behaviour following drying-wetting

The saturated drained stress-strain behaviour, presented in Chapter 5, exhibited marked differences from unsaturated small strain stiffness testing. Although testing was conducted for the same drying-wetting conditions as small strain stiffness testing, all soils showed an increase in initial tangent modulus (E_i) and peak deviator stress (q_{peak}), while also experiencing an increase in dilation. This increase in brittle behaviour and peak stress is not optimal for compacted soils in transport infrastructure as strain softening results in the development of progressive failures in which shear stress along the slip surface varies which can results in abrupt failures comprising of large displacements if pore water pressures rise sufficiently. The observed strain softening behaviour was attributed to changes in effective stress during drying-wetting, described by the CSR. The results highlight that compacted soil behaviour following wetting-drying is dependent on strain range, saturation and degree of drying-wetting. The results also demonstrate the significance of plasticity, showing that very high plasticity clays experience a significant increase in brittle behaviour when drying was increased to residual conditions i.e. due to an increase in the CSR. As a consequence, it's probable that very high plasticity soils incorporated into geostructures which experience greater degrees of drying greater than previously experienced are likely to exhibit a significant change in behaviour in the saturated state when compared to lower plasticity materials.

7.6 Engineering applications

Chapter 6 presented an analysis of the small strain stiffness data using modified plasticity index (I_p') and clay activity (A). In general, a trend is observed between small strain stiffness and plasticity where a decrease in volume (e) was observed for increasing I_p' when drying within the transition zone however, upon wetting to the compacted water content an increase in volume relative to I_p' was observed. This is consistent with changes in suction and microstructure during drying-wetting. This therefore shows potential for asset management allowing for estimation of volume change variation due to drying-wetting based on modified plasticity index. It was noted however that when the

clayey silt was dried to the residual conditions an increase in volume was observed which doesn't conform to the expected trend.

A relationship between small stiffness amplitude at the compacted water content (w_{OMC}), against clay activity (A) showed a similar trend. An increase in small strain stiffness amplitude was recorded for an increase in clay activity, highlighting the need to determine the proportion of clay particles for sandy soils as a small portion of clay particles may control the unsaturated behaviour. Notably the small strain stiffness amplitude reduced for all soils following drying wetting. In the field this suggests that following soil-atmosphere interaction the unsaturated behaviour becomes more uniform.

The small strain stiffness after the application of all drying wetting cycles (w_{OMC}) and Ip' demonstrated a clear link between plasticity and small strain stiffness, showing that an increase in plasticity also results in an increased reduction in small strain stiffness during drying-wetting. Drying-wetting to residual conditions (w_R) and compacted water content (w_{OMC}) (CR) generated the greatest reduction in small strain stiffness, while full saturation (FT/FR) resulted in hydraulic ageing which appears to reduce the loss of small strain shear modulus. The results therefore highlight the importance of plasticity for the unsaturated behaviour of compacted soils. Furthermore, when compacted to the distribution of VCP of soils in the UK, prevailing weather and predicted climate change results suggest that:

- low plasticity compacted Devensian glacial tills found commonly in northern parts of the UK likely have the best unsaturated performance showing least deviation from the compacted state,
- compacted high plasticity soils preset in the midlands and southern England in stiff overconsolidated sedimented clays, are more vulnerable to changes in post compacted changes in water content and significant deterioration due to formation of cracking.
- increased precipitation on the western side of the UK due to prevailing weather patterns may reduce loss of performance due to more frequent saturation of the ground,
- Predicted changes in seasonal precipitation and surface temperature in southern England due to climate change will likely exacerbate the differences in performance of compacted soils in the south compared to the north,
- results would therefore suggest historic geostructures in southern England, which are more likely to have higher plasticity due to natural geology, are anticipated to be more vulnerable to the effects of climate change.

Finally a linear trend was observed between void ratio and small strain shear modulus

at different water content levels for the clayey sandy silt and clayey silt. The clayey sandy silt was also able to show distinction between the drying and wetting pathways. Macroscopic cracking during drying-wetting for the silty clay resulted in significant scatter. The trend appears approximately comparable for all measured water contents and is independent of the number and amplitude of drying-wetting cycles. These finding are promising for asset management allowing variation in performance due to changes in moisture to be captured in a simple manner. This is also significant in light of recent advancement in satellite imagery using L-band Synthetic Aperture Radar to determine water content from satellite imaging.

7.7 Recommended future work

Considering the findings of the thesis the following recommendations for future work can be identified:

- The study was limited to a degree of compaction >90% of MDUW at OMC to allow for suitable comparison between the three soils. However, previous studies have shown the MDUW and water content during compaction has a significant impact on the behaviour of compacted soils during drying-wetting. This is significant for many historical embankments in the UK which were built prior to the mid-20th century and constructed without control on compaction. As a result, the effect of compaction on drying-wetting behaviour is key for understanding their behaviour. Both laboratory testing and field time lapse shear wave velocity surveys to monitor historic geostructures for improved identification of subsurface deformation stiffness and assess the deterioration of performance during service would also be beneficial.
- Plasticity was shown to have a significant impact on the performance of the compacted soils. There appears to be a relationship between change in small strain stiffness and weighted plasticity index following drying-wetting and drying-wetting hysteresis. However, this study was limited to only three different plasticity levels, while also introducing variables such as different particle sizes. This aspect could be further explored by including a greater number of identical soils of differing plasticity. This would therefore allow for the development of simple empirical relationships based on plasticity. For practicing engineers these relationships may better allow for the assessment of change in performance of compacted soils following post compacted changes in water content and thus asset management techniques to manage the impacts of climate change.

- The results of this study have shown that deterioration is prevalent among different soils during drying-wetting. The use of chemical stabilisation with additives such as lime cement are commonplace for remediating shortfalls in performance caused by this deterioration. However, these binders significantly contribute to the CO_2 emissions of a project. In contrast, nature-based solutions (NbS) presents long-lasting, cost-effective and environmentally sustainable methods to increase resilience of the transport network. However, the use of NbS has yet to be fully realised in practice. Indeed, Blackwood and Renaud (2022) note that there are currently significant knowledge gaps that may hinder the uptake of NbS in the rail industry which warrant further research. Building on the findings of this study the effectiveness of nature based solutions on the performance of different soils during wetting-drying could be investigated increasing confidence for the implementation of soft engineering strategies and low carbon solutions to manage the impacts of climate change.
- The results for drying-wetting show common trends for constant water content levels in the e-G_{max} space which could be further investigated and developed for other types of soils. For practicing engineers this would be beneficial due to its simplicity but also the consideration of water content has additional advantages in light of recent advancement in satellite imagery using L-band Synthetic Aperture Radar that enable the determination of water content non-destructively (Ahlmer et al., 2018).
- Another aspect which would benefit from further investigation relates to microstructural changes during drying-wetting. Micro X-ray computed tomography (CT) micrographs suggest that the clayey silt underwent significant changes at a micro pore level during drying wetting, which resulted in significant changes in macro behaviour. However, due to the difficulty observing changes at this scale the mechanisms which result in this behaviour are not fully understood. Furthermore, the mechanisms which produce an increase in saturated brittle stress-strain behaviour during drained shearing remain unclear.
- Finally, the results showed that an increase in the drying boundary resulted in a loss of performance. This therefore indicates that earthwork failures on the transport network may be linked with hotter summers and periods of drought. As a consequence, a retrospective analysis of drought with rainfall data and earth work failures would perhaps provide a better insight into the link between climate and earthwork failures which has been historically analysed only using rainfall data.

List of references

Ahlmer, A.-K., Cavalli, M., Hansson, K., Koutsouris, A.J., Crema, S. and Kalantari, Z. 2018. Soil moisture remote-sensing applications for identification of flood-prone areas along transport infrastructure. *Environmental Earth Sciences.* **77**(14), p533.

Al Mahbub, A. and Haque, A. 2016. X-ray Computed Tomography Imaging of the Microstructure of Sand Particles Subjected to High Pressure One-Dimensional Compression. *Materials (Basel).* **9**(11), p890.

Alawia, M.H. and Rajab, M.I. 2013. Prediction of California bearing ratio of subbase layer using multiple linear regression models. *Road Materials and Pavement Design.* **14**, pp.211–219.

Alonso, E. 1998. Suction and moisture regimes in roadway bases and subgrades. In: *International Symposium on Subdrainage In Roadway Pavements and Subgrades, 11-13 November 1998, Granada, Spain*. pp.57-104.

Anandarajah, A. and Amarasinghe, P.M. 2012. Microstructural Investigation of Soil Suction and Hysteresis of Fine-Grained Soils. *Journal of Geotechnical and Geoenvironmental Engineering.* **138**(1), pp.38-46.

Arroyo, M., Wood, D.M. and Greening, P.D. 2003. Source near-field effects and pulse tests in soil samples. *Geotechnique.* **53**(3), pp.337-345.

Arulnathan, R., Boulanger, R.W. and Riemer, M. 1998. Analysis of Bender Element Tests. *Geotechnical Testing Journal.* **21**, pp.120-131.

ASTM D2845. 2008. *Standard Test Method for Laboratory Determination of Pulse Velocities and Ultrasonic Elastic Constants of Rock.* West Conshohocken, PA, USA: ASTM International.

ASTM D5298-10. 2010. *Standard test method for measurement of soil potential (suction) using filter paper* West Conshohocken, PA, USA: ASTM International

Atkinson, J. and Sallfors, G. 1991. Experimental determination of soil properties. General Report to Session 1. In: *Proc. 10th ECSMFE, Florence*, pp.915-956.

Atterberg, A. 1911. Die Plastizität der Tone (The plasticity of clays). *Internationale Mitteilung für Bodenkunde.* **1**, pp.4-37.

Azizi, A., Musso, G. and Jommi, C. 2019. Effects of repeated hydraulic loads on microstructure and hydraulic behaviour of a compacted clayey silt. *Canadian Geotechnical Journal.* **57**(1), pp.100-114.

Azizi, A., Musso, G., Jommi, C. and Cosentini, R. 2018. Evolving fabric and its impact on the shearing behaviour of a compacted clayey silt exposed to drying-wetting cycles. In: *In Proceedings of the 7th International Conference on Unsaturated Soils (UNSAT2018), Hong Kong, China*. pp.641-646.

BBC News. 2020. Fatal train derailment 'like Hornby set thrown in air'. https://www.bbc.co.uk/news/uk-scotland-north-east-orkney-shetland-54191006 (accessed 15/06/2022)

Bergamo, P., Dashwood, B., Uhlemann, S., Swift, R., Chambers, J.E., Gunn, D.A. and Donohue, S. 2016. Time-lapse monitoring of climate effects on earthworks using surface waves. *Geophysics.* **81**(2), pp.1-15.

Bhreasail, Á.N., Lee, P., O'Sullivan, C., Fenton, C., Hamilton, R., Rockett, P. and Connolley, T. 2012. In-situ observation of cracks in frozen soil using synchrotron tomography. *Permafrost and Periglacial Processes.* **23**(2), pp.170-176.

Biglari, M., d'Onofrio, A., Mancuso, C., Jafari, M.K., Shafiee, A. and Ashayeri, I. 2012. Small-strain stiffness of Zenoz kaolin in unsaturated conditions. *Canadian Geotechnical Journal.* **49**(3), pp.311-322.

Bishop, A.W. 1959. The principle of effective stress *Norwegian Geotechnical Insitute* **106**(39), pp.859-863.

Blackwood, L. and Renaud, F.G. 2022. Barriers and tools for implementing Nature-based solutions for rail climate change adaptation. *Transportation Research Part D: Transport and Environment.* **113**, p103529.

Blewett, J., Blewett, I. and Woodward, P. 2000. Phase and amplitude responses associated with the measurement of shear-wave velocity in sand by bender elements. *Canadian Geotechnical Journal.* **37**(6), pp.1348-1357.

Bonal, J., Donohue, S. and McNally, C. 2012. Wavelet analysis of bender element signals. *Géotechnique.* **62**(3), pp.243-252.

Briggs, K.M., Dijkstra, T.A. and Glendinning, S. 2019. Evaluating the Deterioration of Geotechnical Infrastructure Assets Using Performance Curves. In: *International Conference on Smart Infrastructure and Construction 2019 (ICSIC)*. ICE Publishing, pp.429-435.

Briggs, K.M., Helm, P.R., Smethurst, J.A., Smith, A., Stirling, R., Svalova, A., Trinidad González, Y., Loveridge, F.A. and Glendinning, S. 2023. Evidence for the weather-driven deterioration of ageing transportation earthworks in the UK. *Transportation Geotechnics.* **43**, pp.101-130.

Briggs, K.M., Loveridge, F.A. and Glendinning, S. 2017. Failures in transport infrastructure embankments. *Engineering Geology.* **219**, pp.107-117.

Briggs, K.M., Smethurst, J., Powrie, W. and O'Brien, A.S. 2013. Wet winter pore pressures in railway embankments. *Proceedings of the Institution of Civil Engineers - Geotechnical Engineering.* **166**(5), pp.451-465.

Brignoli, E.G.M., Gotti, M. and Stokoe, K.H. 1996. Measurement of Shear Waves in Laboratory Specimens by Means of Piezoelectric Transducers. *Geotechnical Testing Journal.* **19**(4), pp.384-397.

British Standards Institution. 2022. BS 1377-2:2022. *Methods of test for soils for civil engineering purposes. Classification tests and determination of geotechnical properties.* London: BSI.

Bui, M., I, C. and Priest, J. 2010. The universal void ratio function for small strain shear modulus. In: *Fifth International Conference on Recent Advances in Geotechnical Earthquake Engineering and Soil Dynamics*, *Missouri, USA*. p.29.

Building Research Establishment. 1993. *Low-rise buildings on shrinkable clay soils: Part 1, Digest 240.* Watford: BRE.

Casagrande, A. 1932. Research on the Atterberg Limits of Soil. *Public Roads.* **13**, pp.121-136.

Cheng, Q., Tang, C., Zeng, H., Zhu, C., An, N. and Shi, B. 2020. Effects of microstructure on desiccation cracking of a compacted soil. *Engineering Geology.* **265**, pp.105-418.

Cheng, Z. and Leong, E.C. 2014. A Hybrid Bender Element–Ultrasonic System for Measurement of Wave Velocity in Soils. *Geotechnical Testing Journal.* **37**, pp.201-158.

Cho, G.C. and Santamarina, J.C. 2001. Unsaturated Particulate Materials—Particle-Level Studies. *Journal of Geotechnical and Geoenvironmental Engineering.* **127**(1), pp.84-96.

Clariá, J. and Rinaldi, V. 2007. Shear Wave Velocity of a Compacted Clayey Silt. *Geotechnical Testing Journal.* **30**(5), pp.399-408.

Clarke, D. and Smethurst, J.A. 2010. Effects of climate change on cycles of wetting and drying in engineered clay slopes in England. *Quarterly Journal of Engineering Geology and Hydrogeology.* **43**(4), pp.473-486.

Clayton, C. 2011. Stiffness at small strain: research and practice. *Géotechnique.* **61**(1), pp.5-37.

Costa, P.A., Soares, P., Colaço, A., Lopes, P. and Connolly, D. 2020. Railway critical speed assessment: A simple experimental-analytical approach. *Soil Dynamics and Earthquake Engineering.* **134**, pp.106-156.

Cuisinier, O. and Laloui, L. 2004. Fabric evolution during hydromechanical loading of a compacted silt. *International Journal for Numerical and Analytical Methods in Geomechanics.* **28**(6), pp.483-499.

Culshaw, M.G., Entwisle, D.C., Giles, D.P., Berry, T., Collings, A., Banks, V.J. and Donnelly, L.J. 2017. Chapter 6 Material properties and geohazards. *Geological Society, London, Engineering Geology Special Publications.* **28**(1), pp.599-740.

Da Fonseca, A., Ferreira, C. and Fahey, M. 2009. A Framework Interpreting Bender Element Tests, Combining Time-Domain and Frequency-Domain Methods. *Geotechnical Testing Journal.* **32**(2), pp.91-107.

Díaz-Rodríguez, J.A., Moreno-Carrizales, P. and López-Flores, L. 2001. A study of Soil Microstructure using bender element tests. In: *4th International Conference on Recent Advances in Geotechnical Earthquake Engineering and Soil Dynamics*, *Missouri-Rolla, USA*. pp.210-219.

Dong, K., Connolly, D., Laghrouche, O., Woodward, P., Ho, C. and Alves Costa, P. 2018. The Effect of Soil Non-linearity on Mixed Traffic Railway Lines: Passenger vs Freight Loads. *Proceedings of GeoShanghai 2018 International Conference: Transportation Geotechnics and Pavement Engineering.* Shanghai, China, pp.227-236.

Dong, Y. and Lu, N. 2016. Dependencies of Shear Wave Velocity and Shear Modulus of Soil on Saturation. *Journal of Engineering Mechanics.* **142**(11), pp.401-418.

Dong, Y., Lu, N. and McCartney, J. 2017. Scaling Shear Modulus from Small to Finite Strain for Unsaturated Soils. *Journal of Geotechnical and Geoenvironmental Engineering.* **144**(2), pp.401-410.

Drakopoulos, M., Connolley, T., Reinhard, C., Atwood, R., Magdysyuk, O., Vo, N., Hart, M., Connor, L., Humphreys, B. and Howell, G. 2015. I12: the joint engineering, environment and processing (JEEP) beamline at diamond light source. *Journal of synchrotron radiation.* **22**(3), pp.828-838.

Dyvik, R. and Madshus, C. 1985. Laboratory Measurement of Gmax Using Bender Elements. In: *Proceedings of ASCE Annual Convention: Advances in the Art of Testing Soils under Cyclic Conditions, Detroit*.

Eyles, N. and Sladen, J.A. 1981. Stratigraphy and geotechnical properties of weathered lodgement till in Northumberland, England. *Quarterly Journal of Engineering Geology and Hydrogeology.* **14**(2), pp.129-141.

Farulla, C.A., Ferrari, A. and Romero, E. 2010. Volume change behaviour of a compacted scaly clay during cyclic suction changes. *Canadian Geotechnical Journal.* **47**(6), pp.688-703.

Freeborough, K., Kirkham, M. and Jones, L.D. 2005. *Determination of the shrinking and swelling properties of the London Clay Formation: Laboratory Report - IR/06/058.* Keyworth, Nottingham.

Gajo, A., Fedel, A. and Mongiovì, L. 1997. Experimental analysis of the effects of fluid—solid coupling on the velocity of elastic waves in saturated porous media. *Géotechnique.* **47**(5), pp.993-1008.

Gao, Q.-F., Hattab, M., Jrad, M., Fleureau, J.-M. and Hicher, P.-Y. 2020. Microstructural organization of remoulded clays in relation with dilatancy/contractancy phenomena. *Acta Geotechnica.* **15**(1), pp.223-243.

Gellatley, M.J., McGinnity, B.T., Barker, D.H. and Rankin, W.J. 1995. Interaction of Vegetation with LUL Surface Railway Systems. *Vegetation and slopes: Stabilisation, protection and ecology.* pp.60-71.

Genuchten, V. 1980. A closed-form Eq. for predicting the hydraulic conductivity of unsaturated soils. *Soil Science Journal.* **44**, pp.892-898.

George, L.A., Dewoolkar, M.M. and Znidarcic, D. 2009. Simultaneous Laboratory Measurement of Acoustic and Hydraulic Properties of Unsaturated Soils. *Vadose Zone Journal.* **8**(3), pp.633-642.

Gitirana, G. 2005. *Weather Related Geo-Hazard Assessment Model for railway Embankment Stability* Doctor of Philosophy thesis, University of Saskatchewan.

Glendinning, S., Helm, P., Rouainia, M., Stirling, R., Asquith, J., Hughes, P., Toll, D., Clarke, D., Powrie, W., Smethurst, H., Hughes, D., Kelly, R. and Karim, M. 2015. Research-informed design, management and maintenance of infrastructure slopes: development of a multi-scalar approach. *IOP Conference Series: Earth and Environmental Science.* **26**, pp.207-215.

Glendinning, S., Hughes, P., Helm, P., Chambers, J., Mendes, J., Gunn, D., Wilkinson, P. and Uhlemann, S. 2014. Construction, management and maintenance of embankments used for road and rail infrastructure: implications of weather induced pore water pressures. *Acta Geotechnica.* **9**(5), pp.799-816.

Glendinning, S., Loveridge, F., Starr-Keddle, R.E., Bransby, M.F. and Hughes, P.N. 2009. Role of vegetation in sustainability of infrastructure slopes. *Proceedings of the Institution of Civil Engineers - Engineering Sustainability.* **162**(2), pp.101-110.

Goh, S.G., Rahardjo, H. and Leong, E.C. 2014. Shear Strength of Unsaturated Soils under Multiple Drying-Wetting Cycles. *Journal of Geotechnical and Geoenvironmental Engineering.* **140**(2), pp.6-13.

Greenwood, J.R., Norris, J.E. and Wint, J. 2004. Assessing the contribution of vegetation to slope stability. *Proceedings of the Institution of Civil Engineers - Geotechnical Engineering.* **157**(4), pp.199-207.

Gunn, D., J., D.B.A., Paolo, B. and Shane, D. 2016. Aged embankment imaging and assessment using surface waves. *Proceedings of the Institution of Civil Engineers - Forensic Engineering.* **169**(4), pp.149-165.

Hardin, B.O. 1978. The nature of stress-strain behavior for soils. In: *Volume I of Earthquake Engineering and Soil Dynamics-Proceedings of the ASCE Geotechnical Engineering Division, Pasadena, California*. pp.3-90.

Hardin, B.O. and Richart, F.E. 1963. Elastic Wave Velocities in Granular Soils. *Journal of the Soil Mechanics and Foundations Division.* **89**(1), pp.33-65.

Hasan, A.M. and Wheeler, S.J. 2015. Measuring travel time in bender/extender element tests. *Geotechnical Engineering for Infrastructure and Development.* pp.3171-3176.

Hattab, M. 2011. Critical state notion and microstructural considerations in clays. *Comptes Rendus Mécanique.* **339**(11), pp.719-726.

Head, K.H. 1996. *Manual of soil laboratory testing.* Second edition. ed. Chichester: Wiley.

Head, K.H. and Epps, R.J. 2014. *Manual of soil laboratory testing. Volume 3, Effective stress tests.* [Online]. Third edition ed. Caithness, Scotland: Whittles Publishing. Available from: http://site.ebrary.com/id/10904597

Heitor, A. 2013. *Assessment of post-compaction characteristics of an unsaturated silty sand*. Doctor of Philosophy thesis, University of Wollongong.

Heitor, A., Indraratna, B. and Rujikiatkamjorn, C. 2013. Laboratory study of small-strain behavior of a compacted silty sand. *Canadian Geotechnical Journal.* **50**(2), pp.179-188.

Heitor, A., Indraratna, B. and Rujikiatkamjorn, C. 2015. Effect of suction history on the small strain response of a dynamically compacted soil. In: *12th Conference on Geomechanics Wellington, New Zealand*. pp.61-68.

Heitor, A., Indraratna, B. and Rujikiatkamjorn, C. 2015. The role of compaction energy on the small strain properties of a compacted silty sand subjected to drying–wetting cycles. *Géotechnique.* **65**(9), pp.717-727.

Heitor, A., Indraratna, B. and Rujikiatkamjorn, C. 2016. Small Strain Behaviour of a Compacted Subgrade Soil. *Procedia Engineering.* **143**, pp.260-267.

Heitor, A., Parkinson, J. and Kotzur, T. 2021. The Role of Soil Stabilisation in Mitigating the Impact of Climate Change in Transport Infrastructure with Reference to Wetting Processes. *Applied Sciences.* **11**(3), p1080.

Highways England. 2004. *Design Manual for Roads and Bridges (DMRB), Volume 10, Section 3, Part 2: Landscape Management Handbook.* London: The Stationary Office.

Highways England. 2009. *Climate Change Adaptation Strategy and Framework.* London: Home Office.

Hillel, D. 2003. *Introduction to Environmental Soil Physics.* Burlington: Academic Press.

Hughes, P.N., Glendinning, S., Mendes, J., Parkin, G., Toll, D.G., Gallipoli, D. and Miller, P.E. 2009. Full-scale testing to assess climate effects on embankments. *Proceedings of the Institution of Civil Engineers - Engineering Sustainability.* **162**(2), pp.67-79.

Inci, G., Yesiller, N. and Kagawa, T. 2003. Experimental Investigation of Dynamic Response of Compacted Clayey Soils. *Nazli Yesiller.* **26**(2), pp.125-141.

Jones, L.D. and Hobbs, P.R.N. 2004. *The Shrinkage and Swelling Behaviour of UK Soils: Clays of the Lambeth Group- British Geological Survey Research Report RR/04/01.* Keyworth, Nottingham: BGS.

Jovicic, V., Coop, M.R. and Simic, M. 1996. Objective criteria for determining G_{max} from bender element. *Geotechnique.* **46**(2), pp.357-362.

Khosravi, A., Hashemi, A., Ghadirianniari, S. and Khosravi, M. 2020. Variation of Small-Strain Shear Modulus of Unsaturated Silt under Successive Cycles of Drying and Wetting. *Journal of Geotechnical and Geoenvironmental Engineering.* **146**(7), pp.402-415.

Khosravi, A. and McCartney, J. 2011. Resonant Column Test for Unsaturated Soils With Suction–Saturation Control. *Geotechnical Testing Journal.* **34**, pp.103-102.

Khosravi, A. and McCartney, J.S. 2012. Impact of Hydraulic Hysteresis on the Small-Strain Shear Modulus of Low Plasticity Soils. *Journal of Geotechnical and Geoenvironmental Engineering.* **138**(11), pp.1326-1333.

Khosravi, A., Shahbazan, P. and Pak, A. 2018. Impact of hydraulic hysteresis on the small strain shear modulus of unsaturated sand. *Soils and Foundations.* **58**(2), pp.344-354.

Kim, D.-S., Seo, W.-S. and Kim, M.-J. 2003. Deformation Characteristics of Soils With Variations of Capillary Pressure and Water Content. *Soils and Foundations.* **43**(4), pp.71-79.

Kim, D.-S., Shin, M.-K. and Park, H.-C. 2001. Evaluation of density in layer compaction using SASW method. *Soil Dynamics and Earthquake Engineering.* **21**(1), pp.39-46.

Kitsunezaki, C. 1986. Velocity and attenuation of elastic waves in water-filled sand layers with partial gas saturation and their practical significance. *Geophysical Exploration.* **39**(5), pp.306-321.

Kodikara, J., Islam, T. and Sounthararaja, A. 2018. Review of soil compaction: History and recent developments. *Transportation Geotechnics.* **17**, pp.24-34.

Koliji, A., Laloui, L., Cusinier, O. and Vulliet, L. 2006. Suction Induced Effects on the Fabric of a Structured Soil. *Transport in Porous Media.* **64**(2), pp.261-278.

Koliji, A., Vulliet, L. and Laloui, L. 2010. Structural characterization of unsaturated aggregated soil. *Canadian Geotechnical Journal.* **47**(3), pp.297-311.

Kovacevic, N., Potts, D. and Vaughan, P.R. 2001. Progressive failure in clay embankments due to seasonal climate changes. *Proc Int Conf Soil Mech Geotech Eng.* **3**, pp.2127-2130.

Krautkrämer, J., Krautkrämer, H. and Grabendörfer, W. 1990. *Ultrasonic testing of materials.* Fourth fully revised edition. ed. Berlin: Springer.

Kumar, J. and Madhusudhan, B.N. 2012. Dynamic properties of sand from dry to fully saturated states. *Géotechnique.* **62**(1), pp.45-54.

La Rochelle, P. 1967. Membrane, drain, and area correction in triaxial test on soil samples failing along a single shear plane. In: *3rd Pan-American Conference on Soil Mechanics and Foundation Engineering*, pp.273-292.

Lambe, T.W. 1958. The Structure of Compacted Clays. *Journal of the Soil Mechanics and Foundations Division.* **84**(2), pp.1654-1651-1654-1634.

Lee, J.-S. and Santamarina, J.C. 2005. Bender Elements: Performance and Signal Interpretation. *Journal of Geotechnical and Geoenvironmental Engineering.* **131**(9), pp.1063-1070.

Leong, E.C., Cahyadi, J. and Rahardjo, H. 2009. Measuring shear and compression wave velocities of soil using bender–extender elements. *Canadian Geotechnical Journal.* **46**(7), pp.792-812.

Leong, E.C. and Rahardjo, H. 2002. Factors Affecting the Filter Paper Method for Total and Matric Suction Measurements. *Geotechnical Testing Journal.* **25**.

Leong, E.C., Yeo, S.H. and Rahardjo, H. 2004. Measurement of wave velocities and attenuation using an ultrasonic test system. *Canadian Geotechnical Journal.* **41**(5), pp.844-860.

Leong, E.C., Yeo, S.H. and Rahardjo, H. 2005. Measuring Shear Wave Velocity Using Bender Elements. *Geotechnical Testing Journal.* **28**(5), pp.1-11.

Leroueil, S. 2001. Natural slopes and cuts: movement and failure mechanisms. *Géotechnique.* **51**(3), pp.197-243.

Leroueil, S. and Hight, D. 2003. Behaviour and properties of natural soils and soft rocks. *Characterisation and engineering properties of natural soils.* **1**, pp.29-254.

Li, P. and Shao, S. 2020. Can X-ray computed tomography (CT) be used to determine the pore-size distribution of intact loess? *Environmental earth sciences.* **79**(1), p29.

Li, X., Liang, Z., Ren, K., Yin, S. and Sun, Y. 2023. Effect of Static and Dynamic Methods of Compaction on Mechanical Properties of Silt. *International Journal of Geomechanics.* **23**(7), pp.402-411.

Li, X., Zhang, L.M. and Li, J. 2009. Development of a modified axis translation technique for measuring SWCCs for gravel soils at very low suctions. *Geotechnical testing journal.* **32**(6), pp.478-488.

Likos, W.J. and Lu, N. 2004. Hysteresis of Capillary Stress in Unsaturated Granular Soil. *Journal of Engineering Mechanics.* **130**(6), pp.646-655.

Liu, G., Toll, D., Kong, L.-W. and Asquith, J. 2020. Matric Suction and Volume Characteristics of Compacted Clay Soil under Drying and Wetting Cycles. *Geotechnical Testing Journal.* **43**, pp.201-211.

Liu, W., Sun, X. and Zhou, T. 2020. Impact of drying/wetting on shear stiffness and shear-induced volume change behaviours of unsaturated silty clay. *Iranian Journal of Science and Technology, Transactions of Civil Engineering.* **44**, pp.735-743.

Lloret, A., Villar, M.V., Sánchez, M., Gens, A., Pintado, X. and Alonso, E.E. 2003. Mechanical behaviour of heavily compacted bentonite under high suction changes. *Géotechnique.* **53**(1), pp.27-40.

Loveridge, F., Spink, T.W., O'Brien, A.S., Briggs, K.M. and Butcher, D. 2010. The impact of climate and climate change on infrastructure slopes, with particular reference to southern England. *Quarterly Journal of Engineering Geology and Hydrogeology.* **43**, pp.461-473.

Lowe, J., Bernie, D., Bett, P., Bricheno, L., Brown, S., Calvert, D., Clark, R., Karen, Eagle, Edwards, T., Fosser, G., Maisey, P., McInnes, R., Mcsweeney, C., Yamazaki, K. and Belcher, S. 2019. *UKCP 18 Science Overview Report November 2018 (Updated March 2019).* [Online]. [Accessed 11 April 2021]. Available from: https://www.metoffice.gov.uk/pub/data/weather/uk/ukcp18/science-reports/UKCP18-Overview-report.pdf

Lu, N. 2016. Generalized Soil Water Retention Equation for Adsorption and Capillarity. *Journal of Geotechnical and Geoenvironmental Engineering.* **142**(10), pp.301-319.

Ma, C., Li, J., Jiao, F., Liu, Y., Feng, H., Wang, K., Jiang, H., Jiang, C., Li, Y. and Geng, X. 2023. Physical and Mechanical Behaviors of Compacted Soils under Hydraulic Loading of Wetting–Drying Cycles. *Processes.* **11**(4), p1084.

Ma, R., Cai, C., Li, Z., Wang, J., Xiao, T., Peng, G. and Yang, W. 2015. Evaluation of soil aggregate microstructure and stability under wetting and drying cycles in two Ultisols using synchrotron-based X-ray micro-computed tomography. *Soil and Tillage Research.* **149**, pp.1-11.

Mancuso, C., Vassallo, R. and d'Onofrio, A. 2002. Small strain behavior of a silty sand in controlled-suction resonant column torsional shear tests. *Canadian Geotechnical Journal.* **39**(1), pp.22-31.

Mcginnity, B.T. and Russell, D. 1995. Investigation of London Underground earth structures. *Advances in site investigation practice.* London: Thomas Telford Publishing, pp.230-242.

Mendes, J. 2011. *Assessment of the impact of climate change on an instrumented embankment: an unsaturated soil mechanics approach*. PhD thesis.

Mendes, J. and Toll, D.G. 2016. Influence of Initial Water Content on the Mechanical Behavior of Unsaturated Sandy Clay Soil. *International Journal of Geomechanics.* **16**(6), pD4016005.

Mendoza, C.E. and Colmenares, J.E. 2006. Influence of the Suction on the Stiffness at Very Small Strains. *Unsaturated Soils 2006.* pp.529-540.

Met Office. 2020. *How much does it rain in the UK?* [Online]. [Accessed 31 May 2020]. Available from: https://www.metoffice.gov.uk/weather/learn-about/weather/types-of-weather/rain/how-much-does-it-rain-in-the-uk

Met Office. 2024. *Climate change projections over land.* [Online]. [Accessed 31 May 2024]. Available from: https://www.metoffice.gov.uk/research/approach/collaboration/ukcp/summaries/climate-change-projections-over-land

Mirzababaei, M., Anggraini, V. and Haque, A. 2020. X-ray computed tomography imaging of fibre-reinforced clay subjected to triaxial loading. *Geosynthetics International.* **27**(6), pp.635-645.

Monroy, R., Zdravkovic, L. and Ridley, A. 2010. Evolution of microstructure in compacted London Clay during wetting and loading. *Géotechnique.* **60**(2), pp.105-119.

Moon, S.-W., Ng, Y.C.H. and Ku, T. 2018. Global semi-empirical relationships for correlating soil unit weight with shear wave velocity by void-ratio function. *Canadian Geotechnical Journal.* **55**(8), pp.1193-1199.

Mulmi, S., Sato, T. and Kuwano, R. 2008. Performance of Plate Type Piezo-ceramic Transducers for Elastic Wave Measurements in Laboratory Soil Specimens. *Seisan Kenkyu.* **60**(6), pp.565-569.

Nakagawa, K., Soga, K. and Mitchell, J.K. 1996. Pulse Transmission System for Measuring Wave Propagation in Soils. *Journal of Geotechnical Engineering.* **122**(4), pp.302-308.

Nakagawa, K., Soga, K. and Mitchell, J.K. 1997. Observation of Biot compressional wave of the second kind in granular soils. *Géotechnique.* **47**(1), pp.133-147.

Network Rail. 2015. *Claimte Change Adaptation Report.* London: Network Rail Limited.

Network Rail. 2018. Earthworks Technical Strategy. [Online]. [Accessed 21 October 2020]. Available from: https://www.networkrail.co.uk/wp-content/uploads/2018/07/Earthworks-Technical-Strategy.pdf.

Network Rail. 2020. *Vegetation Management.* [Online]. [Accessed 12 November 2020]. Available from: https://www.networkrail.co.uk/communities/environment/vegetation-management/

Network Rail. 2021. *A Review of Earthworks Management* [Online]. [Accessed 20 August 2021]. Available from: https://www.networkrail.co.uk/wp-content/uploads/2021/03/Network-Rail-Earthworks-Review-Final-Report.pdf

Network Rail. 2021. *A Review of Earthworks Management.* [Online]. [Accessed 20 August 2021]. Available from: https://www.networkrail.co.uk/wp-content/uploads/2021/03/Network-Rail-Earthworks-Review-Final-Report.pdf

Ng, C.W.W. and Menzies, B. 2007. *Advanced Unsaturated Soil Mechanics and Engineering.* Florida, USA: CRC Press.

Ng, C.W.W. and Peprah-Manu, D. 2023. Pore structure effects on the water retention behaviour of a compacted silty sand soil subjected to drying-wetting cycles. *Engineering Geology.* **313**, pp.106-119.

Ng, C.W.W. and Xu, J. 2012. Effects of current suction ratio and recent suction history on small-strain behaviour of an unsaturated soil. *Canadian Geotechnical Journal.* **49**(2), pp.226-243.

Ng, C.W.W., Xu, J. and Yung, S.Y. 2009. Effects of wetting-drying and stress ratio on anisotropic stiffness of an unsaturated soil at very small strains. *Canadian Geotechnical Journal.* **46**(9), pp.1062-1076.

Ng, C.W.W., Xu, J.X. and Y.Yung, S. 2009. Effects of wetting–drying and stress ratio on anisotropic stiffness of an unsaturated soil at very small strains. *Canadian Geotechnical Journal.* **46**(9), pp.1062-1076.

Ng, C.W.W. and Yung, S. 2008. Determination of the anisotropic shear stiffness of an unsaturated decomposed soil. *Géotechnique.* **58**(1), pp.23-35.

Ngoc, T.P. 2020. *Experimental Study on the Small Strain Shear Modulus of Unsaturated Soils*. PhD thesis, University of Technology Sydney.

Ngoc, T.P., Fatahi, B. and Khabbaz, H. 2019. Impacts of Drying-Wetting and Loading-Unloading Cycles on Small Strain Shear Modulus of Unsaturated Soils. *International Journal of Geomechanics.* **19**(8), p04019090.

Ngoc, T.P., Fatahi, B., Khabbaz, H. and Sheng, D. 2020. Impacts of matric suction equalization on small strain shear modulus of soils during air drying. *Canadian Geotechnical Journal.* **57**(12), pp.1982-1997.

Noakes, A.J.P., Mason-Jarvis, L.F., Taylor, G.R. and Evans, E. 2020. Geospatial assessment methods for geotechnical asset management of legacy railway embankments. *Quarterly Journal of Engineering Geology and Hydrogeology.* **53**(2), pp.339-348.

Nowak, P. 2012. Chapter 69 Earthworks design principles. *ICE manual of geotechnical engineering: Volume II.* pp.1043-1046.

Nowak, P. and Gilbert, P. 2015. *Earthworks: a guide.* [Online]. 2 ed. London: ICE. [Accessed 06 Feburary 2020]. Available from: https://www.icevirtuallibrary.com/isbn/9780727741851.

Nowak, P. and Gilbert, P. 2015. Earthworks: an historical perspective. *Earthworks: a guide.* pp.1-14.

Nowamooz, H., Jahangir, E., Masrouri, F. and Tisot, J.-P. 2016. Effective stress in swelling soils during wetting drying cycles. *Engineering Geology.* **210**, pp.33-44.

Nowamooz, H. and Masrouri, F. 2010. Influence of suction cycles on the soil fabric of compacted swelling soil. *Comptes Rendus Geoscience.* **342**(12), pp.901-910.

Nyambayo, V.P., Potts, D.M. and Addenbrooke, T.I. 2004. The Influence Of Permeability On The Stability Of Embankments Experiencing Seasonal Cyclic Pore Water Pressure Changes. In: *Advances in geotechnical engineering: The Skempton conference*, *London, UK*. pp.898-910.

O'Brien, A.S., Ellis, E.A. and Russell, D. 2004. *Old Railway Embankment Clay Fill – Laboratory Experiments, Numerical Modelling and Field Behaviour.* London: Institution of Civil Engineers.

O'Brien, A.S. 2013. *The assessment of old railway embankments: time for a change?* London: Thomas Telford Publishing.

Parker, J.C. and Lenhard, R.J. 1987. A model for hysteretic constitutive relations governing multiphase flow: 1. Saturation-pressure relations. *Water Resources Research.* **23**(12), pp.2187-2196.

Pedrotti, M., Xu, L., Murray, I. and Tarantino, A. 2024. Drying-induced volumetric behaviour of clays interpreted via binary pore-scale modelling. *Computers and Geotechnics.* **165**, p105911.

Pennington, D.S., Nash, D.F. and Lings, M.L. 2001. Horizontally mounted bender elements for measuring anisotropic shear moduli in triaxial clay specimens. *Geotechnical Testing Journal.* **24**(2), pp.133-144.

Perry, J., Pedly, M. and Reid, M. 2003. *Infrastructure embankments C550.* CIRIA: London.

Pham, H., Fredlund, D. and Barbour, S. 2005. A Study of hysteresis models for soil-water characteristic curves. *Canadian Geotechnical Journal.* **42**, pp.1548-1568.

Pincus, H.J., Fam, M. and Santamarina, J. 1995. Study of Geoprocesses with Complementary Mechanical and Electromagnetic Wave Measurements in an Oedometer. *Geotechnical Testing Journal* **18**.

Pires, L.F., Auler, A.C., Roque, W.L. and Mooney, S.J. 2020. X-ray microtomography analysis of soil pore structure dynamics under wetting and drying cycles. *Geoderma.* **362**, p114103.

Porter, O.J. 1939. THE PREPARATION OF SUBGRADES. In.

Prasad, M. and Meissner, R. 1992. Attenuation mechanisms in sands: Laboratory versus theoretical (Biot) data. *Geophysics.* **57**(5), pp.710-719.

Proctor, R.R. 1933. Fundamental principles of soil compaction. *Engineering News Record.* **111**(10), pp.286-289.

Quinn, T. and Brown, M. 2011. Effect of strain rate on isotropically consolidated kaolin over a wide range of strain rates in the triaxial apparatus. In: *Fifth International Symposium on Deformation Characteristics of Geomaterials*: IOS Press, pp.607-613.

RAIB. 2021. *Rail Accident Investigation Interim Report Derailment of a Passenger Train at Carmont, Aberdeenshire 12 August 2020* [Online]. [Accessed 19 August 2021]. Available from: https://assets.publishing.service.gov.uk/government/uploads/system/uploads/attachment_data/file/978828/IR012021_210419_Carmont.pdf

Reddy, B. and Jagadish, K. 1993. The static Compaction of Soils. *Geotechnique.* **43**, pp.337-341.

Reeves, G.M., Sims, I. and Cripps, J. 2006. Clay materials used in construction. *Geological Society Engineering Geology Special Publication.* **21**, pp.1-447.

Ridley, A., McGinnity, B. and Vaughan, P. 2004. Role of pore water pressures in embankment stability. *Proceedings of the Institution of Civil Engineers - Geotechnical Engineering.* **157**(4), pp.193-198.

Rio, J.F.M.E. 2006. *Advances in laboratory geophysics using bender elements*. thesis, University of London, University College London (United Kingdom).

Rojas, J., Mancuso, C. and Danese, D. 2009. Pre-and postconstruction characterization of an embankment fill material. In: *4th Asia Pacific conference on unsaturated soils*, *Newcastle, Australia*. p.455.

Sanchez-Salinero, I., Roesset, J.M. and Stokoe, K.H. 1986. *Analytical studies of body wave propagation and attenuation.* Austin: University of Texas.

Santamarina, J.C. 2003. Soil Behavior at the Microscale: Particle Forces. *Soil Behavior and Soft Ground Construction.* pp.25-56.

Santamarina , J.C., Klein, K. and Fam, M. 2001. *Soils and waves: Particulate materials behaviour characterization and process monitoring.* John Wiley and Sons.

Santamarina, J.C., Klein, K.A., Wang, Y.H. and Prencke, E. 2002. Specific surface: determination and relevance. *Canadian Geotechnical Journal.* **39**(1), pp.233-241.

Sargent, C. 1984. *Britain's railway vegetation.* Cambridge: Institute of Terrestrial Ecology.

Sarsby, R.W. 2013. Compaction and earthworks. *Environmental Geotechnics.* pp.59-76.

Sawangsuriya, A. 2012. Wave Propagation Methods for Determining Stiffness of Geomaterials. *Wave Processes in Classical and New Solids.* Rijeka: IntechOpen.

Sawangsuriya, A., Edil, T. and Bosscher, P. 2009. Modulus-Suction-Moisture Relationship for Compacted Soils in Postcompaction State. *Journal of Geotechnical and Geoenvironmental Engineering.* **135**(10), pp.1390-1403.

Sawangsuriya, A., Edil, T.B. and Bosscher, P.J. 2008. Modulus−suction−moisture relationship for compacted soils. *Canadian Geotechnical Journal.* **45**(7), pp.973-983.

Seed, H.B. and Chan, C.K. 1959. Structure and Strength Characteristics of Compacted Clays. *Journal of the Soil Mechanics and Foundations Division.* **85**(5), pp.87-128.

Serratrice, J.-F. 2022. Static compaction in laboratory of treated fine soils. In: *5th International Seminar on Earthworks in Europe, Prague, Czech Republic*.

Sharma, R. 1998. *Mechanical behaviour of unsaturated highly expansive clays*. thesis, University of Oxford.

Shih, J.Y., Thompson, D.J. and Zervos, A. 2017. The influence of soil nonlinear properties on the track/ground vibration induced by trains running on soft ground. *Transportation Geotechnics.* **11**, pp.1-16.

Shirley, I.M. 1978. *A User's Guide to Diagnostic Ultrasound.* London: Pitman Medical.

Shrestha, A., Jotisankasa, A., Chaiprakaikeow, S., Pramusandi, S., Soralump, S. and Nishimura, S. 2019. Determining Shrinkage Cracks Based on the Small-Strain Shear Modulus–Suction Relationship. *Geosciences.* **9**(9), p362.

Sivakugan, N. 2021. *Soil Mechanics and Foundation Engineering: Fundamentals and Applications.* 1st Edition ed. New York: McGraw-Hill Education.

Sivakumar, V., Tan, W.C., Murray, E.J. and McKinley, J.D. 2006. Wetting, drying and compression characteristics of compacted clay. *Géotechnique.* **56**(1), pp.57-62.

Skempton, A.W. 1996. Embankments and Cuttings on the Early Railways. *Construction History.* **11**, pp.33-49.

Slavova, D.Z., Weidinger, D.M., Sevi, A.F. and Ge, L. 2010. Evaluation of Compacted Silt Characteristics by Ultrasonic Pulse Velocity Testing. *GeoFlorida 2010.* pp.1284-1293.

Smith, J. 2015. *Examining Soil Based Construction Materials through X-Ray Computed Tomography*. Doctor of Philosophy thesis, Durham University.

Stephenson, R. 1978. Ultrasonic Testing for Determining Dynamic Soil Moduli. *ASTM Special Technical Publication.* pp. 179-195.

Stirling, R.A., Glendinning, S. and Davie, C.T. 2017. Modelling the deterioration of the near surface caused by drying induced cracking. *Applied Clay Science.* **146**, pp.176-185.

Stirling, R.A., Toll, D.G., Glendinning, S., Helm, P.R., Yildiz, A., Hughes, P.N. and Asquith, J.D. 2020. Weather-driven deterioration processes affecting the performance of embankment slopes. *Géotechnique.* **71**(9), pp.1-13.

Suits, L., Sheahan, T. and Vesga, L. 2009. Direct Tensile-Shear Test (DTS) on Unsaturated Kaolinite Clay. *Geotechnical Testing Journal.* **32**(5), pp.397-409.

Suits, L., Sheahan, T.C., Leong, E., Yeo, S.H. and Rahardjo, H. 2005. Measuring Shear Wave Velocity Using Bender Elements. *Geotechnical Testing Journal.* **28**(5), pp.488-498.

Sun, W.-J. and Cui, Y.-J. 2018. Investigating the microstructure changes for silty soil during drying. *Géotechnique.* **68**(4), pp.370-373.

Suwal, L.P. and Kuwano, R. 2013. Disk shaped piezo-ceramic transducer for P and S wave measurement in a laboratory soil specimen. *Soils and Foundations.* **53**(4), pp.510-524.

Takahashi, H. and Tachi, Y. 2019. 3D-microstructure analysis of compacted Na-and Cs-montmorillonites with nanofocus X-ray computed tomography and correlation with macroscopic transport properties. *Applied Clay Science.* **168**, pp.211-222.

Take, W.A. and Bolton, M.D. 2011. Seasonal ratcheting and softening in clay slopes, leading to first-time failure. *Géotechnique.* **61**(9), pp.757-769.

Tang, A.M., Hughes, P.N., Dijkstra, T.A., Askarinejad, A., Brenčič, M., Cui, Y.J., Diez, J.J., Firgi, T., Gajewska, B., Gentile, F., Grossi, G., Jommi, C., Kehagia, F., Koda, E., ter Maat, H.W., Lenart, S., Lourenco, S., Oliveira, M., Osinski, P., Springman, S.M., Stirling, R., Toll, D.G. and Van Beek, V. 2018. Atmosphere–vegetation–soil interactions in a climate change context; impact of changing conditions on engineered transport infrastructure slopes in Europe. *Quarterly Journal of Engineering Geology and Hydrogeology.* **51**(2), pp.156-168.

Tang, A.M., Vu, N. and Cui, Y. 2011. Effects of the maximum soil aggregates size and cyclic wetting–drying on the stiffness of a lime-treated clayey soil. In: *Partial Saturation in Compacted Soils*. Géotechnique, pp.35-43.

Tang, C.-S., Cheng, Q., Gong, X., Shi, B. and Inyang, H.I. 2023. Investigation on microstructure evolution of clayey soils: A review focusing on wetting/drying process. *Journal of Rock Mechanics and Geotechnical Engineering.* **15**(1), pp.269-284.

Tarantino, A. 2009. A water retention model for deformable soils. *Géotechnique.* **59**(9), pp.751-762.

Tarantino, A. and Col, E.D. 2008. Compaction behaviour of clay. *Geotechnique.* **58**(3), pp.199-213.

Terzaghi, K. 1926. Principles of final soil classification. *Public Roads.* **8**, pp.41–53.

Thom, R., Sivakumar, R., Sivakumar, V., Murray, E.J. and Mackinnon, P. 2007. Pore size distribution of unsaturated compacted kaolin: the initial states and final states following saturation. *Géotechnique.* **57**(5), pp.469-474.

Toll, D., Lourenço, S., Mendes, J., Gallipoli, D., Evans, F., Augarde, C., Cui, Y., Tang, A.-M., Rojas Vidovic, J., Pagano, L., Mancuso, C., Zingariello, C. and Tarantino, A. 2011. Soil suction monitoring for landslides and slopes. *Quarterly Journal of Engineering Geology and Hydrogeology.* **44**, pp.23-33.

Toll, D., Mendes, J., Gallipoli, D., Glendinning, S. and Hughes, P. 2012. Investigating the impacts of climate change on slopes: Field measurements. *Geological Society London Engineering Geology Special Publications.* **26**, pp.151-161.

van Genuchten, M.T. 1980. A Closed-form Equation for Predicting the Hydraulic Conductivity of Unsaturated Soils. *Soil Science Society of America Journal.* **44**(5), pp.892-898.

Vanapalli, S. 2009. Shear strength of unsaturated soils and its applications in geotechnical engineering practice. In: *Keynote Address 4th Asia-Pacific Conf. on Unsaturated Soils. New Castle, Australia*, pp.579-598.

Vanapalli, S.K. and Fredlund, D.G. 2000. Comparison of Different Procedures to Predict Unsaturated Soil Shear Strength. *Advances in Unsaturated Geotechnics.* pp.195-209.

Vanapalli, S.K., Fredlund, D.G. and Pufahl, D.E. 1996. The Relationship Between the Soil-Water Characteristic Curve and the Unsaturated Shear Strength of a Compacted Glacial Till. *Geotechnical Testing Journal* **19**(3), pp.259-268.

Varley, J. 2018. *The Network Rail Vegetation Management Review.* London: Home Office.

Vassallo, R., Mancuso, C. and Vinale, F. 2007. Effects of net stress and suction history on the small strain stiffness of a compacted clayey silt. *Canadian Geotechnical Journal.* **44**(4), pp.447-462.

Vesga, L.F. 2008. Equivalent Effective Stress and Compressibility of Unsaturated Kaolinite Clay Subjected to Drying. *Journal of Geotechnical and Geoenvironmental Engineering.* **134**(3), pp.366-378.

Viggiani, G. and Atkinson, J.H. 1995. Interpretation of bender element tests. *Geotechnique.* **45**(1), pp.149–154.

Vinale, F., d'Onofrio, A., Mancuso, C., Santucci, F. and Tatsuoka, F. 1999. The pre-failure behaviour of soils as construction materials. In: *Second International Conference on Pre-failure Behaviour of Geomaterials Torino, Italy*. pp.27-29.

Walker, C., Heitor, A. and Clarke, B. 2022. Influence of Weather-Driven Processes on the Performance of UK Transport Infrastructure with Reference to Historic Geostructures. *Applied Sciences.* **12**(15), p7461.

Walker, C., Heitor, A. and Clarke, B.G. 2023. Impact of drying-wetting cycles on the small strain behaviour of compacted clay. *Transportation Geotechnics.* **42**, p101063.

Wang, G. and Wei, X. 2015. Modeling swelling–shrinkage behavior of compacted expansive soils during wetting–drying cycles. *Canadian Geotechnical Journal.* **52**(6), pp.783-794.

Weidinger, D. 2008. *Laboratory Analysis of Small Strain Moduli in Compacted Silts*. Masters thesis, Missouri University.

Whalley, W.R., Jenkins, M. and Attenborough, K. 2012. The velocity of shear waves in unsaturated soil. *Soil and Tillage Research.* **125**, pp.30-37.

Wheeler, S.J., Sharma, R.S. and Buisson, M.S.R. 2003. Coupling of hydraulic hysteresis and stress–strain behaviour in unsaturated soils. *Géotechnique.* **53**(1), pp.41-54.

Wu, S., Gray, D.H. and Richart Jr, F. 1984. Capillary effects on dynamic modulus of sands and silts. *Journal of Geotechnical Engineering.* **110**(9), pp.1188-1203.

Xu, J. and Zhou, C. 2016. A simple model for the hysteretic elastic shear modulus of unsaturated soils. *Journal of Zhejiang University-Science A.* **17**(7), pp.589-596.

Yeadon, H.L. 2010. Preston By-pass: the first motorway in the UK. *Proceedings of the Institution of Civil Engineers - Engineering History and Heritage.* **163**(2), pp.117-128.

Yesiller, N., Inci, G. and Miller, C. 2000. Ultrasonic Testing for Compacted Clayey Soils. *Civil and Environmental Engineering.* **287**, pp.54-68.

Ying, Z., Cui, Y.-J., Benahmed, N. and Duc, M. 2021. Changes of small strain shear modulus and microstructure for a lime-treated silt subjected to wetting-drying cycles. *Engineering Geology.* **293**, p106334.

Zhang, L., Zhang, S., Liu, X. and Sun, Y. 2021. Characterizing the Effect of Water Content on Small-Strain Shear Modulus of Qiantang Silt. *Journal of Marine Science and Engineering.* **9**(12), p1363.

Zhiming, C., Danda, S. and Gary, F. 2023. Mechanical behaviour of soil under drying–wetting cycles and vertical confining pressures. *Environmental Geotechnics.* **1**, pp.1-11.

Zhongzhi, F., Shengshui, C., Enyue, J., Guoying, L. and Yang, L. 2020. Using Clay-Gravel Mixtures as the Impervious Core Materials in Rockfill Dams. In: Zhongzhi, F. and Erich, B. eds. *Dam Engineering.* Rijeka: IntechOpen, p.Ch. 1.

Appendix A
Literature Review Addendum

A.1 General

This section provides additional information to Sections 2.5 presented in the literature review. For this, it details further information regarding climate change modelling in the UK, the role of plasticity for in unsaturated soils and a review of research concerning formation of desiccation in compacted soils.

A.2 Climate change

Historic geostructures will experience changes in their geomechanical performance due to variations of seasonal patterns of precipitation and drought owing to increases in surface temperature. These predicted future surface temperature changes are based on several scenarios designated Representative Concentration Pathways (RCP) (Met Office, 2018). RCPs are split by a range of radiative forcing values found in the literature resulting from prediction of internal drivers such as greenhouse gases against a preindustrial baseline, at the year 2100 (van Vuuren et al., 2011). Radiative forcing concerns the net change in radiative flux in the upper atmosphere, expressed as Watts per square meter (IPCC Data Distribution Centre, 2019). The surface temperature change and assumptions for each of the radiative forcing pathways is presented in Table A-1. It clearly demonstrates the indeterminate but probabilistic nature of future temperature change and thus the need to factor these probabilities into infrastructure management and design.

Table A-1 RCPs and their resulting global mean surface temperature change from pre-industrial baseline by 2100 (adapted from Met Office (2018) and van Vuuren et al. (2011)).

RCP (Wm^2)	Temp change by 2081 – 2100 (°C)	Assumptions
2.6	1.6	Population – approx. 8.75 billion by 2100 Global GDP increase of $375 trillion by 2100 Primary energy consumption of 750 EJ by 2100 Use of bioenergy and carbon capture and storage resulting in negative emissions by 2100
4.5	2.8	Population – approx. 9 billion by 2100 Global GDP increase of $300 trillion by 2100 Primary energy consumption of 900 EJ by 2100 Same energy mix as RCP 2.6 but a less extreme move to low carbon technologies and larger energy demand
6.0	2.4	Population – approx. 9.75 billion by 2100 Global GDP increase of $225 trillion by 2100 Primary energy consumption of 750 EJ by 2100 Same use of fossil fuels as RCP 8.5 but reduction in energy demand reduces release of emissions
8.5	4.3	Population – 12 billion by 2100 Low per capita income growth Global GDP increase of $250 trillion by 2100 High primary energy consumption 1750 EJ by 2100 Increase in use of fossil fuels due to low technology development

The understanding of the impact of climate change in the UK began with development of the Climate Change Impacts Review Group (CCIRG), which produced CCIRG91 followed by CCIRG96, in both 1991 and 1996 respectively. Subsequently, in 1998 the UK Climate Impacts Programme (UKCIP) was developed and published the UKCIP98 report. Unlike the original work, UKCIP98 produced climate scenarios which were aimed at assisting with national assessments of the impacts and adaptation to climate change (Hulme and Dessai, 2008). Thereafter, UKCIP02 scenarios produced higher spatial resolutions based off four IPCC storylines (Hulme and Dessai, 2008). More recently, UK Climate Projections (UKCP) have been published beginning with UKCP09 scenarios, in 2009. This approach allowed for future climate to be quantified in probabilistic projections used for understanding uncertainty required for adaptation (Jenkins et al., 2009). UKCP18 represents the most recent generation of these climate models, although as UKCP09 predates UKCP18, UKCP09 is found within much of literature prior to 2018.

UKCP18 builds on past predictions and provides a more precise spatial resolution (Lowe et al., 2019). Figure A-1 shows the observed and future predicted changes for

temperature and precipitation in the UK for UKCP18 (Lowe et al., 2019). Nonetheless, there are several limitations in the scenario predictions of future UK weather conditions made in UKCP18 that can be summarised as follows (Lowe et al., 2019):

- the results are dependent on assumptions made in the RCPs – future pathways may be different or more complex than expected,
- probabilistic projections depend upon several statistical dataset assumptions which are made using expert judgement and may change,
- global climate models have greater confidence for long-term climate averages than extreme events,
- climate projections will evolve with time as modelling methods are improved and computer power is increased.

As a consequence, the predicted range of outcomes for climate change produced by the models should be used with caution. This is especially important for extreme event patterns, which have a significant influence on the impacts of climate on earthworks and built geostructures. While the future climate trends support the conclusion that climate change will impact the behaviour of geostructures the effect and extent of the impacts remain uncertain.

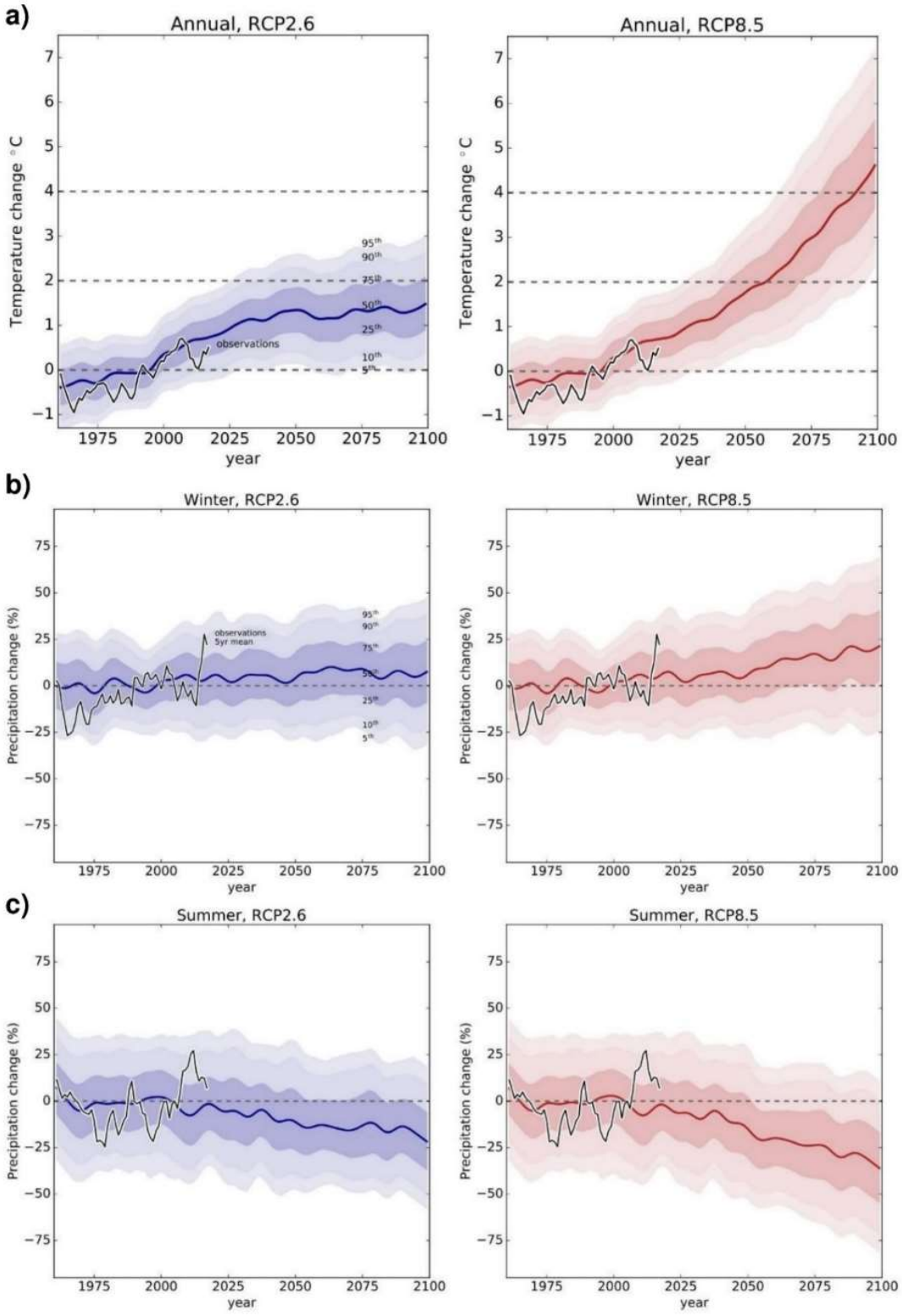


Figure A-1 UK weather data (black lines) and UKCP18 forecasts (median value blue and red lines, while the 5th, 10th, 25th, 50th, 75th, 90th, and 95th percentiles are shaded) represented in terms of: (a) mean temperature; (b) percentage summer precipitation change and (c) percentage winter precipitation change, for both RCP 2.6 in blue and 8.5 in red (contains public sector information licensed under the Open Government Licence v3.0, http://www.nationalarchives.gov.uk/doc/open-government-licence/version/3/, © Crown copyright, Met Office, (2019)).

A.3 Plasticity

During changes in moisture the proportion of clay and its mineralogy, thus plasticity, also significantly influences the unsaturated behaviour of a compacted soil. For instance, significant volume change is associated with high plasticity clays resulting from sorption of water molecules into the interlayer sites of swelling minerals such as smectites (intra-crystalline swelling) (Reeves et al., 2006). This can be captured by measuring the specific surface area (SSA) of a material., Clay minerals in high plasticity soils contain both external and internal surfaces which contribute to relatively large SSA (e.g.,. montmorillonite 0.8km^2/kg versus kaolinite 0.015 0.8km^2/kg) (Arthur et al., 2018). In high plasticity soils, both capillary and physicochemical forces (van der Waals attraction and electric double-layer repulsions) generate suction. This contributes to the wide range of water contents that negative pore water pressures can resist external loading when compared to coarse soils (Zhou and Lu, 2021). Its noted that even small amount of fines can impact the behaviour of coarse grained soils as fines fill larger pore spaces and control permeability (Santamarina et al., 2002).

Past research has also shown the degree of hysteresis (SWRC) between wetting and drying curves is linked to plasticity. Gapak and Tadikonda (2018) tested this relationship on compacted bentonites, where total suction was measured using a combination of Dewpoint Hygrometer and Vapour Equilibrium techniques for both initial drying and main wetting curves. During initial drying, the SWRC of highly plastic samples showed the greatest water retention capacity, converging with lower plasticity SWRC above 5,000 kPa. The relationship between suction and water content of the main wetting path showed identical behaviour. It was also found that higher plasticity bentonites produced an increase in hysteresis i.e. a larger difference between the wetting and drying paths. Another interesting finding was that the relationship between the degree of hysteresis and liquid limit was shown to increase linearly. Gapak and Tadikonda (2018) suggest that this difference results from the microstructural differences in the soil, where higher plasticity clays have a greater number of micropores due to the increase in clay fraction and therefore the SSA.

A.4 Desiccation cracking

The predicted increase in surface temperature is expected to result in an increase in the formation of desiccation cracks during summer months. Desiccation cracks act as preferential pathways for precipitation to percolate into the ground. This results from an increase in near surface permeability and pore water pressures, which is important for historic geostructures e.g. reactivation of relict failures (Tang et al., 2018). Cheng et al. (2020) suggests that factors affecting the formation of desiccation cracks can be

categorised into:

- Internal factors – mineral composition, fines content, water retention characteristics and tensile strength
- External factors – temperature, relative humidity and wetting and drying cycles

Costa et al. (2013) highlighted that desiccation cracks in clay forms due to stress build up at flaws within a material. This is because cracks form when the tensile strength of the soil is exceeded by matric suction induced tensile stresses (Tang et al., 2018a). These flaws include other micro cracks, delamination's, foreign inclusions such as air bubbles or high stiffness particles (sand and gravel). Other influences of desiccation formation include, flaw distribution, soil fracture energy, desiccation rate and particle size distribution.

Cheng et al. (2020) showed that the formation of desiccation cracks is intrinsically linked to compacted soils bimodal pore structure. Testing using image analysis investigated the effect of desiccation on Xiashu compacted soil during air-drying while maintaining measurement of water content. Results showed that for soil samples compacted dry of optimum, random cracks were initiated evenly on the soil surface. In comparison, slurry samples showed branching sub-cracks producing an orthogonal pattern. Furthermore, Mercury Intrusion Porosimetry (MIP) demonstrated that changes in soil microstructure and increase in macro pores (interaggregate pores), when compacted dry side of optimum, were the main influence of the observed desiccation cracking pattern. It is postulated that as the soil volume shrinks the macro pores also shrink and there is a rearrangement of aggregates. These macro pores have a larger pore size resulting in higher strain energy prior to cracking and therefore can be seen as planes of weakness allowing for crack initiation.

It was also shown that soil specimens compacted wet of optimum presented a similar cracking pattern to material prepared as a slurry. This again yields from the pore structure, which is unimodal for both materials. Consequently, it was shown that with an increasing compaction water content, both the water content at the initiation of cracking and crack density decreased, while crack width increased. Therefore, it is likely that soils compacted at lower densities have an increased probability for the development of greater crack density which are initiated at higher water contents. This is relevant to historic compaction techniques used in the construction of geostructures in the UK, as this research suggests they may be more vulnerable to initiation of desiccation cracking at higher water contents.

Both Tang et al. (2019b) and Julina and Thyagaraj (2019) introduced the use of X-ray Computed Tomography (X-ray CT) to measure volumetric changes during shrinkage and internal crack formation. Prior to this, volumetric measurements of desiccation cracks

were primarily undertaken via the Mercury Intrusion Porosimetry (MIP) method. However, Julina and Thyagaraj (2019) showed that the use of X-ray CT and image analysis produces results which are similar to that of MIP. This is advantageous as it is a non-destructive technique and therefore allows for the measurement of the development of volume changes during the drying process. Use of X-ray CT and image analysis by Tang et al. (2019) was able to show the increased accuracy when calculating volumetric shrinkage strain and volume compared to traditional geometric measurements, which underestimated shrinkage up to 90%. Julina and Thyagaraj (2019) also touched upon the effect wetting and drying cycles on desiccation. It was found that after an initial wetting and drying cycle, cracks formed were smaller. After a subsequent cycle of wetting and drying numerous cracks then developed. This was attributed to the change in the bimodal pore structure i.e. the formation of increased macro pores. These findings concur with hypothesis made by Stirling et al. (2020) and therefore would suggest an important link between the microstructure of compacted soils and desiccation cracking present on embankments.

Many detailed microstructural desiccation studies presented in literature are conducted in laboratory conditions on relatively small samples of soil. This is extremely limiting as desiccation cracks interact with vegetation and are not limited by size in the same way as laboratory samples. However, recent publication of work by Yu et al. (2021) describes field testing investigating the development and evolution of desiccation on the Achilles Bionics test embankment. The study was the first prolonged crack survey on transport embankment with meteorological and hydrological data. The data was primarily collected on the southern side of the embankment and produced several interesting findings:

- the poorly compacted panel had the greatest cracks with 11 of the 19 cracks present on the slope,
- a linear cracking style was observed which contrasts with polygonal style generally seen in the laboratory (thought to be a result of root density),
- wind data showed a sheltering of the northern slope while increased solar radiation exposure on the southern face, which resulted in increased vegetation diversity (hypothesized to result in preferential crack formation on the southern slope),
- the upper section of the southern slope was subject to higher matric suctions during drying periods which was attributed to drainage under gravity, increased wind exposure and surface runoff.

Measurement of the developing cracks on the embankment showed four stages of crack propagation: initiation of a crack, expansion of the crack to its maximum width and depth, minor contraction, and closure during winter. Similar patterns have also been observed

in other poorly compacted manmade geostructures in heritage assets such as Baile Hill mound (Figure A-2).



Figure A-2 Example of desiccation cracks observed in Baile Hill (York) heritage asset.

These observations are also in agreement with laboratory data reported by Cheng et al. (2020) where the water content at which desiccation cracking was initiated was directly impacted by compaction conditions. These novel findings demonstrate the holistic nature of engineered soils and the link between the soil pore structure and its behaviour, which has significant implications for its future performance. Compacted soils which have a larger macro pore structure are likely to be more vulnerable to the onset of desiccation cracking. The predicted changes in rainfall and surface temperatures associated with climate change means these preferential pathways will allow water to enter slopes at greater rates and make them vulnerable to pore water pressure changes. This is particularly poignant for historic geostructures due to the reduced compactive effort during their construction.

References

Alawia, M.H. and Rajab, M.I. 2013. Prediction of California bearing ratio of subbase layer using multiple linear regression models. *Road Materials and Pavement Design.* **14**, pp.211–219.

Arthur, E., Tuller, M., Moldrup, P., Greve, M.H., Knadel, M. and de Jonge, L.W. 2018. Applicability of the Guggenheim–Anderson–Boer water vapour sorption model for estimation of soil specific surface area. *European Journal of Soil Science.* **69**(2), pp.245-255.

Atterberg, A. 1911. Die Plastizität der Tone (The plasticity of clays). *Internationale Mitteilung für Bodenkunde.* **1**, pp.4-37.

Briggs, K.M., Loveridge, F.A. and Glendinning, S. 2017. Failures in transport infrastructure embankments. *Engineering Geology.* **219**, pp.107-117.

Casagrande, A. 1932. Research on the Atterberg Limits of Soil. *Public Roads.* **13**, pp.121-136.

Cheng, Q., Tang, C., Zeng, H., Zhu, C., An, N. and Shi, B. 2020. Effects of microstructure on desiccation cracking of a compacted soil. *Engineering Geology.* **265**, pp.105-418.

Costa, S., Kodikara, J. and Shannon, B. 2013. Salient factors controlling desiccation cracking of clay in laboratory experiments. *Géotechnique.* **63**(1), pp.18-29.

Gapak, Y. and Tadikonda, V.B. 2018. Hysteretic Water-Retention Behavior of Bentonites. *Journal of Hazardous, Toxic, and Radioactive Waste.* **22**(3), p04018008.

Gellatley, M.J., McGinnity, B.T., Barker, D.H. and Rankin, W.J. 1995. Interaction of Vegetation with LUL Surface Railway Systems *Vegetation and slopes: Stabilisation, protection and ecology.* pp.60-71.

Glendinning, S., Loveridge, F., Starr-Keddle, R.E., Bransby, M.F. and Hughes, P.N. 2009. Role of vegetation in sustainability of infrastructure slopes. *Proceedings of the Institution of Civil Engineers - Engineering Sustainability.* **162**(2), pp.101-110.

Greenwood, J.R., Norris, J.E. and Wint, J. 2004. Assessing the contribution of vegetation to slope stability. *Proceedings of the Institution of Civil Engineers - Geotechnical Engineering.* **157**(4), pp.199-207.

Highways England. 2004. *Design Manual for Roads and Bridges (DMRB), Volume 10, Section 3, Part 2: Landscape Management Handbook.* London: The Stationary Office.

Hulme, M. and Dessai, S. 2008. Negotiating future climates for public policy: a critical assessment of the development of climate scenarios for the UK. *Environmental Science and Policy.* **11**, pp.54-70.

IPCC Data Distribution Centre. 2019. Definition of Terms Used Within the DDC Pages. [Online]. [Accessed 20 October 2020]. Available from: https://www.ipcc-data.org/guidelines/pages/glossary/glossary_r.html.

Jenkins, G., Murphy, J., Sexton, D., Lowe, J., Jones, P. and Kilsby, C. 2009. *UK Climate Projection Briefing Report.* [Online]. [Accessed 21 October 2021].

Julina, M. and Thyagaraj, T. 2019. Quantification of desiccation cracks using X-ray tomography for tracing shrinkage path of compacted expansive soil. *Acta Geotechnica.* **14**(1), pp.35-56.

Kodikara, J., Islam, T. and Sounthararaja, A. 2018. Review of soil compaction: History and recent developments. *Transportation Geotechnics.* **17**, pp.24-34.

Lowe, J., Bernie, D., Bett, P., Bricheno, L., Brown, S., Calvert, D., Clark, R., Karen, Eagle, Edwards, T., Fosser, G., Maisey, P., McInnes, R., Mcsweeney, C., Yamazaki, K. and Belcher, S. 2019. *UKCP 18 Science Overview Report November 2018 (Updated March 2019).* [Online]. [Accessed 11/05/2021]. Available from: https://www.metoffice.gov.uk/pub/data/weather/uk/ukcp18/science-reports/UKCP18-Overview-report.pdf

Mcginnity, B.T. and Russell, D. 1995. Investigation of London Underground earth structures. *Advances in site investigation practice.* pp.230-242.

Met Office. 2018. *UKCP18 Guidance: Representative Concentration Pathways.* London: Department for Environment Food & Rural Affairs.

Nowak, P. 2012. Chapter 69 Earthworks design principles. *ICE manual of geotechnical engineering: Volume II.* pp.1043-1046.

Nowak, P. and Gilbert, P. 2015. *Earthworks: a guide.* [Online]. 2 ed. London: ICE. [Accessed 06 Feburary 2020]. Available from: https://www.icevirtuallibrary.com/isbn/9780727741851.

Nowak, P. and Gilbert, P. 2015. Earthworks: an historical perspective. *Earthworks: a guide.* pp.1-14.

O'Brien, A.S., Ellis, E.A. and Russell, D. 2004. *Old Railway Embankment Clay Fill – Laboratory Experiments, Numerical Modelling and Field Behaviour.* London: Institution of Civil Engineers.

Perry, J., Pedly, M. and Reid, M. 2003. *Infrastructure embankments C550.* CIRIA: London.

Porter, O.J. 1939. The Preparation of Subgrades.

Proctor, R.R. 1933. Fundamental principles of soil compaction. *Engineering News Record.* **111**(10), pp.286-289.

Reeves, G.M., Sims, I. and Cripps, J. 2006. Clay materials used in construction. *Geological Society Engineering Geology Special Publication.* **21**, pp.1-447.

Santamarina, J.C., Klein, K.A., Wang, Y.H. and Prencke, E. 2002. Specific surface: determination and relevance. *Canadian Geotechnical Journal.* **39**(1), pp.233-241.

Sargent, C. 1984. *Britain's railway vegetation* Cambridge: Institute of Terrestrial Ecology.

Sarsby, R.W. 2013. Compaction and earthworks. *Environmental Geotechnics.* pp.59-76.

Skempton, A.W. 1996. Embankments and Cuttings on the Early Railways. *Construction History.* **11**, pp.33-49.

Stirling, R.A., Toll, D.G., Glendinning, S., Helm, P.R., Yildiz, A., Hughes, P.N. and Asquith, J.D. 2020. Weather-driven deterioration processes affecting the performance of embankment slopes. *Géotechnique.* **71**(9), pp.1-13.

Tang, A.M., Hughes, P.N., Dijkstra, T.A., Askarinejad, A., Brenčič, M., Cui, Y.J., Diez, J.J., Firgi, T., Gajewska, B., Gentile, F., Grossi, G., Jommi, C., Kehagia, F., Koda, E., ter Maat, H.W., Lenart, S., Lourenco, S., Oliveira, M., Osinski, P., Springman, S.M., Stirling, R., Toll, D.G. and Van Beek, V. 2018a. Atmosphere–vegetation–soil interactions in a climate change context; impact of changing conditions on engineered transport infrastructure slopes in Europe. *Quarterly Journal of Engineering Geology and Hydrogeology.* **51**(2), pp.156-168.

Tang, C., Zhu, C., Leng, T., Shi, B., Cheng, Q. and Zeng, H. 2019b. Three-dimensional characterization of desiccation cracking behavior of compacted clayey soil using X-ray computed tomography. *Engineering Geology.* **255**, pp.1-10.

Terzaghi, K. 1926. Principles of final soil classification. *Public Roads.* **8**, pp.41–53.

van Vuuren, D.P., Edmonds, J., Kainuma, M., Riahi, K., Thomson, A., Hibbard, K., Hurtt, G.C., Kram, T., Krey, V., Lamarque, J.-F., Masui, T., Meinshausen, M., Nakicenovic, N., Smith, S.J. and Rose, S.K. 2011. The representative concentration pathways: an overview. *Climatic Change.* **109**(1), p5.

Yeadon, H.L. 2010. Preston By-pass: the first motorway in the UK. *Proceedings of the Institution of Civil Engineers - Engineering History and Heritage.* **163**(2), pp.117-128.

Yu, Z., Eminue, O.O., Stirling, R., Davie, C. and Glendinning, S. 2021. Desiccation cracking at field scale on a vegetated infrastructure embankment. *Géotechnique Letters.* **11**(1), pp.88-95.

Zhou, B. and Lu, N. 2021. Correlation between Atterberg Limits and Soil Adsorptive Water. *Journal of Geotechnical and Geoenvironmental Engineering.* **147**(2), p04020162.

Appendix B
Methodology Addendum

B.1 General

This appendices provides further details with reference to the methodology in Section 3. This includes details regarding the ratio of components used to produce selected soil mixtures in Table B-1. A summary of reported index properties of soils in the UK, used to select characteristics of the soil mixtures, are also presented in Table B-2. This is then followed by the presentation of the measurement attenuation using the ultrasonic pulse transmission test for the clayey silt and clayey sandy silt, which complements Section 3.7. Finally an example of the silty clay drying-wetting wave forms are presented to complement the clayey silt and clayey sandy silt wave forms presented in Section 3.7.3.4

Table B-1 Proportion of components used to create soil mixtures.

Components		Clayey sandy silt (%)	Silty clay (%)
RS Minerals Ltd, UK	Ball clay	10	45
	Wyoming Bentonite	5	15
US Silica, USA	MIN-U-SIL5	15	0
	MIN-U-SIL15	5	10
	SIL-COL-SIL	15	30
David Ball Group Ltd, UK	Fraction A	2	0
	Fraction B	8	0
	Fraction C	0	0
	Fraction D	40	0

Table B-2 Summary of the properties of select engineering clays within the UK

Pre-Quaternary Deposits (Southern England)						
Clay Type	Description	Location	Mineral Composition	Atterberg Limits		Particle Size Distribution
				Unweathered	Weathered	
London Clay	Tertiary age, firm to stiff, over-consolidated silty clay which overlies the older Lambeth Beds (Reeves et al., 2006)	Present in the London and Hampshire basins and outcrops in Greater London, Essex, Kent, Hampshire, Sussex, and the Isle of Wight (Cripps and Taylor, 1986)	Silt - quartz Clay -illite 19%, smectite 60%, kaolinite 18%, chlorite 12% (average values) Minor – Feldspar, carbonate and pyrite (Kemp and Wagner, 2006)	LL – (70-84) 77% PL – (23-29) 26% PI – (44-57) 51% Particle density – 2.68 – 2.84 Mg/m^3 (Cripps and Taylor, 1986)	LL – (69-86) 78% PL – (24-29) 27% PI – (43-58) 51% (Reeves et al., 2006)	Clay Fraction – 55% Silt Fraction – 45% Sand Fraction – <1% Gravel Fraction – 0% (Freeborough et al., 2005)
Gault Clay	Cretaceous age, sequence of over-consolidated silty clays, mudstones and thin siltstones which represent the youngest Cretaceous deposit (Reeves et al., 2006)	Outcrops as a narrow strip running north east from Dorset to Norfolk, but also outcrops North and South Downs in south east England (Forster et al., 1995)	Silt – quartz Clay – kaolinite 14%, illite 13%, smectite 71% Minor - calcite macro fossils (Cripps and Taylor, 1987) and (Reeves et al., 2006)	LL – [60-120%] PL – [18-36%] PI – [27-55%] Particle density – 2.6-2.87 Mg/m^3 (Reeves et al., 2006)	LL – [70-92%] PL – [25-34%] PI – [44-80%] (Reeves et al., 2006)	Clay Fraction – 15%-65% Silt Fraction – (similar to clay fraction) Sand Fraction – <1% Gravel Fraction – 0% (Forster et al., 1995)
Weald Clay	Thinly bedded variable clay ranging from silty clay to sand, mudstone and thinly bedded crystalline limestones (Reeves et al., 2006)	The outcrop is constrained to the weald basin in south east England and the cliffs of the Isle of Wight (Reeves et al., 2006)	Clay – illite 25%, illite-smectite 29%, kaolinite 24%, chlorite 19% (Reeves et al., 2006)	LL – [36-55] PL – [25-30] PI – [11-28] (Cripps and Taylor, 1987)	LL – [42-82%] PL – [26-31%] PI – [26-40%] (Cripps and Taylor, 1987)	Clay Fraction – 20-32% Silt Fraction – No data Sand Fraction – No data Gravel Fraction – No data

Clay Type	Description	Location	Mineral Composition	Atterberg Limits		Particle Size Distribution
				Unweathered	Weathered	
Kimmeridge Clay	Consists of silty sandy calcareous mudstones and thin siltstones which are known to rapidly weather to clays, well known due to the presence of hydrocarbon (Gallois, 2004)	The outcrop runs continuously from Dorset coast to the Yorkshire coast, generally sub cropping beneath younger rocks or superficial deposits (Gallois, 2004)	Clay – illite 17%, illite-smectite 57%, kaolinite 23% (Reeves et al., 2006)	LL – 51% PL – 22% PI – 29% Given as mean values (Cripps and Taylor, 1987)	*No Data*	Clay Fraction – 57% Silt Fraction – No data Sand Fraction – No data Gravel Fraction – No data
Oxford Clay	Jurassic period, fissured, heavily over-consolidated clay deposited in shallow marine conditions (Reeves et al., 2006)	Present from the south west to north east of England (Batchelder et al., 1998)	Total Wt%: kaolinite 7%, illite 21%, illite-smectite 15%, quartz 28%, calcite 12% Minor: feldspar, gypsum, pyrite and chlorite (Batchelder et al., 1998)	LL – (35-80) 49% PL – (21-25) 24% PI – (23-31) 26% (Reeves et al., 2006)	*No Data*	Clay Fraction – 28% Silt Fraction – 25% Sand Fraction – 47% Gravel Fraction – 0% (Batchelder et al., 1998)
Lias Clay	Clay formations deposited in the Jurassic within a series of basins – diagenesis due to burial has also produced several mudstones rather than over-consolidated clays (Reeves et al., 2006)	Outcrops across England, much like the Oxford Clay, between the south west and north east (P.R.N. Hobbs et al., 2012)	Clay fraction - illite/smectite 48%, illite 27%, kaolinite 19% and chlorite 6% (P.R.N. Hobbs et al., 2012)	LL – [56-75] 59% PL – [25-29] 27% PI – [28-36] 32% (Reeves et al., 2006)	LL – [56-75] 62% PL – [26-34] 30% PI – [26-42] 32% (Reeves et al., 2006)	Clay Fraction – 23-42% Silt Fraction – 44-59% Sand Fraction – 4-13.5% Gravel Fraction – 0-1% (P.R.N. Hobbs et al., 2012)

Quaternary Deposits Glacial Till (Northern England)

Clay Type	Description	Location	Mineral Composition	Atterberg Limits		Particle Size Distribution
				Unweathered	Weathered	
Unweathered Till	Tills are split into several categories depending on their deposition, which has strong influence on their geotechnical properties – the simplest of which is terrestrial and fluvial deposition (Clarke, 2018)	Anglican and Devensian ice sheets covered some 60% of the British Isles as such glacioterrestrial and glaciofluvial deposits found up to Bristol Channel to the Wash (Trenter, 1999)	Holderness Tills silt clay fraction (Bell and Forster, 1991): Illite – <50% Kaolinite – 20-40% Quartz – 5-20%	North-eastern England average: PL – [9-30] 17% LL – [5-61] 40% PI – [0-45] 23% Plasticity has a wide range, depending on the depositional and post depositional processes, usually plotting as CL or CI along the T-line (Reeves et al., 2006)		Cohesive Matrix Till: Gravel Fraction - 0-30% Sand Fraction – 0-30% Fines Fraction – 70-100% Granular Matrix Tills: Gravel Fraction - 0-55% Sand Fraction –30-55% Fines Fraction – 45-70% Well Graded Till: Gravel Fraction - 0-85% Sand Fraction –55-85% Fines Fraction – 15-45% Granular Tills: Gravel Fraction - 0-100% Sand Fraction –85-100% Fines Fraction – 0-15% (Trenter, 1999)
Weathered Tills	Weathered tills are produced by oxidation, hydration and leaching and mechanical disintegration (Clarke, 2018)	Eyles and Sladen (1981) showed that weathering owing to oxidation of Northumberland lodgement tills resulted in an increase in the clay and silt content and therefore also the plasticity up the T-line	Weathering results in the increased presence of active secondary clay minerals		North-eastern England average: PL – [13-32] 20% LL – [27-63] 45% PI – [10-43] 25% Weathering increases silt, clay, and water contents – and therefore increases plasticity ranges from CI to CH (Reeves et al., 2006)	

**Liquid Limit (LL), Plastic Limit (PL), Plasticity Index (PI)*
**Atterberg limits given as either: range and mean [XX-XX%] XX or as first and third quartiles and median (XX-XX) XX%*

B.2 Ultrasonic Attenuation

Attenuation of the acoustic response in porous materials can be used to characterise its microstructural properties e.g. grain size and porosity. Furthermore the associated reduction in amplitude of the received wave may impact determination of the first arrival and thus wave velocity in the time domain (Gao et al., 2022). Material attenuation (α) in a medium can be defined by both scattering (α_s) and absorption (α_a) as follows:

$$\alpha = \alpha_a + \alpha_s \tag{B.1}$$

However, geometric attenuation can also occur where the amplitude of a wave decreases as it spreads within a volume (Owino and Jacobs, 1999). Absorption results from internal friction from work done at material interfaces, elastic hysteresis, heat conduction, relaxation phenomenon and changes in molecular structure. The degrees at which these mechanisms influence attenuation depend on the material phase i.e. liquid, gas, solid and frequency of the wave (Krautkrämer et al., 1990). Scattering losses result from differences of impedance within an inhomogeneous material. The most simple scattering loss occurs at the transducer soil interface where there may be a significant impedance difference. Scattering also depends on the ratio of wave length to the diameter of the inhomogeneity (Szilard, 1982).

In soils, attenuation of ultrasonic waves is therefore dependent on frequency, specimen length, specimen homogeneity, its porosity, grain size and saturation (Krautkrämer et al., 1990; Leong et al., 2004). In this case, a reduction in both mean pore diameter and particle size has been shown to reduce the degree of attenuation within the ultrasonic frequency range for both shear and compressional waves. As a result, sands show increased attenuation when compared to silts and clays (Prasad and Meissner, 1992; Yamamoto and Turgut, 1988). Furthermore, attenuation due to changes in saturation have been shown to be complex due to differences in the propagation of the shear and compressional waves (Oelze et al., 2002; Liu et al., 2002; Lo and Sposito, 2013; Mavko and Nur, 1979; Jia et al., 2021). For example, the compressional wave shows significant changes in attenuation when saturation drops from 100% to 99.9% due to presence of a small amount of gas, which reduces the bulk modulus of the fluid (Nakagawa et al., 1997). In comparison, shear waves propagate through the soil skeleton and as a result, attenuation is associated with changes in the capillary forces (requisite to changes in saturation) which increase the inter-particle contact forces.

However, only few studies have reported soil attenuation in unsaturated conditions during drying and wetting. George et al. (2009) reports attenuation for compacted Bonny silt and a heterogeneous mix of sand, silt and clay sized particles. The results show significant decreases in compressional wave attenuation during drying from saturated

conditions and hysteresis between drying and wetting paths. However, shear wave attenuation was shown to remain relatively constant over 100 kPa matric suction range tested. The soils tested had less than 5% fines, and a water retention behaviour typical of silts and sands (residual states achieved at 100kPa matric suction). It is likely that for soils with larger percentages of clay size particles, the shear wave attenuation would show some connection to the water retention behaviour as there is a larger variation in matric suction and microstructural changes. Therefore, in section the attenuation during drying-wetting cycles is also evaluated to further understand the changes in propagation of shear waves using the ultrasonic test system in unsaturated conditions.

Attenuation was determined for the shear wave component of the ultrasonic system to better understand the propagation of waves during changes in water content. The attenuation (α) for specimens of length L was evaluated using the frequency spectra of Fourier transformation of the transmitted (A_t) and received waves (A_r), as follows:

$$\alpha = \frac{1}{L} ln\left(\frac{T \cdot A_t}{A_r}\right) \tag{B.2}$$

$$T = \frac{4 \cdot z \cdot z_s}{(z + z_s)^2} \tag{B.3}$$

Where T is the transmission coefficient for the transducer (z) and specimen (z_s) acoustic impedance. The difference in acoustic impedance of the transducer platen and soil specimen results in reflection of the incident wave (scattering). Calculation of the change in percentage of transmission for the ultrasonic waves during a drying and wetting cycle (assuming that that the transducer impedance is equal to aluminium) is presented in Figure B-1.

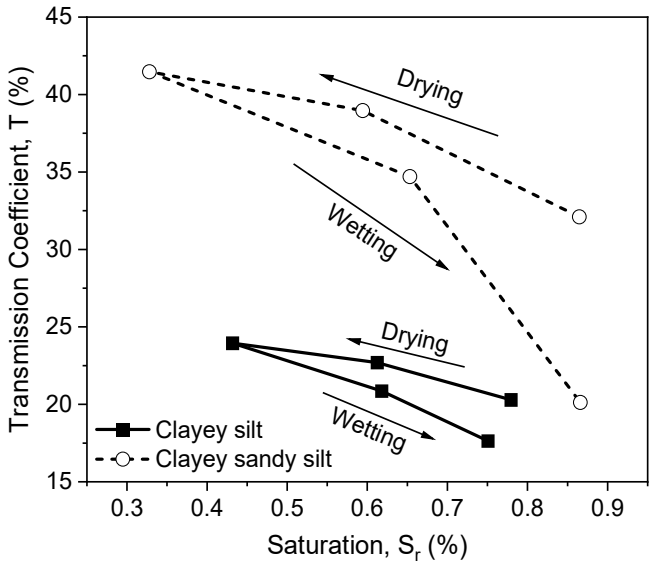


Figure B-1 Transmission coefficient of shear wave soil ultrasonic transducer interface during drying and wetting for compacted: a) clayey silt and b) clayey sandy silt.

As shown in Figure B-1, the clayey silt has a significantly lower transmission coefficient when compared to the clayey sandy silt. This is likely associated with differences in their void ratio and stiffness, thus impedance mismatch between the specimen and transducer. Furthermore, the clayey sandy silt produces a much larger degree of variation in wave transmission during drying and wetting, which reflects the variation in in impedance of the specimen. For example, transmission for the compacted clayey silt has a range of only 6.3% while the clayey sandy silt has a range of 23.9% (Figure B-1). This is important to consider, particularly with significant ranges in water content i.e. scattering at high water contents may result in significant attenuation and distortion of the received signal, thus the need for more appropriate impedance match between the transducer and specimens.

The transmitted magnitude (A_t) of the shear wave transducers was determined from the Fourier transform of the received signal (A_r) for three lengths of aluminium rod (Figure B-2). In this case, A_t is defined as the intercept of the linear trend line with the Y-axis as the transducer impedance and rod impedance are expected to be approximately equal. Furthermore, the slope of the line can be used to determine the attenuation coefficient of the material. Three lengths of compacted kaolin clay are also presented to check the assumption made in Eq. B.3 whereby the Y-axis intercept can be used to determine the transmission coefficient.

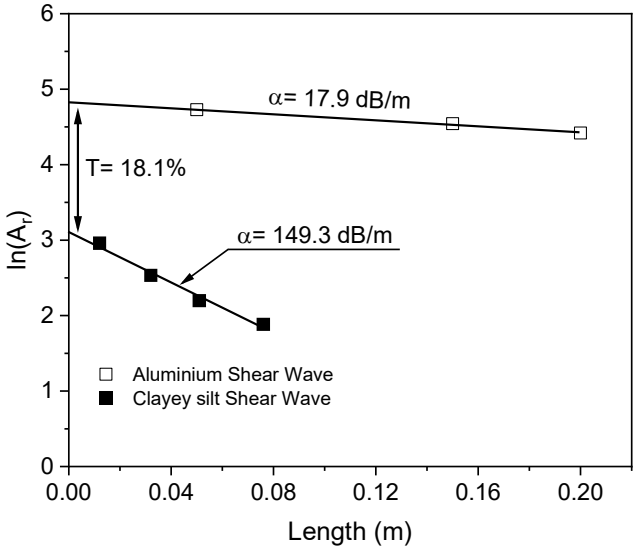


Figure B-2 Variation in ln(A_r) against aluminium and clayey silt specimen lengths for ultrasonic shear wave transducers.

The results show the clayey silt shear wave transmission coefficient at 28% water content was 18.1%, which is in agreement with the calculated value of 21% (Figure B-2). Its thus probable that the impedance of the transducers is slightly greater than assumed. Figure B-3 shows the calculated shear wave attenuation coefficient (α) for the both the clayey silt and clayey sandy silt specimens against saturation (S_r) during the selected drying and wetting cycle. As attenuation is frequency dependant, calculations were completed at approximately same frequencies for both soils during drying and wetting. However, it should be noted the natural frequency of the ultrasonic-soil system is dependent on the stiffness of the specimen which is altered during changes in water content. The results show that for the clayey silt-transducer natural resonant frequency, f_{out} ranges from 21 kHz at the 15% water content and 16 kHz upon wetting at 28% water content. While the compacted clayey sandy silt ranges from 22 kHz at the 5% water content and 12 kHz at 13.5% water content upon wetting. The resonance is therefore within a somewhat narrow range. As result, frequency has considerably smaller influence on attenuation when compared to other factors such as scattering (e.g. Figure B-1).

The results presented in Figure B-2 show good agreement with Figure B-3, i.e. compacted clayey silt attenuation coefficient calculated using Eq. B.2 corresponds to the slope of natural logarithm of the received wave. Furthermore, Figure B-3 shows that the clayey sandy silt experiences greater attenuation compared to the clayey silt at the same saturation, despite the increased transmission coefficient. This is expected as soils with larger average particle size diameter have been shown to have increased attenuation in saturated and dry conditions (Prasad and Meissner, 1992). However, the results confirm

that this is also true for unsaturated conditions on both drying and wetting paths.

Furthermore, both specimens show a significant reduction in attenuation coefficient during drying. For instance, upon drying from the compacted water content (S_r=78%) to 15% water content (S_r = 43%), the clayey silt shows a 78% reduction in attenuation. Both soils also show a hysteretic response whereby the attenuation on the drying path is less than the wetting path. This behaviour is intuitive in the context of changes in suction, saturation and void ratio during drying-wetting pathways.

These results show the feasibility for the use of shear wave attenuation as a qualitative measure of changes in water content and degree of saturation in soils that are incorporated into operational infrastructure. Determination of attenuation coefficient may also provide an estimate of the material in the ground without any intrusive investigation. This would require a wider understanding of the impact of different soil compositions, confining stresses during drying-wetting. The relationship between shear and compressional wave velocities and shear and compressional wave attenuation proposed by Prasad and Meissner (1992) may also aid distinguishing between ground conditions and saturation due to the difference in propagation of the shear wave and compressional wave.

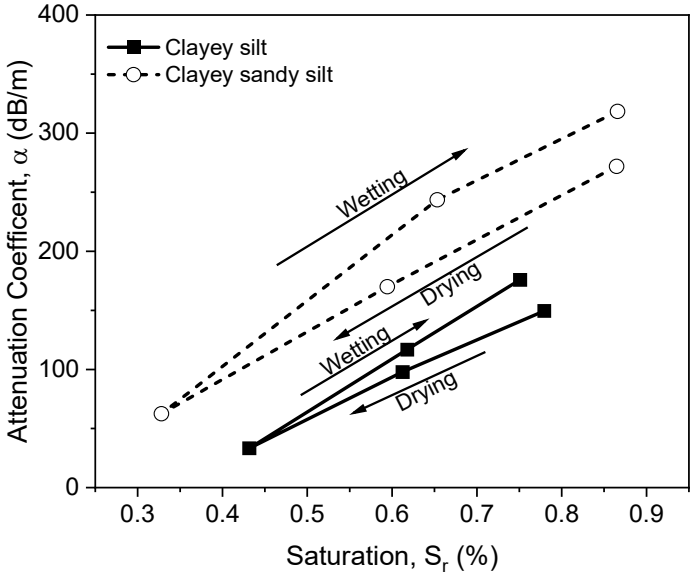


Figure B-3 Attenuation coefficient of shear waves in clayey silt and clayey sandy silt using the ultrasonic system during a drying and wetting cycle.

B.3 Silty clay drying-wetting waveform

An example of the silty clay waveforms collected for the FT drying-wetting pathway, equivalent to drying-wetting waveforms for the clayey silt and clayey sandy silt presented in Section 3.7.3.4, is presented in Figure B-4.

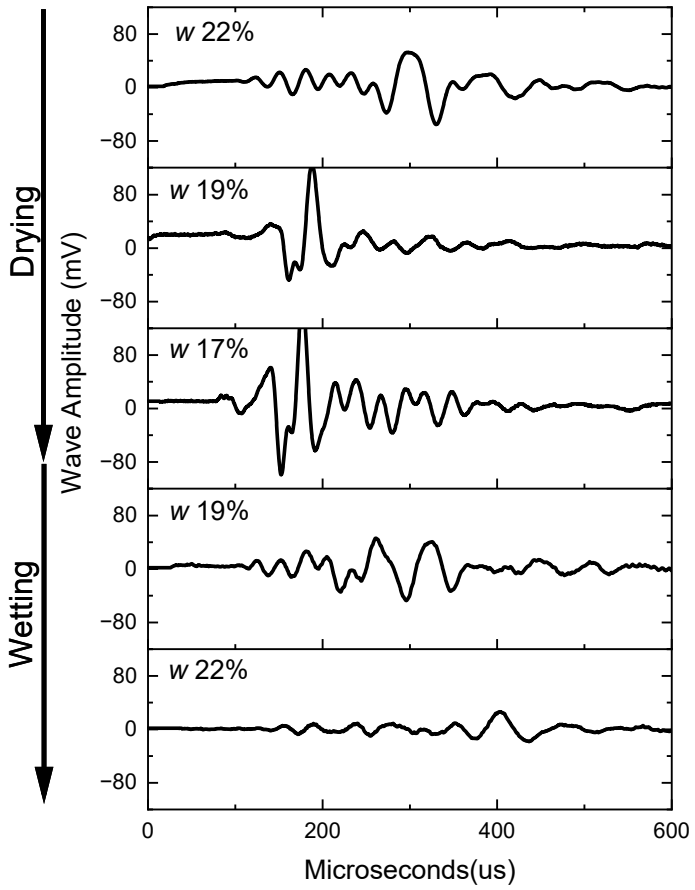


Figure B-4 Silty clay waveforms collected during drying-wetting at select water content levels for FT conditions.

References

Batchelder, M., Mather, J.D. and Joseph, J.B. 1998. The Stability of the Oxford Clay as a Mineral Liner for Landfill. *Water and Environment Journal.* **12**(2), pp.92-97.

Bell, F.G. and Forster, A. 1991. The geotechnical characteristics of the till deposits of Holderness. *Geological Society, London, Engineering Geology Special Publications.* **7**(1), pp.111-118.

Clarke, B.G. 2018. The engineering properties of glacial tills. *Geotechnical Research.* **5**(4), pp.262-277.

Cripps, J.C. and Taylor, R.K. 1986. Engineering Characteristics of British Over-Consolidated Clays and Mudrocks I. Tertiary Deposits. *Engineering Geology.* **22**, pp.349-276.

Cripps, J.C. and Taylor, R.K. 1987. Engineering Characteristics of British Over-consolidated Clays and Mudrocks. II. Mesozoic Deposits *Engineering Geology.* **23**, pp.213-253.

Eyles, N. and Sladen, J.A. 1981. Stratigraphy and geotechnical properties of weathered lodgement till in Northumberland, England. *Quarterly Journal of Engineering Geology and Hydrogeology.* **14**(2), pp.129-141.

Forster, A., Hobbs, P.R.N., Cripps, A.C., Entwistle, D.C., Fenwick, S.M.M., Raines, M.R., Hallam, J.R., Jones, L.D., Self, S.J. and Meakin, J.L. 1995. *Engineering geology of British rocks and soils: Gault clay WN/94/31.* Keyworth, Nottingham

Freeborough, K., Kirkham, M. and Jones, L.D. 2005. *Determination of the shrinking and swelling properties of the London Clay Formation: Laboratory Report - IR/06/058.* Keyworth, Nottingham.

Gallois, R.W. 2004. The Kimmeridge Clay: the most intensively studied formation in Britain. *Journal of the Open University Geological Society.* **25**.

Gao, Y., Zheng, X., Wang, H. and Luo, W. 2022. Effect of Wave Attenuation on Shear Wave Velocity Determination Using Bender Element Tests. *Sensors (Basel).* **22**(3).

George, L.A., Dewoolkar, M.M. and Znidarcic, D. 2009. Simultaneous Laboratory Measurement of Acoustic and Hydraulic Properties of Unsaturated Soils. *Vadose Zone Journal.* **8**(3), pp.633-642.

Jia, F., Cheng, H., Liu, S.-h. and Magnanimo, V. 2021. Elastic wave velocity and attenuation in granular material. *EPJ Web of Conferences.*

Kemp, S.J. and Wagner, D. 2006. *The mineralogy, geochemistry and surface area of mudrocks from the London Clay Formation of southern England - IR/06/060.* Keyworth, Nottingham

Krautkrämer, J., Krautkrämer, H. and Grabendörfer, W. 1990. *Ultrasonic testing of materials.* Fourth fully revised edition. ed. Berlin ;: Springer.

Leong, E.C., Yeo, S.H. and Rahardjo, H. 2004. Measurement of wave velocities and attenuation using an ultrasonic test system. *Canadian Geotechnical Journal.* **41**(5), pp.844-860.

Liu, Z., Rector, J.W., Nihei, K.T., Tomutsa, L., Myer, L.R. and Nakagawa, S. 2002. Extensional wave attenuation and velocity in partially-saturated sand in the sonic frequency range. *SEG Technical Program Expanded Abstracts 2001.* pp.1808-1811.

Lo, W.-C. and Sposito, G. 2013. Acoustic waves in unsaturated soils. *Water Resources Research.* **49**(9), pp.5674-5684.

Mavko, G.M. and Nur, A. 1979. Wave attenuation in partially saturated rocks. *GEOPHYSICS.* **44**(2), pp.161-178.

Nakagawa, K., Soga, K. and Mitchell, J.K. 1997. Observation of Biot compressional wave of the second kind in granular soils. *Géotechnique.* **47**(1), pp.133-147.

Oelze, M.L., O'Brien, W.D. and Darmody, R.G. 2002. Measurement of Attenuation and Speed of Sound in Soils. *Soil Science Society of America Journal.* **66**(3), pp.788-796.

Owino, J.O. and Jacobs, L.J. 1999. Attenuation Measurements in Cement-Based Materials Using Laser Ultrasonics. *Journal of Engineering Mechanics.* **125**(6), pp.637-647.

P.R.N. Hobbs, D.C. Entwisle, K.J Northmore, M.G.Sumbler, L.D .Jones, S. Kemp, S. Self, M. Barron and J.L. Meakin. 2012. *Engineering geology of British rocks and soils : Lias Group.* Keyworth: BGS.

Prasad, M. and Meissner, R. 1992. Attenuation mechanisms in sands: Laboratory versus theoretical (Biot) data. *GEOPHYSICS.* **57**(5), pp.710-719.

Reeves, G.M., Sims, I. and Cripps, J. 2006. Clay materials used in construction. *Geological Society Engineering Geology Special Publication.* **21**, pp.1-447.

Szilard, J. 1982. *Ultrasonic Testing: Non-conventional Testing Techniques.* Wiley.

Trenter, N.A. 1999. *Engineering in Glacial Tills C504.* London: CIRIA.

Yamamoto, T. and Turgut, A. 1988. Acoustic wave propagation through porous media with arbitrary pore size distributions. *The Journal of the Acoustical Society of America.* **83**(5), pp.1744-1751.